

University of Louisville

ThinkIR: The University of Louisville's Institutional Repository

Electronic Theses and Dissertations

8-2022

Search for a dark leptophilic scalar produced in association with taupair in electron-positron annihilation at center-of-mass energies near 10.58 GeV.

Diptaparna Biswas
University of Louisville

Follow this and additional works at: <https://ir.library.louisville.edu/etd>



Part of the [Elementary Particles and Fields and String Theory Commons](#)

Recommended Citation

Biswas, Diptaparna, "Search for a dark leptophilic scalar produced in association with taupair in electron-positron annihilation at center-of-mass energies near 10.58 GeV." (2022). *Electronic Theses and Dissertations*. Paper 3967.

<https://doi.org/10.18297/etd/3967>

This Doctoral Dissertation is brought to you for free and open access by ThinkIR: The University of Louisville's Institutional Repository. It has been accepted for inclusion in Electronic Theses and Dissertations by an authorized administrator of ThinkIR: The University of Louisville's Institutional Repository. This title appears here courtesy of the author, who has retained all other copyrights. For more information, please contact thinkir@louisville.edu.

SEARCH FOR A DARK LEPTOPHILIC SCALAR PRODUCED IN
ASSOCIATION WITH $\tau^+\tau^-$ PAIR IN e^+e^- ANNIHILATION AT
CENTER-OF-MASS ENERGIES NEAR 10.58 GeV

By

Diptaparna Biswas

M.S. in Physics, 2017

A Dissertation

Submitted to the Faculty of the

College of Arts and Sciences of the University of Louisville

in Partial Fulfillment of the Requirements

for the Degree of

Doctor of Philosophy

in Physics

Department of Physics and Astronomy

University of Louisville

Louisville, Kentucky

August 2022

Copyright 2022 by Diptaparna Biswas

All rights reserved

SEARCH FOR A DARK LEPTOPHILIC SCALAR PRODUCED IN
ASSOCIATION WITH $\tau^+\tau^-$ PAIR IN e^+e^- ANNIHILATION AT
CENTER-OF-MASS ENERGIES NEAR 10.58 GeV

By

Diptaparna Biswas
M.S. in Physics, 2017

Dissertation approved on

June 30, 2022

by the following dissertation Committee:

Prof. Swagato Banerjee

Prof. Chris Davis

Prof. Thomas Riedel

Prof. David N. Brown

ACKNOWLEDGMENTS

First and foremost, I would like to thank my parents, without the love and support of whom I would not have been where I am today.

I would like to thank Prof. Swagato Banerjee for giving me the opportunity to work with him. I am grateful for his help and support through all the years of my Ph.D. program. I count myself lucky to have an amazing mentor like him.

Many thanks to the Brookhaven National Laboratory for supporting the Ozaki exchange program, which allowed me to be stationed at KEK in Japan and have a first-hand experience with the experiment, and special thanks to Prof. Mikihiko Nakao for being my mentor at KEK and guiding me during and after the period of the Ozaki exchange program.

I thank all members of my Ph.D. thesis committee: Prof. David N. Brown, Prof. Chris L. Davis and Prof. Thomas Riedel. Their engagement with my research and guidance significantly improved my knowledge as well as the quality of this thesis. I thank Prof. John Kielkopf for his kind effort in fixing the L^AT_EX template.

A special thanks to Atanu Pathak for many enlightening discussions and help towards my Ph.D. program.

I am very thankful to the Belle and Belle II collaborations for giving me the opportunity to successfully perform this research.

Last, but not the least, I thank all other professors, my fellow graduate students in the department of Physics and Astronomy at the University of Louisville, friends, and any other people I had the chance to work with.

ABSTRACT

SEARCH FOR A DARK LEPTOPHILIC SCALAR PRODUCED IN ASSOCIATION WITH $\tau^+\tau^-$ PAIR IN e^+e^- ANNIHILATION AT CENTER-OF-MASS ENERGIES NEAR 10.58 GeV

Diptaparna Biswas

June 30, 2022

Dark matter is believed to be a form of matter which seemingly accounts for approximately 85% of the matter in the universe and about 27% of its total mass-energy density. It doesn't participate in electromagnetic interaction, i.e. doesn't interact with light. Consequently, we cannot 'see' it using optical or radio telescope and hence the name 'dark' matter. However, it participates in gravitational interaction, and we hypothesize its existence based on a variety of astrophysical observations, including gravitational effects, that cannot be explained by the accepted theories of gravity unless we account for more matter than can be perceived through electromagnetic interaction. Apart from explaining those observations, the existence of dark matter may also explain the anomalous magnetic moment of muon, violation of lepton flavor universality, or may unlock the path towards supersymmetry. In brief, the existence of dark matter will not only provide us a signature of 'new physics', but it is also crucial in establishing a scientific understanding of the observed universe.

The existence of dark matter can be probed in various ways, one of them is called 'collider search', where highly energetic particles are smashed together to form

unstable and exotic particles. Along with dark matter, new force-carrier particles that interact with dark matter can also be searched for in such experiments. This kind of interaction is known as dark interaction and together with dark matter, they form the ‘dark sector’ of particles, something beyond the standard model of particle physics. In this thesis, a search for such dark sector candidates that couple with tau lepton is presented, which has been carried out using the collision data at (or near) $\Upsilon(4S)$ resonance collected using the improved silicon vertex detector, the so-called SVD2 dataset, from the Belle experiment.

The Belle II detector, successor of this Belle detector, is built around the world’s highest luminosity electron-positron collider SuperKEKB, located at the KEK accelerator complex in Japan. In this thesis, a general overview of the SuperKEKB accelerator and the Belle II experiment is also presented. On the technical contribution part, my job as the deputy of operations and slowcontrol developer for the K-long and Muon (KLM) detector is discussed in this thesis. Also, my contribution in the upgrade of various parts of the Data Acquisition (DAQ) system of this experiment is described in detail.

TABLE OF CONTENTS

Acknowledgments	iii
Abstract	iv
List of Tables	ix
List of Figures	x
Introduction	1
I.1 Observational evidence of dark matter	2
I.2 Dark matter candidates	6
I.3 Dark sector: dark matter and dark forces	8
I.4 Search strategies for dark sector candidates	9
I.5 Overview of this thesis	10
SuperKEKB accelerator and Belle II experiment	12
II.1 Introduction	12
II.2 The SuperKEKB accelerator	13
II.3 Overview of the Belle II experiment	14
II.4 Detectors used at the Belle II experiment	14
II.5 Trigger System	22
Slowcontrol system of the KLM detector	26
III.1 Overview of the K-Long and Muon (KLM) detector	26

III.2	Dark current monitoring for KLM background measurement	32
III.3	Slowcontrol interfaces for the status and configuration registers of the KLM frontend electronics	32
III.4	RPC gasflow monitoring system	34
III.5	Interlock system for KLM high-voltage supply	35
	Upgrade of the Data Acquisition (DAQ) system	37
IV.1	Overview of the DAQ system of the Belle II experiment	37
IV.2	Upgrade of the DAQ database systems	44
IV.3	Improvement of the configuration software for the trigger timing dis- tribution system	45
IV.4	Development of the slow-control system for the PCIe40 based readout	45
	Dark scalar model and Monte Carlo (MC) generation	47
V.1	Effect of initial state radiation (ISR)	50
V.2	Signal cross-section calculation	51
V.3	Comparing two complementary processes with identical final states .	53
V.4	Signal Monte-Carlo sample generation	54
	Analysis of Belle data	55
VI.1	Outline of the analysis	55
VI.2	KEKB accelerator and Belle Detector	57
VI.3	Data and Monte-Carlo samples	60
VI.4	Reconstruction	62
VI.5	Results from blinded analysis	106
VI.6	Results from unblinded analysis	111
	Summary and Outlook	133
	REFERENCES	135

Appendix A: Feynman diagrams of the signal process	141
For $e^+e^- \rightarrow \tau^+\tau^-\phi_L, \phi_L \rightarrow e^+e^-$ channel	141
For $e^+e^- \rightarrow \tau^+\tau^-\phi_L, \phi_L \rightarrow \mu^+\mu^-$ channel	144
Appendix B: Comparison between two methods of selecting the ϕ_L candidate .	146
Appendix C: Study of the photon conversion vertices	148
Appendix D: Data-MC comparison plots for BDT input variables	151
For $e^+e^- \rightarrow \tau^+\tau^-\phi_L, \phi_L \rightarrow e^+e^-$ channel	151
For $e^+e^- \rightarrow \tau^+\tau^-\phi_L, \phi_L \rightarrow \mu^+\mu^-$ channel	161
Appendix E: BDT diagnostic plots	170
Kolmogorov-Smirnov test for overtraining detection	170
ROC curves and AUC scores	172
Curriculum Vitae	174

LIST OF TABLES

1	Properties of different dark matter candidates.	7
2	List of the available MC samples relevant to this analysis. The cross-section values listed in this table are the ones used for the MC sample production.	60
3	List of scale factors for $\phi_L \rightarrow e^+e^-$ (left) and $\phi_L \rightarrow \mu^+\mu^-$ (right) channels, along with their errors. The compositions are calculated from the respective general control regions.	100
4	The background compositions of the invariant mass distributions in the general control regions of $\phi_L \rightarrow e^+e^-$ (top) and $\phi_L \rightarrow \mu^+\mu^-$ (bottom) channels.	106

LIST OF FIGURES

1	Galactic rotation curve	3
2	Gravitational lensing	4
3	Coma cluster	5
4	Bullet cluster	6
5	Dark matter detection experiments	9
6	SuperKEKB and Belle II	13
7	Pixel Detector (PXD)	15
8	Silicon Vertex Detector (SVD)	16
9	Vertex Detector (VXD)	17
10	Central Drift Chamber (CDC)	18
11	Time of Propagation (TOP) counter	20
12	Aerogel Ring Imaging Cherenkov (ARICH) detector	20
13	Different parts of the KLM detector. BB, BF, EB and EF stand for barrel backward, barrel forward, endcap backward and endcap forward respectively.	29
14	Different components of the KLM frontend electronics.	30
15	Live background level monitoring plots for different sub-detectors as displayed in the Belle II Commissioning Group (BCG) control room. The pink trace in the top plot corresponds to the KLM background level.	33
16	The interface between the KLM status and configuration registers and different DAQ databases.	33

17	The gas mixing station for the KLM detector, producing a mixture of argon, Freon and butane.	34
18	The GUI to monitor RPC gas supply status, as displayed on the KLM shifter PC.	35
19	Different components of the RPC gasflow monitoring system.	36
20	Different components of the KLM high voltage interlock system.	36
21	Initial design of the Belle II data acquisition system	38
22	Image of a Common Pipelined Platform for Electronics Readout (COPPER) board. Each of the four slots, as seen on the left side of the image, is connected to a daughter board, called High-Speed Link Board (HSLB) and serves one belle2link connection.	39
23	Image of a PCIe40 readout card. There are total 48 slots for belle2link connections, some of them are visible on the left side of the image.	40
24	Image of an FTSW board.	42
25	The slow-control system for the PCIe40 based readout system.	46
26	The RunControl GUI for the PCIe40 based readout system.	46
27	The 90% CL limits on the coupling ξ as a function of the ϕ_L mass from <i>BABAR</i> (green) and other experiments (gray). The parameter space preferred by the muon anomalous magnetic moment is shown as a red band.	48
28	Dominant Feynman diagrams for the $e^+e^- \rightarrow \tau^+\tau^-\phi_L$, $\phi_L \rightarrow e^+e^-$ process.	49
29	Dominant Feynman diagrams for $e^+e^- \rightarrow \tau^+\tau^-\phi_L$, $\phi_L \rightarrow \mu^+\mu^-$ process.	49
30	Comparison of $\ell^+\ell^-$ invariant mass distributions between KKMC/PHOTOS and MadGraph/MGISR generators for two SM processes: $e^+e^- \rightarrow \mu^+\mu^-$ (left) and $e^+e^- \rightarrow \tau^+\tau^-$ (right).	50
31	Decay width of the $\phi_L \rightarrow e^+e^-$ and $\phi_L \rightarrow \mu^+\mu^-$ processes (left) and the branching ratios of the different decay modes of the dark scalar (right) as a function of its mass, for $\xi = 1$	51

32	Cross-section of the signal process $e^+e^- \rightarrow \tau^+\tau^-\phi_L, \phi_L \rightarrow e^+e^-$ for $\xi = 1$ as a function of the dark scalar mass.	52
33	Cross-section of the signal process $e^+e^- \rightarrow \tau^+\tau^-\phi_L, \phi_L \rightarrow \mu^+\mu^-$ as a function of the dark scalar mass, for $\xi = 1$. The cross-section is shown in both linear (left) and log (right) scale.	52
34	Comparison of the cross-sections of $e^+e^- \rightarrow \tau^+\tau^-\phi_L, \phi_L \rightarrow \mu^+\mu^-$ and $e^+e^- \rightarrow \mu^+\mu^-\phi_L, \phi_L \rightarrow \tau^+\tau^-$ processes for different ϕ_L mass points.	53
35	The KEKB accelerator complex.	58
36	The Belle detector.	59
37	Distribution of the e^+e^- invariant mass for ϕ_L candidates with different opening angle ranks at two different mass points ($\phi_L \rightarrow e^+e^-$ channel).	63
38	Distribution of the $\mu^+\mu^-$ invariant mass for ϕ_L candidates with different opening angle ranks at two different mass points ($\phi_L \rightarrow \mu^+\mu^-$ channel).	64
39	Fraction of MC truth matched ϕ_L candidates corresponding to different opening angle ranks. This shows the fraction of signal we retain by selecting only the smallest opening angle candidate, for different mass points in $\phi_L \rightarrow e^+e^-$ (left) and $\phi_L \rightarrow \mu^+\mu^-$ (right) channels.	64
40	Signal distribution of e^+e^- invariant mass for different ϕ_L mass points.	66
41	Signal distribution of $\mu^+\mu^-$ invariant mass for different ϕ_L mass points.	66
42	Rectangular sideband cuts are to suppress the two-photon and $\ell^+\ell^-$ backgrounds.	68
43	Result of TauDecayMarker showing the τ^+ and τ^- decay modes in SM taupair sample, for $\phi_L \rightarrow e^+e^-$ channel. The bottom plot is a zoomed in version of the lower left corner of the top plot.	70
44	ρ^- decay modes, faking the signal process.	71
45	Distribution of the invariant mass of the ϕ_L candidate and its closest photon	72
46	Finding the optimal veto window to suppress the ρ^- decay events	73

47	Reducing the SM backgrounds in $\phi_L \rightarrow e^+e^-$ channel without noticeable decrease in signal strength using the background suppression cuts. The signal sample in this plot was generated with $m_{\phi_L} = 50$ MeV. In the legend, $b\bar{b}$ should be understood as $B\bar{B}$. This applies to all figures in this document.	74
48	Distributions of the BDT input variables used for $\phi_L \rightarrow e^+e^-$ channel.	79
49	Correlation among the BDT input variables for the signal sample in $\phi_L \rightarrow e^+e^-$ channel. The signal sample used for this BDT training is obtained by mixing signal events for $m_{\phi_L} = 30$ MeV, 40 MeV, 50 MeV, 60 MeV, 70 MeV, 80 MeV, 90 MeV, 100 MeV, 120 MeV, 140 MeV, 150 MeV, 160 MeV, 180 MeV and 200 MeV in equal proportions.	80
50	Correlation among the BDT input variables for the $\tau^+\tau^-$ sample in $\phi_L \rightarrow e^+e^-$ channel.	81
51	Correlation among the BDT input variables for the e^+e^- sample in $\phi_L \rightarrow e^+e^-$ channel.	82
52	Correlation among the BDT input variables for the $q\bar{q}$ sample in $\phi_L \rightarrow e^+e^-$ channel.	83
53	Correlation among the BDT input variables for the $b\bar{b}$ sample in $\phi_L \rightarrow e^+e^-$ channel.	84
54	Distributions of the different BDT scores for signal and background MC samples, for $\phi_L \rightarrow e^+e^-$ channel. The plot on the right shows the relative contribution of each input variable.	85
55	Distribution of signal_score for different MC samples in $\phi_L \rightarrow e^+e^-$ channel. This variable is used to define our signal region and general control region.	85
56	Distributions of the BDT input variables used for $\phi_L \rightarrow \mu^+\mu^-$ channel.	88

57	Correlation among the BDT input variables for the signal sample in $\phi_L \rightarrow \mu^+\mu^-$ channel. The signal sample used for this BDT training is obtained by mixing signal events for $m_{\phi_L} = 0.225$ GeV, 0.5 GeV, 1.0 GeV, 2.0 GeV and 5.0 GeV in equal proportions.	89
58	Correlation among the BDT input variables for the $\tau^+\tau^-$ sample in $\phi_L \rightarrow \mu^+\mu^-$ channel.	90
59	Correlation among the BDT input variables for the $\mu^+\mu^-$ sample in $\phi_L \rightarrow \mu^+\mu^-$ channel.	91
60	Correlation among the BDT input variables for the $q\bar{q}$ sample in $\phi_L \rightarrow \mu^+\mu^-$ channel.	92
61	Correlation among the BDT input variables for the $b\bar{b}$ sample in $\phi_L \rightarrow \mu^+\mu^-$ channel.	93
62	Distributions of the different BDT scores for signal and background MC samples, for $\phi_L \rightarrow \mu^+\mu^-$ channel. The plot on the right shows the relative contribution of each input variable.	94
63	Distribution of signal_score for different MC samples in $\phi_L \rightarrow \mu^+\mu^-$ channel. This variable is used to define our signal region and general control region.	94
64	Result of TauDecayMarker showing the τ^+ and τ^- decay modes in SM taupair sample, for $\phi_L \rightarrow \mu^+\mu^-$ channel. From this plot, we conclude that lots of pions are faking as muons.	96
65	Distribution of thrust before (left) and after (right) applying PID corrections in $\phi_L \rightarrow \mu^+\mu^-$ channel. The signal sample was generated with $m_{\phi_L} = 2$ GeV. The signal distributions are barely visible, as these plots are for the general control region.	96

66	Calculating the scale factors by performing a binned simultaneous fit of the thrust distributions across the two channels. The background suppression cuts are applied in both of these plots. The top two plots are for $\phi_L \rightarrow e^+e^-$ channel and the bottom ones are for $\phi_L \rightarrow \mu^+\mu^-$ channel.	101
67	Distributions of thrust in $\tau^+\tau^-$ control region for $\phi_L \rightarrow e^+e^-$ channel using the scale factors obtained from (left) general control region vs. (right) $\tau^+\tau^-$ control region.	102
68	Distributions of thrust in $q\bar{q}$ control region for $\phi_L \rightarrow e^+e^-$ channel using the scale factors obtained from (left) general control region vs. (right) $q\bar{q}$ control region.	102
69	Distributions of thrust in $b\bar{b}$ control region for $\phi_L \rightarrow e^+e^-$ channel using the scale factors obtained from (left) general control region vs. (right) $b\bar{b}$ control region.	103
70	Distributions of thrust in Bhabha control region for $\phi_L \rightarrow e^+e^-$ channel using the scale factors obtained from (left) general control region vs. (right) Bhabha control region.	103
71	Distributions of thrust in $\tau^+\tau^-$ control region for $\phi_L \rightarrow \mu^+\mu^-$ channel using the scale factors obtained from (left) general control region vs. (right) $\tau^+\tau^-$ control region.	104
72	Distributions of thrust in $q\bar{q}$ control region for $\phi_L \rightarrow \mu^+\mu^-$ channel using the scale factors obtained from (left) general control region vs. (right) $q\bar{q}$ control region.	104
73	Distributions of thrust in $b\bar{b}$ control region for $\phi_L \rightarrow \mu^+\mu^-$ channel using the scale factors obtained from general control region (left) vs. using the ones from $b\bar{b}$ control region (right).	105
74	Distributions of e^+e^- and $\mu^+\mu^-$ invariant masses shown in the general control region (with data)	106

75	Distributions of e^+e^- and $\mu^+\mu^-$ invariant masses shown in the general control region and signal region (without data)	108
76	Distributions of e^+e^- and $\mu^+\mu^-$ invariant mass with cuts <code>signal_score>0.95</code> and <code>signal_score>0.65</code> respectively. The y-axis is in log scale.	109
77	Signal selection efficiency of the BDT	110
78	Distributions of e^+e^- and $\mu^+\mu^-$ invariant mass in signal regions (with data)	111
79	Example of histograms used for HistoSys uncertainties	113
80	Estimating the systematic error associated with the BDT selection efficiency in $\phi_L \rightarrow e^+e^-$ channel.	114
81	Fit results for $m_{\phi_L} = 0.04$ GeV in $\phi_L \rightarrow e^+e^-$ channel.	118
82	Fit results for $m_{\phi_L} = 0.05$ GeV in $\phi_L \rightarrow e^+e^-$ channel.	118
83	Fit results for $m_{\phi_L} = 0.1$ GeV in $\phi_L \rightarrow e^+e^-$ channel.	119
84	Fit results for $m_{\phi_L} = 0.15$ GeV in $\phi_L \rightarrow e^+e^-$ channel.	119
85	Fit results for $m_{\phi_L} = 0.2$ GeV in $\phi_L \rightarrow e^+e^-$ channel.	120
86	Fit results for $m_{\phi_L} = 0.25$ GeV in $\phi_L \rightarrow \mu^+\mu^-$ channel	123
87	Fit results for $m_{\phi_L} = 0.5$ GeV in $\phi_L \rightarrow \mu^+\mu^-$ channel	124
88	Fit results for $m_{\phi_L} = 1.0$ GeV in $\phi_L \rightarrow \mu^+\mu^-$ channel	124
89	Fit results for $m_{\phi_L} = 1.5$ GeV in $\phi_L \rightarrow \mu^+\mu^-$ channel	125
90	Fit results for $m_{\phi_L} = 2.0$ GeV in $\phi_L \rightarrow \mu^+\mu^-$ channel	125
91	Fit results for $m_{\phi_L} = 2.5$ GeV in $\phi_L \rightarrow \mu^+\mu^-$ channel	126
92	Fit results for $m_{\phi_L} = 3.0$ GeV in $\phi_L \rightarrow \mu^+\mu^-$ channel	126
93	Fit results for $m_{\phi_L} = 3.5$ GeV in $\phi_L \rightarrow \mu^+\mu^-$ channel	127
94	Fit results for $m_{\phi_L} = 4.0$ GeV in $\phi_L \rightarrow \mu^+\mu^-$ channel	127
95	Fit results for $m_{\phi_L} = 4.5$ GeV in $\phi_L \rightarrow \mu^+\mu^-$ channel	128
96	Fit results for $m_{\phi_L} = 5.0$ GeV in $\phi_L \rightarrow \mu^+\mu^-$ channel	128
97	Fit results for $m_{\phi_L} = 5.5$ GeV in $\phi_L \rightarrow \mu^+\mu^-$ channel	129
98	Fit results for $m_{\phi_L} = 6.0$ GeV in $\phi_L \rightarrow \mu^+\mu^-$ channel	129
99	Fit results for $m_{\phi_L} = 6.5$ GeV in $\phi_L \rightarrow \mu^+\mu^-$ channel	130

100	Observed upper limits on the cross-section (in black) at 90% CL, and observed significance (in red) for $\phi_L \rightarrow e^+e^-$ channel (top) and $\phi_L \rightarrow \mu^+\mu^-$ channel (bottom) as a function of the dark scalar mass.	131
101	Observed exclusion region in ξ vs. m_{ϕ_L} plot	132
1	Feynman diagrams for $e^+e^- \rightarrow \tau^+\tau^-\phi_L, \phi_L \rightarrow e^+e^-$ process (part 1) . . .	142
2	Feynman diagrams for $e^+e^- \rightarrow \tau^+\tau^-\phi_L, \phi_L \rightarrow e^+e^-$ process (part 2) . . .	143
3	Feynman diagrams for $e^+e^- \rightarrow \tau^+\tau^-\phi_L, \phi_L \rightarrow \mu^+\mu^-$ process (part 1) . .	144
4	Feynman diagrams for $e^+e^- \rightarrow \tau^+\tau^-\phi_L, \phi_L \rightarrow \mu^+\mu^-$ process (part 2) . .	145
5	Comparison between two candidate selection strategies for $\phi_L \rightarrow e^+e^-$ channel.	146
6	Comparison between two candidate selection strategies for $\phi_L \rightarrow \mu^+\mu^-$ channel.	147
7	Distributions of e^+e^- invariant mass and transverse distance from IP for SM taupair background and signal.	149
8	Generator (left) and reconstructed (right) level distributions of the transverse distance of the $\gamma \rightarrow e^+e^-$ vertex from the IP.	149
9	Generator (left) and reconstructed (right) level distributions of the position of the $\gamma \rightarrow e^+e^-$ vertex.	149
10	Generator (left) and reconstructed (right) level distributions of the position of the $\gamma \rightarrow e^+e^-$ vertex along with e^+e^- invariant mass.	150
11	Data-MC comparison of a BDT input variable in $\phi_L \rightarrow e^+e^-$ channel . .	151
12	Data-MC comparison of a BDT input variable in $\phi_L \rightarrow e^+e^-$ channel . .	152
13	Data-MC comparison of a BDT input variable in $\phi_L \rightarrow e^+e^-$ channel . .	152
14	Data-MC comparison of a BDT input variable in $\phi_L \rightarrow e^+e^-$ channel . .	153
15	Data-MC comparison of a BDT input variable in $\phi_L \rightarrow e^+e^-$ channel . .	153
16	Data-MC comparison of a BDT input variable in $\phi_L \rightarrow e^+e^-$ channel . .	154

17	Data-MC comparison of a BDT input variable in $\phi_L \rightarrow e^+e^-$ channel . .	154
18	Data-MC comparison of a BDT input variable in $\phi_L \rightarrow e^+e^-$ channel . .	155
19	Data-MC comparison of a BDT input variable in $\phi_L \rightarrow e^+e^-$ channel . .	155
20	Data-MC comparison of a BDT input variable in $\phi_L \rightarrow e^+e^-$ channel . .	156
21	Data-MC comparison of a BDT input variable in $\phi_L \rightarrow e^+e^-$ channel . .	156
22	Data-MC comparison of a BDT input variable in $\phi_L \rightarrow e^+e^-$ channel . .	157
23	Data-MC comparison of a BDT input variable in $\phi_L \rightarrow e^+e^-$ channel . .	157
24	Data-MC comparison of a BDT input variable in $\phi_L \rightarrow e^+e^-$ channel . .	158
25	Data-MC comparison of a BDT input variable in $\phi_L \rightarrow e^+e^-$ channel . .	158
26	Data-MC comparison of a BDT input variable in $\phi_L \rightarrow e^+e^-$ channel . .	159
27	Data-MC comparison of a BDT input variable in $\phi_L \rightarrow e^+e^-$ channel . .	159
28	Data-MC comparison of a BDT input variable in $\phi_L \rightarrow e^+e^-$ channel . .	160
29	Data-MC comparison of a BDT input variable in $\phi_L \rightarrow \mu^+\mu^-$ channel . .	161
30	Data-MC comparison of a BDT input variable in $\phi_L \rightarrow \mu^+\mu^-$ channel . .	161
31	Data-MC comparison of a BDT input variable in $\phi_L \rightarrow \mu^+\mu^-$ channel . .	162
32	Data-MC comparison of a BDT input variable in $\phi_L \rightarrow \mu^+\mu^-$ channel . .	162
33	Data-MC comparison of a BDT input variable in $\phi_L \rightarrow \mu^+\mu^-$ channel . .	163
34	Data-MC comparison of a BDT input variable in $\phi_L \rightarrow \mu^+\mu^-$ channel . .	163
35	Data-MC comparison of a BDT input variable in $\phi_L \rightarrow \mu^+\mu^-$ channel . .	164
36	Data-MC comparison of a BDT input variable in $\phi_L \rightarrow \mu^+\mu^-$ channel . .	164
37	Data-MC comparison of a BDT input variable in $\phi_L \rightarrow \mu^+\mu^-$ channel . .	165
38	Data-MC comparison of a BDT input variable in $\phi_L \rightarrow \mu^+\mu^-$ channel . .	165
39	Data-MC comparison of a BDT input variable in $\phi_L \rightarrow \mu^+\mu^-$ channel . .	166
40	Data-MC comparison of a BDT input variable in $\phi_L \rightarrow \mu^+\mu^-$ channel . .	166
41	Data-MC comparison of a BDT input variable in $\phi_L \rightarrow \mu^+\mu^-$ channel . .	167
42	Data-MC comparison of a BDT input variable in $\phi_L \rightarrow \mu^+\mu^-$ channel . .	167
43	Data-MC comparison of a BDT input variable in $\phi_L \rightarrow \mu^+\mu^-$ channel . .	168
44	Data-MC comparison of a BDT input variable in $\phi_L \rightarrow \mu^+\mu^-$ channel . .	168

45	Data-MC comparison of a BDT input variable in $\phi_L \rightarrow \mu^+\mu^-$ channel . .	169
46	Data-MC comparison of a BDT input variable in $\phi_L \rightarrow \mu^+\mu^-$ channel . .	169
47	Distributions of each BDT score for train and test datasets, in $\phi_L \rightarrow e^+e^-$ channel. The result of the Kolmogorov-Smirnov test is shown in the plots.	170
48	Distributions of each BDT score for train and test datasets, in $\phi_L \rightarrow \mu^+\mu^-$ channel. The result of the Kolmogorov-Smirnov test is shown in the plots.	171
49	ROC curve for each BDT score for train and test datasets, in $\phi_L \rightarrow e^+e^-$ channel. The TPR and FPR values are shown for the cut at 0.5.	172
50	ROC curve for each BDT score for train and test datasets, in $\phi_L \rightarrow \mu^+\mu^-$ channel. The TPR and FPR values are shown for the cut at 0.5.	173

CHAPTER I

INTRODUCTION

Dark matter is the newly hypothesized type of matter that participates in the gravitational interaction but not in the electromagnetic interaction. Since light doesn't interact with it, it cannot be observed in any optical means, hence called *dark*. Neither optical nor radio telescopes can directly detect it, but we know about its existence through indirect astronomical observations.

More than 80% of the mass in the universe is believed to be in the form of dark matter, still it has not been detected in the laboratory or in other detection experiments yet. The primary evidences for the existence of dark matter are from its gravitational impact on the visible astronomical objects. This includes the early observations of the large motions of galaxies in clusters, the motions of stars and gas in the galaxies, observations of the large scale structures in the universe, gravitational lensing, etc.

The extensive observed astronomical data consistently show the dominance of dark matter and quantify its amount and distribution, assuming general relativity is valid. The data inform us that the dark matter is nonbaryonic, is *cold*, i.e., used to move non-relativistically in the early universe [1], and interacts only *weakly* with matter other than through gravity.

However, we still have no idea what this dark matter is made of. This is one of the most fundamental open questions in cosmology and particle physics. Its existence

requires an extension of our current understanding of particle physics, and its non-existence points to a modification of our accepted theory of gravity, on a cosmological scale.

I.1 Observational evidence of dark matter

One of the early evidences of the dark matter is the observations by Fritz Zwicky in 1933 [2], who showed that the velocities of the galaxies in the Coma cluster are much higher than the expected velocities, calculated solely from the sum of the individual galaxy masses, thus requiring a significant amount of additional “matter”, that couldn’t be observed.

Galactic Rotation Curves

While studying different galaxies, it is invariably found that the stellar rotational velocity remains constant, or *flat*, with increasing distance away from the galactic center. This is highly counterintuitive, since, based on Newton’s law of gravity, the rotational velocity would steadily decrease for stars further away from the galactic center. As an analogy, in the case of our solar system, the inner planets travel faster around the Sun than the outer planets (e.g. the Earth travels around the sun at about 100,000 km/hr, while Saturn, which is further out, travels at only one third this speed). One way to speed up the outer planets would be to add more mass to the solar system, between the planets. By the same argument, the flat galactic rotation curves seem to suggest that each galaxy is surrounded by significant amounts of matter, invisible to us. It has been postulated, and generally accepted, that the dark matter would have to be located in a massive, roughly spherical halo enshrouding each galaxy [3].

This is illustrated in Fig. 1, where the velocity profile of the Triangulum galaxy, also known as Messier 33, is displayed as a function of radial distance from the galactic center [4]. The baryonic matter which accounts for the gas and disk cannot alone

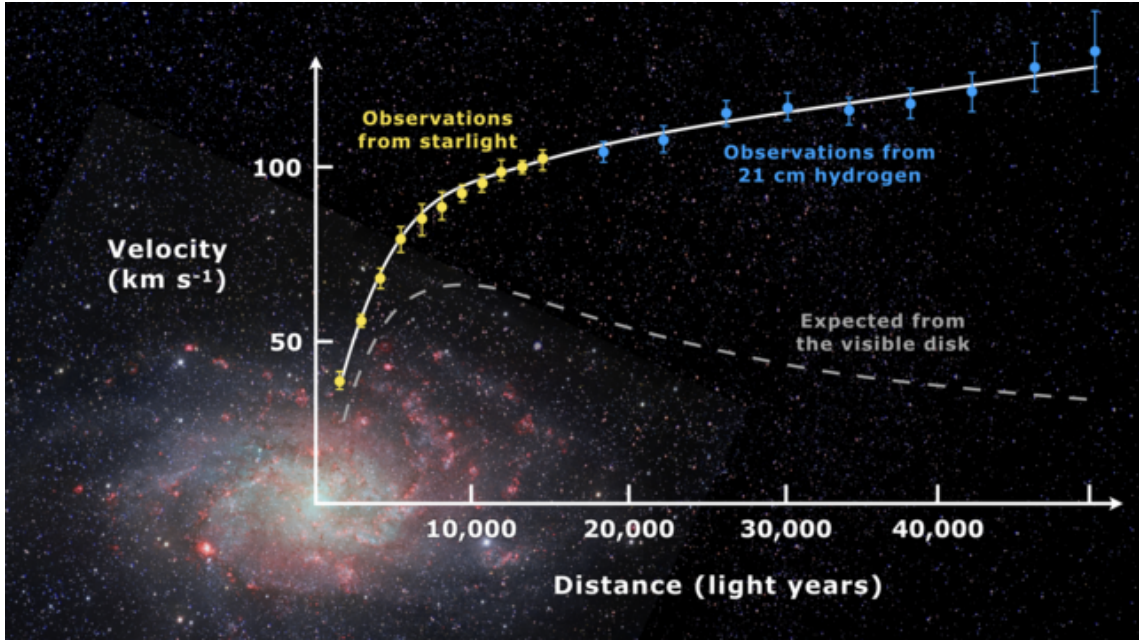


Figure 1. Galactic rotation curve for Messier 33 galaxy, showing disk and gas contribution plus the dark matter halo contribution needed to match the data.

explain the galactic rotation curve. However, adding a dark matter halo allows a good fit to data.

Gravitational Lensing

Einstein’s general theory of relativity predicts that mass distorts the shape of space-time, which in turn causes light to bend. This effect can be used to detect the existence of mass even if it doesn’t emit any light. Gravitational lensing is such an example of such effect, where the light emitted by distant galaxies passes by massive objects in the universe and the gravitational pull from these objects bends or “lenses” the light. Lensing measurements indicate the existence of enormous quantities of dark matter, both in galaxies and in clusters of galaxies.

Fig. 2 shows an example of strong gravitational lensing. The image on the right shows a computer reconstruction of a foreground cluster inferred by lensing observations made by Tyson et al. using the Hubble Space Telescope [5]. This extremely rich cluster contains many galaxies, indicated by the peaks in the figure. In addition

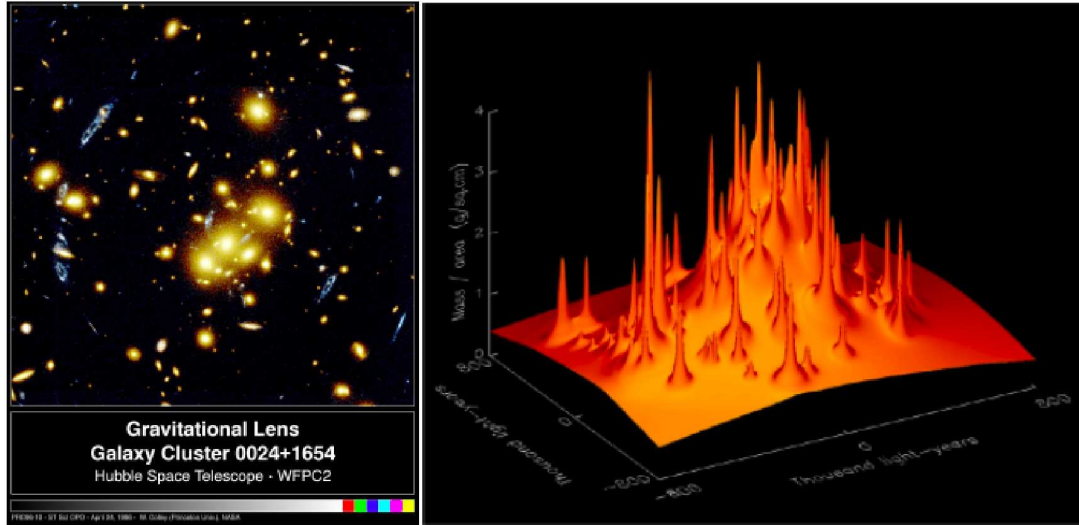


Figure 2. (Left) The foreground cluster of galaxies gravitationally lenses the blue background galaxy into multiple images. (Right) A computer reconstruction of the lens shows a smooth background component not accounted for by the mass of the luminous objects.

to these galaxies, there is clearly a smooth component, which is the dark matter contained in clusters in between the galaxies. The lensing effect helps us in probing the existence of dark matter at a much larger distance than what is possible from the galactic rotation curves.

Hot gas in clusters

Hot gas in clusters provide another evidence of dark matter. The left image in Fig. 3 shows the Coma Cluster, as seen by optical telescopes. The right image was obtained using ROSAT x-ray telescope by Briel & Henry in 1997. The X-ray image indicates the presence of hot gas. The existence of this gas in the cluster can only be explained by the presence of a large amount of dark matter that provides the potential well to attract the gas. Without the additional mass of dark matter, the hot gas would have escaped from the cluster.

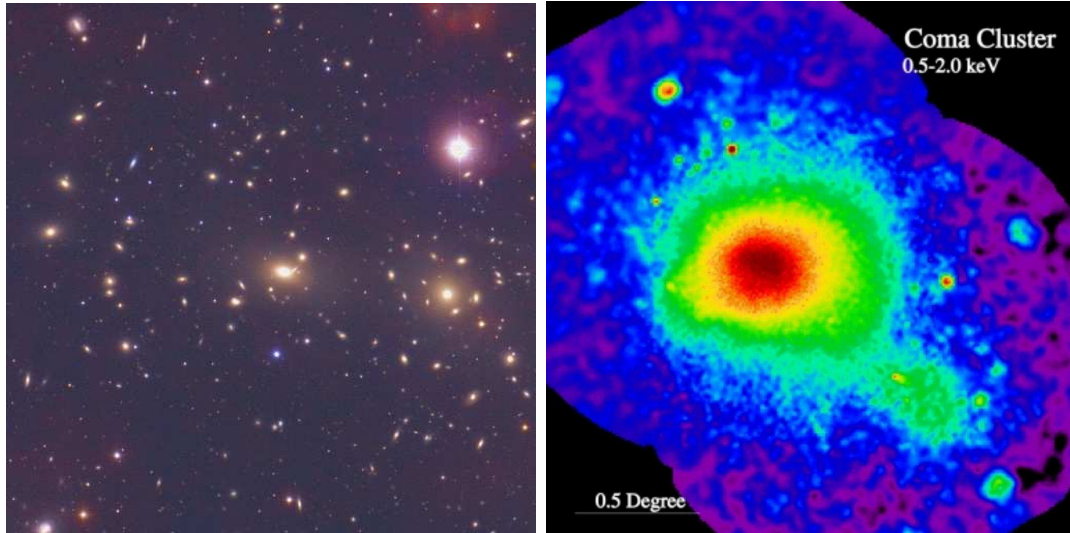


Figure 3. (Left) Optical image of Coma Cluster. (Right) X-ray image from ROSAT satellite.

Bullet clusters

The Bullet Cluster consists of two colliding clusters of galaxies. More specifically, the name Bullet Cluster refers to the smaller subcluster, moving away from the larger one. Fig. 4 shows an image of the bullet cluster taken by the Chandra X-ray observatory, where the baryonic matter is shown in pink and the dark matter is shown in blue. The distribution of the dark matter has been deduced from the gravitational lensing. During the merging of the two smaller clusters, the dark matter has passed through the collision point, but the baryonic matter is slowed down due to friction and has accumulated to a single region at the center of the new cluster.

This is an extraordinary evidence of dark matter because it cannot be explained by the modified theories of gravity, which tries to provide alternative explanations of all these observational evidences without the help of dark matter. No modified theory of gravitation can explain why these two types of matter would behave differently during the collision.

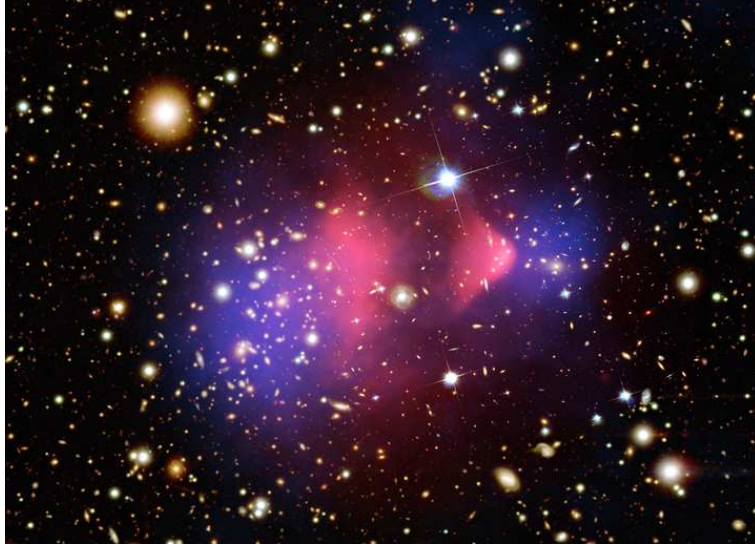


Figure 4. Collision of the bullet cluster shows baryonic matter (pink) separated from dark matter (blue). The distribution of dark matter is deduced from gravitational lensing.

Primordial nucleosynthesis

When the universe was a few hundred seconds old, at a temperature of ten billion degrees kelvin, deuterium became stable: $p + n \rightarrow D + \gamma$. Once deuterium forms, helium and lithium form as well. The formation of the heavier elements such as carbon, nitrogen, and oxygen took another billion years. Then the stars started to form, with densities high enough for fusing three helium atoms into a single carbon atom. The predictions from the Big Bang are 25% ${}^4_2\text{He}$, 10^{-5} deuterium, and 10^{-10} ${}^7_3\text{Li}$ abundance by mass. These predictions exactly match the measured values, as long as atoms are only 4% of the total constituents of the universe.

I.2 Dark matter candidates

Most of the current dark matter models use the concept of quantum field theory to describe the properties of elementary particle candidates. So, they can be characterized by the mass and spin of the proposed dark matter particle, as shown in Table 1. This table and the brief descriptions of the different types of dark matter candidates in this section are taken from this review paper [6].

Type	Particle Spin	Approximate Mass Scale
Axion	0	$\mu\text{eV} - \text{meV}$
Inert Higgs Doublet	0	50 GeV
Sterile Neutrino	1/2	keV
Neutralino	1/2	10 GeV - 10 TeV
Kaluza-Klein UED	1	TeV

Table 1. Properties of different dark matter candidates.

Axions

The axion is one of the earliest suggestions for a dark matter candidate, and in fact one of the most attractive ones. This is because its existence was motivated by solving the strong CP problem in particle physics, and its possible role for dark matter comes as an extra bonus. However, in the cosmological context, a disadvantage of axion is that the axion needed to solve the CP problem only solves the dark matter problem for a limited mass range.

Inert Higgs

This is an example of weakly interacting massive particles (WIMP) and is one of the most minimal extensions of the Standard Model. It is proposed that a model with two Higgs doublets containing a discrete symmetry could contain a state, the lightest neutral scalar or pseudoscalar boson, which is stable. This model contains a dark matter candidate, a particle that does not couple directly to Standard Model fermions and is stable due to the discrete symmetry of the model.

Sterile neutrinos

The neutrino was a favored dark matter candidate in the period starting in the end of the 1970s, with the first calculations of the relic density for massive neutrinos. Sterile neutrinos do not interact through standard weak interactions, but communicate with the rest of the neutrino sector through fermion mixing. From the results of the neutrino oscillations experiments, it seems that it is very plausible that they make

up some fraction of the dark matter in the universe, but most of the dark matter is probably of some other form.

Neutralino

Neutralinos are hypothetical particles, which appear in different theories of supersymmetry. In the Minimal Supersymmetric Standard Model (MSSM), there are four neutralinos that are fermions and are electrically neutral. Since these neutralinos are Majorana fermions, they are identical to their antiparticles. As a heavy, stable particle, the lightest neutralino is an excellent candidate to form the universe's cold dark matter. In many models, the lightest neutralino can be produced thermally in the hot early universe and give rise to the right relic density needed to account for the observed dark matter.

Kaluza-Klein Particles in Universal Extra Dimensions (UED)

Kaluza-Klein (KK) theory is a classical unified field theory of gravitation and electromagnetism, which extends the idea of 4D space-time to a fifth dimension. This provides a viable particle dark matter candidate arising from extra dimensional extensions of the standard model. The most interesting aspect of this type of dark matter is that it provides an example of a spin-1 dark matter candidate. This type of dark matter appears in models of universal extra dimensions, where all SM fields propagate in the higher dimensional bulk, and is stable due to a new type of parity, known as KK parity.

I.3 Dark sector: dark matter and dark forces

The dark matter candidates interact with each other and with ordinary matter through some hypothetical interactions, called dark force. The mediators of these dark forces form another hidden sector of particles, which, together with dark matter and dark energy, forms the dark sector of particle physics. Notable candidates in

this new hidden sector are the dark photon, the dark Z boson, the dark Higgs and other dark scalar candidates. Apart from being the mediator of dark forces, these particles may provide explanations for several unexplained observed phenomena, for example, the anomalous magnetic moment of muons, beryllium-8 decay anomaly, etc.

A special type of such dark scalar is leptophilic dark scalar, which couples predominantly with the standard model leptons, but not with quarks. The proposed models for these leptophilic dark scalars have an interaction term proportional to the mass of the SM lepton it couples to. In this thesis, a search for such dark scalar candidates is presented, where the dark scalar is produced in association with a $\tau^+\tau^-$ pair using the data from Belle experiment at the KEKB e^+e^- collider.

I.4 Search strategies for dark sector candidates

The experiments to probe the existence of dark matter and other dark sector particles can be classified into 3 categories, as shown in Fig. 5.

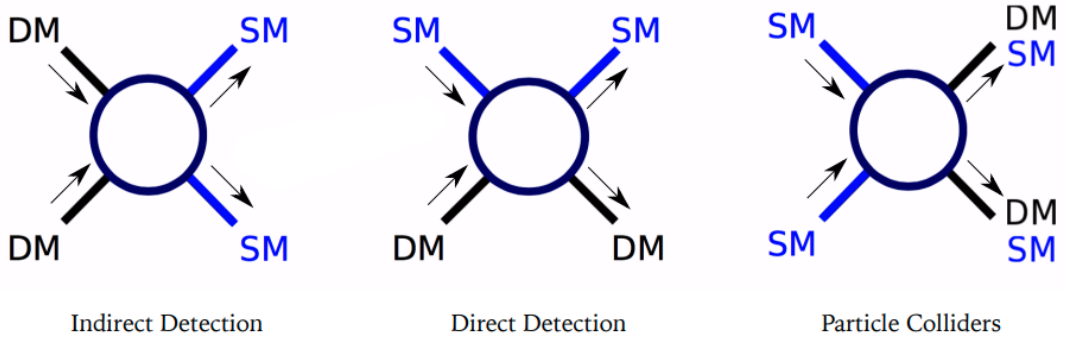


Figure 5. Classification of dark matter detection experiment. DM and SM in this figure corresponds to dark matter and standard model particles, respectively. The circle represents the point/region of collision/interaction. The arrows show the direction of the particles.

Direct search

In these experiments, the dark sector particle interacts with a standard model particle through kinetic mixing or weak interaction and scatters away, leaving the same or a different standard model particle. This kind of searches are performed at the Large Underground Xenon (LUX) experiment, the XENON experiment, the Cryogenic Dark Matter Search (CDMS), the Coherent Germanium Neutrino Technology (CoGeNT) experiment, etc.

Indirect search

In these experiments, two dark sector particles interact with each other and produce standard model particles that we try to detect. This kind of searches are performed at the Fermi Large Area Telescope, Alpha Magnetic Spectrometer (AMS), Payload for Antimatter Matter Exploration and Light-nuclei Astrophysics (PAMELA) etc.

Collider search

In these experiments, two standard model particles interact with each other and produce a pair of dark sector particles. Although these dark sector particles cannot be detected, they produce a signature missing momentum distribution, which indicates their presence in the final state. In some cases, a dark sector mediator is produced, which in turn decays into a pair of standard model particles, that can be detected. This kind of searches are performed at *BABAR*, Belle/Belle II, Tevatron, different experiments at Large Hadron Collider (LHC), etc.

I.5 Overview of this thesis

Search for a dark leptophilic scalar produced in association with $\tau^+\tau^-$ pair using the electron-positron collision data collected at the Belle experiment is presented in this thesis. The activities related to the development of the slowcontrol system for the

K-Long and Muon (KLM) detector and the upgrade of the Data Acquisition (DAQ) system of the Belle II experiment are also discussed.

The thesis is divided into the following chapters, the Chapter 1 being this introduction to a general overview of dark matter searches at colliders and provides the motivation for the search performed in this thesis.

In Chapter 2, the structures of the Belle II detector and the SuperKEKB accelerator are discussed, along with a general overview of the Belle II experiment.

In Chapter 3 and 4, technical contributions in the KLM and DAQ groups of the Belle II experiment are discussed. These include the development of the slowcontrol system for the KLM detector and activities related to the upgrade of the different parts of the DAQ system of the Belle II experiment.

In Chapter 5, the phenomenological model of leptophilic dark scalar is presented. The steps to calculate the signal branching ratio using MadGraph and generate signal Monte Carlo sample using Tauola are also discussed.

In Chapter 6, the analysis of the data obtained from the electron-positron annihilation events at the Belle experiment to search for the dark sector candidates are presented. Modern machine learning tools, such as Boosted Decision Tree (BDT), has been used to separate signal from background. HistFactory, the statistical tool developed for Higgs discovery, has been used in this analysis.

In Chapter 7, the conclusion of this search for the dark sector candidates is presented.

CHAPTER II

SUPERKEKB ACCELERATOR AND BELLE II EXPERIMENT

II.1 Introduction

Electron-positron collider experiments are effective tools for discovering new Physics, as demonstrated by the important role played by the B-factories. The two B-factory experiments (Belle at KEKB, *BABAR* at PEP-II) observed the first large signals of CP violation in the decay of B meson in 2001, which to some extent serves as an explanation of the matter-antimatter asymmetry observed in our universe. These results demonstrated that Kobayashi and Maskawa's hypothesis for the origin of the CP violation is correct and provided the experimental foundation for their 2008 Nobel Prize in Physics.

The Belle II experiment at the world's highest luminosity accelerator, the SuperKEKB collider in Japan, is the lone successor to these prominent B-factory experiments and will play a significant role in moving the field forward. Although these experiments are known as B-factories, they serve versatile purposes apart from studying the Physics of B mesons, for example, to search for new Physics in the decay of tau leptons, D mesons and other low-multiplicity processes including the searches for Dark Sector.

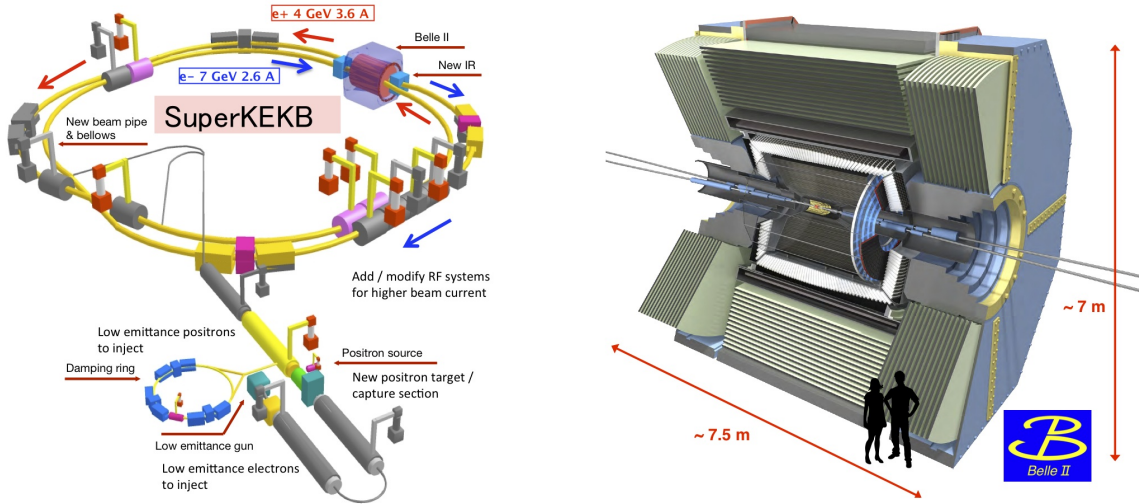


Figure 6. A schematic diagram of the SuperKEKB electron-positron collider and the Belle II detector. [7]

II.2 The SuperKEKB accelerator

The SuperKEKB accelerator is the next generation electron-positron collider after KEKB, located at the KEK accelerator complex in Tsukuba, Japan. The main motivation for this substantial upgrade is to increase the instantaneous luminosity of the machine from $2.1 \times 10^{34} \text{ cm}^{-2}\text{s}^{-1}$ (KEKB) to $8 \times 10^{35} \text{ cm}^{-2}\text{s}^{-1}$, to reach the statistics needed for the physics goals of the Belle II experiment. This nearly 40 times increase of instantaneous luminosity required a substantial upgrade to the accelerator complex [8]. The essential elements in the increase of the luminosity are a reduction in the beam size at the collision point by a factor of 20, from about $1 \mu\text{m}$ to 50 nm, and an increase in the currents by a factor of 2 as compared to KEKB. These two changes are collectively known as ‘nano-beam’ scheme [9]. Compared to KEKB, the two beams collide at an even larger angle of 83 mrad (22 mrad in KEKB). A somewhat lower beam energy asymmetry of 7 GeV (electrons) and 4 GeV (positrons), instead of 8 GeV and 3.5 GeV, was chosen to reduce the beam losses due to Touschek scattering [10], arising from Coulomb interactions between particles in the same beam bunch, in the lower energy beam. This is expected to reduce the spatial separation

between B-mesons, studied in time dependent CP violation measurements, but leads to slight improvements in solid angle acceptance for missing energy decays.

The upgraded accelerator complex houses a new electron injection gun, a new target for positron production, and a new additional damping ring for the positron beam. The upgrade of the accelerator also includes redesigned lattices of the low energy and high energy rings, replacing short dipoles with longer ones (in the LER), new TiN-coated beam pipes with ante-chambers, modified the RF system, and a completely redesigned IR [11].

II.3 Overview of the Belle II experiment

The Belle II detector is the successor of the Belle detector. The goal of this Belle II upgrade was to maintain the same level performance of the Belle detector in the new high luminosity environment with much higher background levels.

II.4 Detectors used at the Belle II experiment

The Belle II detector is made of these 7 sub-detectors, which are responsible for vertexing, tracking, particle identification and energy measurement. The trigger and data acquisition system makes it possible for those sub-detectors to work in unison.

Pixel Detector (PXD)

The PXD system is used for the precise vertex reconstruction required for the study of the decays with displaced vertex. It is tailored to withstand the high beam background of SuperKEKB accelerator. Since the boost of SuperKEKB accelerator is less than that of KEKB (0.28 vs 0.43) achieving the same proper time resolution requires much better vertex resolution. This is achieved by reducing the radius of the first active layer. Studies estimate a conservative 20 times increase of the expected background hit rate, due to 50 times higher event rates (event rate is proportional

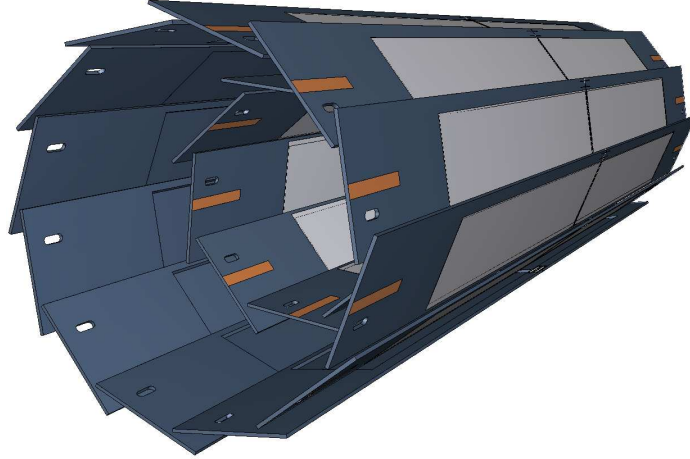


Figure 7. Schematic view of the geometrical arrangement of the sensors for the PXD. The light gray surfaces are the sensitive DEPFET pixels, which are thinned to 50 microns and cover the entire acceptance of the tracker system. The full length of the outer modules is 174 mm. [12]

to the instantaneous luminosity) and double beam currents. The pixel detector is built using Depleted Field Effect Transistor (DEPFET) technology, which allows for thin sensors of $50 \mu\text{m}$ thickness. This DEPFET technology combines the electronics components responsible for detection and amplification in a single device. The readout electronics for PXD are placed outside the acceptance region of the detector to decrease the material budget which contributes to multiple scattering. The PXD consists of two layers of sensors (Fig. 7), with radii of 14 mm and 22 mm. These two layers consist of 8 and 12 sensors respectively. Due to very high background occupancy, the amount of data collected by PXD is too much to store or process. The information from the other sub-detectors are used to calculate the Region of Interest (RoI) to reduce the volume of the transferred and stored PXD data.

Silicon Vertex Detector (SVD)

The silicon strip detector of the Belle II experiment starts from just outside the pixel detector and reaches a larger radius than in Belle. The SVD is a double-sided silicon strip detector made from an n-doped bulk region, implanted on one side with long, highly p-doped strips parallel to the beam and on the other side with short, highly

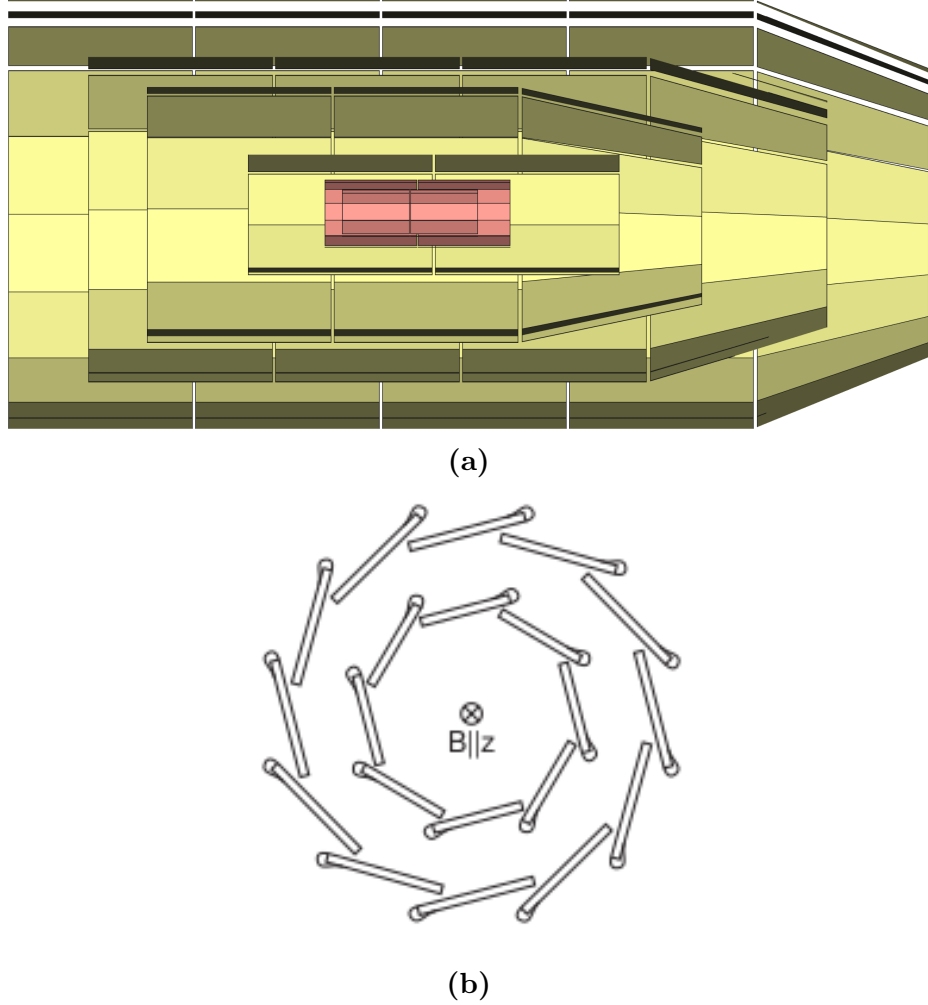


Figure 8. Schematic diagram of the Silicon Vertex Detector (SVD). (a) Longitudinal cross-section of the SVD, showing the detector size and acceptance. The boost direction is to the right. (b) The windmill structure of the SVD modules. [12]

n-doped strips perpendicular to the beam. Charged particles passing through an SVD module's bulk region produce electron-hole pairs via ionization. The p-n strips are reverse biased, so that the electrons drift to the nearest n-strip and the holes drift to the nearest p-strip. The signals generated by each strip are amplified, shaped, buffered in an analog pipeline, and digitized by a Flash ADC upon a trigger.

The SVD has four layers and consists of 187 sensors, each with a thickness of $300 \mu\text{m}$. It is made up of modules of three different shapes: rectangular modules for the inner layer of size $122.8 \text{ mm} \times 38.4 \text{ mm}$, rectangular modules for the three outer layers of size of $122.8 \text{ mm} \times 57.6 \text{ mm}$ and trapezoidal modules with a size of 122.8



Figure 9. PXD is fitted inside SVD to form the whole vertex detector (VXD) and ready to be installed at the interaction point.

mm \times 57.6–38.4 mm. The latter are used as slanted modules for the most forward sensors of the three outer SVD layers in order to cover the complete acceptance region of the Belle II detector (Figure 8a). All SVD sensors have 768 long p-strips. The sensors of the innermost layer have 768 short n-strips, while all other modules have 512 short n-strips. The modules of both the PXD and SVD are arranged in an overlapping “windmill” structure (Figure 8b). This geometry minimizes inactive gaps at the sensor junctions and ensures that most particle tracks originating from the interaction point must pass through an active detector surface in every VXD layer. The silicon strips readout is based on APV25 chips, which have a shorter shaping time with respect to Belle VA1TA chips to withstand higher background.

The pixel detector (PXD) and silicon vertex detector (SVD) together form the vertex detector (VXD) as shown in Figure 9.

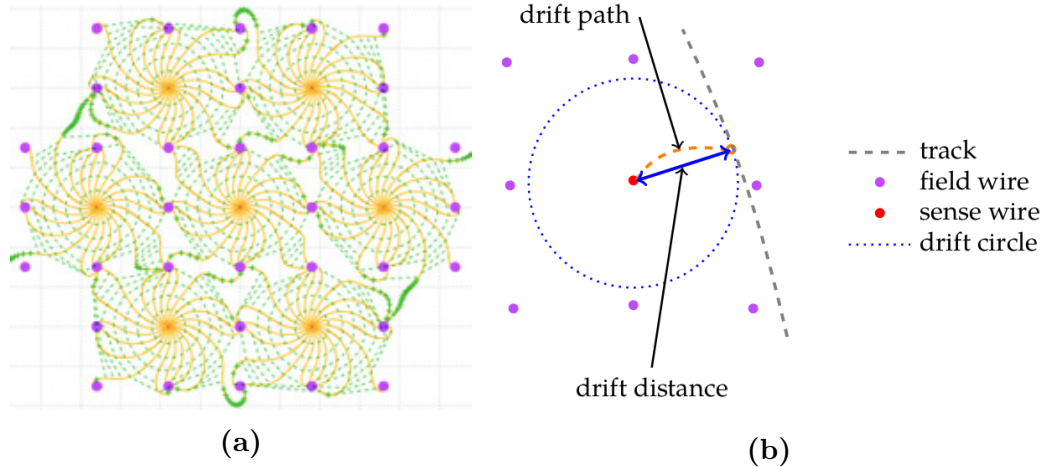


Figure 10. Schematic diagram of the Central Drift Chamber (CDC). (a) Equipotential lines of the electric field (green dashed lines) and drift paths of electrons (yellow lines) in the CDC cells. [13] (b) A schematic diagram of a single CDC cell with a hit.

Central Drift Chamber (CDC)

The Central Drift Chamber (CDC) is the particle tracking device of the Belle II detector. It has three main purposes -

- Together with PXD and SVD, it reconstructs the tracks of the charged particles and measures their momenta.
- It provides important information used for particle identification by measuring the characteristic energy loss of charged particles due to ionization in the gas volume.
- It acts as the source of the most reliable trigger for events with charged particle.

The CDC has a cellular structure, where each cell is uniquely identified by a combination of field and sense wires. Each sense wire is surrounded by 8 field wires, forming a square-like shape. Neighboring cells share field wires (see Figure 10) and are grouped into layers. All the cells in a layer are equidistant from the z -axis.

There are total 56 layers organized in 9 super-layers. The size of a squared cell varies from 10 mm for the innermost super-layer to 18.2 mm for the outermost ones. It

is filled with 50% helium-50% ethane gas mixture and contains 14336 tungsten sense wires of 30 μm diameter. To generate the required electric field gradient, aluminum wires of 126 μm diameter are used. The whole structure is supported by two carbon-fiber reinforced cylinders and aluminum end-plates.

The measured spatial resolution of the CDC is about 100 μm , while the relative precision of the dE/dx measurement for particles with an incident angle of 90° is around 12%.

Time of Propagation (TOP) detector

The TOP detector is one of the dedicated particle ID detectors of the Belle II experiment. It consists of 16 quartz bars with size 2700 mm \times 450 mm \times 20 mm placed around the CDC. All surfaces of those bars, except one, are completely reflecting. The Cherenkov light emitted by particles traversing the quartz bar reflects multiple times inside that bar and finally comes out of that transparent surface (see Figure 11).

For each quartz bar, there is a spherical mirror on the forward end to focus the light and a prism at the backward end to expand the Cherenkov ring image before detection. 32 micro-channel plate photo multiplier tubes (MCP-PMTs), arranged in two rows at the end of the prism, are used to detect the Cherenkov light. The Cherenkov image is reconstructed using the two coordinates of the transparent surface and precise timing information provided by the PMT.

Aerogel Ring Imaging Cherenkov (ARICH) detector

The ARICH detector is designed to differentiate between K and π particles at the whole p_T range, and differentiate among π , μ and e below 1 GeV/c. It is made of the following components: an aerogel radiator that produces Cherenkov photons, an expansion volume that allows to form light rings, and an array of position sensitive photon detectors which are able to detect single photons with a good resolution.

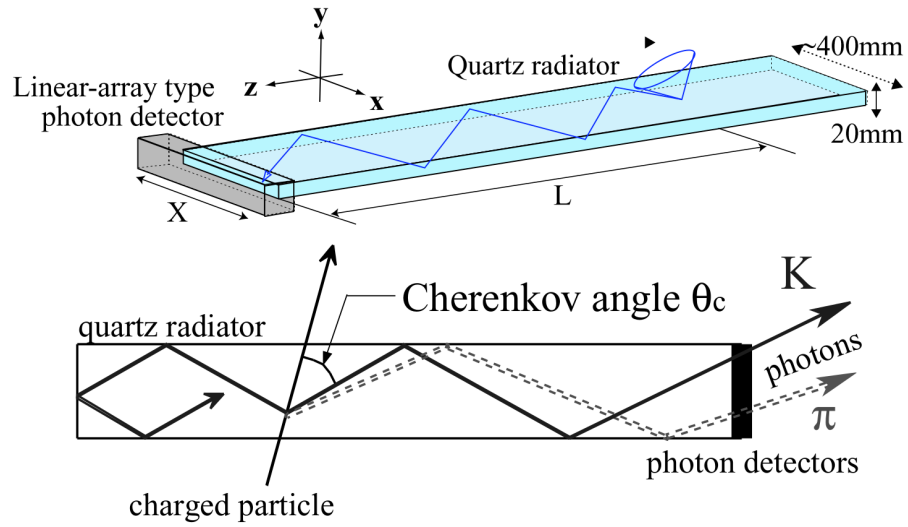


Figure 11. A schematic diagram of a single quartz bar of Time of Propagation (TOP) counter, showing the path of Cherenkov light inside it. [12]

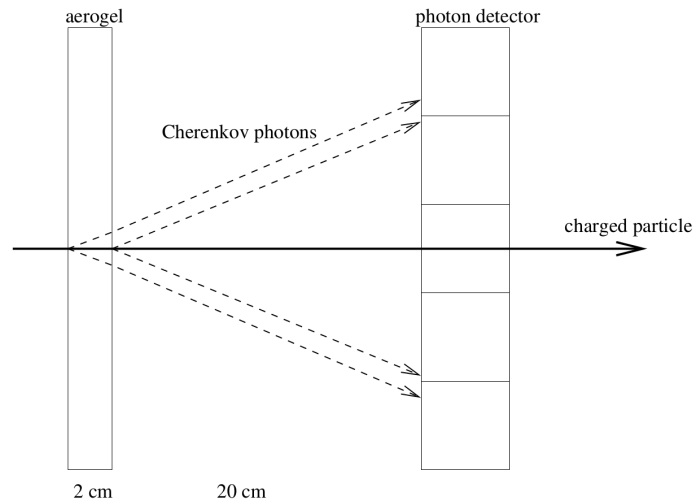


Figure 12. A schematic diagram of the ARICH detector. The components from left to right are: the aerogel radiator, the expansion volume, and the position sensitive photon detector. [12]

Hexagonal aerogel tiles are arranged to cover the vertical area at a z-distance of 167 cm from the interaction point starting from a radius of 410 mm till the radius of 1140 mm. Next to the radiator, there is an ~ 20 cm wide gap where the Cherenkov light cone can spread. The photons are then detected by nine radial layers using a total of 540 Hybrid Avalanche Photo Detectors (HAPD). The achieved angular resolution between tracks, as obtained from phase 3 data, is ~ 4.5 mrad.

Electromagnetic Calorimeter (ECL)

The electromagnetic calorimeter (ECL) is a cylindrical detector that encloses the CDC, ARICH and TOP detectors. It is responsible for detecting photons as well as measuring the energy deposition associated with tracks. It is a high resolution calorimeter, which is able to detect neutral particles in a wide energy range, from 20 MeV up to 4 GeV. It is built of CsI(Tl) scintillation crystals, of size 6 cm \times 6 cm each, which have a high light output, a short radiation length and good mechanical properties. It covers the range of $12^\circ < \theta < 155^\circ$ in the polar angle and weighs a total of 43 tons. The ECL is divided into two parts: barrel and endcap. The barrel part consists of 6624 crystals and the endcap part consists of 2112 crystals.

At the end of each crystal, a photomultiplier tube (PMT) is attached, which detects light emitted by the scintillator. The amount of light detected by the PMT is used to measure the energy deposition. Tracks with a cluster of activated crystals in its vicinity are can be identified as electrons, which deposit significantly more energy in the calorimeter as compared to muons. Clusters with no associated track can be interpreted as photons or other neutral particles.

K-Long and Muon (KLM) detector

The KLM detector is the outermost sub-detector in the Belle II experiment. The purpose of this detector is to detect K_L^0 mesons and measure the momentum of muons. It is made up of alternating sandwiches of 4.7 cm thick iron slabs and active

detector elements located outside the superconducting solenoid. The iron plates serve as the flux-return for the solenoid. The KLM detector has two parts - Barrel KLM (BKLM) and Endcap KLM (EKLM). The BKLM is coaxial to the beam axis and has 15 active detector layers - 13 outermost layers made of resistive plate chambers and two innermost layers made of scintillators read out by photomultiplier tubes. The EKLM is located at the two ends of the Belle II detector, perpendicular to the beam axis. The whole KLM detector covers the polar angle range of $20^\circ < \theta < 155^\circ$.

Energy deposits in the KLM not associated with a track are K_L^0 candidates, and those associated with a track are muon candidates. The magnitude of reconstructed K_L^0 momentum obtained from the KLM detector is proportional to the size of the KLM cluster, which provides a very rough estimate.

A detailed description of the structure and operation of the KLM detector is presented in Section III.1.

II.5 Trigger System

The high luminosity upgrade of SuperKEKB accelerator will increase the event rate to 20 kHz. This will require a robust but flexible trigger system to discriminate the signal events from the background hits, which are expected to be 20 times larger than at KEKB. Considering the high charged track multiplicity in $B\bar{B}$ event final states, an obvious trigger requirement could've been higher number of tracks in the event. However, there are other physics processes of interest, for example, some τ decays and dark sector searches, that have zero or just two tracks in their final states. This makes it much more difficult to separate signal and background. Moreover, such low multiplicity processes have the same topology as Bhabha scattering events, which have a huge cross-section at $\Upsilon(4S)$ CM energy (~ 300 nb) compared to the typical signal cross-sections (~ 1 nb). Therefore, naively vetoing the Bhabha events to reduce the total event rate also loses efficiency of the low multiplicity events. To cope with these challenges, a smart and efficient trigger system is essential. The Belle II trigger

system largely follows the same principles that successfully worked for Belle, but implemented with modern technologies which are able to support the much higher projected event rate. The trigger system is composed of both hardware and software triggers. The hardware trigger is called the Level 1 (L1) trigger and the software trigger is called the High Level Trigger (HLT).

Level 1 (L1) Trigger

The L1 trigger is composed of several sub-trigger systems, which combines information from various sub-detectors using the Global Reconstruction Logic (GRL). The output of this system is sent to the Global Decision Logic (GDL), responsible for issuing the trigger signal. In Belle II, all the trigger system components are built using the Field Programmable Gate Array (FPGA) technology, which makes the logic configurable as required.

The CDC trigger finds and characterizes the tracks. The 2D track finding algorithm remains the same as the Belle experiment. The 3D track finding algorithm uses the information of the z-coordinates of the hits and rejects most of the background coming from Touschek scattering. This is because, these scattering events are largely displaced in z-direction with respect to the interaction region. The maximum allowed 5 μs latency of the L1 trigger system requires the 3D track finding to be finished in no more than 1 μs , which is achieved using neural networks.

The ECL trigger uses two complementary trigger schemes: a total energy trigger and an isolated cluster counting technique. The total energy trigger is sensitive to events with high electromagnetic energy deposition. The cluster counting technique, on the other hand, is sensitive to multi-hadronic events with low energy clusters, which may appear from minimum ionizing particles (MIP) as well. The ECL trigger is also able to recognize the back-to-back topology of the Bhabha events with a high purity, which is fundamental for ensuring a high trigger efficiency of low multiplicity processes. The single calorimeter cluster trigger, in association with at least one non-

electron track in the opposite direction, is fundamental for the detection of radiative two-track processes, which include the background processes for the search of dark photons and axion like particles (ALP).

The trigger for non-radiative di-muon events uses a combination of two-track trigger from CDC and single high-energetic muon track trigger provided by KLM.

The L1 trigger can sustain a maximum rate of 30 kHz. However, the goal is to keep the trigger rate as low as possible, while ensuring a high efficiency ($> 99\%$) for interesting physics processes, mainly hadronic events. The raw data collected using L1 trigger is then forwarded to the high level trigger for further background rejection using fully reconstructed objects.

High Level Trigger (HLT)

The HLT is a software trigger designed for further backgrounds suppression. Its main purpose is to reduce the load of data written to the permanent storage at a maximum design output event rate of 10 kHz. Events selected by the L1 trigger undergo the full online reconstruction using the outputs from all the sub-detectors except the PXD. The HLT uses a set of conditions to classify the events into several categories. Those conditions are called the ‘physics trigger’ and the categories are called ‘HLT skins’. The physics trigger is able to classify the events into categories like $B\bar{B}$, hadron, taupair etc.

The HLT also calculates the Region of Interest (ROI) for the PXD detector using information from other sub-detectors. Since the total amount of information collected by PXD is huge, only the selected PXD hits that lies in the ROI are stored to the disk and used to complete the event reconstruction.

In the commissioning period known as Phase 1, from February 2016 to June 2016, the solenoid was not active, and no collisions took place. During the Phase 2 data taking from February 2018 to July 2018, the HLT was in monitoring mode and no software filter was applied to the L1 triggered events, resulting in a very favorable

condition to collect events with topologies interesting for dark sector searches. In the Phase 3 data taking starting from March 2019, the HLT filtering has been turned on due to the higher luminosity, which may suppress this type of events.

Technical details of the architecture and operation of the high level trigger has been discussed in section 4.1.2.

CHAPTER III

SLOWCONTROL SYSTEM OF THE KLM DETECTOR

III.1 Overview of the K-Long and Muon (KLM) detector

Introduction

KLM is the largest and the outermost sub-detector used in Belle II experiment. Its purpose is to detect muons and long-lived neutral K_L^0 mesons. Belle II KLM is an updated version of Belle KLM. In Belle, gaps in the segmented flux return of the Belle solenoid were populated with resistive plate chambers (RPC). KLM is divided into a barrel and two endcaps. In Belle II, in the endcaps and two inner layers of the barrel RPCs were replaced with scintillator plastic modules because of relatively large deadtime of RPCs and high anticipated background level at Belle II.

Active materials used in the KLM detector

In the KLM sub-detector of Belle II experiment, two types of active components are used for detecting the particles passing through it. Those are called:

- Resistive Plate Chamber (RPC)
- Scintillator

Resistive Plate Chamber (RPC)

In RPCs used in KLM sub-detectors are made of 2.4 mm thick glass electrodes separated by 1.9-mm thick noryl spacers, epoxied in place. The glass electrodes, although technically insulating, do conduct electricity but with a very high bulk resistivity of $\sim 5 \times 10^{12} \Omega \cdot \text{cm}$. High voltage is distributed to the electrodes via a thin layer of carbon-doped paint on the outer surfaces of each electrode. This layer has a surface resistance of $10^6 - 10^8 \Omega/\text{sq.}$ and is transparent to fast pulses. The energized electrodes maintain a quiescent uniform electric field of up to 4.3 kV/mm in the gas-filled gap. The current drawn from the high voltage supply corresponds to roughly $1 \mu\text{A}/\text{m}^2$ of the electrode area, and most of this flows through the noryl spacers. We use a gas mixture of 62% Freon, 30% argon, and 8% butane-silver (a mixture of 70% n-butane and 30% isobutane). A charged particle going through an RPC ionizes the gas molecules along its path. The electric field then accelerates the electrons toward the anode and the ions toward the cathode. In the strong electric field, the electrons initiate more ionization, leading to a streamer between the electrodes. The streamer is imaged on a plane of external pickup strips, each about 5 cm in width. These strips, separated from an outer conducting ground plane by dielectric foam, behave like a transmission line with a characteristic impedance of about 50Ω . Orthogonal pickup strip planes are mounted on either side of a pair of RPCs to form a superlayer. During the normal high-electric-field operation, the amplitude of a streamer's image pulse is large enough that it can be detected without amplification.

Scintillator

Scintillators are a type of material that emits a photon when an energetic particle passes through it. The scintillator strips used in KLM detector have a cross-section of $(7 - 10) \times 40$ mm and a length of up to ~ 2.8 m. The strip width is a compromise between the desire to limit the total number of channels and need for reasonable spatial resolution for muon and K_L^0 reconstruction. This granularity is similar to the

average cathode-strip granularity of the RPCs. Individual scintillators are covered with a diffuse reflective coating. Each strip has a groove in the center to accommodate a wavelength shifting (WLS) fiber. Scintillator light is caught by this fiber and transported to the silicon photomultiplier (SiPM) sensor. The WLS fiber is read out from one side. The far end of the WLS fiber is mirrored to double the light yield at the SiPM. The WLS fiber is glued to the scintillator to increase the efficiency of the light collection. The SiPM is coupled to the fiber end. It is fixed and aligned with the fiber using a plastic housing.

Different parts of the KLM detector

The KLM detector is primarily divided into two parts:

- Barrel KLM (BKLM)
- Endcap KLM (EKLM)

Each of these two parts is divided into several sectors, as shown in Fig. 13

Barrel KLM (BKLM)

The barrel KLM is divided into forward and backward halves, each with eight sectors (octants). There are 15 layers of active components in each sector. The two innermost layers in the barrel are made of scintillators and rest of them are made of RPCs.

Endcap KLM (EKLM)

The endcap KLM is divided into two parts: forward endcap and backward endcap. Each endcap is divided into four sectors (quadrants). There are 14 layers of active components in forward endcap and 12 layers of active components in backward endcap. All the layers in the endcaps are made of scintillators.

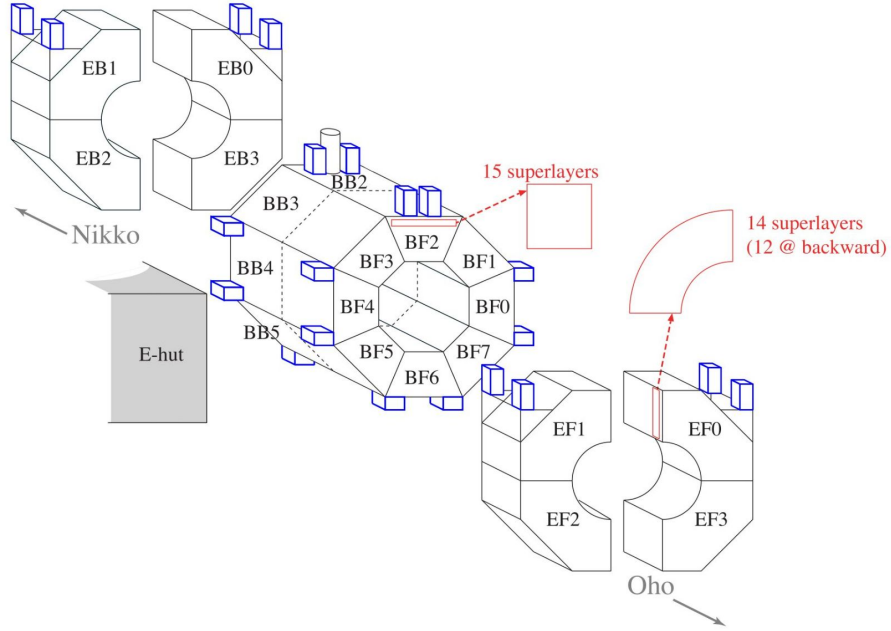


Figure 13. Different parts of the KLM detector. BB, BF, EB and EF stand for barrel backward, barrel forward, endcap backward and endcap forward respectively.

Front-end electronics of the KLM detector

The front-end electronics is responsible for collecting the signal from the active components, digitizing them and sending them to the readout of the Belle II data acquisition system. The whole front-end electronics system for the KLM detector is housed in 36 different crates, located in different places of the Belle II detector. 16 crates with RPC front-end electronics (FEE) are located all around the detector. 4 crates with the barrel scintillator FEE, also called scintillator motherboards (MB), are located on top of the detector. 16 crates with the endcap FEE are located in the four shelves on the endcap doors.

Different components of the KLM frontend electronics are shown in Fig. 14.

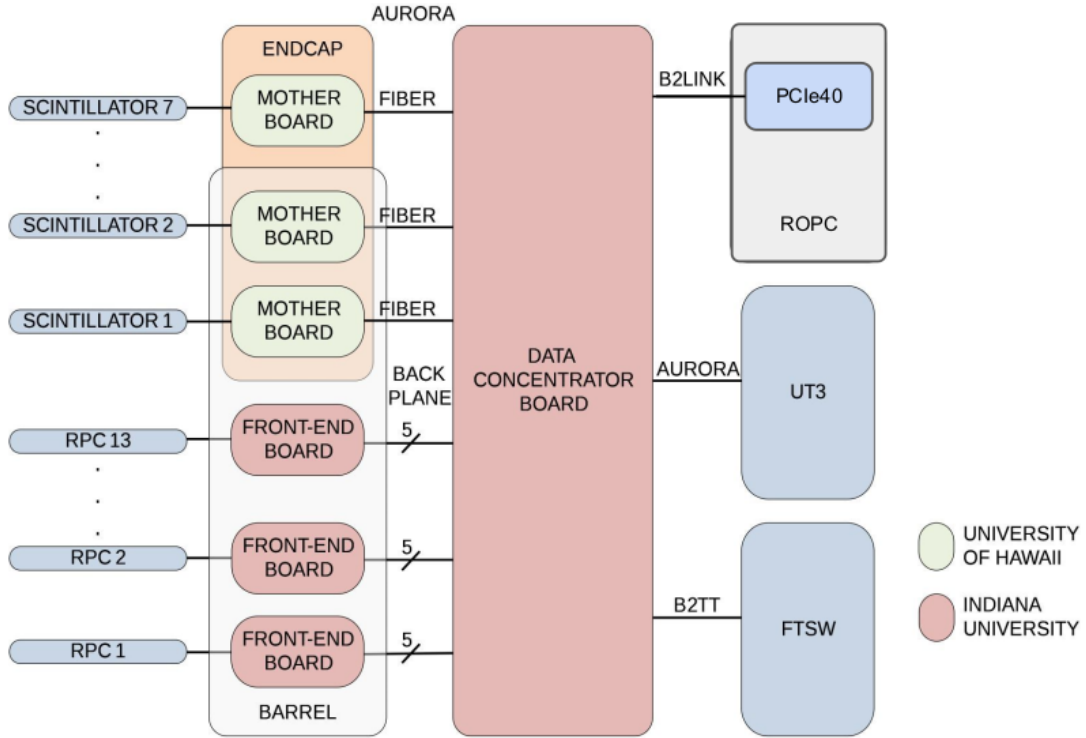


Figure 14. Different components of the KLM frontend electronics.

Data Concentrator (DC)

The data concentrator (DC) boards collect data from multiple detector modules, create packets with important timing information based on external trigger and finally transmit them to the readout system. Each data concentrator has interfaces to receive data from 13 RPC front-end board and 7 scintillator motherboards. The data concentrators are also connected to the PCIe40 readout system, UT3 trigger and front-end timing switches (FTSW).

Each data concentrator is connected to a single *channel* of the PCIe40 readout board using a pair of optical fibers. They communicate with each other through the belle2link protocol, which allows two-way communication between them for slowcontrol purposes and one way flow of data packets from the data concentrator to the PCIe40 readout.

The communication between the data concentrator and FTSW is made through

`b2tt` protocol over an Ethernet cable. The FTSWs are in turn connected to the trigger timing distribution (TTD) system and provides valuable timing information needed for building the data packets. The TTD system is also used to reprogram the firmware of the front-end electronics boards.

In BKLM, up to 13 RPC frontend boards and 2 scintillator motherboards are connected to a single data concentrator. In EKLM, up to 7 scintillator motherboards are connected to a single data concentrator. This means, all the FEE boards in each BKLM sector are connected to one data concentrator and all the FEE boards in each EKLM sector are connected to two data concentrators.

RPC front-end board

The RPC front-end boards collects and digitizes signals from the RPC channels and sends them to the data concentrator. Each RPC front-end board has two front panel connectors, each of them can be connected to 48 receiver and discriminator channels. The first 48 channels in the top front panel connector are connected to negative RPC pulses, and the remaining 48 channels in the bottom front panel connector are connected to positive RPC pulses. The discriminator threshold is controlled by a DAC and can be modified by sending slowcontrol configuration through the corresponding data concentrator.

Scintillator motherboard

The scintillator motherboard provides the scintillator frontend interface and comprises a data interface and a control interface. The data interface is the scintillator electronics transmitter and contains trigger data, DAQ data, and status data. The control interface is the scintillator electronics receiver and contains control parameters. The scintillator motherboards collect data from the scintillators, digitize them and send them to the data concentrators. They also receive control signals from the

data concentrators, which are used to set and retrieve different status and configuration parameters.

III.2 Dark current monitoring for KLM background measurement

I modified the high voltage control code to create EPICS variables that monitor the residual charge leakage in the KLM sub-detector, known as dark currents. For the barrel part, the system reports the monitored dark currents and their safety limits in the forward and backward halves of the detector. For the endcap part, it reports the dark currents from the innermost and outermost layers of the forward and backward endcaps. These dark currents are a measure of beam-related backgrounds originating from the crossing of electron and positron beams near the interaction point. The ratio of the total dark current and its limit in the KLM is used as a measure of the background level and is displayed at the control room of Belle II Commissioning Group (BCG) as shown in Fig. 15. Such online monitoring is necessary for optimal functioning of new facilities (e.g. Nano-Beam scheme) provided by the SuperKEKB accelerator and to ensure good data quality for a high luminosity environment as in the Belle II experiment.

III.3 Slowcontrol interfaces for the status and configuration registers of the KLM frontend electronics

I added two new functionalities in the KLM slow-control system to enable communication between the KLM DC registers and the online DAQ database systems at KEK: the configuration database and archiver database. One functionality, which exports the contents of the important DC status registers as Experimental Physics and Industrial Control System (EPICS) variables and stores them in the archiver database, is currently up and running. The live and archived values of these status registers can be obtained using the Belle II EPICS archiver appliance. The other functionality allows one to set the DC and FEE configuration registers from the values stored in the

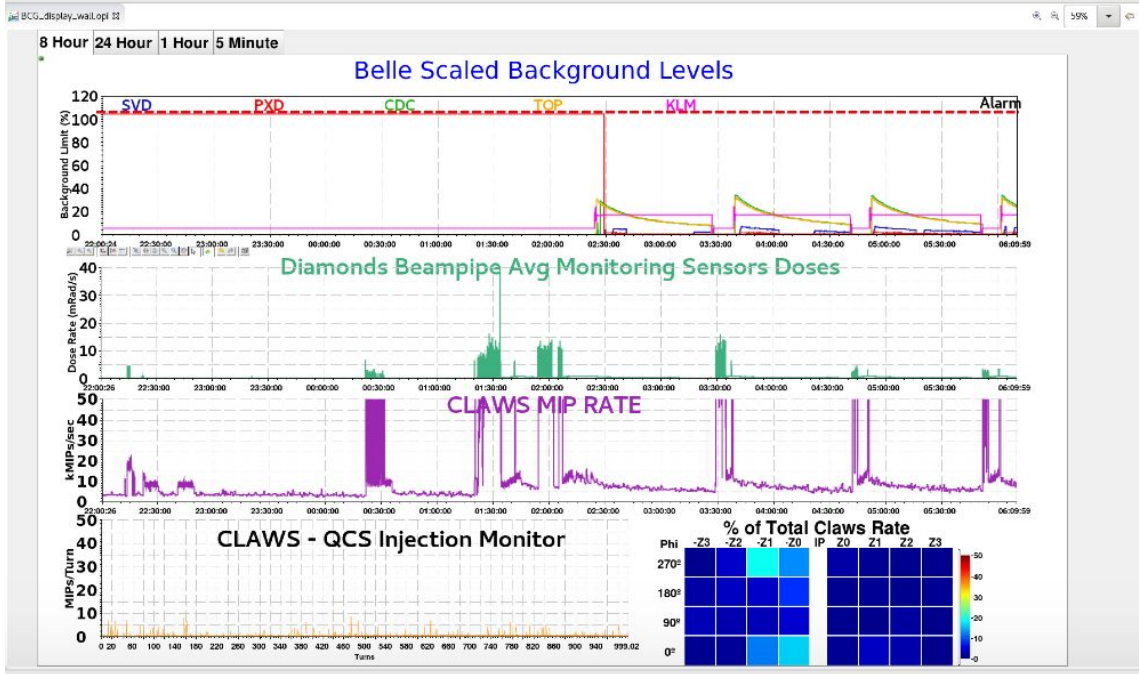


Figure 15. Live background level monitoring plots for different sub-detectors as displayed in the Belle II Commissioning Group (BCG) control room. The pink trace in the top plot corresponds to the KLM background level.

Config. DB. Useful parameters like the RPC thresholds and RPC look-back window can be controlled using this feature. This makes it possible to selectively suppress noisy RPC channels by setting higher threshold values for them.

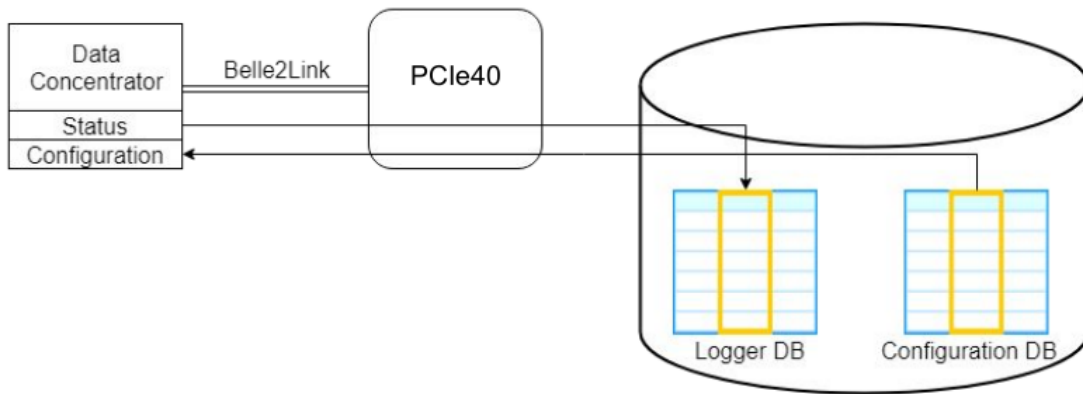


Figure 16. The interface between the KLM status and configuration registers and different DAQ databases.

III.4 RPC gasflow monitoring system

The RPC present in the KLM sub-detector requires a constant supply of argon, Freon, and butane gas mixture of a particular ratio. If this gas supply is interrupted or the ratio of the component gases gets altered, the KLM data quality gets affected and if the supply is interrupted for too long, it causes high voltage trips, leading to long interruption of the data taking process. The gas mixing station for the KLM detector is shown in Fig. 17.



Figure 17. The gas mixing station for the KLM detector, producing a mixture of argon, Freon and butane.

To prevent this, I created a system for online monitoring of the RPC gas supply. Using this system, one can remotely monitor the mass flow rates of each of the component gases and take necessary actions if any deviation from the desired rates is noticed. The gas flow rates are also stored in the EPICS archiver appliance as well as the Elasticsearch-Logstash-Kibana (ELK) system for debugging data quality issues and other future references. If there is any deviation beyond some threshold value, the monitoring system also informs the KLM expert shifters via RocketChat (official communication platform for Belle II members) messages using the ElastAlert facility of the ELK system. The GUI for monitoring the RPC gas supply status is shown in

Fig. 18

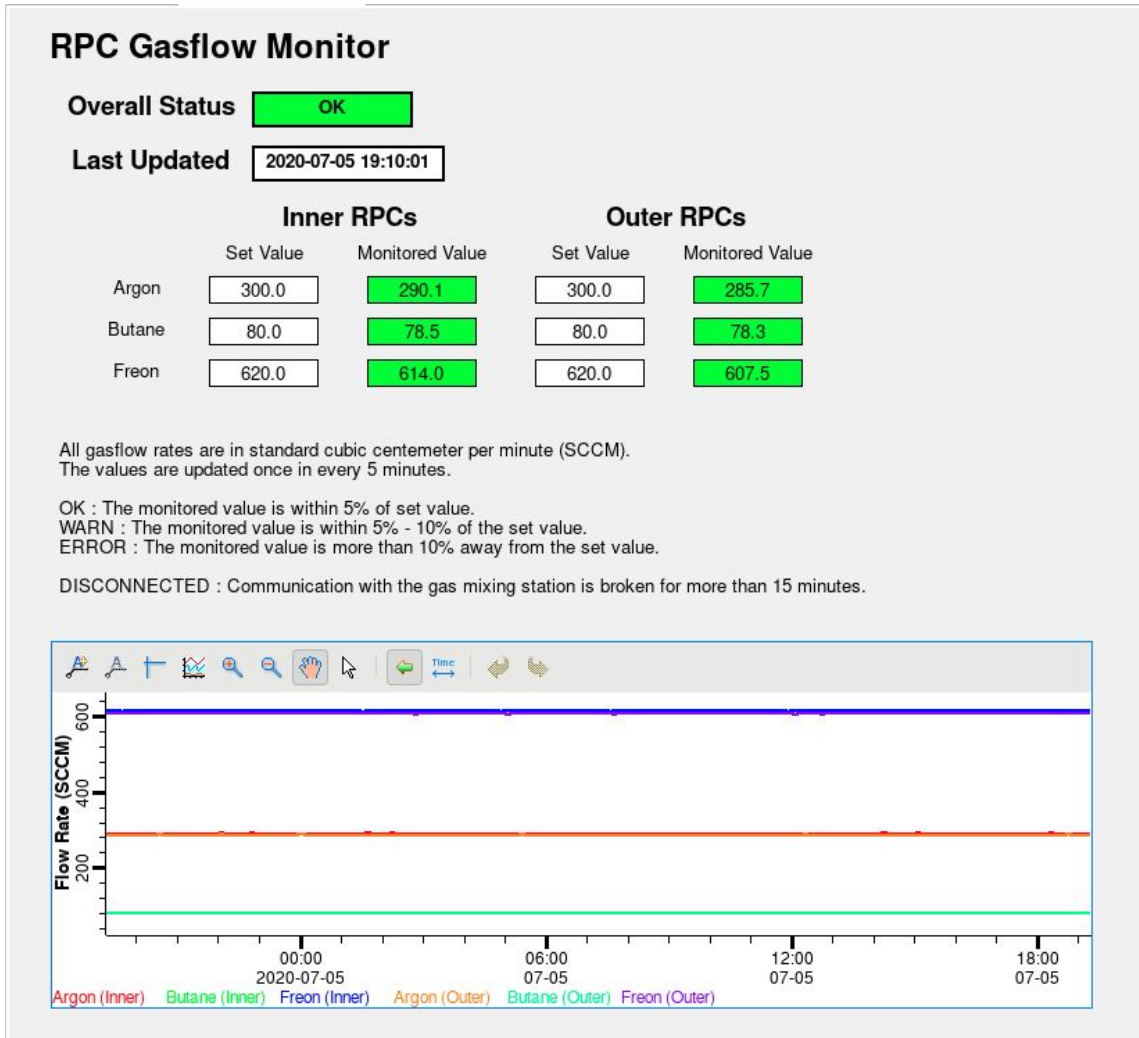


Figure 18. The GUI to monitor RPC gas supply status, as displayed on the KLM shifter PC.

The diagram in Fig. 19 shows the overall design of the RPC gasflow monitoring system.

III.5 Interlock system for KLM high-voltage supply

The interlock for KLM HV supply protects the system in the event of water leak, earthquake, fire etc. accidental hazards. It receives an input from the center interlock system which triggers the interlock system under those events and the interlock

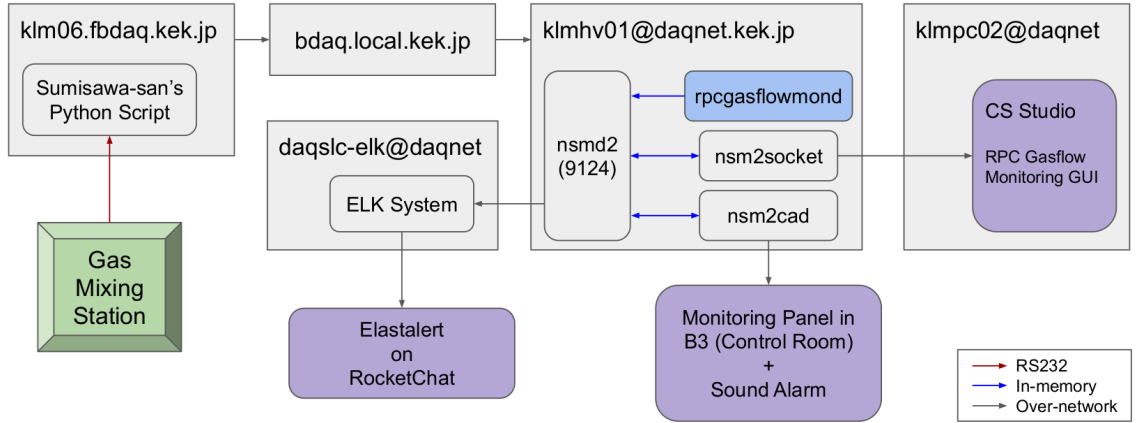


Figure 19. Different components of the RPC gasflow monitoring system.

immediately turns off the HV supply. I programmed the interlock PLC and installed it next to the HV supply crates on the second floor of the electronics hut. Then I connected it to the central interlock located on the first floor of the electronics hut with a pair of ribbon cables. The PLC is connected to the scintillator HV supply and the RPC fan-out box with LEMO cables. The fan-out box is connected to the RPC HV supply crates and distributes the PLC output signal among them. The design of the whole system is shown in Fig. 20.

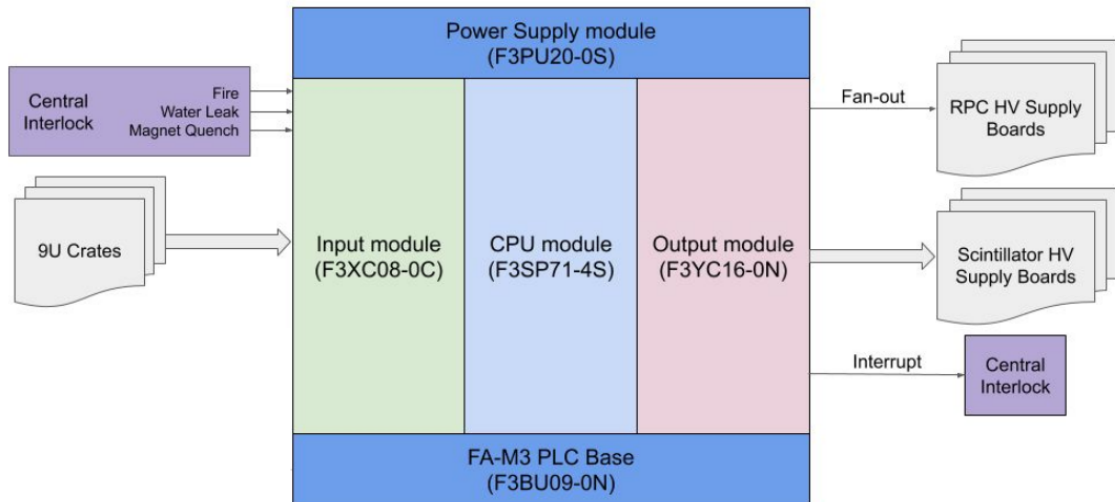


Figure 20. Different components of the KLM high voltage interlock system.

CHAPTER IV

UPGRADE OF THE DATA ACQUISITION (DAQ) SYSTEM

IV.1 Overview of the DAQ system of the Belle II experiment

The Belle II experiment is expected to reach maximum trigger rate as high as 20 kHz, with the raw event size of more than 1 MB. The data acquisition (DAQ) system of this experiment was designed to support a trigger rate to 30 kHz. The Belle II DAQ system uses a synchronous trigger flow control. The digitized data from all sub-detectors, except the PXD, are transferred to unified readout modules (COPPER) via a high speed optical link (Belle2link). The data are then collected by the readout PCs via Ethernet. In the upgraded PCIe40 based readout, the optical links are connected to the PCIe40 readout boards, housed in the readout PCs itself. The event building is performed in the readout PCs and the built events are sent to the high level trigger (HLT) for software trigger. In case of PXD, an FPGA-based readout system (ONSEN) is used. The amount of PXD data is greatly reduced using region-of-interest (RoI) information from HLT, which tells the expected PXD hit positions of the reconstructed charged tracks. The HLT sends the selected events to the storage system. The storage system also receives filtered event data from the PXD onsen based on the RoI provided by the HLT. The storage system combines them and stores the full event as RAW data. The storage is in turn connected to ExpressReco, which obtains the full event, including the PXD data, and provides online event display and data quality monitoring (DQM) plots.

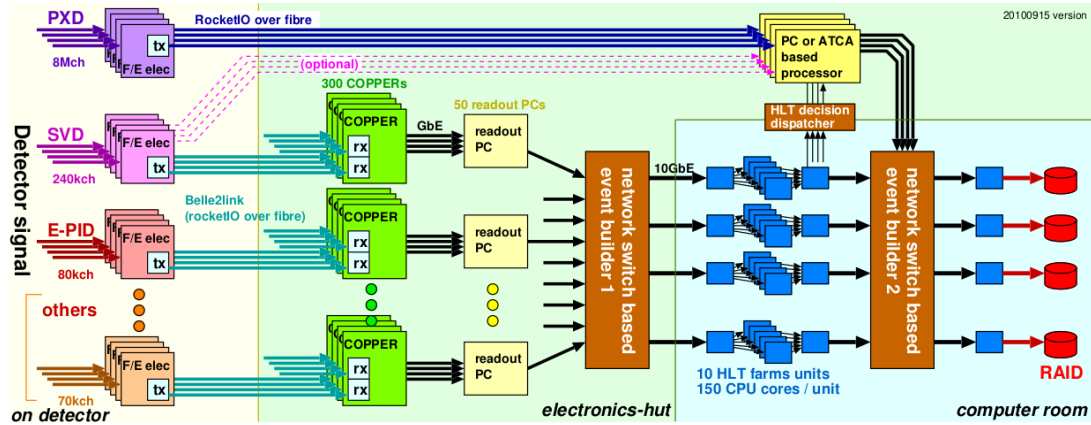


Figure 21. Initial design of the Belle II data acquisition system. [14]

Fig. 21 shows the schematic diagram of the DAQ system of the Belle II system before PCIe40 upgrade.

Different components of the DAQ system

Different parts of the Belle II data acquisition system, before and after PCIe40 upgrade, are discussed below.

Common Pipelined Platform for Electronics Readout (COPPER)

The Common Pipelined Platform for Electronics Readout (COPPER) is the readout electronics initially designed for the Belle II DAQ system. The COPPER modules are located in the electronics-hut, which is around 20 m away from the detector. The COPPERs receive data from the sub-detector front-end electronics through optical fibers, which transmits data according to the belle2link protocol.

Each COPPER module is a 9U VME module with a custom J0 connector, and has a slot for a processor PMC (PCI mezzanine card), a PMC slot for a trigger receiver card, and slots called FINESSE, where custom daughter boards, known as High-speed Link Board (HSLB), are plugged in. These cards are interconnected via a 32-bit PCI bus and a custom local bus. A new processor based on the 1.6 GHz Intel Atom Z530 chip was developed to power the COPPER module. It collects data from the PCI bus

and transmit them through an on-board Gigabit Ethernet port without disturbing the main PCI bus.

The COPPER system was tested to successfully withstand up to 40 kHz of the level-1 trigger rate. An image of a COPPER board is shown in Fig. 22.

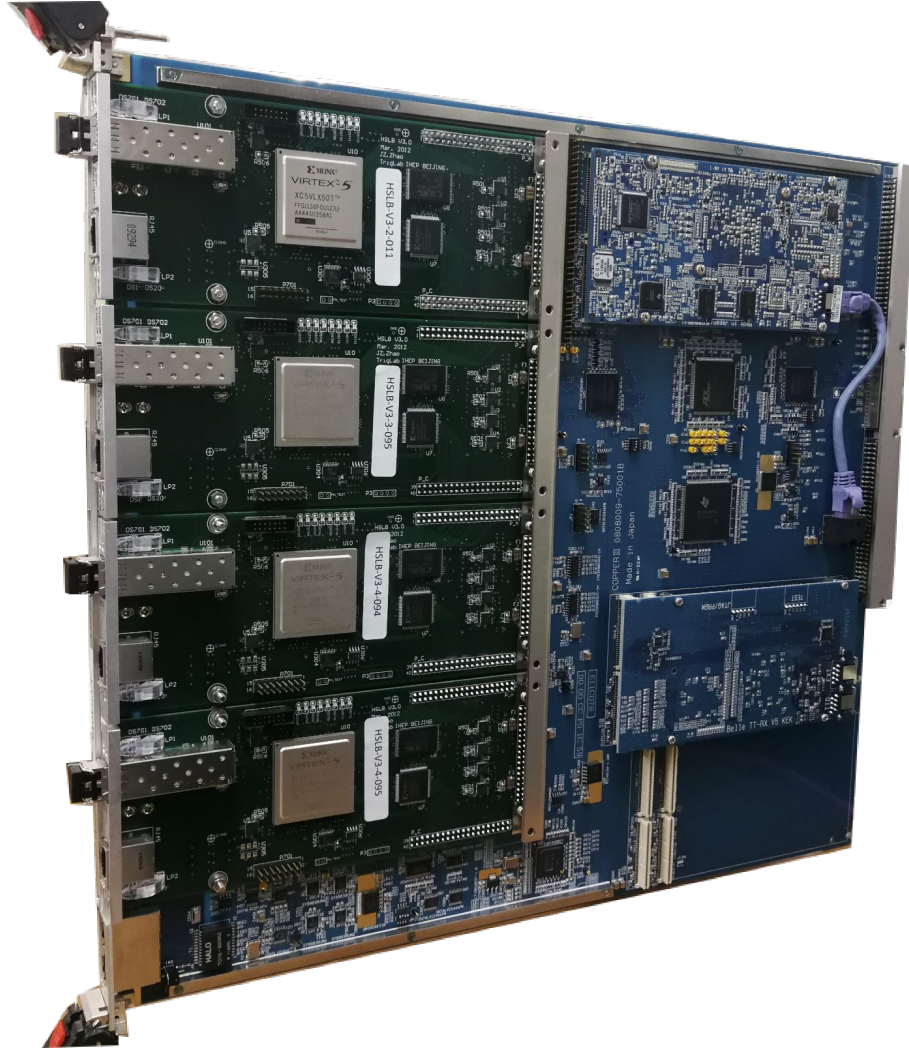


Figure 22. Image of a Common Pipelined Platform for Electronics Readout (COPPER) board. Each of the four slots, as seen on the left side of the image, is connected to a daughter board, called High-Speed Link Board (HSLB) and serves one belle2link connection.

PCIe40 readout

PCIe40 is a next-generation readout module based on the PCIe3.0 specification, with a much higher throughput of 100 Gbps. This module is also used for the DAQ upgrade of the LHCb and ALICE experiments at the Large Hadron Collider (LHC).

To integrate with the existing Belle II DAQ system, the design of the firmware and software for the PCIe40 board needed to be modified. The new PCIe40 based readout system retains all the functionalities of the existing COPPER based readout system. So, no modification in the firmware and hardware of the sub-detector FEE was required. Unlike the existing COPPER boards, which are standalone single board computers, the PCIe40 readout cards are plugged in a PCIe3.0 slot of the readout PC. This makes the whole structure of the Belle II readout system much more compact. Moreover, a single PCIe40 board can serve up to 48 bidirectional optical links (Belle2link) as compared to only 4 links for the COPPER module.

Once the readout upgrade is complete for all the sub-systems, the whole Belle II system will work with only 20 PCIe40 boards, replacing 203 COPPER boards used presently. An image of a PCIe40 card is shown in Fig. 23.



Figure 23. Image of a PCIe40 readout card. There are total 48 slots for belle2link connections, some of them are visible on the left side of the image.

Read-out PC (ROPC)

Readout PCs (ROPC) are regular server grade computers that are mounted in server racks. In case of COPPER based readout, the ROPC receives data from the COPPER boards through Gigabit Ethernet cables. In case of the PCIe40 based readout, the PCIe40 board is itself plugged in into a PCIe3.0 slot in the motherboard of the ROPC. The COPPER to PCIe40 upgrade has greatly reduced the number of ROPCs required for each sub-detector. For example, in case of KLM, with COPPER based readout, there used to be 3 ROPCs, connected with total 8 COPPER boards, serving total 32 FEEs. After PCIe40 upgrade, there is just a single ROPC that houses a single PCIe40 boards, which serves all 32 KLM FEEs.

Frontend Switch (FTSW) and Trigger Time Distribution (TTD)

The sub-detector frontend electronics, as well as, the readout systems are driven by a system clock of 127 MHz derived from accelerator's 509 MHz radio frequency (RF), or reduced frequency clocks generated from the system clock. These clocks are also synchronized to the beam revolution of 100 kHz (5120 RF cycles). The trigger timing is encoded in a 254 Mbps serial signal. The signal is encoded into a 32 bit word and then 8b10b encoded, and also carries various fast control signals. This scheme is developed based on experiences with a similar serialized trigger distribution scheme used in Belle experiment.

Four pairs of a CAT7 cable are used to distribute the clock and serialized trigger information, and to receive the fast status of the front-end board for the trigger flow control. A front-end timing switch (FTSW) module has been developed that can be mounted to a 6U VME rack. It can distribute the timing signals to up to 20 destinations. By cascading this module in 3 stages, the entire system of about 1000 destinations is covered. Sub-detectors are electronically isolated from each other and from the electronics-hut by a fiber based connection. Since serialization is made directly inside the FPGA, a low-latency timing distribution and status collection



Figure 24. Image of an FTSW board.

scheme is possible by avoiding the unnecessary deserialization-serialization pair at each stage.

An image of an FTSW board is shown in Fig. 24.

High Level Trigger (HLT)

The high level trigger (HLT) of the Belle II data acquisition system collects data from the readout PCs, discards uninteresting events using full event reconstruction, provides data quality monitoring (DQM) histograms for all the sub-detectors except PXD and generates RoI for PXD, which helps in greatly reducing the amount of PXD transmitted to storage.

The HLT system is designed to withstand a maximum event rate of 30 kHz, each event being around 100 kB in size. This requires 3 GB/s through the whole system. To achieve this very high online data processing rate, the HLT farm is made of 20 HLT units. Each HLT unit has one input server, one output server, one control server and up to 20 worker nodes. Each worker node is equipped with one or more CPUs, providing 16-40 physical cores per node. The input, worker and output nodes are connected with each other using 10GbE cables, whereas the control node is connected to others using GbE cables.

Originally, UNIX ring buffer based RFARM parallel processing system was used to implement the parallel processing. This used to have a problem of persistent memory state, even after all HLT worked processes were killed, making the system difficult to recover without full reboot. Recently, the RFARM based parallelization has been replaced by a ZeroMQ based implementation, which has greatly improved the stability of the HLT system.

Storage

The online data storage of the Belle II DAQ system is made of several independent STORE units, which are placed behind each of the HLT units. These STORE nodes are connected to the output nodes of the corresponding HLT units through local networks. The STORE unit is also accessible from the control node of the corresponding HLT unit.

Each STORE unit has 10 partitions, each of which has a capacity of about 9 TB. Data are written to a given partition with the aim that data transfer takes place once a partition is full and writing has moved to a new partition. The STORE servers may accumulate data from several runs before initiating a request to transfer raw files to the offline side.

Once the run data is ready to be transferred, a file called “list_send” is created by the `filedb` process running on the STORE server. The `list_send` file contains a list

of all the SROOT/ROOT files that are ready to be copied, along with a checksum for every file. Separate list_send files are created for each STORE unit.

ExpressReco (ERECO)

The ExpressReco is the last part of the Belle II system and situated at the end of the online data flow pipeline. It samples events from the storage, combines the corresponding event data from PXD, and uses this combined information to produce online event display and data quality monitoring plots for all the sub-detectors including PXD. There are two ERECO units available, each of which can work independently. The structure of each ERECO unit is similar to an HLT unit, except it does not have any output node. The distribution of events among the ERECO worker nodes uses the RFARM mechanism and currently being replaced by a ZeroMQ based implementation.

IV.2 Upgrade of the DAQ database systems

The DAQ database system of the Belle II experiment has two important components: the Configuration database and the Logger database. The Configuration database stores the various configurations of the sub-detectors, for example, thresholds, high voltage supply, firmware version, etc. The Logger database stores the log messages from different sub-detectors and contains important debugging information. This database also stores the details of each run, for example, duration, magnetic field, luminosity, etc. Previously, both of the Configuration database and the Logger database were hosted on the same physical server and managed by the same PostgreSQL server instance. After this upgrade, the Configuration database and Logger database have been separated to two different PostgreSQL server instances. A new physical server has also been prepared to work as the fallback for both the Configuration database and Logger database. This new backup server is set up as a hot-spares and is automatically synchronized with the primary database servers.

IV.3 Improvement of the configuration software for the trigger timing distribution system

Previously, all the mappings of the connections of trigger time distribution (TTD) tree, masking information of the frontend electronics, frontend timing switch (FTSW) Ethernet port numbers, and other information needed for the configuration software for the TTD system (`ttaddr`) were hard-coded in several header files, typically one of each sub-detector, in the source code of this program. To make some hardware changes, one needs to modify the header files and then recompile the `ttaddr` program to make it work. The `ttaddr` source code has been modified so that it can now retrieve all the required configuration from the database. All the existing settings previously stored in the header files have been migrated to the respective configuration database tables. This not only eliminates the hassle of recompiling `ttaddr` every time some change is made to the hardware configuration, but also keeps the record of all the previous configurations in the database.

IV.4 Development of the slow-control system for the PCIe40 based read-out

The data acquisition system of the Belle II experiment is currently transitioning from COPPER based readout to PCIe40 based readout system. PCIe40 is the next generation readout system originally developed for the LHCb experiment at CERN. A new set of slow-control daemons have been developed to control the data acquisition using this new readout system, as well as to configure and monitor the sub-detector frontend electronics through the optical fiber connected to the PCIe40 board. The KLM frontend specific code has also been modified to work with the new system. Fig. 25 shows different components of the slowcontrol system for this new PCIe40 based readout.

The new local RunControl GUI for the KLM sub-detector is shown in Fig. 26.

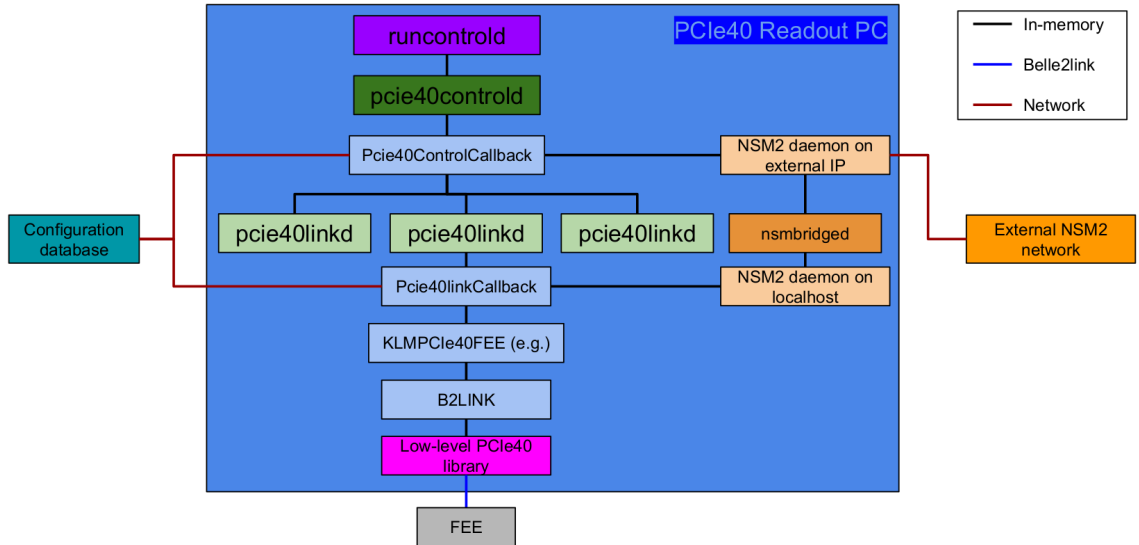


Figure 25. The slow-control system for the PCIe40 based readout system.

This new GUI provides the functionality of setting both belle2link side masking and TTD side masking directly from the GUI. The belle2link side making is set by the `pcie40linkd` daemons and the TTD side masking is set through the Config. DB interface of the `ttaddr` command. This greatly simplifies the procedure of excluding the problematic part of a sub-detector during data taking.

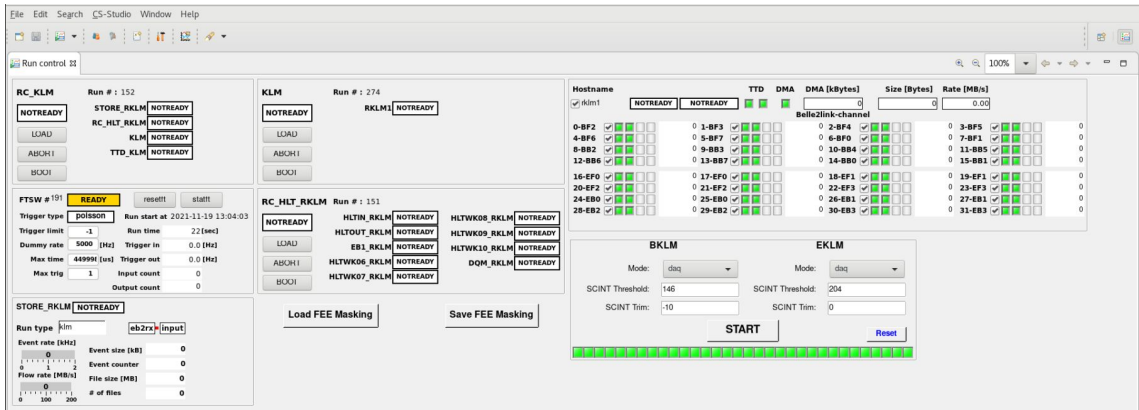


Figure 26. The RunControl GUI for the PCIe40 based readout system.

CHAPTER V

DARK SCALAR MODEL AND MONTE CARLO (MC) GENERATION

Many of the beyond standard model (BSM) theories predict the existence of additional scalars other than the Higgs boson. The possible coupling between such a new scalar ϕ_L and SM particles is constrained by SM gauge invariance. The mixing between this dark scalar and the SM Higgs boson gives rise to couplings proportional to SM fermion masses. If this new scalar couples to both quarks and leptons, the existence of such particles is strongly constrained by the searches for rare flavor-changing neutral current decays of mesons, e.g. $B \rightarrow K\phi$ and $K \rightarrow \pi\phi$ [15], where ϕ is a generic dark scalar candidate that couples to both quarks and leptons. However, these bounds are evaded if the coupling of the scalar to quarks is suppressed and this scalar interacts preferentially with leptons. In the MeV - GeV range, such new scalars could mediate interactions between the SM and dark matter, as well as account for the observed discrepancy in the muon anomalous magnetic moment [16]. This leads us to the search for a dark leptophilic scalar.

The interaction between the dark scalar and SM leptons can be described using this term in the Lagrangian [17]:

$$L = -\xi \sum_{\ell=e,\mu,\tau} \frac{m_\ell}{v} \bar{\ell} \phi_L \ell \quad (1)$$

Here ϕ_L is our leptophilic dark scalar, ξ denotes the strength of flavor-independent coupling to SM leptons and $v = 246$ GeV is the SM Higgs vacuum expectation value.

The present exclusion region between the coupling constant ξ and the mass of dark scalar m_{ϕ_L} is shown in Fig. 27 taken from a recent result [18] from *BABAR* collaboration, obtained using 514 fb^{-1} of data.

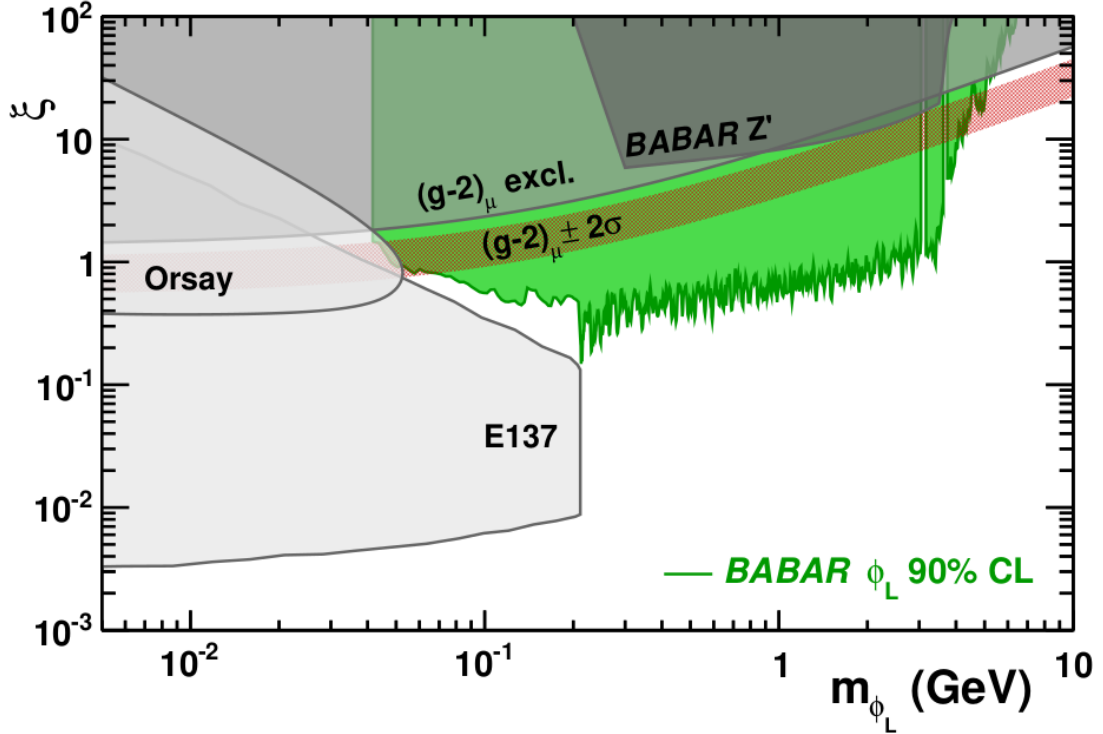


Figure 27. The 90% CL limits on the coupling ξ as a function of the ϕ_L mass from *BABAR* (green) and other experiments (gray). The parameter space preferred by the muon anomalous magnetic moment is shown as a red band.

The signal cross-sections for different mass points are calculated using MadGraph 5 [19]. MadGraph is a framework that provides necessary tools for the computation of cross-section and event generation for standard model (SM) and various new physics extensions. The leptophilic dark scalar model is described in this [17] paper. In $e^+e^- \rightarrow \tau^+\tau^-\phi_L$ process, because of the mass dependent coupling with the SM leptons, the dark scalar particle is far more likely to radiate from the tau leptons. This makes the diagrams shown in Fig. 28 and Fig. 29 the dominant ones for the respective channels. The complete list of Feynman diagrams for each channel, as obtained from MadGraph, is given in Appendix A.

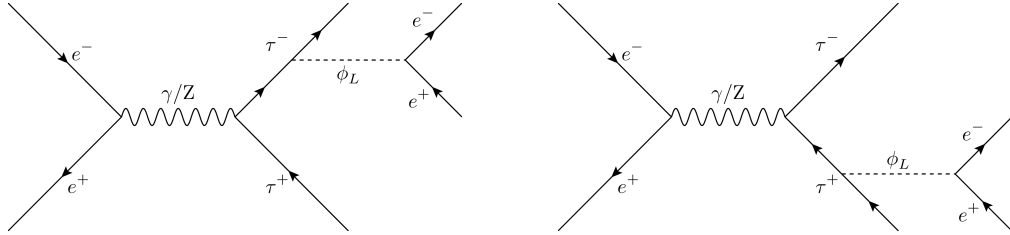


Figure 28. Dominant Feynman diagrams for the $e^+e^- \rightarrow \tau^+\tau^-\phi_L$, $\phi_L \rightarrow e^+e^-$ process.

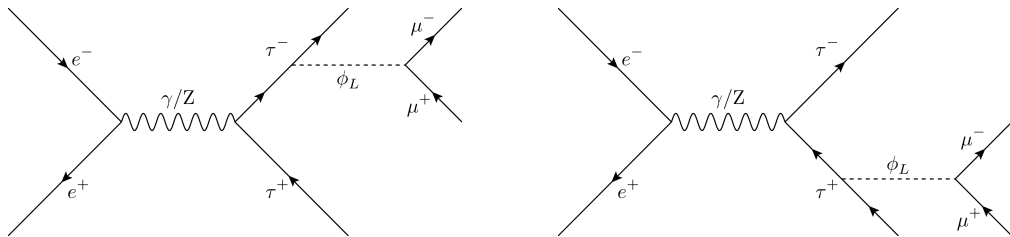


Figure 29. Dominant Feynman diagrams for $e^+e^- \rightarrow \tau^+\tau^-\phi_L$, $\phi_L \rightarrow \mu^+\mu^-$ process.

V.1 Effect of initial state radiation (ISR)

The effect of ISR was simulated using the MGISR plugin. This MadGraph plugin is introduced in this [20] paper, and the source code is available on GitHub [21].

However, we plan to generate our signal MC sample using KKMC [22] and PHOTOS [23], so that we can subsequently decay the tau leptons in all possible decay modes using Tauola [24]. So we need to validate the modeling of ISR in MadGraph/MGISR against KKMC/PHOTOS. For this purpose, we study these two SM processes: $e^+e^- \rightarrow \mu^+\mu^-$ and $e^+e^- \rightarrow \tau^+\tau^-$.

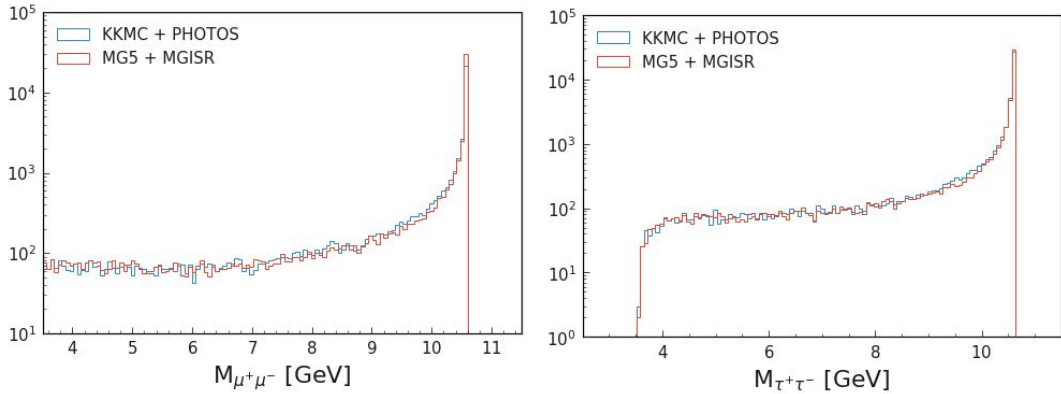


Figure 30. Comparison of $\ell^+\ell^-$ invariant mass distributions between KKMC/PHOTOS and MadGraph/MGISR generators for two SM processes: $e^+e^- \rightarrow \mu^+\mu^-$ (left) and $e^+e^- \rightarrow \tau^+\tau^-$ (right).

The comparison of generator level lepton pair invariant mass shows excellent agreement between KKMC/PHOTOS and MadGraph as illustrated in Fig. 30.

V.2 Signal cross-section calculation

The MadGraph model for the dark leptophilic scalar is built from the interaction term in the Lagrangian using the FeynCalc [25] package in Mathematica [26]. We calculate the cross-section by running MadGraph [19] simulation using this model along with the MGISR [20, 21] plugin to account for ISR correction.

The plot in Fig. 32 shows the cross-section of the $e^+e^- \rightarrow \tau^+\tau^-\phi_L, \phi_L \rightarrow e^+e^-$ process in the range where the dark scalar mass is in between 40 MeV and the di-muon mass. The cross-section quickly drops as we cross the di-muon mass, as above this mass, the dark scalar predominantly decays to a $\mu^+\mu^-$ pair as shown in the right plot from the paper [17] that introduces this dark scalar model. The plots in Fig. 33 show the cross-section of the $e^+e^- \rightarrow \tau^+\tau^-\phi_L, \phi_L \rightarrow \mu^+\mu^-$ process in the range where the dark scalar mass is over the di-muon mass. The cross-section drops as we cross the taupair mass, but unlike the previous case, the drop is not that extreme. This is also evident from the right plot of Fig. 31, where we see that the drop in the branching ratio of $\phi_L \rightarrow e^+e^-$ after crossing di-muon mass is way larger than the drop in the branching ratio of $\phi_L \rightarrow \mu^+\mu^-$ after crossing the taupair mass.

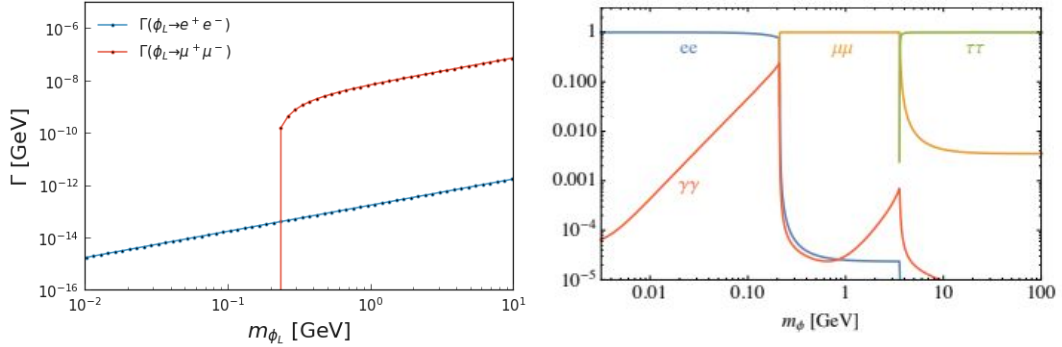


Figure 31. Decay width of the $\phi_L \rightarrow e^+e^-$ and $\phi_L \rightarrow \mu^+\mu^-$ processes (left) and the branching ratios of the different decay modes of the dark scalar (right) as a function of its mass, for $\xi = 1$.

The decay widths of the dark scalar is shown as a function of its mass in the left plot of Fig. 31. The right plot, taken from this [17] paper, agrees with the partial

decay widths shown in the left plot.

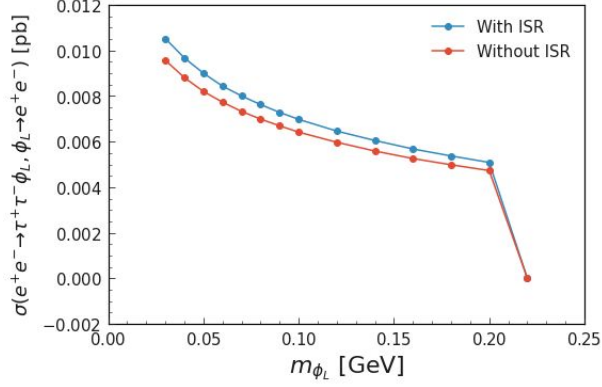


Figure 32. Cross-section of the signal process $e^+e^- \rightarrow \tau^+\tau^-\phi_L, \phi_L \rightarrow e^+e^-$ for $\xi = 1$ as a function of the dark scalar mass.

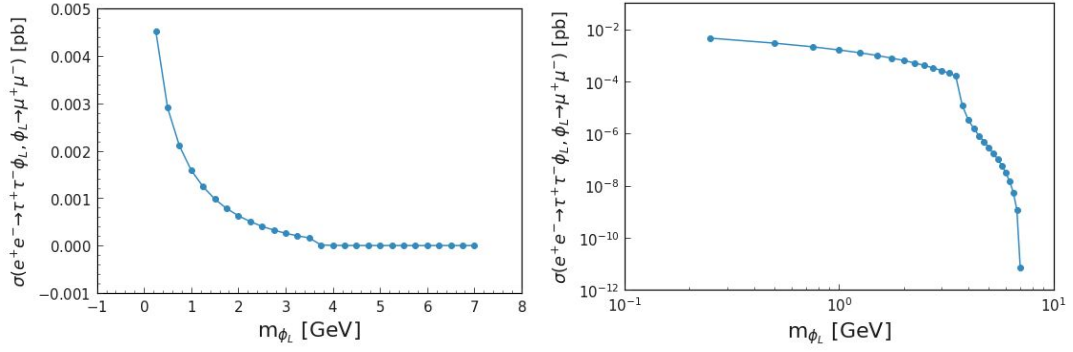


Figure 33. Cross-section of the signal process $e^+e^- \rightarrow \tau^+\tau^-\phi_L, \phi_L \rightarrow \mu^+\mu^-$ as a function of the dark scalar mass, for $\xi = 1$. The cross-section is shown in both linear (left) and log (right) scale.

V.3 Comparing two complementary processes with identical final states

Let's compare these two complementary processes with identical final states:

- $e^+e^- \rightarrow \tau^+\tau^-\phi_L, \phi_L \rightarrow \mu^+\mu^-$
- $e^+e^- \rightarrow \mu^+\mu^-\phi_L, \phi_L \rightarrow \tau^+\tau^-$

In both cases, we have $\mu^+\mu^-\tau^+\tau^-$ in our final states. So we compare the theoretical cross-sections of these two processes. Below 5.7 GeV, our signal process is more promising than the complimentary one as shown in Fig. 34. Above 5.7 GeV, the sensitivity of the upper limit falls dramatically, as shown in the published *BABAR* result. So the complementary process, with slightly higher cross-section, doesn't help to exclude any new region.

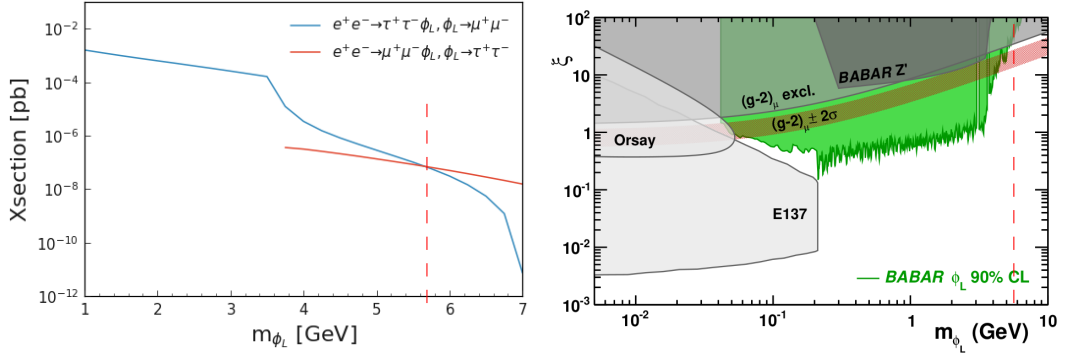


Figure 34. Comparison of the cross-sections of $e^+e^- \rightarrow \tau^+\tau^-\phi_L, \phi_L \rightarrow \mu^+\mu^-$ and $e^+e^- \rightarrow \mu^+\mu^-\phi_L, \phi_L \rightarrow \tau^+\tau^-$ processes for different ϕ_L mass points.

V.4 Signal Monte-Carlo sample generation

We use KKMC to generate the signal MC sample, as it allows us to use Tauola to subsequently decay the tau leptons into all possible decay modes. The emission of the dark scalar has been simulated using PHOTOS++. Originally, PHOTOS++ is used to model emission of lepton pairs from γ/Z propagator. The functionality of PHOTOS++ has been extended [27] to simulate the emission of a dark scalar, decaying to a lepton pair.

A new switch IPAIRPHOTOS has been introduced for the KKMC/Tauola/PHOTOS++ generator pipeline, which controls the emission of the dark scalar -

- IPAIRPHOTOS = 0: $e^+e^- \rightarrow \tau^+\tau^- (\gamma)$
- IPAIRPHOTOS = 1: $e^+e^- \rightarrow \tau^+\tau^- \phi_L(\gamma), \phi_L \rightarrow e^+e^-$
- IPAIRPHOTOS = 2: $e^+e^- \rightarrow \tau^+\tau^- \phi_L(\gamma), \phi_L \rightarrow \mu^+\mu^-$
- IPAIRPHOTOS = -1: generic SM mixture with internal conversion, i.e. $e^+e^- \rightarrow \tau^+\tau^- (\gamma), \tau^+\tau^- e^+e^- (\gamma), \tau^+\tau^- \mu^+\mu^- (\gamma)$

The KKMC generator with the latest Tauola and PHOTOS++ packages are now part of the basf2 framework. The signal MC sample for Belle has been generated using basf2, with the help of B2BII package. The BelleMCOutput module of the B2BII package allows us to store the generated signal events in a binary format compatible with Belle sim+reco script. We add the OverrideGenerationFlags module before invoking the generator in our basf2 script and turn off the bpsmear module in the Belle gsim script as instructed in this [28] presentation.

CHAPTER VI

ANALYSIS OF BELLE DATA

VI.1 Outline of the analysis

We search for this dark scalar candidate in the $e^+e^- \rightarrow \tau^+\tau^-\phi_L$ channel, where ϕ_L decays in two decay modes, depending on its mass. In the mass range less than the di-muon mass, we consider the decay mode $\phi_L \rightarrow e^+e^-$ and in the mass range above that, we consider the decay mode $\phi_L \rightarrow \mu^+\mu^-$. We restrict our search in the mass range 40 MeV to 6.5 GeV.

We look for events with 4 good tracks. The net charge of the event is required to be zero. In $\phi_L \rightarrow e^+e^-$ channel, we require at least one e^- and one e^+ track. Similarly, in $\phi_L \rightarrow \mu^+\mu^-$ channel, we require at least one μ^- and one μ^+ track. We combine them to form the dark scalar candidate. The other two tracks correspond to the 1-prong decays of the two tau leptons.

Reconstruction of dark scalar candidate

While reconstructing the $\phi_L \rightarrow \ell^+\ell^-$ ($\ell = e, \mu$) decay, depending on the number of ℓ^+ and ℓ^- in the event, there can be up to 4 ϕ_L candidates -

- 1 ℓ^+ and 1 ℓ^- : 1 ϕ_L candidate
- 2 ℓ^+ and 1 ℓ^- : 2 ϕ_L candidates
- 1 ℓ^+ and 2 ℓ^- : 2 ϕ_L candidates

- 2 ℓ^+ and 2 ℓ^- : 4 ϕ_L candidates

We fit the $\phi_L \rightarrow \ell^+\ell^-$ vertex to require the ℓ^+ and ℓ^- tracks to come from the same point in space. At this stage, we don't put any constraint on the position of this vertex. After the vertexing cut, if multiple ϕ_L candidates survive, we choose the one with the smallest opening angle. This ensures there is exactly one candidate per selected event.

Reconstruction of the tau leptons

Once we choose our ϕ_L candidate, we are left with two other tracks that are not the daughters of this candidate. We assume those two tracks come from 1-prong decays of the two tau leptons.

Since we started with 4 tracks with net charge zero, and we combine two oppositely charged tracks to form our dark scalar candidate, it is already ensured that we are left with two oppositely charged tracks. We reconstruct a τ^+ and a τ^- from those two tracks. Finally, we combine these 3 particles (τ^+ , τ^- and ϕ_L) to form the νpho candidate and that completes our reconstruction chain.

Obtaining the exclusion region

We choose a number of mass points in our search range of 40 MeV to 6.5 GeV. We try to measure the cross-section of the process $e^+e^- \rightarrow \tau^+\tau^-\phi_L, \phi_L \rightarrow \ell^+\ell^-$, where $\ell = e$ or μ depending on the mass point. We use $\ell^+\ell^-$ invariant mass as our discriminating variable, as we should expect a bump in the distribution of this variable if we discover a dark scalar particle of that particular mass. We fit signal and background distributions of this variable with the distribution obtained from data and calculate the upper limit on cross-section. Once we find an upper limit of this cross-section, we can translate it to an upper limit on the coupling constant ξ . In this way, we get the upper limit of ξ as a function of the dark scalar mass and obtain the exclusion region.

VI.2 KEKB accelerator and Belle Detector

The KEKB is an electron-positron collider situated at the KEK accelerator laboratory in Tsukuba, Japan. This asymmetric collider achieved a peak luminosity of $2.1 \times 10^{34} \text{cm}^{-2}\text{s}^{-1}$ in June 2009, which is more than double of its designed value. An integrated luminosity of 1018fb^{-1} was accumulated with the help of Belle detector till December 2009.

Fig. 35 shows the KEKB accelerator complex [29], which has a circumference of approximately 3 km. Each positron in the lower energy ring (LER) is accelerated to an energy of 3.5 GeV and each electron in the high energy ring (HER) is accelerated to an energy of 6.5 GeV before collision. KEKB stores beam currents up to 2.0 A in the LER and 1.35 A in the HER.

The Belle detector [30] was placed at the interaction point (IP) of the KEKB electron-positron collider. The detector was a large-solid-angle magnetic spectrometer consisting of a silicon vertex detector (SVD), a central drift chamber (CDC), an array of aerogel threshold Cherenkov counters (ACC), time-of-flight scintillation counters (TOF), and a CsI(Tl) crystal electromagnetic calorimeter (ECL), all located inside a superconducting solenoid providing an axial magnetic field of 1.5 T. An iron flux-return located outside the solenoid coil was instrumented with resistive plate chambers to detect K_L^0 mesons and muons (KLM).

The z-axis of the detector and the solenoid are along the positron beam, i.e. the positrons move in the negative z direction. The CDC measures the longitudinal and transverse momentum components of a charged track. The track coordinates near the IP are provided by the SVD. Photon detection and energy measurements are performed by the ECL. The identification of pions, kaons and protons is performed using information from TOF and ACC. Fig. 36 shows a schematic diagram of the Belle detector along with its different sub-detectors.

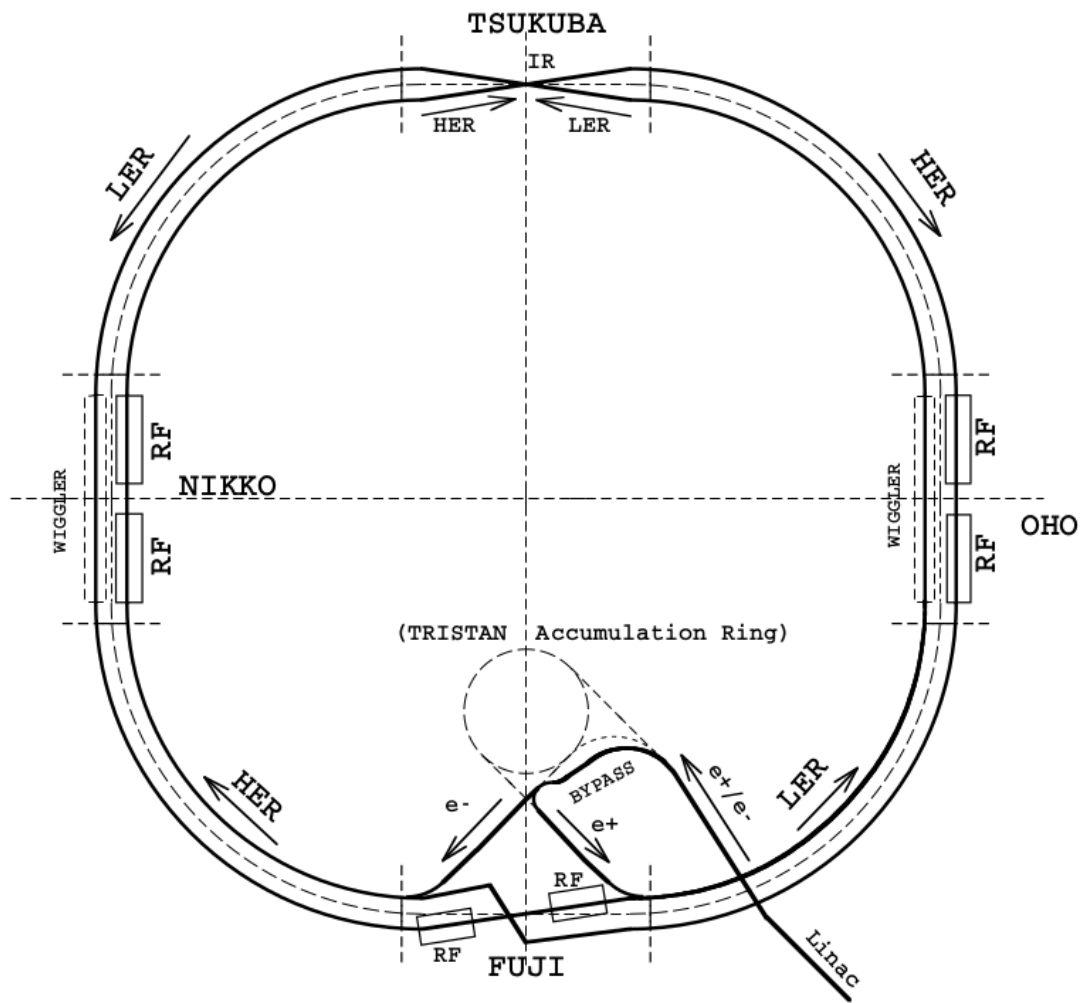


Figure 35. The KEKB accelerator complex.

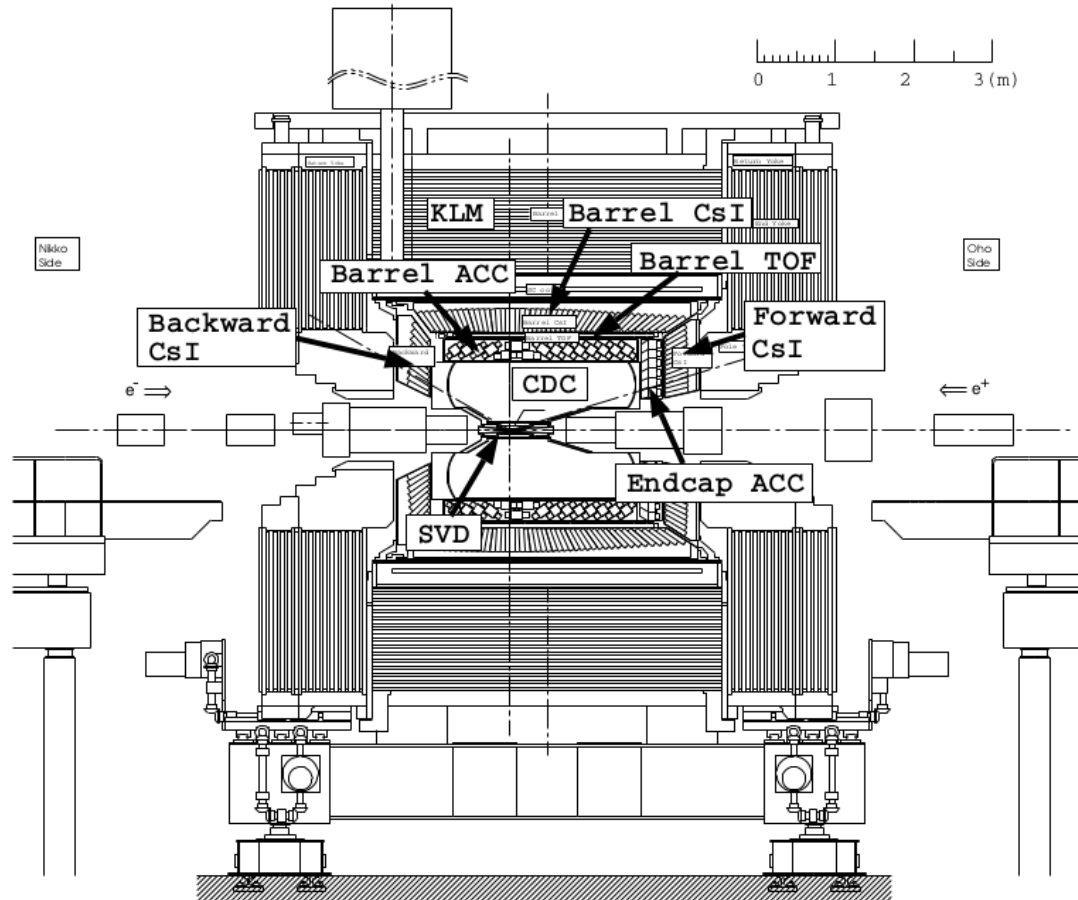


Figure 36. The Belle detector.

VI.3 Data and Monte-Carlo samples

We use the SVD2 dataset collected at $\Upsilon(4S)$ resonance along with some continuum data collected at a slightly less energy. This dataset corresponds to the data collected after the upgrade of the SVD sub-detector in October 2003. The total amount of analyzed data is 625.897 fb^{-1} , obtained from these two datasets:

- $\Upsilon(4S)$: 562.152 fb^{-1} (Exp. 31 to Exp. 65)
- Continuum: 63.745 fb^{-1} (Exp. 31 to Exp. 65)

We have analyzed both HadronBJ and tau_skimB skimmed datasets as the HadronBJ skim also includes some taupair events. However, there is some overlap between these two skims, as the J/ψ events are included in both of them. To take care of this situation, we don't process any J/ψ event from the HadronBJ skimmed dataset. We have used case-B MC samples for these SM processes:

Process	Cross-section at $\Upsilon(4S)$	N_{MC}/N_{Data}	Exp
$e^+e^- \rightarrow q\bar{q}$ ($q = u, d, s$)	2.09 nb	6	31 - 65
$e^+e^- \rightarrow c\bar{c}$	1.3 nb	6	31 - 65
$e^+e^- \rightarrow B^0\bar{B}^0$	0.525 nb	10	31 - 65
$e^+e^- \rightarrow B^+B^-$	0.525 nb	10	31 - 65
$e^+e^- \rightarrow e^+e^-$	$123.5 \pm 0.2 \text{ nb}$	0.2	31 - 35
$e^+e^- \rightarrow \mu^+\mu^-$	$1.005 \pm 0.001 \text{ nb}^1$	10	31 - 65
$e^+e^- \rightarrow \tau^+\tau^-$	$0.919 \pm 0.003 \text{ nb}$	10	31 - 65
$e^+e^- \rightarrow e^+e^-e^+e^-$	40.9 nb	9.8	35 - 51, 55 - 65
$e^+e^- \rightarrow e^+e^-\mu^+\mu^-$	18.9 nb	9.8	35 - 51, 55 - 65
$e^+e^- \rightarrow e^+e^-(u\bar{u}/d\bar{d})$	12.5 nb	9.9	31 - 51, 55 - 65
$e^+e^- \rightarrow e^+e^-s\bar{s}$	0.227 nb	9.9	31 - 51, 55 - 65
$e^+e^- \rightarrow e^+e^-c\bar{c}$	0.03 nb	9.9	31 - 51, 55 - 65

Table 2. List of the available MC samples relevant to this analysis. The cross-section values listed in this table are the ones used for the MC sample production.

The cross-section values listed in this table are the ones used during the production of Belle official MC samples. They can be slightly different from the latest accepted numbers.

The $q\bar{q}$, Bhabha, $\mu^+\mu^-$, and two-photon MC samples are generated using Evt-Gen [32], BHLUMI [33], KKMC [22], and AAFHB [34] respectively. The $\tau^+\tau^-$ samples are generated using KKMC + Tauola.

VI.4 Reconstruction

We use the following preselection cuts to select our signal event:

- The number of tracks in the event is equal to 4. Each track satisfies these cuts:

$$dr \leq 1.0 \text{ cm and } \text{abs}(dz) \leq 5.0 \text{ cm}$$

$$p_T > 0.06 \text{ GeV (in barrel) or } p_T > 0.10 \text{ GeV (in endcaps)}$$

- Sum of the charges of those 4 tracks is equal to 0.
- At least two of those tracks pass $\text{eID} \geq 0.9$ cut (for $\phi_L \rightarrow e^+e^-$ channel) or $\text{muID} \geq 0.9$ cut (for $\phi_L \rightarrow \mu^+\mu^-$ channel).
- We apply additional rectangular cuts based on the missing mass and the theta of the missing momentum of the event. It is described in detail later in this section.

In $\phi_L \rightarrow e^+e^-$ channel, we combine one electron track and one positron track to form the ϕ_L candidate. In $\phi_L \rightarrow \mu^+\mu^-$ channel, we combine two oppositely charged muon tracks to form the ϕ_L candidate. We apply vertexing to require those two tracks to come from the same point. However, we don't put any constraint on the position of this vertex.

Background Suppression

Removing combinatorial background

As pointed out in Section VI.1, both $\phi_L \rightarrow e^+e^-$ and $\phi_L \rightarrow \mu^+\mu^-$ channels suffer from combinatorial background if multiple leptons of the flavor same as the flavor for the daughter of ϕ_L are present.

In $\phi_L \rightarrow \ell^+\ell^-$ ($\ell = e, \mu$) channel, depending on the number of ℓ^+ and ℓ^- in the event, there can be up to 4 ϕ_L candidates -

- 1 ℓ^+ and 1 ℓ^- : 1 ϕ_L candidate

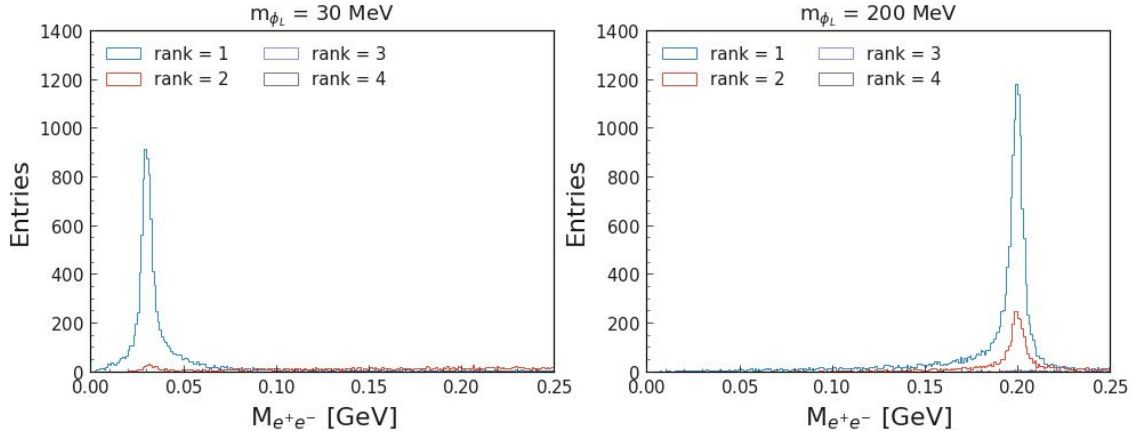


Figure 37. Distribution of the e^+e^- invariant mass for ϕ_L candidates with different opening angle ranks at two different mass points ($\phi_L \rightarrow e^+e^-$ channel).

- 2 ℓ^+ and 1 ℓ^- : 2 ϕ_L candidates
- 1 ℓ^+ and 2 ℓ^- : 2 ϕ_L candidates
- 2 ℓ^+ and 2 ℓ^- : 4 ϕ_L candidates

However, only one of them corresponds to the true ϕ_L and rest of them are combinatorial background. In order to get rid of those, we use a simple but effective strategy: we keep the candidate with the smallest opening angle and discard the rest.

There is some fine detail we want to emphasize here. We first perform the vertex fit to remove some ϕ_L candidates, and then we apply our strategy of keeping the candidate with the smallest opening angle. So the final *signal* candidate we end up selecting is not necessarily the one with the smallest opening angle out of all possible candidates.

We show the distributions of $\ell^+\ell^-$ invariant mass of the ϕ_L candidate for different opening angle ranks in Fig. 37 and Fig. 38. In these plots, rank=1 corresponds to the candidate with the smallest opening angle.

These plots show that the peaks in $\ell^+\ell^-$ invariant mass distributions are mostly made of the smallest opening angle candidates.

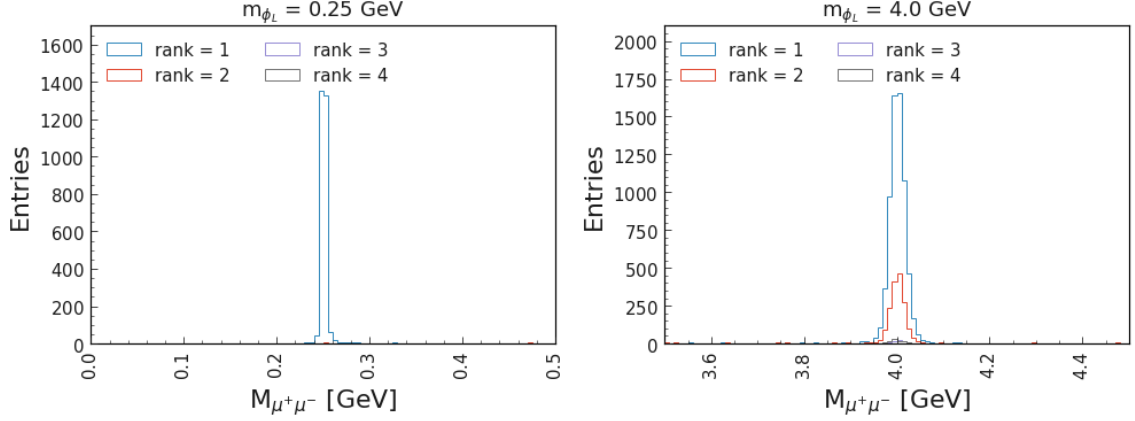


Figure 38. Distribution of the $\mu^+\mu^-$ invariant mass for ϕ_L candidates with different opening angle ranks at two different mass points ($\phi_L \rightarrow \mu^+\mu^-$ channel).

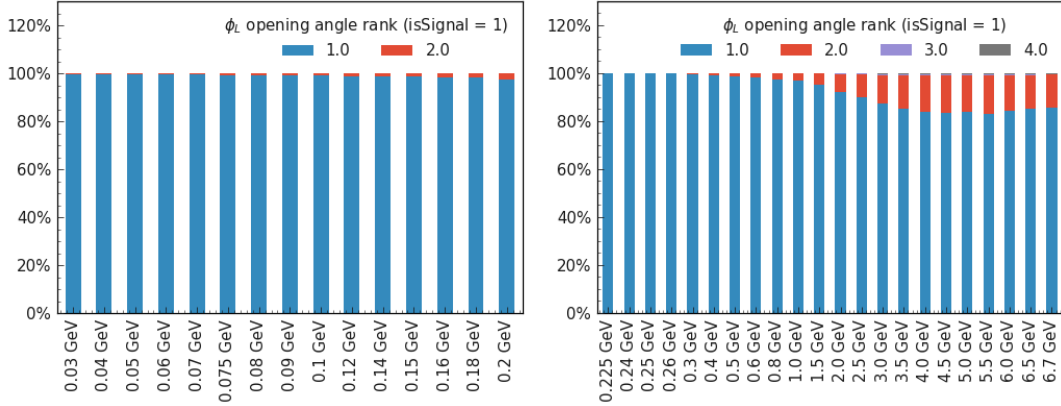


Figure 39. Fraction of MC truth matched ϕ_L candidates corresponding to different opening angle ranks. This shows the fraction of signal we retain by selecting only the smallest opening angle candidate, for different mass points in $\phi_L \rightarrow e^+e^-$ (left) and $\phi_L \rightarrow \mu^+\mu^-$ (right) channels.

In order to quantify how much signal we retain by choosing only the smallest opening angle candidate as our signal candidate, we take the help of MC truth matching. In the plots in Fig. 39, we show the fractions of MC truth matched signal candidates corresponding to different opening angle ranks. This shows the fraction of signal we retain by selecting only the smallest opening angle candidate, i.e. the efficiency of this selection criteria.

Our strategy of selecting the smallest opening angle candidate will also select some

background candidates, i.e. the purity of this selection criteria is not 100%. However, we cannot calculate the purity of this cut by following the similar MC truth based strategy. One way could have been to calculate these fractions the other way around, i.e. we first select only the rank=1 candidates and then find out the fractions of those corresponding to isSignal=1 and isSignal=0. But that doesn't give us the purity of this cut, as isSignal=0 does not necessarily correspond to a background candidate. In other words, we can calculate the efficiency of this rank=1 cut by assuming the purity of isSignal=1 to be 100%, which is a fair assumption, but we cannot calculate the purity of this cut as it requires us to know the efficiency of isSignal=1 (or the purity of isSignal=0), which we don't know.

We have also investigated the alternate approach to select the ϕ_L candidate of the highest χ^2 probability obtained from the vertex fit. However, the opening angle based approach works better for the most of the mass range. A comparison between the performance of these two approaches is discussed in Appendix B.

The signal distributions of the e^+e^- invariant mass (for $\phi_L \rightarrow e^+e^-$ channel) using this candidate selection criteria are shown in Fig. 40, for different mass points.

The signal distributions of the $\mu^+\mu^-$ invariant mass (for $\phi_L \rightarrow \mu^+\mu^-$ channel) using this candidate selection criteria are shown in Fig. 41, for different mass points.

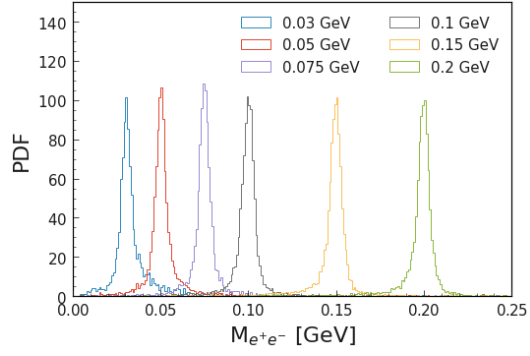


Figure 40. Signal distribution of e^+e^- invariant mass for different ϕ_L mass points.

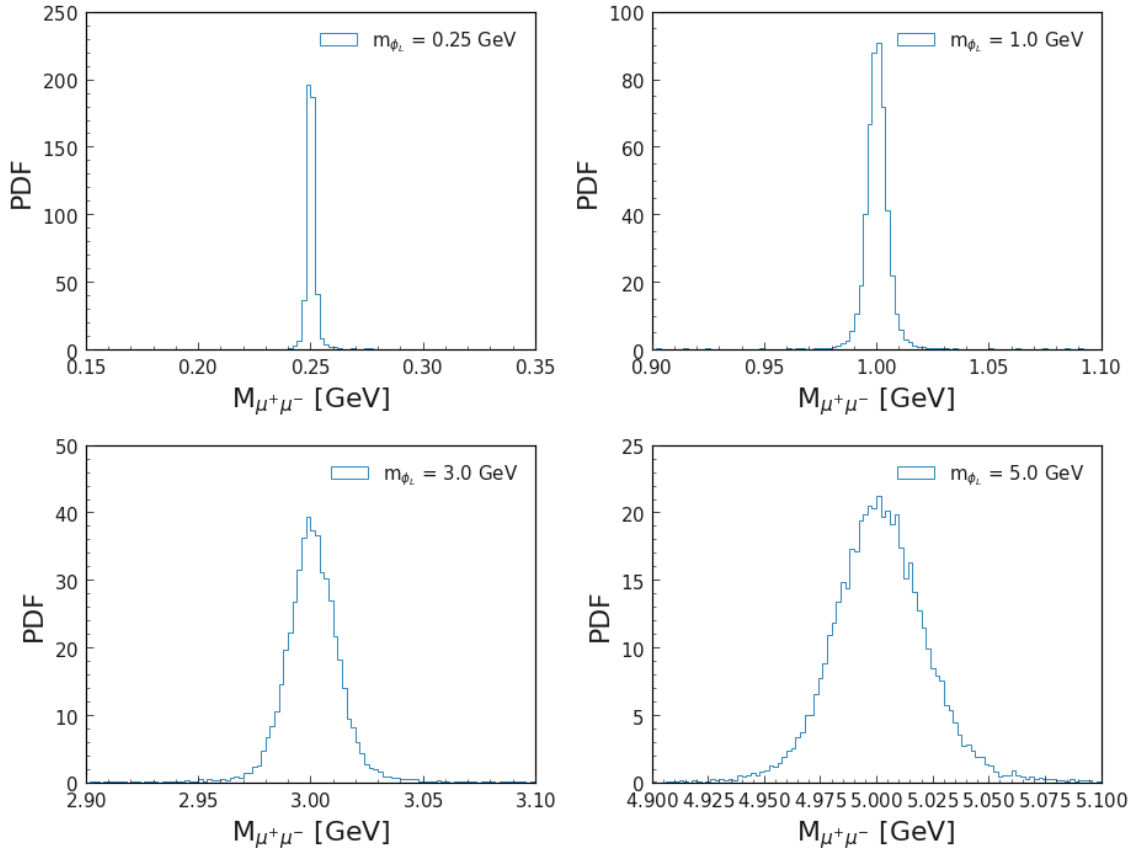


Figure 41. Signal distribution of $\mu^+\mu^-$ invariant mass for different ϕ_L mass points.

Suppressing two-photon and $\ell^+\ell^-$ backgrounds

We use rectangular sideband cuts on the invariant mass and theta of the missing momentum. The goal of these cuts is to suppress the two-photon and $\ell^+\ell^-$ backgrounds. In terms of basf2 variables, these two cuts are -

- $4 \text{ GeV}^2 < \text{missingMass2OfEvent} < 36 \text{ GeV}^2$
- $0.5236 (30^\circ) < \text{missingMomentumOfEventCMS_theta} < 2.618 (150^\circ)$

Fig. 42 shows the distribution of these two variables for different background and signal samples. The black rectangle at the center defines our cuts: any event outside this rectangle is discarded.

This pair of cuts is referred to as “rectangular sideband cuts” for the rest of this text. These cuts are used as part of preselection and are used in the rest of the analysis, including all signal and control region plots, for both of the channels.

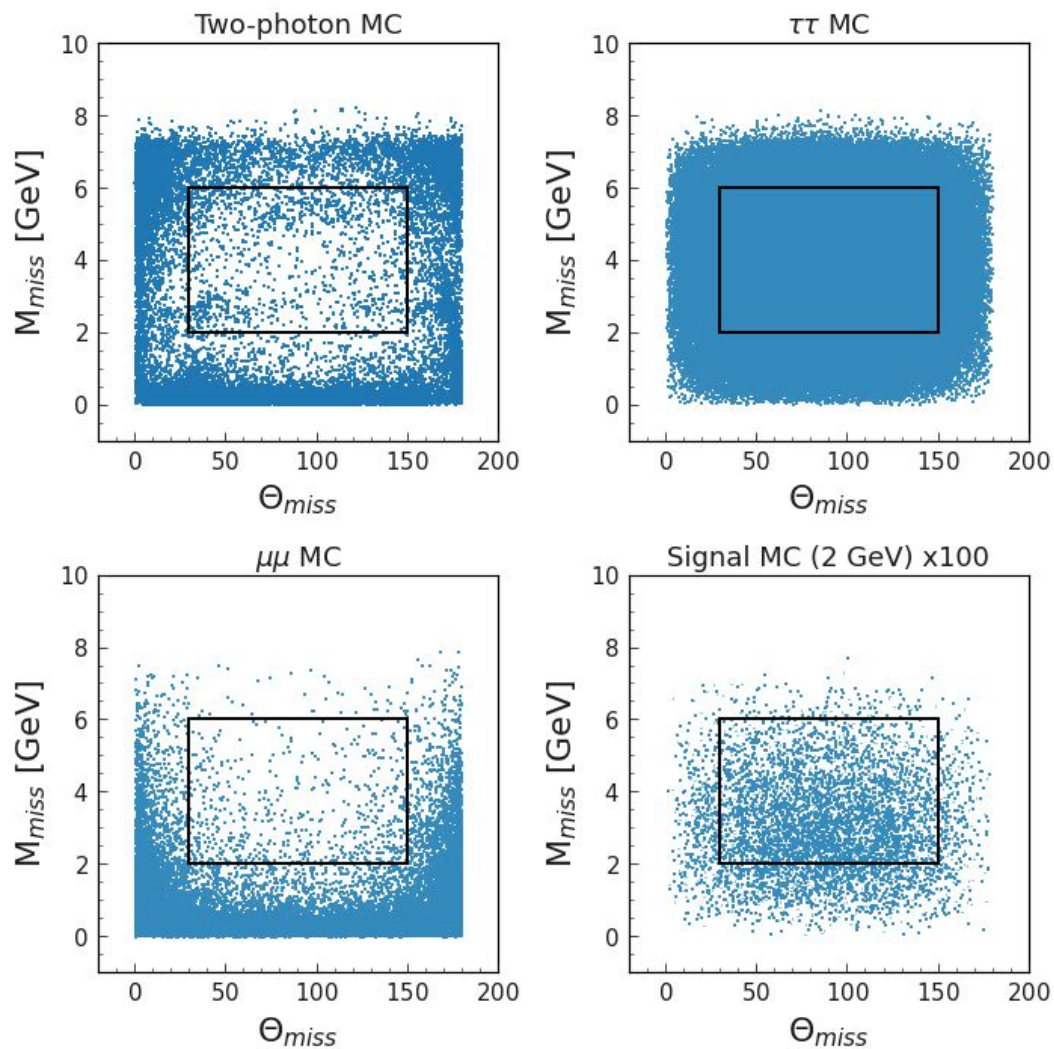


Figure 42. Rectangular sideband cuts are to suppress the two-photon and $\ell^+\ell^-$ backgrounds.

Suppressing ρ^\pm decay events from taupair sample

In order to understand the SM taupair background, we use a basf2 module called TauDecayMarker. It uses MC truth level information to identify the decay modes of τ^+ and τ^- in a taupair event. Since our signal events have 4 tracks, we expected most of the taupair background to come from 3x1-prong tau decays, i.e. one of the taus decays in 3-prong and the other decays in 1-prong decay mode. However, the result of TauDecayMarker says otherwise: most of the taupair background comes from 1x1 tau decay.

Fig. 43 shows that most of the background comes from the events where decays of τ^+ or τ^- produces ρ^+ or ρ^- . The subsequent decays ρ^+ or ρ^- produces 3 tracks, which in turn mimics our signal event.

Let's take the case where τ^- decays as $\tau^- \rightarrow \rho^- \nu_\tau$. Now this ρ^- can decay in the following two ways to mimic the final state of our signal process:

- $\rho^- \rightarrow \pi^- \pi^0, \pi^0 \rightarrow e^+ e^- \gamma$
- $\rho^- \rightarrow \pi^- \pi^0, \pi^0 \rightarrow \gamma \gamma, \gamma \rightarrow e^+ e^-$

Fig. 44 shows how a ϕ_L candidate can be formed from the descendants a ρ^- . We can verify this from the PDG of the MC matched particle of ϕ_L as well as from the PDG of the MC mother of the daughter tracks.

hl_mcPDG	
Value	Count
22	7913
111	1807
213	2
11	2

hl.e_0_genMotherPDG	
Value	Count
22	7308
111	1474
15	14
0	1

It is also apparent from Fig. 44 how such background can be suppressed. If we combine the ϕ_L candidate and its closest photon, and then take the invariant mass of them, it should be close to the mass of a π^0 .

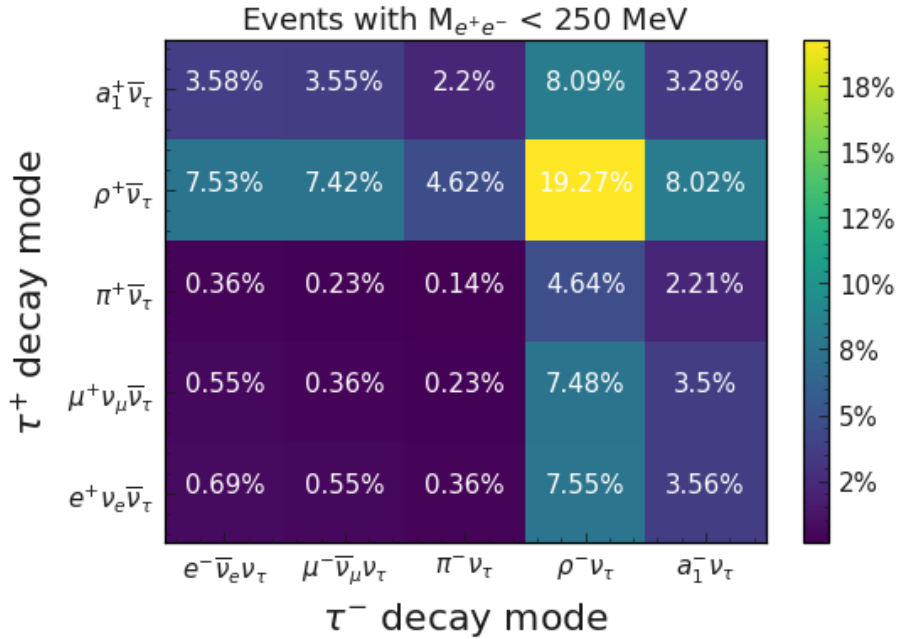
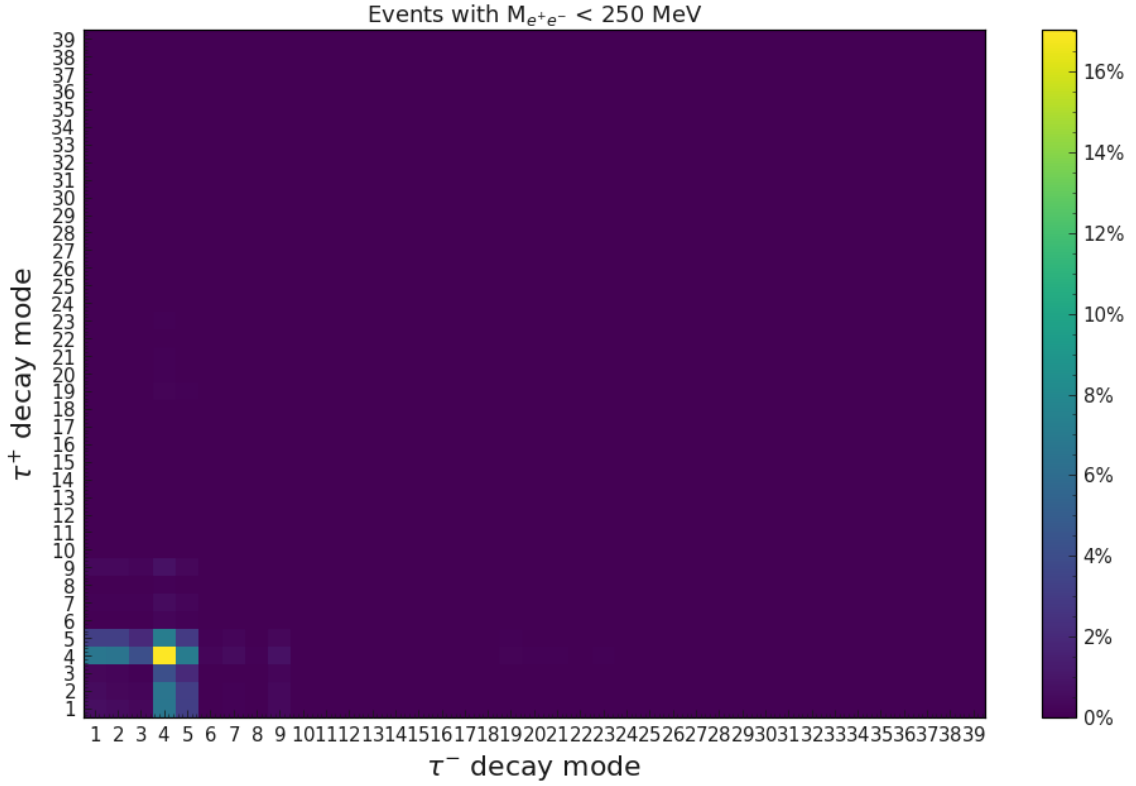


Figure 43. Result of TauDecayMarker showing the τ^+ and τ^- decay modes in SM taupair sample, for $\phi_L \rightarrow e^+e^-$ channel. The bottom plot is a zoomed in version of the lower left corner of the top plot.

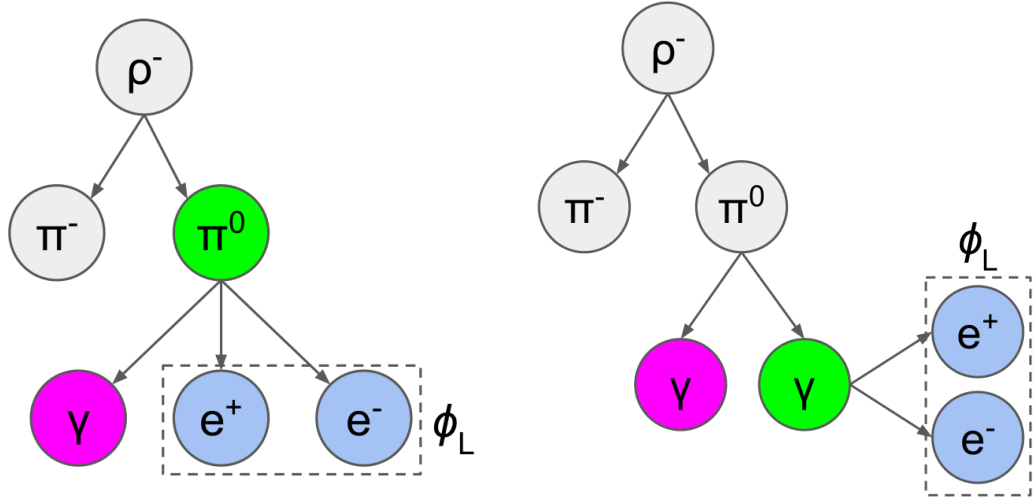


Figure 44. ρ^- decay modes, faking the signal process.

The left plot in Fig. 45 shows the distribution of this variable (blue shaded region) for taupair MC sample, after the preselection and rectangular sideband cuts. We fit it with a double Gaussian distribution (red solid line) to verify that it indeed peaks at π^0 mass. The fit range is shown in dashed red lines.

The right plot in Fig. 45 shows the distribution of the transverse distance of the $\phi_L \rightarrow e^+e^-$ vertex from IP, for two different decay modes shown in Fig. 44. However, the distributions do not show the structure of the inner detector. This is investigated in the independent study reported in Appendix C.

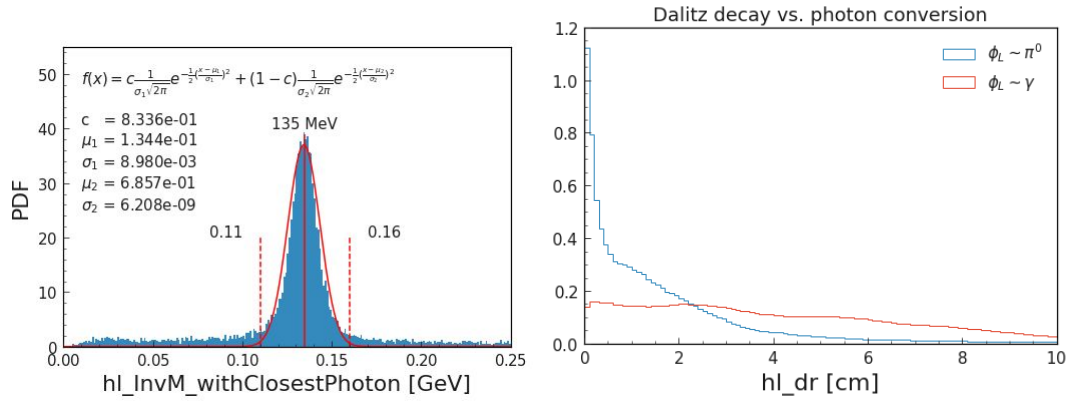


Figure 45. Distribution of the invariant mass of the ϕ_L candidate and its closest photon for taupair sample (left). For the background events coming from ρ decays, this quantity should peak at π^0 mass. Distributions of the transverse distance of the $\phi_L \rightarrow e^+e^-$ vertex from IP, for two different decay modes, shown in Fig. 44 (right).

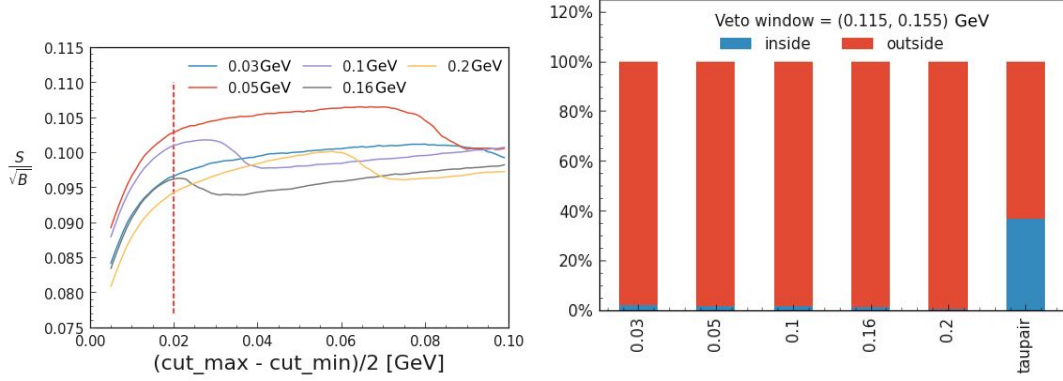


Figure 46. (Left) FOM as a function of the half-width of the veto window. (Right) Fraction of signal and taupair events surviving after the chosen optimal window.

In order to veto these ρ decay events, we choose a window around the peak, which is at the π^0 mass, and discard any event that falls inside this mass range. To find the optimal width of this window, we maximize the figure of merit (FOM), defined by $\frac{S}{\sqrt{B}}$, where S and B are the number of signal and background events surviving after the cut.

The left plot of Fig. 46 shows how the FOM changes with the increase of the width of the veto window for different mass points. We notice that till 0.02 GeV, all the graphs increase steadily. However, beyond this point, the graphs of some mass points start to decrease, whereas others increase very slowly. This makes 0.02 GeV to be the optimal half-width of our veto window. This makes our ρ veto cut to be:

$$\text{hl_InvM_withClosestPhoton} < 0.115 \text{ GeV or hl_InvM_withClosestPhoton} > 0.155 \text{ GeV}$$

The right plot of Fig. 46 shows the effect of this veto cut on the signal and taupair background events. We see that this cut removes only a few signal events, but suppresses the taupair background by a lot.

This cut is applied to $\phi_L \rightarrow e^+e^-$ channel only.

Suppressing background from photon conversion

There is one more cut applied to the $\phi_L \rightarrow e^+e^-$ channel. This cut is on the position of ϕ_L decay vertex and used to remove the background generated from $\gamma \rightarrow e^+e^-$ conversion inside the detector material. We require this vertex to be within 1 cm of the collision axis. In terms of basf2 variable, this cut is defines as -

$$\text{hl_dr} < 1 \text{ cm}$$

We don't need this cut for $\phi_L \rightarrow \mu^+\mu^-$ channel as the corresponding photon conversion process, $\gamma \rightarrow \mu^+\mu^-$, is suppressed by a factor of 10^{-4} .

Fig. 47 shows the effect of the successive cuts in suppressing the SM backgrounds.

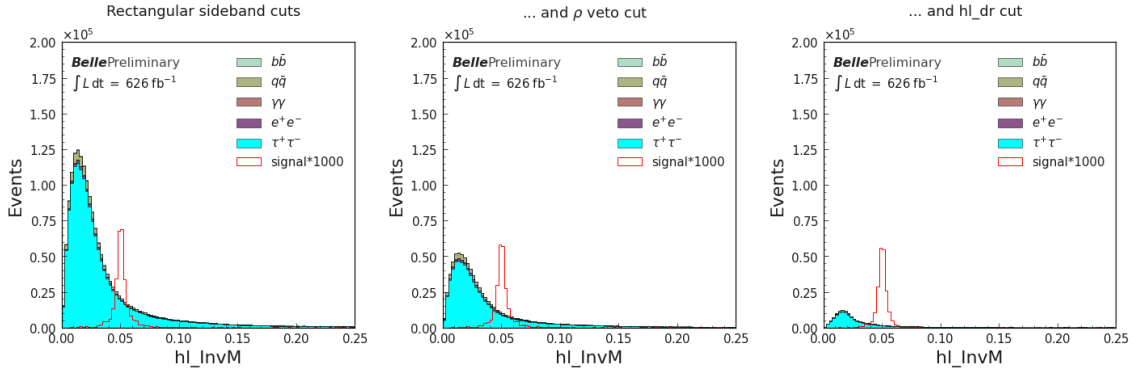


Figure 47. Reducing the SM backgrounds in $\phi_L \rightarrow e^+e^-$ channel without noticeable decrease in signal strength using the background suppression cuts. The signal sample in this plot was generated with $m_{\phi_L} = 50$ MeV. In the legend, $b\bar{b}$ should be understood as $B\bar{B}$. This applies to all figures in this document.

Defining signal and control regions

We train a multi-class boosted decision tree (BDT) with the MC samples and a cocktail of the signal samples of different mass points. For each event, the BDT produces 4 or 5 numbers which corresponds to the likelihood of that event to belong to either of these categories -

- signal
- $\tau^+\tau^-$
- e^+e^- (only for $\phi_L \rightarrow e^+e^-$ channel)
- $q\bar{q}$ ($q = u, d, s, c$)
- $b\bar{b}$

For any event, the sum of these 5 numbers is always equal to 1. For the subsequent discussion, we call them `signal_score`, `tautau_score`, `bhabha_score`, etc.

We use these numbers to define our signal region, general control region, as well as the control regions enriched with particular types of events.

Using these BDT scores, we define our signal and control regions in the following way -

- Signal region: `signal_score` > 0.5
- General control region: `signal_score` < 0.5
- Taupair control region: `tautau_score` > 0.5
- Bhabha control region: `bhabha_score` > 0.5 (only for $\phi_L \rightarrow e^+e^-$ channel)
- $q\bar{q}$ control region: `qqbar_score` > 0.5
- $b\bar{b}$ control region: `bbbar_score` > 0.5

The `GradientBoostingClassifier` model available in the `scikit-learn` [35] package has been used to construct our BDTs. For both $\phi_L \rightarrow e^+e^-$ and $\phi_L \rightarrow \mu^+\mu^-$ channels, there are 18 BDT input variables. Both of the BDTs were trained with the following options:

- Number of trees: 100
- Maximum depth of each tree: 3
- Loss function: multiclass `log_loss`

The multiclass `log_loss` function is defined as:

$$L_{\log}(Y, P) = -\log \Pr(Y|P) = -\frac{1}{N} \sum_{i=0}^{N-1} \sum_{k=0}^{K-1} y_{i,k} \log p_{i,k} \quad (2)$$

where N is the number of examples in the training set and K is the number of classes. The values $y_{i,k}$ are the true labels for each example, i.e. it is 1 if the i^{th} example belongs to class k and 0 otherwise. The values $p_{i,k}$ are the class likelihoods as predicted by the BDT, i.e. the probability that the i^{th} example belongs to the class k .

Details of the BDT for $\phi_L \rightarrow e^+e^-$ channel

The BDT input variables used in this channel are listed below, along with their meaning:

- **thrust**: Thrust of the event.
- **hl_openingAngle**: The angle between the e^+ and e^- tracks forming the $\phi_L \rightarrow e^+e^-$ vertex.
- **missingMass2OfEvent**: Square of the invariant mass calculated from the missing 4-momenta of the event.
- **hl_dr**: Transverse distance between the IP and the $\phi_L \rightarrow e^+e^-$ vertex.
- **nPi0**: Number of reconstructed π^0 in the event. We combine two photons from the `gamma:mdst` list and check if their invariant mass is in between 105 MeV and 165 MeV.
- **missingMomentumOfEventCMS_theta**: The angle between the positive z-axis and the missing momentum of the event.
- **hl_InvM_withClosestPhoton**: Invariant mass of the reconstructed ϕ_L candidate and its closest photon.
- **totalPhotonsEnergyOfEvent**: Sum of the energies of all the reconstructed photons in the “gamma:mdst” list.
- **minAngle_hl_tau_track**: Angle between the reconstructed ϕ_L candidate and its closest charged track reconstructed as τ^+ or τ^- .
- **nElectrons**: Number of charged tracks identified as electron in the event.
- **angle_tau_tracks**: Angle between the two tracks reconstructed as τ^+ and τ^- .
- **hl_E**: Energy of the reconstructed ϕ_L candidate.

- **hl_energyOfClosestPhoton**: Energy of the photon closest to the reconstructed ϕ_L candidate.
- **foxWolframR4**: Ratio of the 4th to the 0th order Fox Wolfram moments.
- **visibleEnergyOfEventCMS**: Total visible energy of the event as seen from the CMS frame.
- **foxWolframR3**: Ratio of the 3rd to the 0th order Fox Wolfram moments.
- **hl_e_0_pt**: Transverse momentum of the e^+ track forming the ϕ_L candidate.
- **hl_e_1_pt**: Transverse momentum of the e^- track forming the ϕ_L candidate.

Distributions of the BDT input variables used in this channel are shown in Fig. 48.

The extent of correlation among the BDT input variables for different types of events in $\phi_L \rightarrow e^+e^-$ channel are shown in Fig. 49, Fig. 50, Fig. 51, Fig. 52 and Fig. 53.

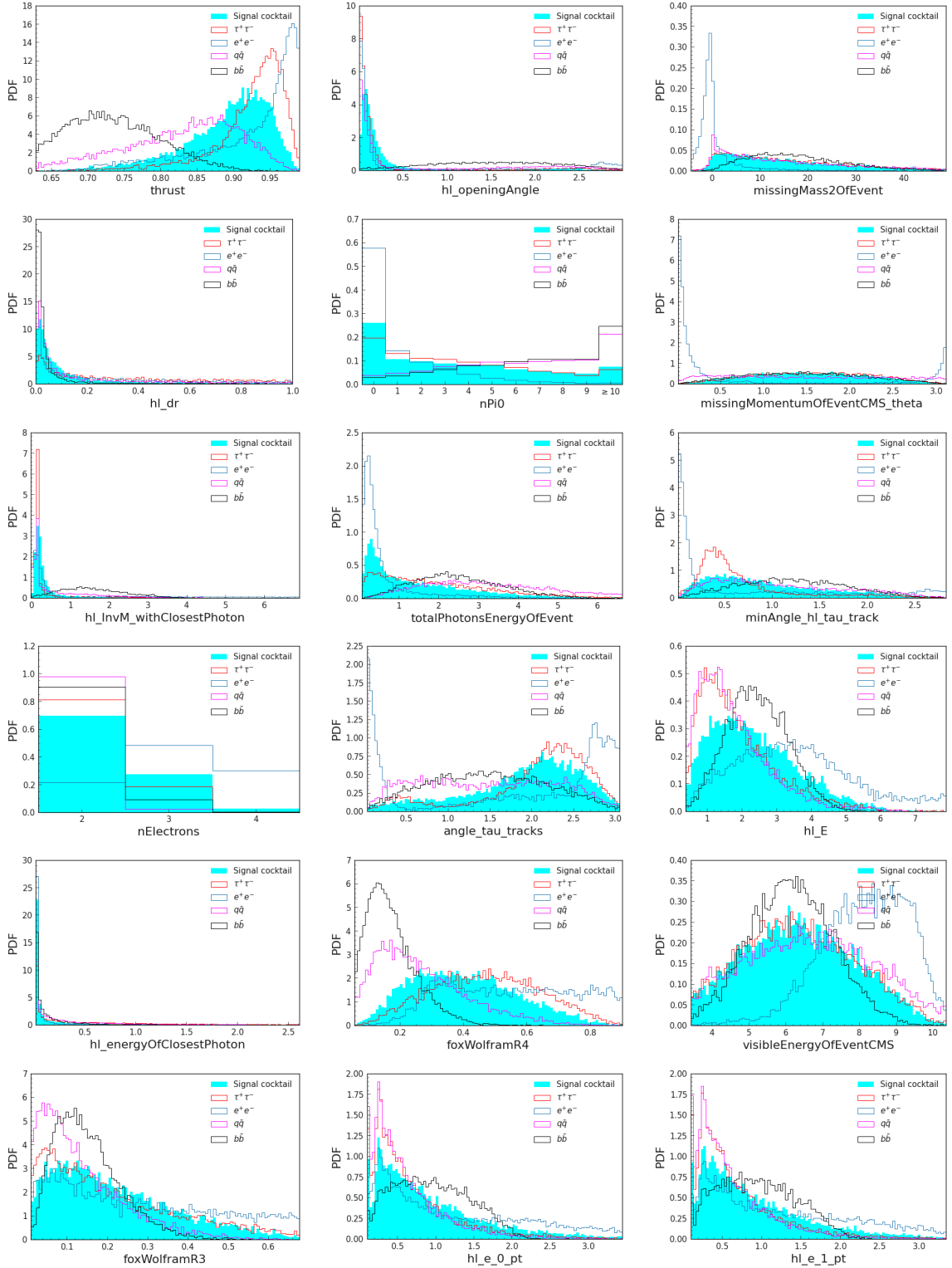


Figure 48. Distributions of the BDT input variables used for $\phi_L \rightarrow e^+e^-$ channel.

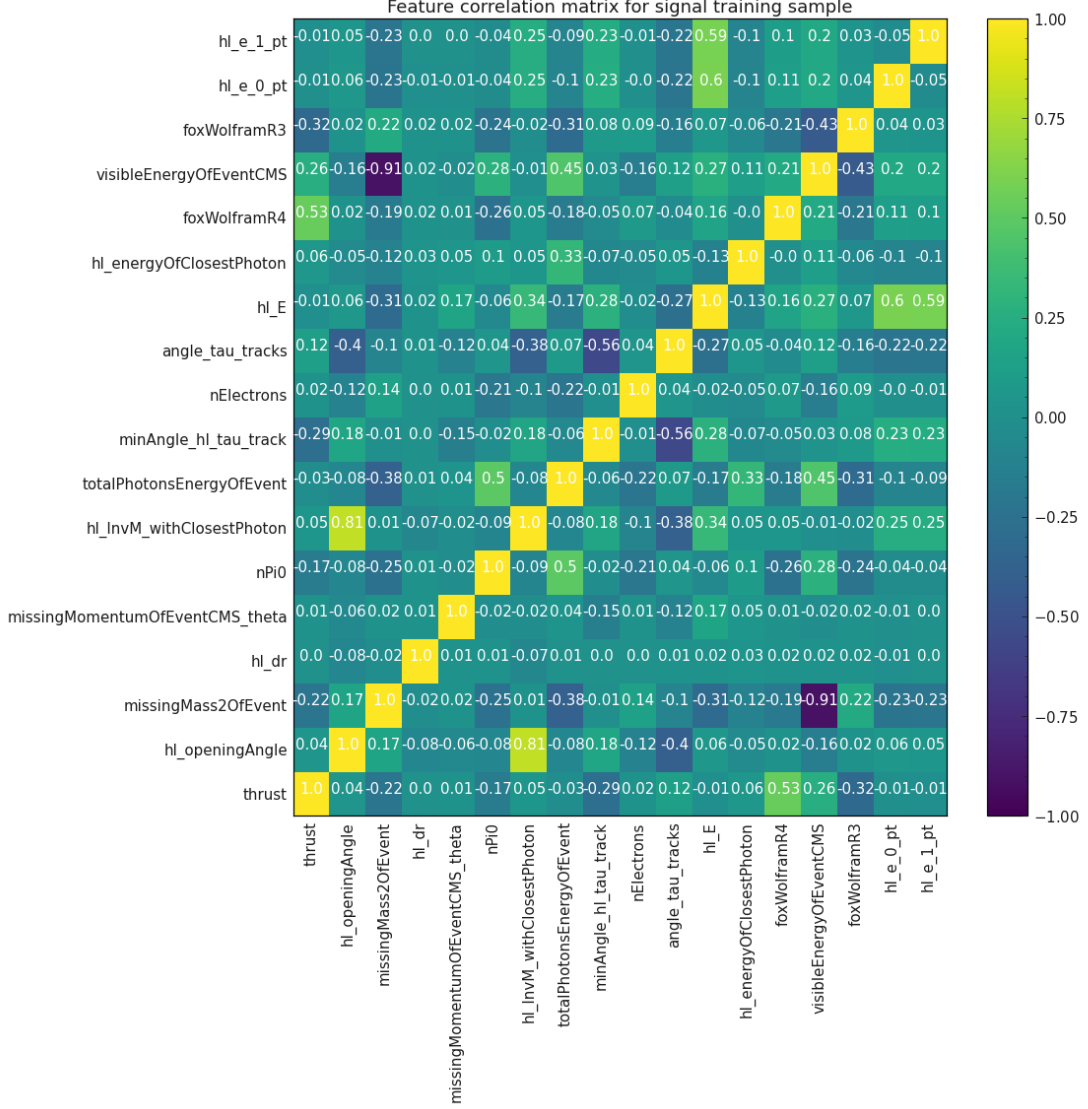


Figure 49. Correlation among the BDT input variables for the signal sample in $\phi_L \rightarrow e^+e^-$ channel. The signal sample used for this BDT training is obtained by mixing signal events for $m_{\phi_L} = 30$ MeV, 40 MeV, 50 MeV, 60 MeV, 70 MeV, 80 MeV, 90 MeV, 100 MeV, 120 MeV, 140 MeV, 150 MeV, 160 MeV, 180 MeV and 200 MeV in equal proportions.

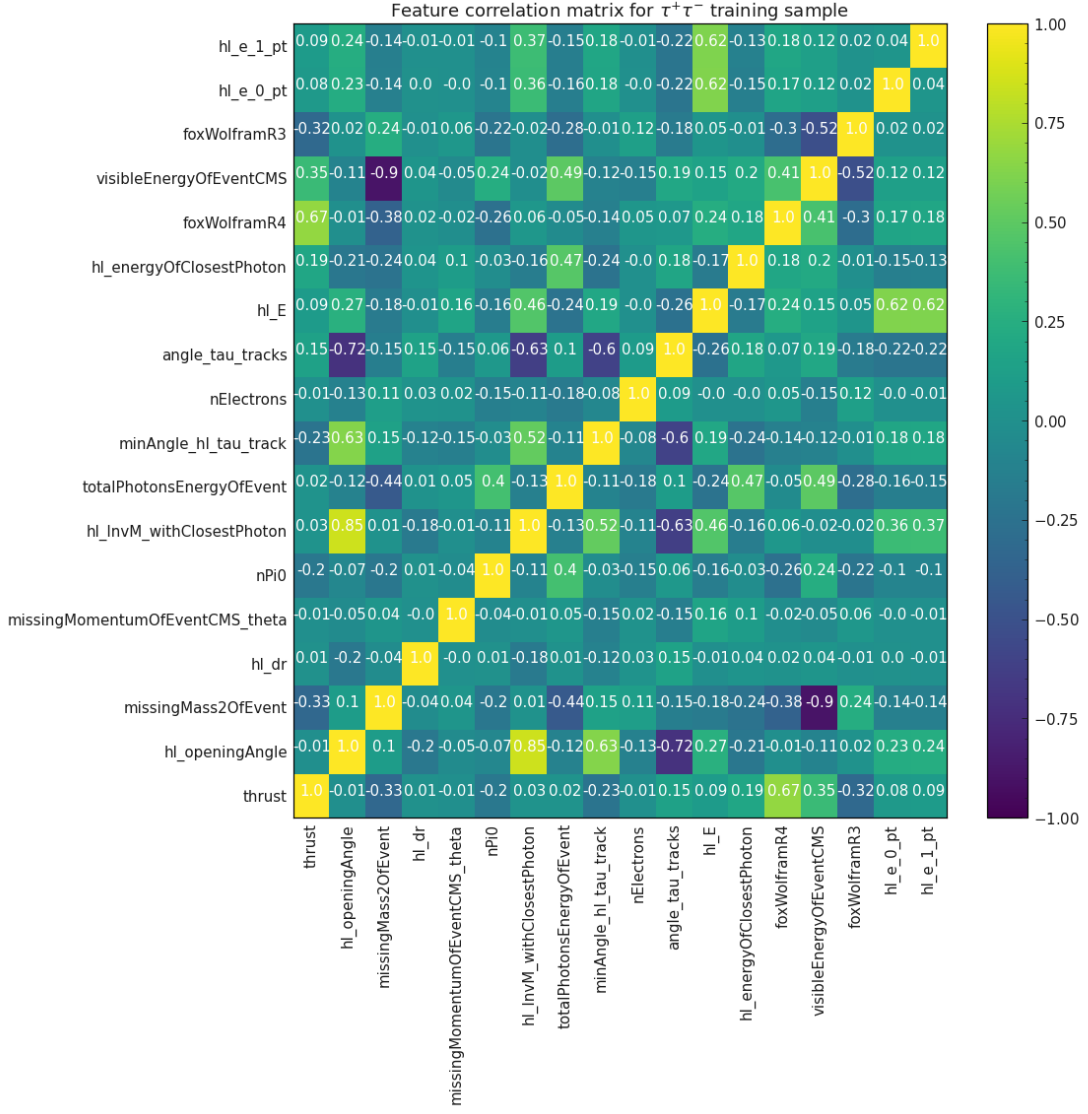


Figure 50. Correlation among the BDT input variables for the $\tau^+\tau^-$ sample in $\phi_L \rightarrow e^+e^-$ channel.

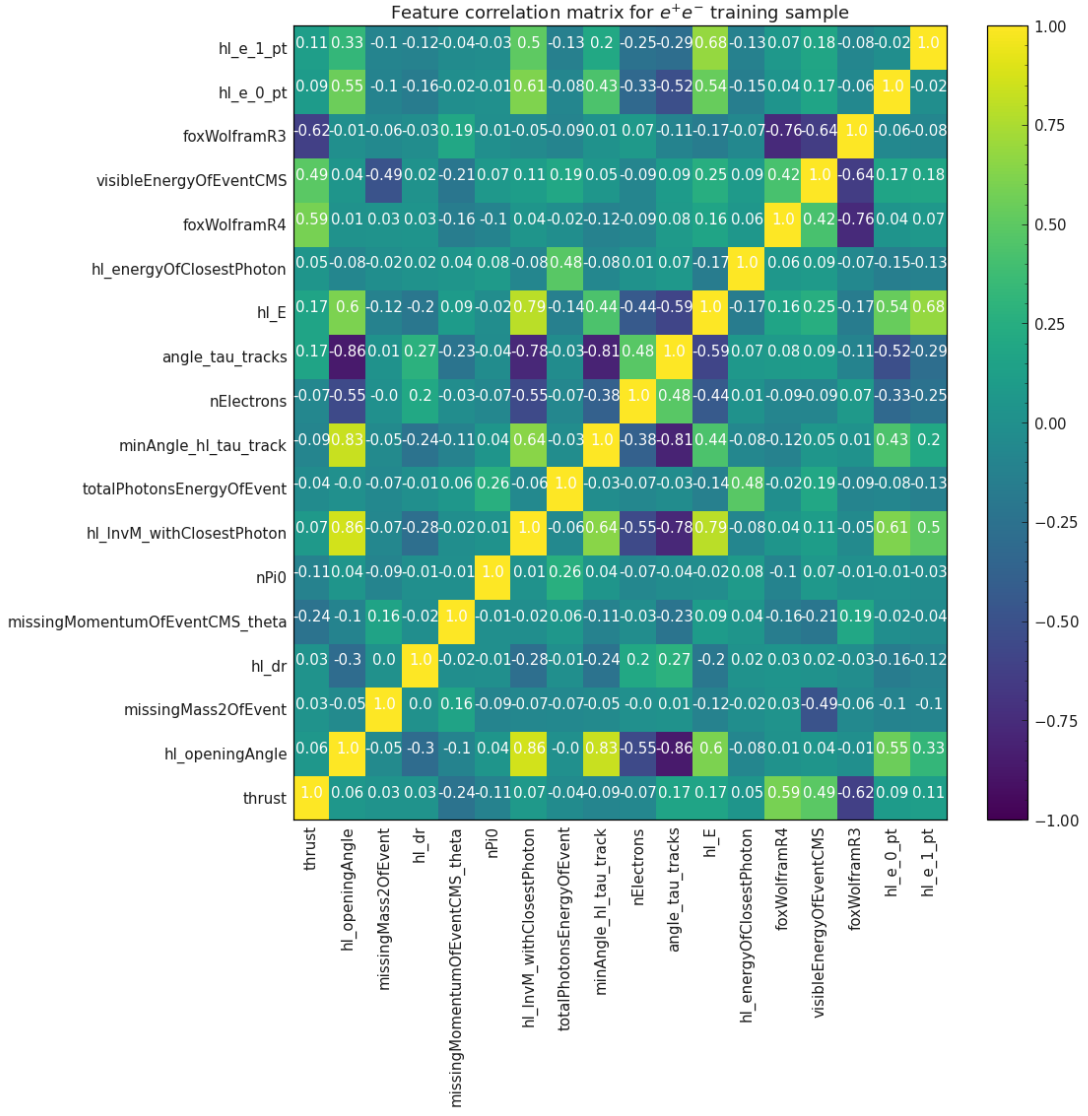


Figure 51. Correlation among the BDT input variables for the e^+e^- sample in $\phi_L \rightarrow e^+e^-$ channel.

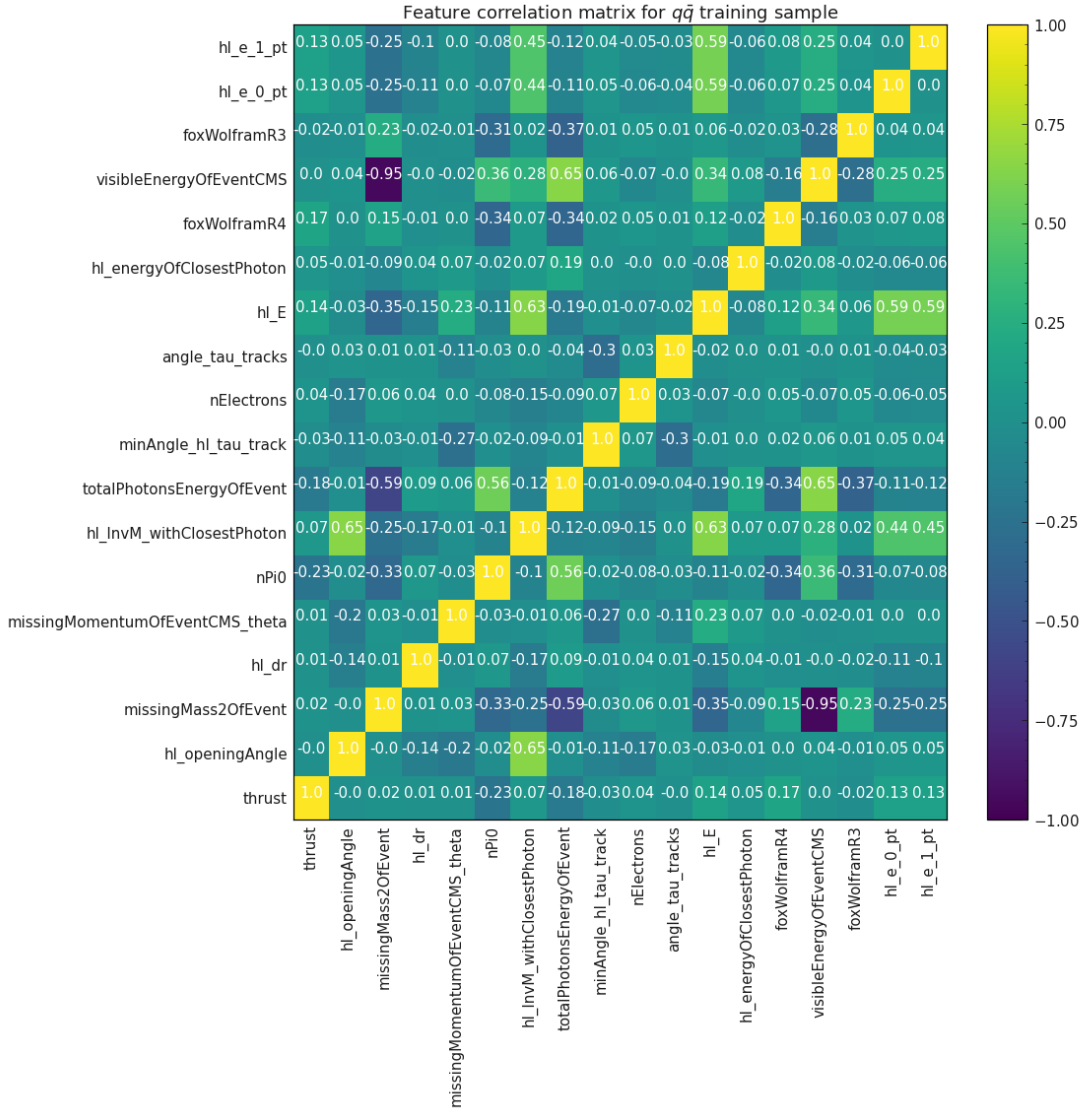


Figure 52. Correlation among the BDT input variables for the $q\bar{q}$ sample in $\phi_L \rightarrow e^+e^-$ channel.

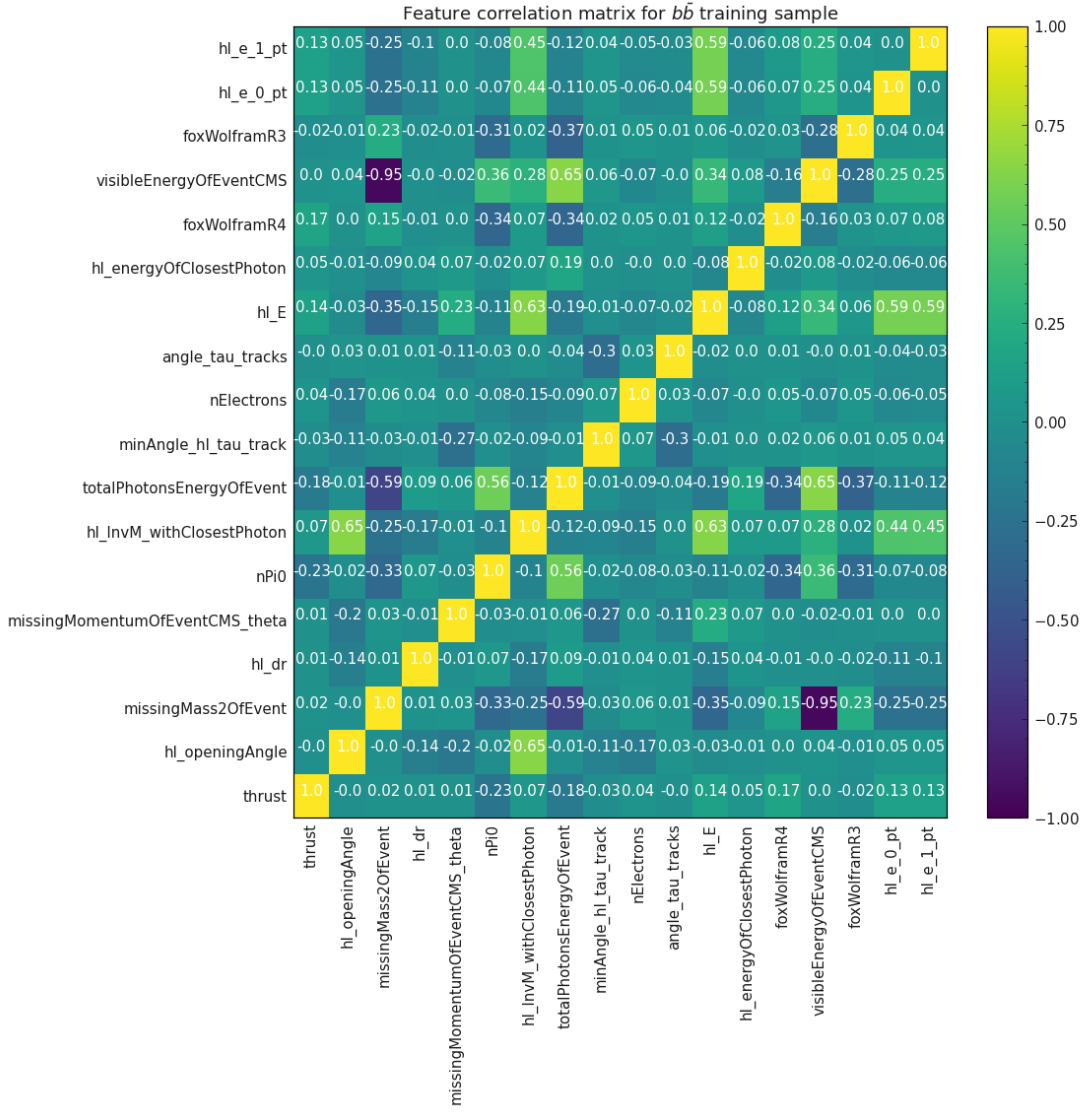


Figure 53. Correlation among the BDT input variables for the $b\bar{b}$ sample in $\phi_L \rightarrow e^+e^-$ channel.

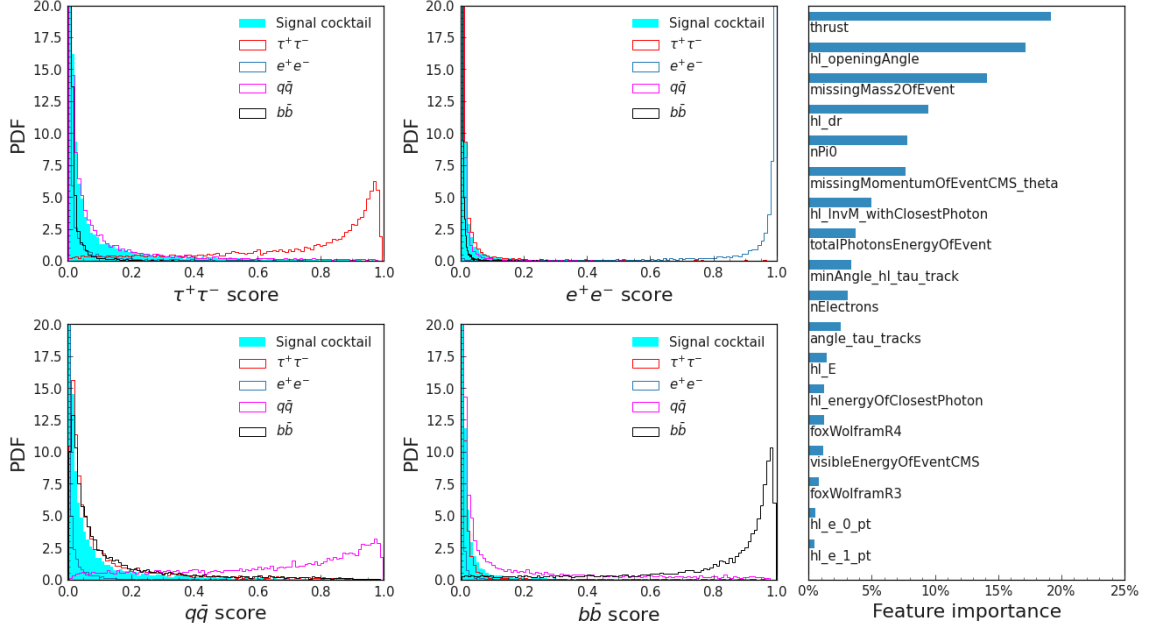


Figure 54. Distributions of the different BDT scores for signal and background MC samples, for $\phi_L \rightarrow e^+e^-$ channel. The plot on the right shows the relative contribution of each input variable.

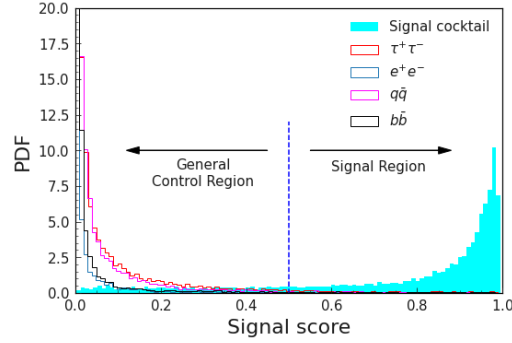


Figure 55. Distribution of signal_score for different MC samples in $\phi_L \rightarrow e^+e^-$ channel. This variable is used to define our signal region and general control region.

Fig. 54 shows the performance and feature importance of the BDT for $\phi_L \rightarrow e^+e^-$ channel. Fig. 55 shows the definitions of the signal region and general control region in this channel.

Details of the BDT for $\phi_L \rightarrow \mu^+ \mu^-$ channel

The BDT input variables used in this channel are listed below, along with their meaning:

- **tau_0_tau_1_InvM**: Invariant mass of the two tracks reconstructed as τ^+ and τ^- .
- **thrust**: Thrust of the event.
- **missingMass2OfEvent**: Square of the invariant mass calculated from the missing 4-momenta of the event.
- **hl_E**: Energy of the reconstructed ϕ_L candidate.
- **totalPhotonsEnergyOfEvent**: Sum of the energies of all the reconstructed photons in the “gamma:mdst” list.
- **nPi0**: Number of reconstructed π^0 in the event. We combine two photons from the “gamma:mdst” list and check if their invariant mass falls between 105 MeV and 165 MeV.
- **visibleEnergyOfEventCMS**: Total visible energy of the event, as seen from the CMS frame.
- **nElectrons**: Number of charged tracks identified as electron.
- **hl_openingAngle**: The angle between the μ^+ and μ^- tracks forming the $\phi_L \rightarrow \mu^+ \mu^-$ vertex.
- **hl_mu_1_pt**: Transverse momentum of the μ^- track forming the ϕ_L candidate.
- **missingMomentumOfEventCMS_theta**: The angle between the positive z-axis and the missing momentum of the event, as seen from the CMS frame.
- **hl_mu_0_pt**: Transverse momentum of the μ^+ track forming the ϕ_L candidate.

- **foxWolframR3**: Ratio of the 3rd to the 0th order Fox Wolfram moments.
- **nMuons**: Number of charged tracks identified as muons.
- **foxWolframR4**: Ratio of the 4th to the 0th order Fox Wolfram moments.
- **hl_mu_0_piIDBelle**: Output of the pion-kaon discriminator for the μ^+ track forming the ϕ_L candidate.
- **hl_dr**: Transverse distance between the IP and the $\phi_L \rightarrow \mu^+\mu^-$ vertex.
- **hl_mu_1_piIDBelle**: Output of the pion-kaon discriminator for the μ^- track forming the ϕ_L candidate.

Distributions of the BDT input variables used in this channel are shown in Fig. 56.

The extent of correlation among the BDT input variables for different types of events in $\phi_L \rightarrow \mu^+\mu^-$ channel are shown in Fig. 57, Fig. 58, Fig. 59, Fig. 60 and Fig. 61.

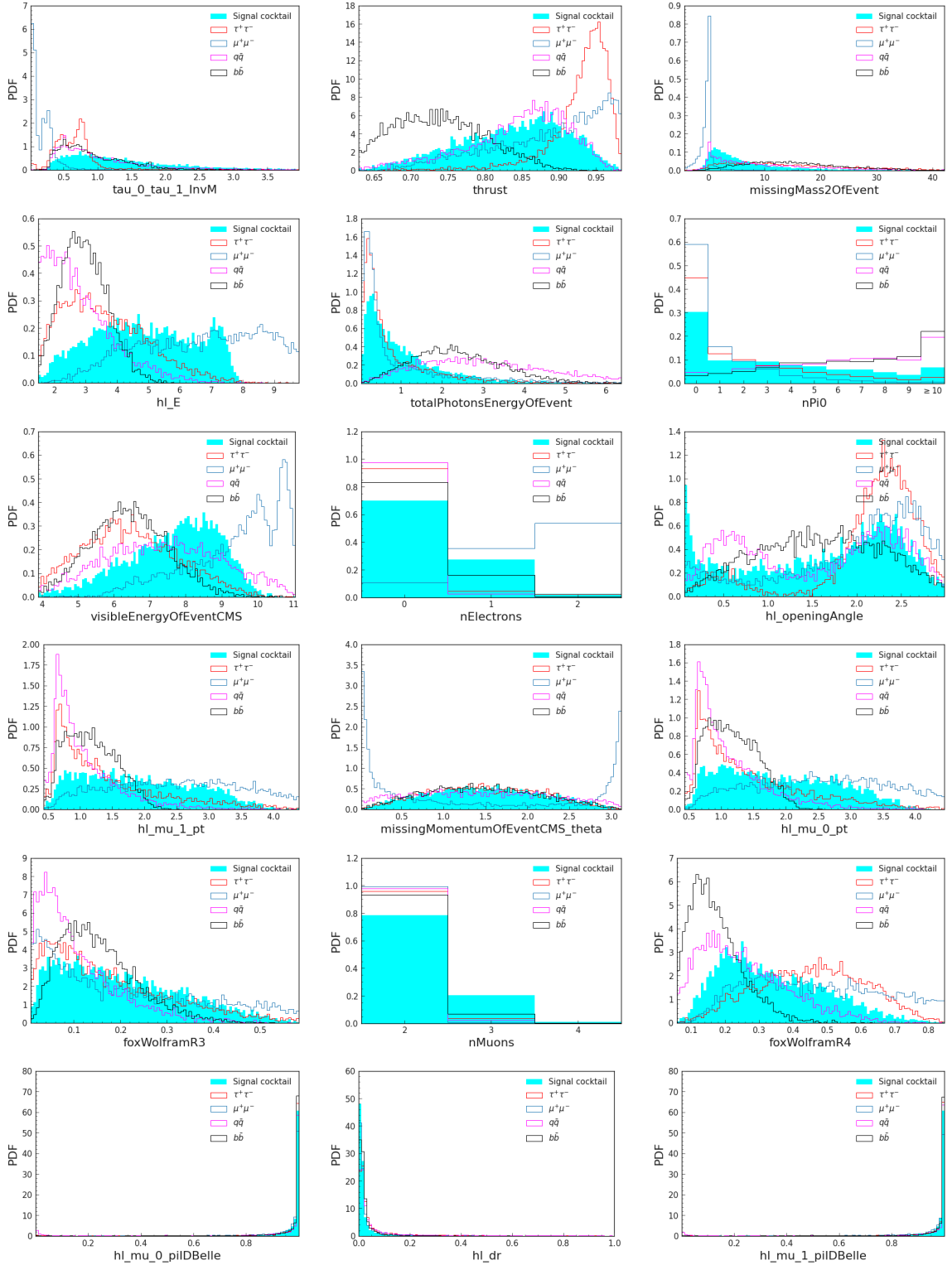


Figure 56. Distributions of the BDT input variables used for $\phi_L \rightarrow \mu^+ \mu^-$ channel.

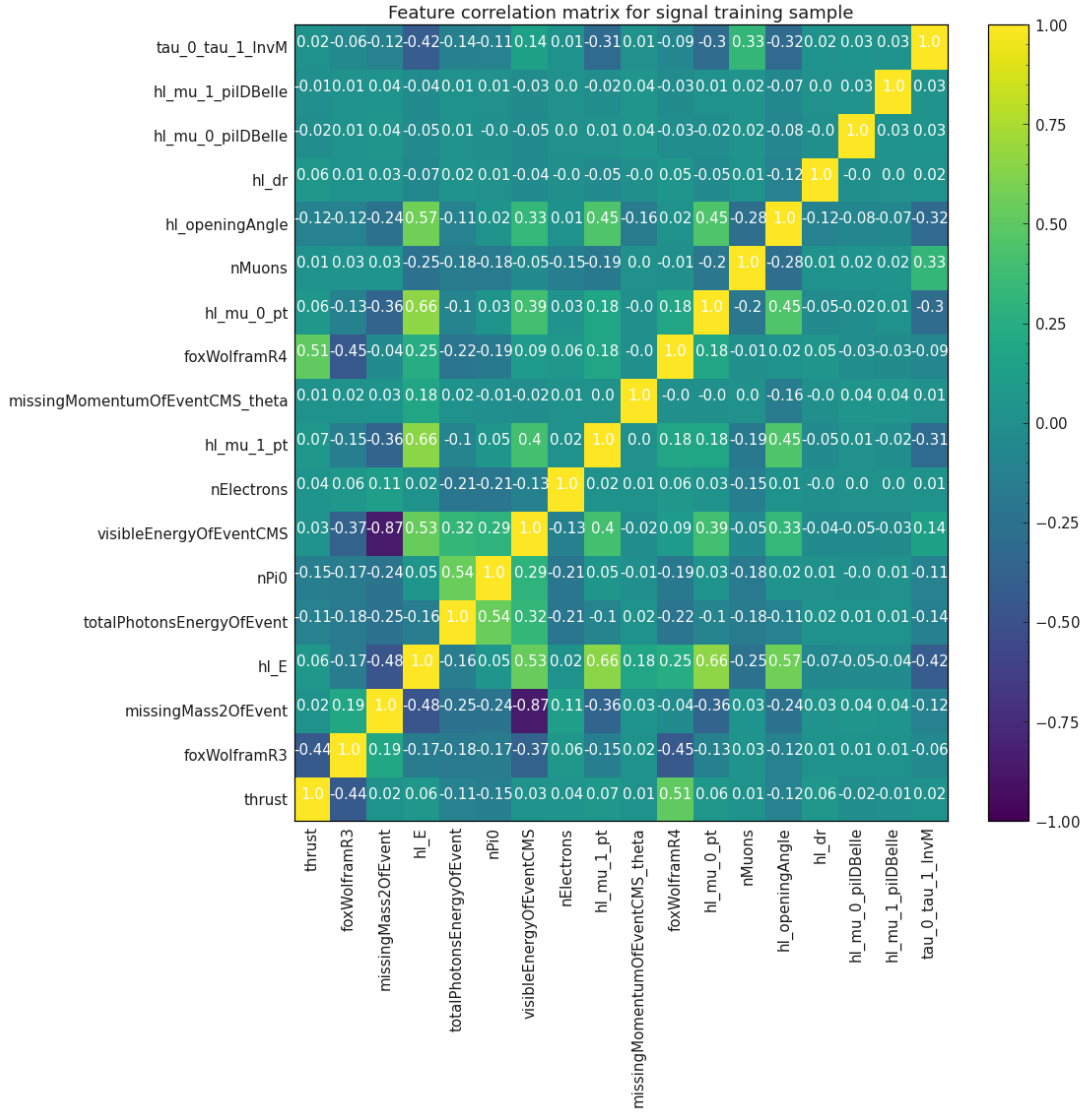


Figure 57. Correlation among the BDT input variables for the signal sample in $\phi_L \rightarrow \mu^+\mu^-$ channel. The signal sample used for this BDT training is obtained by mixing signal events for $m_{\phi_L} = 0.225$ GeV, 0.5 GeV, 1.0 GeV, 2.0 GeV and 5.0 GeV in equal proportions.

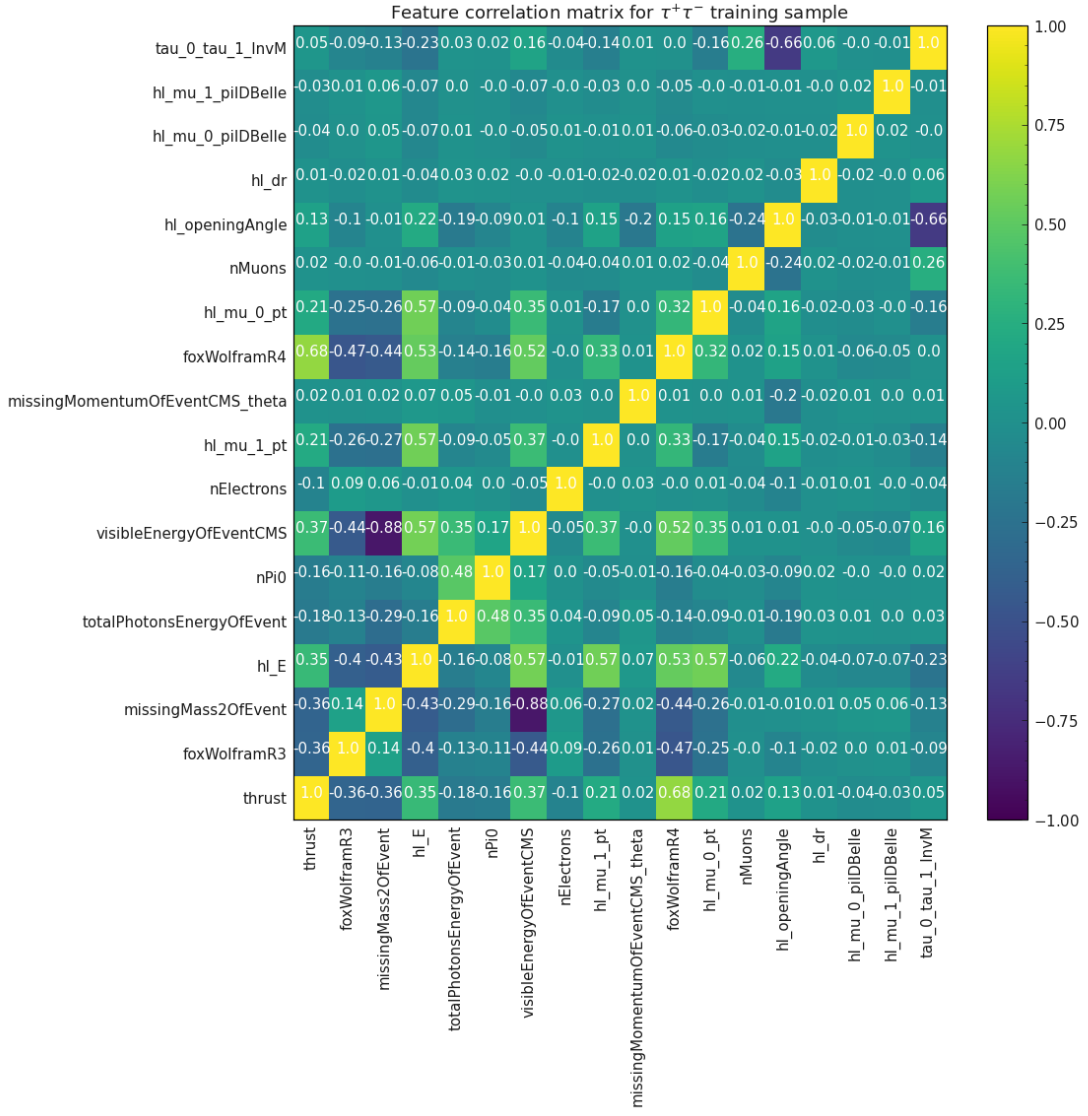


Figure 58. Correlation among the BDT input variables for the $\tau^+\tau^-$ sample in $\phi_L \rightarrow \mu^+\mu^-$ channel.

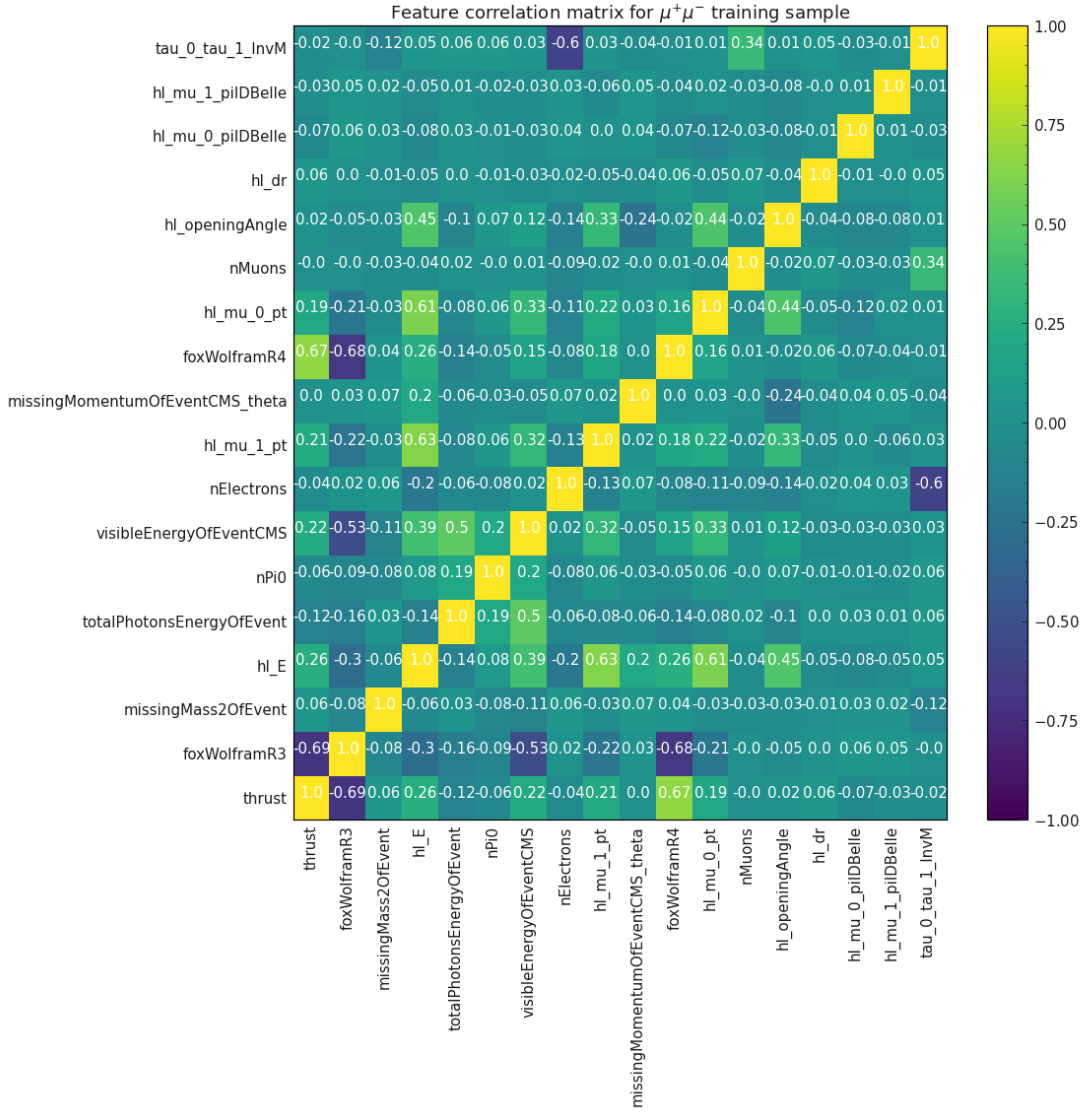


Figure 59. Correlation among the BDT input variables for the $\mu^+\mu^-$ sample in $\phi_L \rightarrow \mu^+\mu^-$ channel.

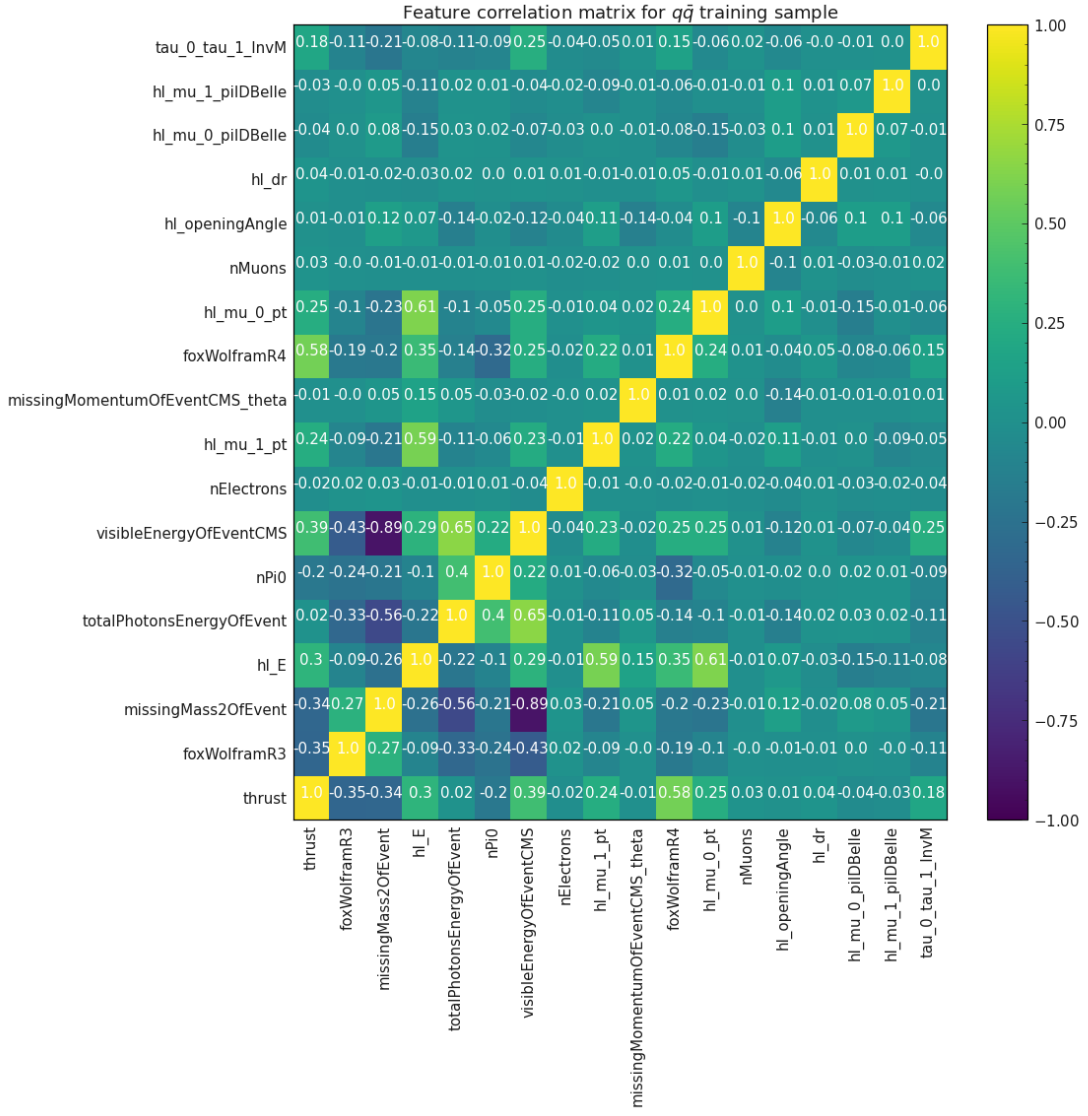


Figure 60. Correlation among the BDT input variables for the $q\bar{q}$ sample in $\phi_L \rightarrow \mu^+\mu^-$ channel.

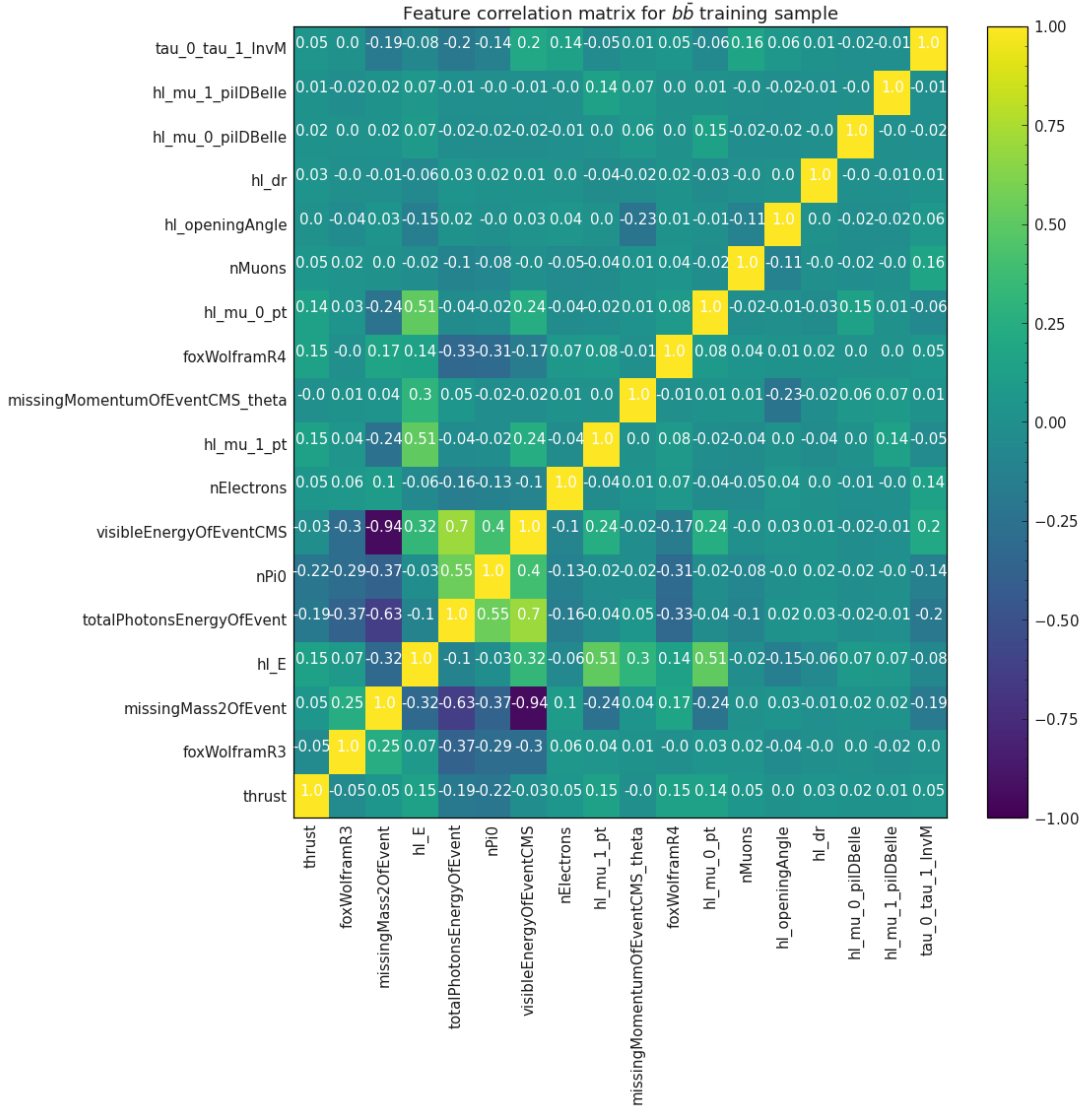


Figure 61. Correlation among the BDT input variables for the $b\bar{b}$ sample in $\phi_L \rightarrow \mu^+\mu^-$ channel.

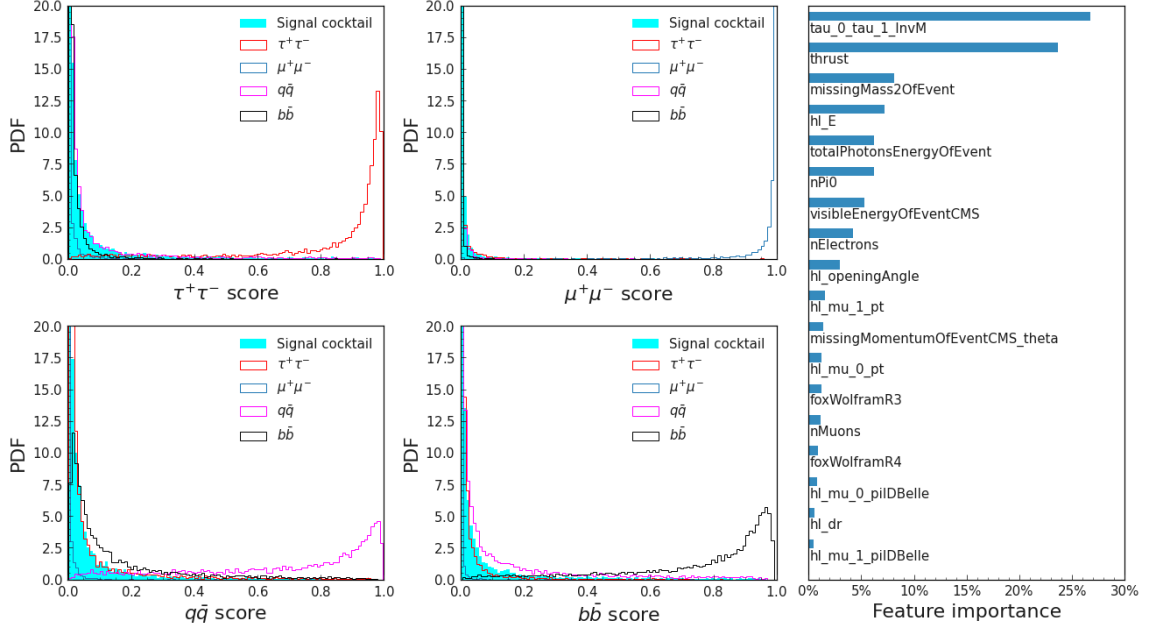


Figure 62. Distributions of the different BDT scores for signal and background MC samples, for $\phi_L \rightarrow \mu^+\mu^-$ channel. The plot on the right shows the relative contribution of each input variable.

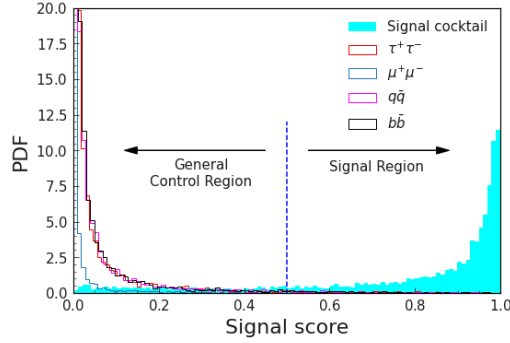


Figure 63. Distribution of signal_score for different MC samples in $\phi_L \rightarrow \mu^+\mu^-$ channel. This variable is used to define our signal region and general control region.

Fig. 62 shows the performance and feature importance of the BDT for $\phi_L \rightarrow \mu^+\mu^-$ channel. Fig. 63 shows the definitions of the signal region and general control region in this channel.

The data-MC comparison plots for all the BDT input variables are shown in Appendix D.

PID correction

Applying electronID and muonID corrections

We use the LID correction factors as described in Belle Note 954. We use the numbers from the tables updated in 2009. These electronID (muonID) correction factor tables contain $\epsilon_{Data}/\epsilon_{MC}$ for a true electron (muon), where ϵ_{Data} and ϵ_{MC} are the efficiency of a particular electronID (muonID) cut for data and MC sample, respectively.

In $\phi_L \rightarrow e^+e^-$ channel, we apply these electronID correction factors only to those ϕ_L daughter tracks whose MC truth matched particle is an electron. Similarly, in $\phi_L \rightarrow \mu^+\mu^-$ channel, we apply these muonID correction factors only to those ϕ_L daughter tracks whose MC truth matched particle is a muon.

Applying pion mis-ID correction

In $\phi_L \rightarrow \mu^+\mu^-$ channel, the result of TauDecayMarker is shown in Fig. 64. The major background for the $\phi_L \rightarrow \mu^+\mu^-$ channel comes from the taupair events, where one of the tau decays contains 3 charged pions, which are faking as muons, i.e. passing our muonID > 0.9 cut. So we apply correction factors for the pion mis-identification efficiency. This correction factor is calculated as $\epsilon_{Data}/\epsilon_{MC}$, where ϵ_{Data} and ϵ_{MC} are the efficiency of our muonID cut for true pions, for data and MC sample respectively.

We create our own tables from the D^{*+} ntuples available on KEKCC². Similar to the regular muonID correction factor tables, we calculate these correction factor tables by dividing the SVD2 dataset into three groups: exp 31-39, exp 41-49 and exp 51-65. We also use the same theta and momentum bins for our tables. We choose the correction factor to be 0 for the bins where the data efficiency is 0.

In $\phi_L \rightarrow \mu^+\mu^-$ channel, these correction factors are applied to only those ϕ_L daughter tracks whose MC truth matched particle is a pion.

Fig. 65 shows the effect of PID correction in $\phi_L \rightarrow \mu^+\mu^-$ channel.

²Many thanks to Shohei Nishida-san for providing these ntuples.

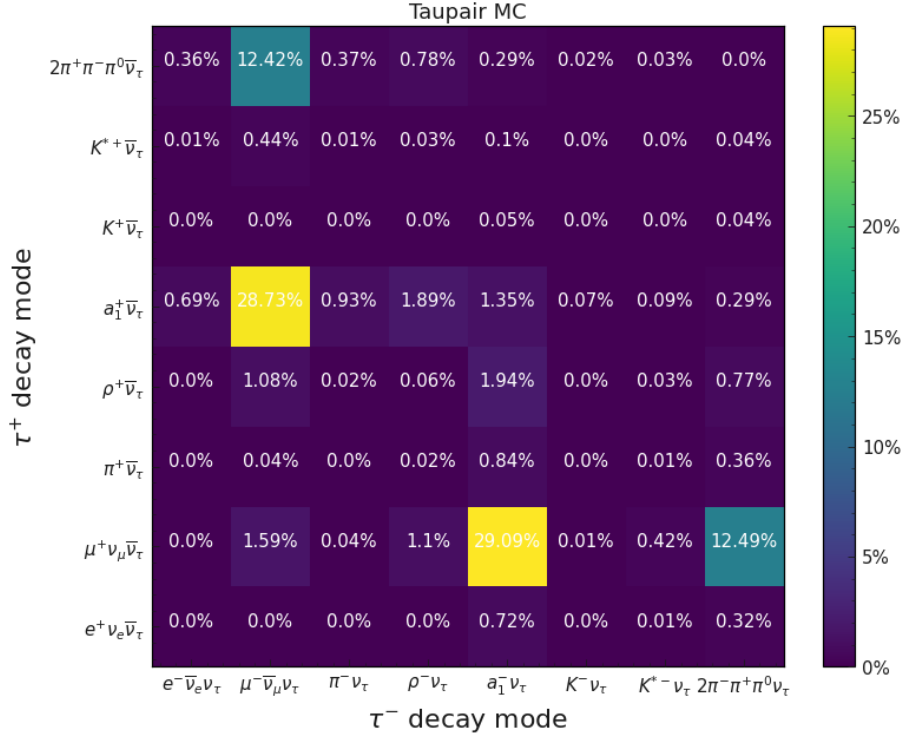


Figure 64. Result of TauDecayMarker showing the τ^+ and τ^- decay modes in SM taupair sample, for $\phi_L \rightarrow \mu^+ \mu^-$ channel. From this plot, we conclude that lots of pions are faking as muons.

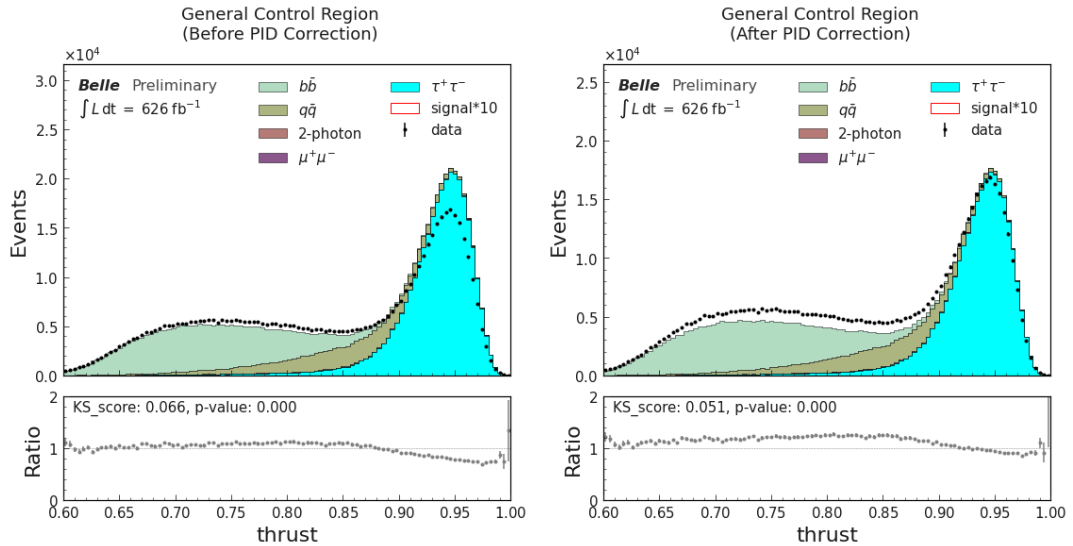


Figure 65. Distribution of thrust before (left) and after (right) applying PID corrections in $\phi_L \rightarrow \mu^+ \mu^-$ channel. The signal sample was generated with $m_{\phi_L} = 2$ GeV. The signal distributions are barely visible, as these plots are for the general control region.

Calculating scale factors for MC samples

We calculate the scaling factors using binned simultaneous fit over all the background MC samples with data to get the scaling factors. We use the thrust distribution to perform this binned fit using the mean squared error (MSE) loss function. The mathematical formulation of the binned simultaneous fit is described below.

Mathematical formulation of binned simultaneous fit

For perfect data-MC agreement in a stacked histogram, we require the following -

$$n_{\tau^+\tau^-}^{(i)} + n_{e^+e^-}^{(i)} + n_{\gamma\gamma}^{(i)} + n_{q\bar{q}}^{(i)} + n_{b\bar{b}}^{(i)} = n_{data}^{(i)} \quad (3)$$

where $n_s^{(i)}$ is the number of entries in the i^{th} bin of the histogram of sample s . This should be true for all the bins.

However, we find that we need scaling factors for the MC samples to get data-MC agreement. In this case, the equation looks like this -

$$c_{\tau^+\tau^-} n_{\tau^+\tau^-}^{(i)} + c_{e^+e^-} n_{e^+e^-}^{(i)} + c_{\gamma\gamma} n_{\gamma\gamma}^{(i)} + c_{q\bar{q}} n_{q\bar{q}}^{(i)} + c_{b\bar{b}} n_{b\bar{b}}^{(i)} = n_{data}^{(i)} \quad (4)$$

These scaling factors c_s are the same for all bins, i.e. they are sample specific. So if our thrust histogram has 100 bins, we have 100 such equations. However, there are only 5 scaling factors (c_s) that we need to calculate.

This is an over-determined system, and hence we try to find the ‘‘best fit’’ values of the scaling factors. The intuition is: those 5 scaling factors should have such values so that each of these 100 equations can be satisfied as closely as possible -

$$\sum_{s \in samples} c_s n_s^{(i)} = n_{data}^{(i)} \quad (5)$$

So, we define our MSE loss function in this way -

$$loss = \frac{1}{N_{bins}} \sum_{i \in bins} (n_{data}^{(i)} - \sum_{s \in samples} c_s n_s^{(i)})^2 \quad (6)$$

Our goal is to find 5 scaling factors that minimize this loss value subject to those 100 equations, one for each bin of our thrust histogram.

Calculating scale factors using binned simultaneous fit

Although we could follow the procedure described above for both of our channels separately and obtain two sets of scale factors for our MC samples, we adopt a slightly more complicated procedure to ensure that the scale factors for $\tau^+\tau^-$, $q\bar{q}$ and $b\bar{b}$ samples are the same for both of the channels.

To ensure this, we fit the thrust distributions obtained from the general control regions of the two channels simultaneously. So, in this case, we have total 200 bins (100 from each thrust distribution) and 6 MC samples:

- $\tau^+\tau^-$: Common for both channels.
- $q\bar{q}$: Common for both channels.
- $b\bar{b}$: Common for both channels.
- e^+e^- : Only for $\phi_L \rightarrow e^+e^-$ channel.
- 2-photon-ee : Only for $\phi_L \rightarrow e^+e^-$ channel.
- 2-photon-mumu : Only for $\phi_L \rightarrow \mu^+\mu^-$ channel.

We do not include $\mu^+\mu^-$ sample in this fit since the number of $\mu^+\mu^-$ events in the general control region, after the rectangular sideband cut, is too small to get a reliable scale factor. Instead, we fix the scale factor for the $\mu^+\mu^-$ sample to be 1.

We treat the two-photon background for the two channels as two different MC samples, since the two-photon sample is actually a luminosity scaled mixture of different samples like $e^+e^-e^+e^-$, $e^+e^-\mu^+\mu^-$, $e^+e^-q\bar{q}$ ($q = u, s, c$), etc. and the dominant two-photon processes that can fake the signal are different for these two channels. This allows the two-photon sample to have different scale factors in the two channels.

For each of these 6 samples, the first 100 bins corresponds to the distribution obtained from the $\phi_L \rightarrow e^+e^-$ channel and the last 100 bins corresponds to the distribution obtained from the $\phi_L \rightarrow \mu^+\mu^-$ channel. For the samples that are common

in both channels, we have non-zero bin-content in all (most) of the 200 bins. However, for the samples that are applicable to only one channel, we have zero bin-content in either first 100 bins or last 100 bins. The distribution obtained from data has non-zero bin-content in all (most) of the 200 bins.

Once we have this set up, we calculate the scale factors and their errors using the following procedure:

- We find all 6 scale factors from the general control regions of the two channels. We apply the rectangular sideband cuts in both channels to suppresses the two-photon events. This helps us in obtaining more reliable scale factors, since the number of events from the unsimulated 4-lepton processes is greatly reduced. In $\phi_L \rightarrow e^+e^-$ channel, we also apply `h1_dr` cut and ρ veto cut to suppress some taupair background.
- We take the difference between the scale factor obtained from the simultaneous fit across two channels and the scale factor obtained from the corresponding special control region of a particular channel as the systematic uncertainty for that scale factor in that channel. This implies that although we have the same median value for the scale factors for $\tau^+\tau^-$, $q\bar{q}$ and $b\bar{b}$ samples in both of the channels, the errors on these scale factors are different in each channel. For the two-photon samples, we treat the statistical errors in the scale factor calculation as the systematic uncertainties in their scale factors.
- We scale the e^+e^- (or $\mu^+\mu^-$) invariant mass histograms in the general CR and check the data-MC agreement.
- We use the same scaling factors in our signal region to perform the final fit to obtain the upper limits on the cross-section of the signal process and the coupling constant.

The scale factors and their errors for are shown in Table 3.

$\phi_L \rightarrow e^+e^-$		
MC sample	Composition	Scale factor
$\tau^+\tau^-$	34.71%	1.00 ± 0.06
e^+e^-	3.07%	1.70 ± 0.41
2-photon	5.25%	3.96 ± 0.14
$q\bar{q}$	16.56%	1.36 ± 0.04
$b\bar{b}$	40.41%	1.16 ± 0.01
$\phi_L \rightarrow \mu^+\mu^-$		
MC sample	Composition	Scale factor
$\tau^+\tau^-$	46.07%	1.00 ± 0.11
$\mu^+\mu^-$	0.11%	1.00 ± 0.00
2-photon	0.04%	0.10 ± 0.01
$q\bar{q}$	16.38%	1.36 ± 0.08
$b\bar{b}$	37.40%	1.16 ± 0.02

Table 3. List of scale factors for $\phi_L \rightarrow e^+e^-$ (left) and $\phi_L \rightarrow \mu^+\mu^-$ (right) channels, along with their errors. The compositions are calculated from the respective general control regions.

Fig. 66 shows the thrust distributions in $\phi_L \rightarrow e^+e^-$ and $e^+e^- \rightarrow \mu^+\mu^-$ channels, with and without the scale factors. The scale factors are obtained by performing a binned simultaneous fit on these distributions across the two channels. The background compositions of these distributions after applying the scale factors are listed in Table 3.

Fig. 67, Fig. 68, Fig. 69, and Fig. 70 shows the comparison between the performance of the scale factors obtained from the general control region and performance of the scale factors obtained from the special control regions in $\phi_L \rightarrow e^+e^-$ channel.

Fig. 71, Fig. 72, and Fig. 73 shows the comparison between the performance of the scale factors obtained from the general control region and performance of the scale factors obtained from the special control regions in $\phi_L \rightarrow \mu^+\mu^-$ channel.

The difference between these two sets of scale factors is used to estimate the systematic uncertainty.

The rectangular sideband cuts remove most of the $\mu^+\mu^-$ events. Hence, we don't

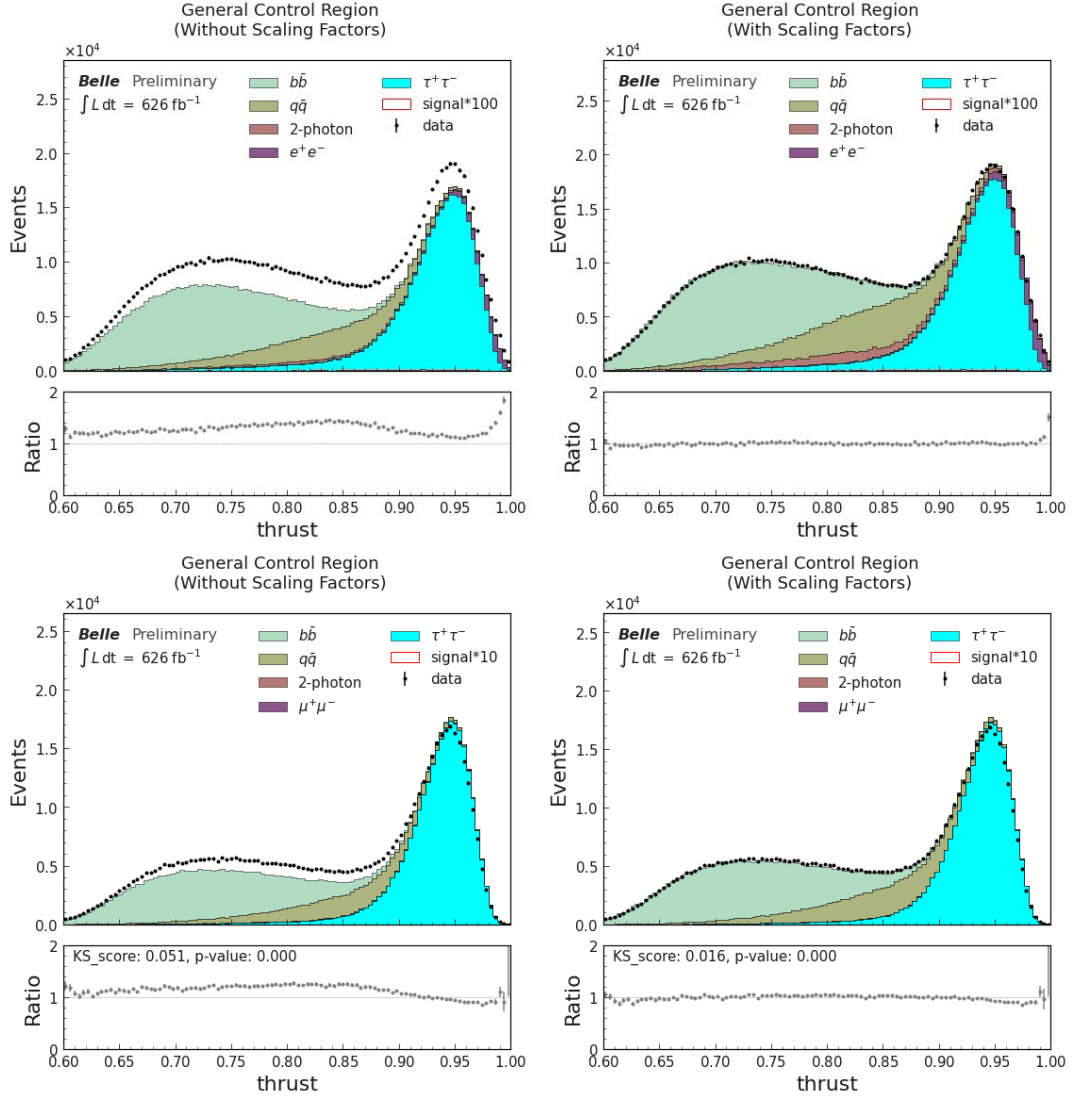


Figure 66. Calculating the scale factors by performing a binned simultaneous fit of the thrust distributions across the two channels. The background suppression cuts are applied in both of these plots. The top two plots are for $\phi_L \rightarrow e^+e^-$ channel and the bottom ones are for $\phi_L \rightarrow \mu^+\mu^-$ channel.

have an enough number of events in $\mu^+\mu^-$ control region to show the data-MC agreement. We set the error of the $\mu^+\mu^-$ scale factor to be 0.

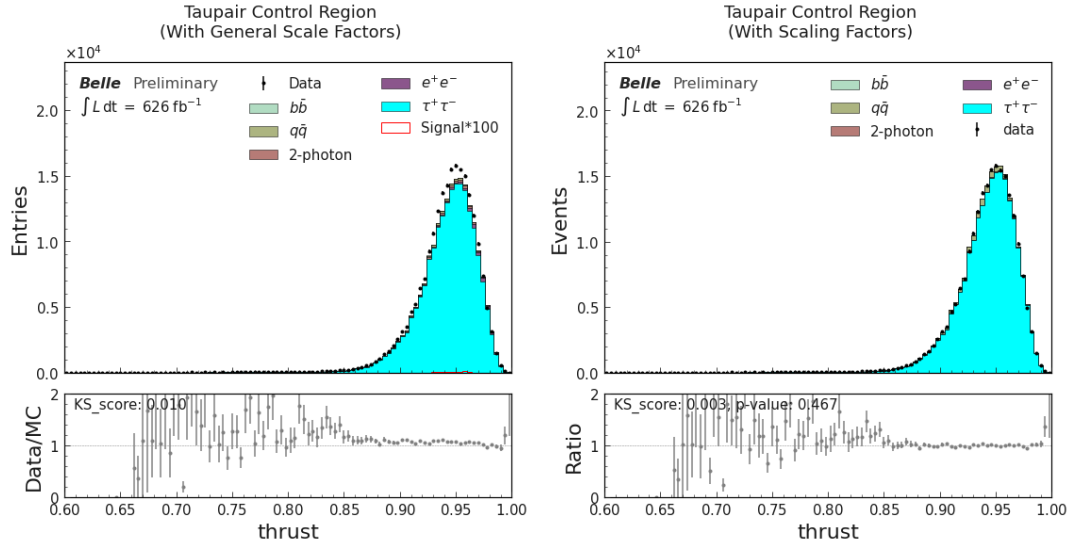


Figure 67. Distributions of thrust in $\tau^+\tau^-$ control region for $\phi_L \rightarrow e^+e^-$ channel using the scale factors obtained from (left) general control region vs. (right) $\tau^+\tau^-$ control region.

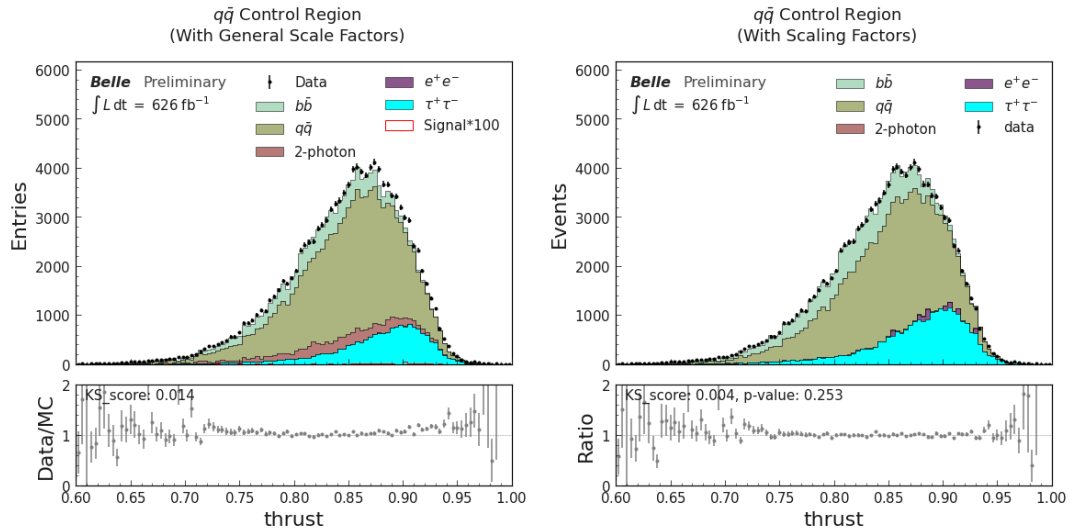


Figure 68. Distributions of thrust in $q\bar{q}$ control region for $\phi_L \rightarrow e^+e^-$ channel using the scale factors obtained from (left) general control region vs. (right) $q\bar{q}$ control region.

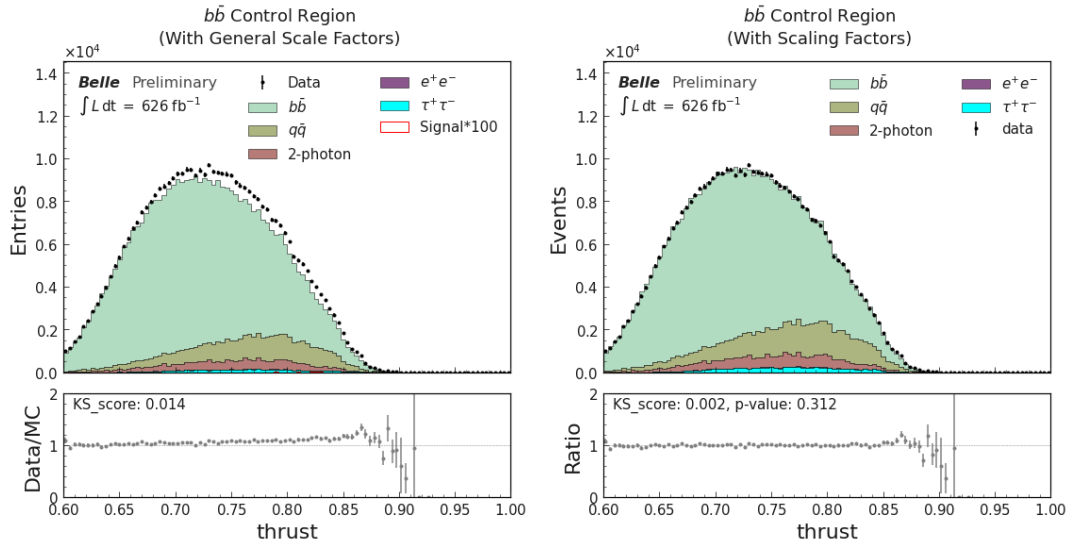


Figure 69. Distributions of thrust in $b\bar{b}$ control region for $\phi_L \rightarrow e^+e^-$ channel using the scale factors obtained from (left) general control region vs. (right) $b\bar{b}$ control region.

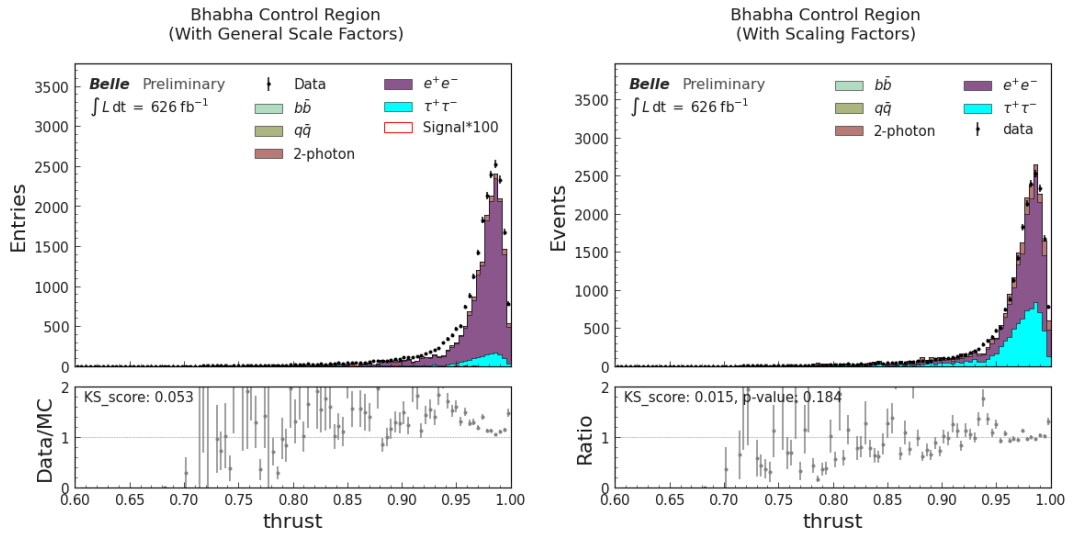


Figure 70. Distributions of thrust in Bhabha control region for $\phi_L \rightarrow e^+e^-$ channel using the scale factors obtained from (left) general control region vs. (right) Bhabha control region.

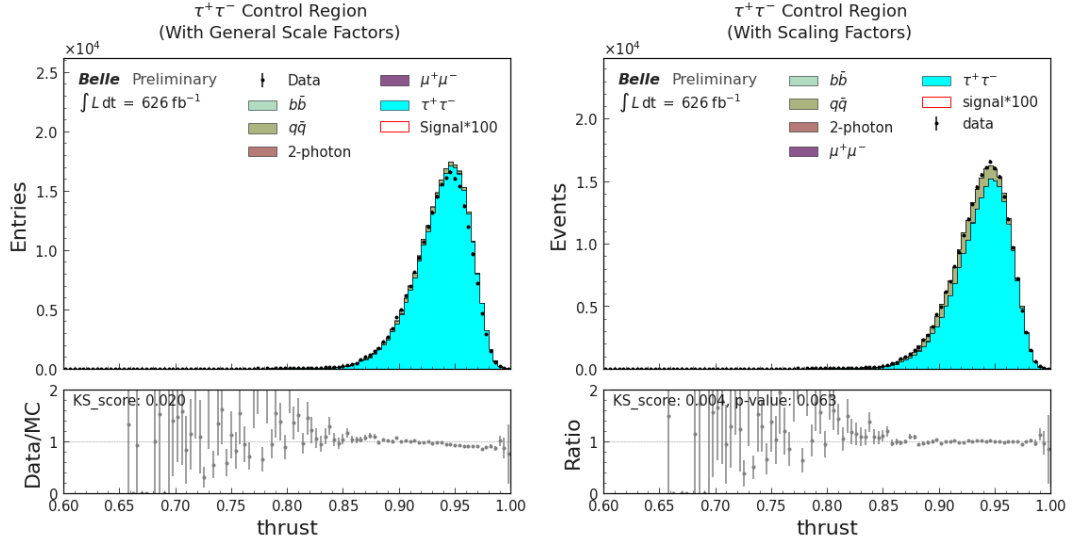


Figure 71. Distributions of thrust in $\tau^+\tau^-$ control region for $\phi_L \rightarrow \mu^+\mu^-$ channel using the scale factors obtained from (left) general control region vs. (right) $\tau^+\tau^-$ control region.

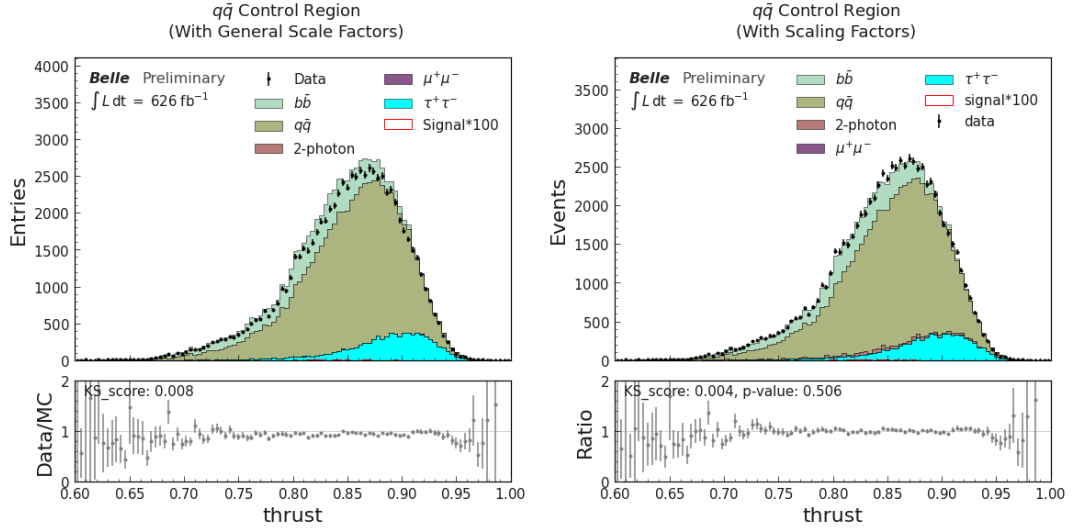


Figure 72. Distributions of thrust in $q\bar{q}$ control region for $\phi_L \rightarrow \mu^+\mu^-$ channel using the scale factors obtained from (left) general control region vs. (right) $q\bar{q}$ control region.

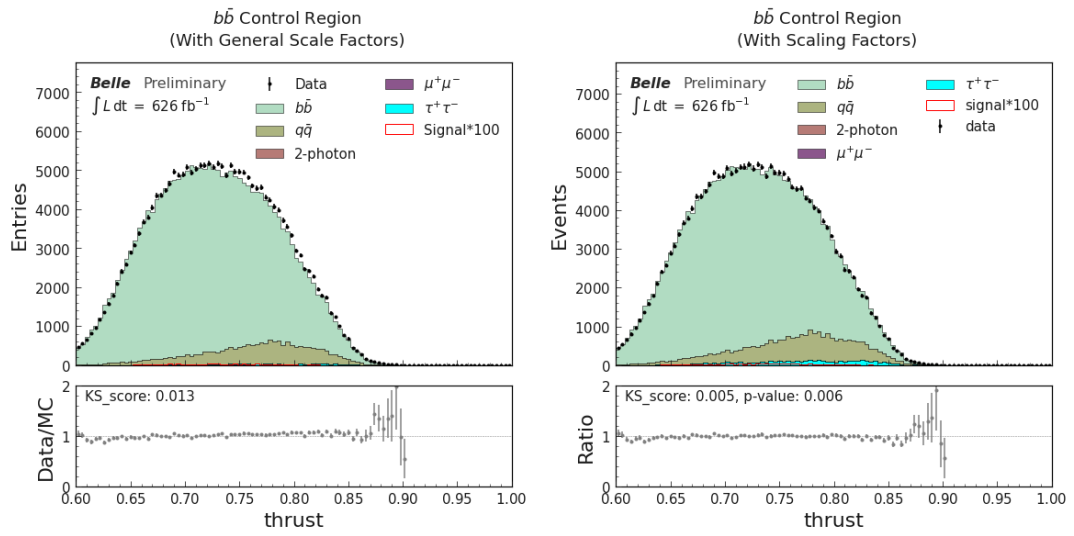


Figure 73. Distributions of thrust in $b\bar{b}$ control region for $\phi_L \rightarrow \mu^+\mu^-$ channel using the scale factors obtained from general control region (left) vs. using the ones from $b\bar{b}$ control region (right).

VI.5 Results from blinded analysis

Data-MC agreement in control regions

Fig. 74 shows data-MC agreement in the general control regions for both $\phi_L \rightarrow e^+e^-$ and $\phi_L \rightarrow \mu^+\mu^-$ channels. The background compositions of these plots are listed in Table 4

$\phi_L \rightarrow e^+e^-$		$\phi_L \rightarrow \mu^+\mu^-$	
MC sample	Composition	MC sample	Composition
$\tau^+\tau^-$	69.97%	$\tau^+\tau^-$	46.07%
e^+e^-	3.28%	$\mu^+\mu^-$	0.11%
2-photon	2.62%	2-photon	0.04%
$q\bar{q}$	10.36%	$q\bar{q}$	16.38%
$b\bar{b}$	13.77%	$b\bar{b}$	37.40%

Table 4. The background compositions of the invariant mass distributions in the general control regions of $\phi_L \rightarrow e^+e^-$ (top) and $\phi_L \rightarrow \mu^+\mu^-$ (bottom) channels.

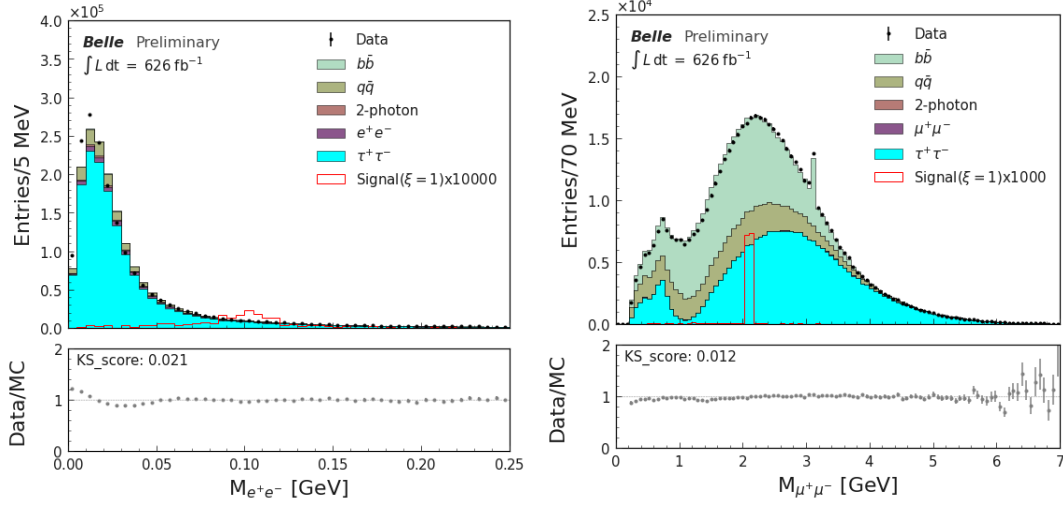


Figure 74. Data and MC distributions of e^+e^- invariant mass (for $\phi_L \rightarrow e^+e^-$ channel) and $\mu^+\mu^-$ invariant mass (for $\phi_L \rightarrow \mu^+\mu^-$ channel) in general control region after applying all corrections and scale factors. The signal samples were generated with $m_{\phi_L} = 100$ MeV and 2.1 GeV respectively.

Distributions of the discriminating variable

The e^+e^- invariant mass has been used as the discriminating variable for $\phi_L \rightarrow e^+e^-$ channel and the $\mu^+\mu^-$ invariant mass has been used as the discriminating variable for $\phi_L \rightarrow \mu^+\mu^-$ channel. Fig. 75 shows the distributions of these variables in signal and control regions.

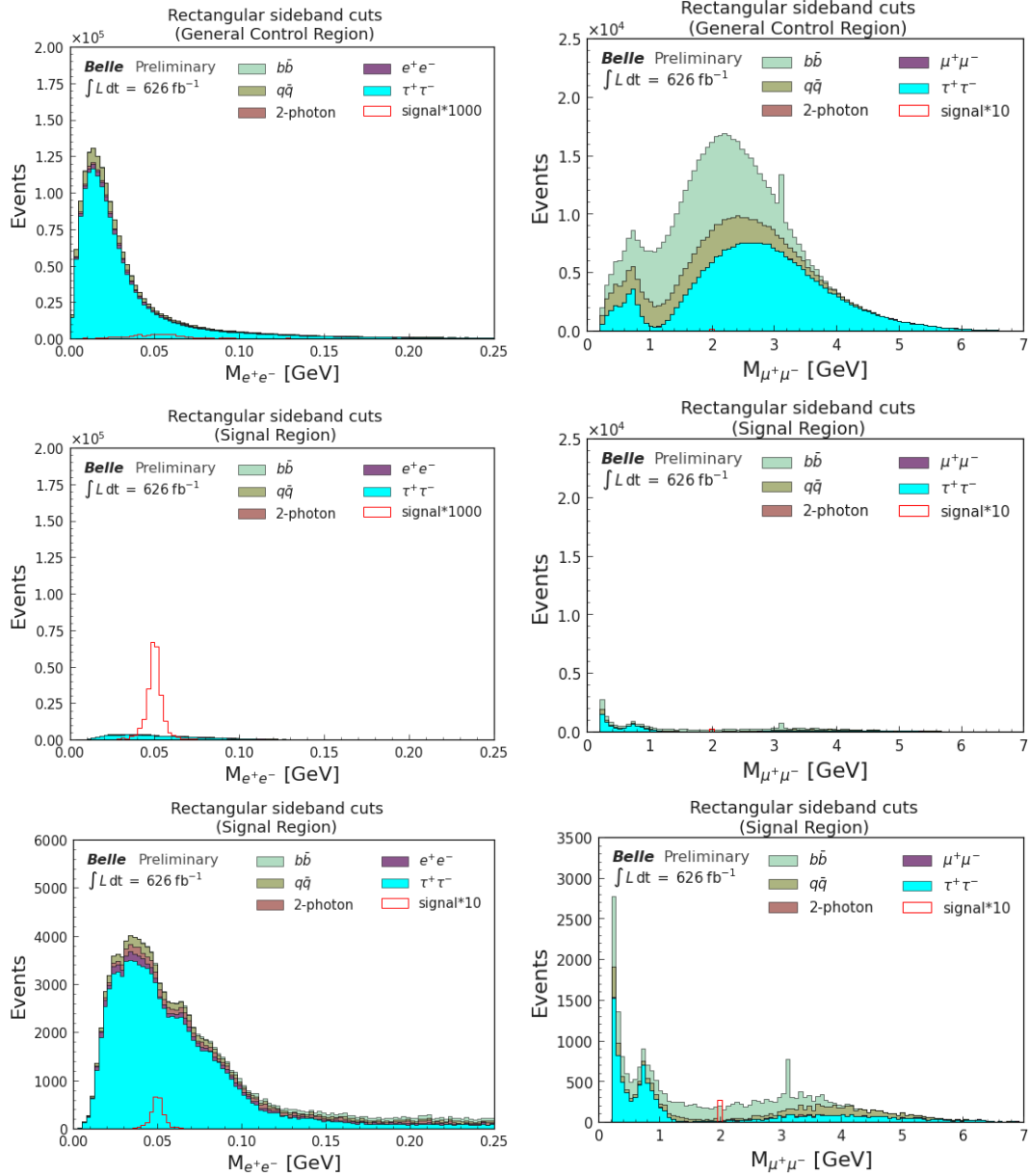


Figure 75. Distributions of e^+e^- and $\mu^+\mu^-$ invariant masses shown in the general control region and signal region. The bottom two plots are the enlarged versions of the middle two plots. The bottom left plot uses a smaller signal multiplicative factor than the one used in the middle left plot.

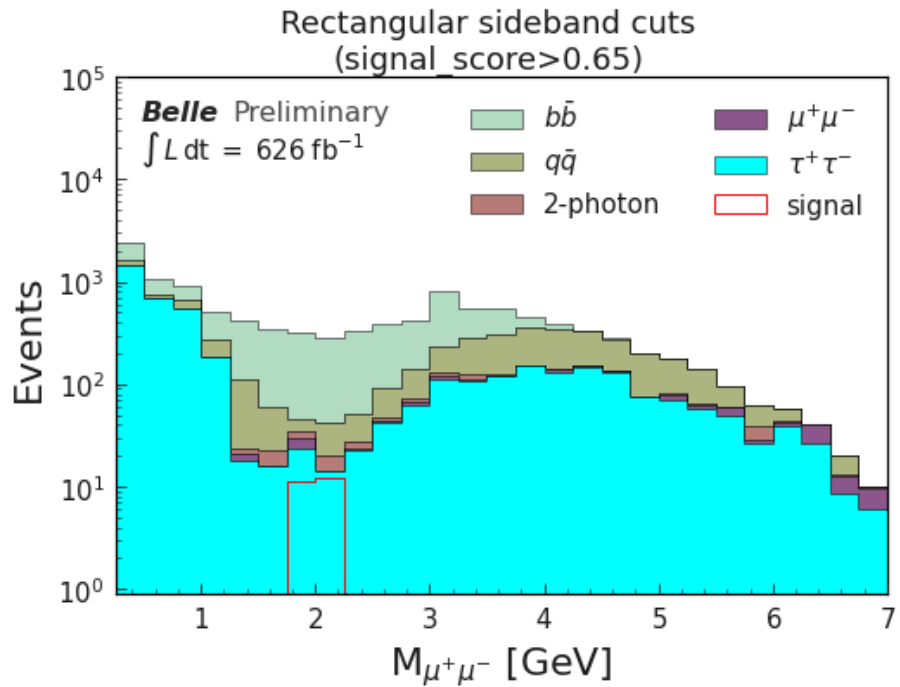
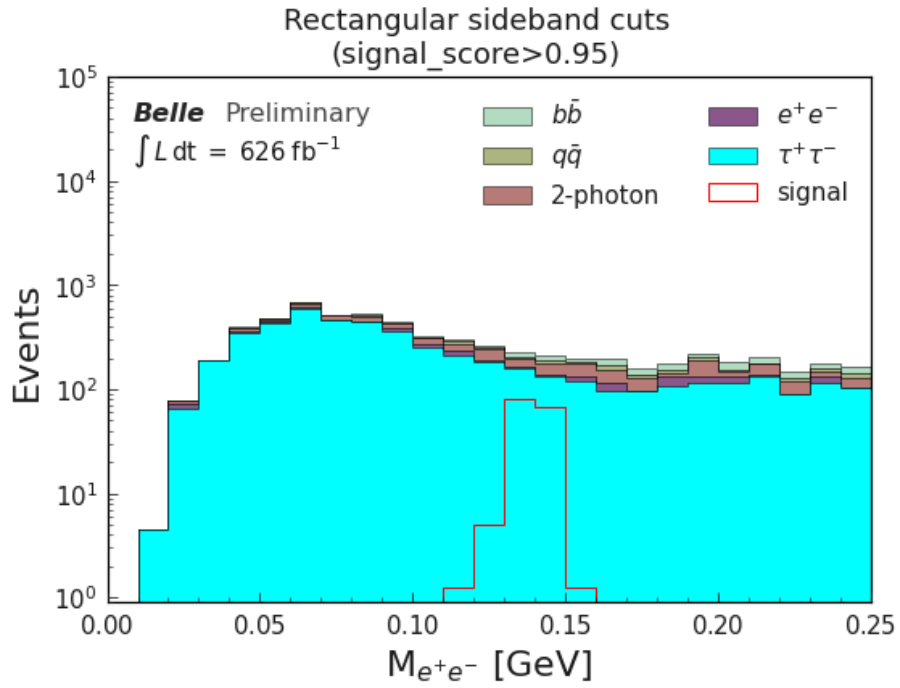


Figure 76. Distributions of e^+e^- and $\mu^+\mu^-$ invariant mass with cuts `signal_score>0.95` and `signal_score>0.65` respectively. The y-axis is in log scale.

Signal selection efficiency

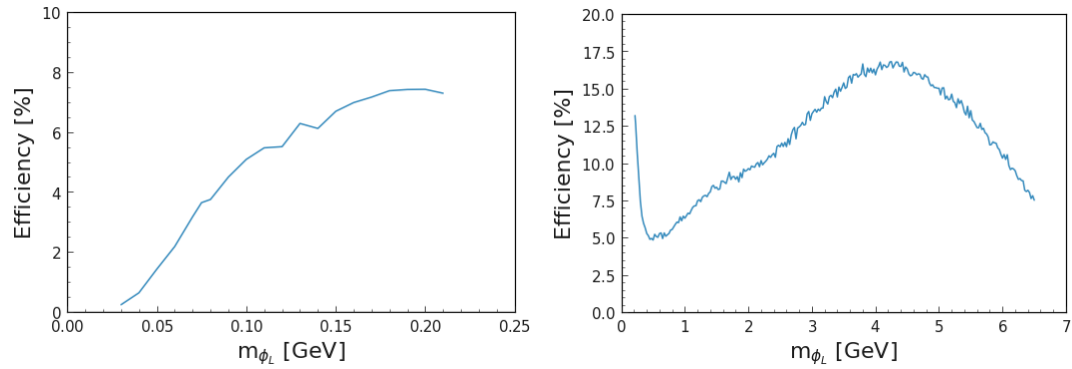


Figure 77. Signal selection efficiency for $\phi_L \rightarrow e^+e^-$ (left) and $\phi_L \rightarrow \mu^+\mu^-$ (right) channels are shown for the BDT cuts `signal_score>0.95` and `signal_score>0.65` respectively.

The signal selection efficiency for $\phi_L \rightarrow e^+e^-$ (left) and $\phi_L \rightarrow \mu^+\mu^-$ (right) channels are shown in Fig. 77, for the BDT cuts `signal_score>0.95` and `signal_score>0.65` respectively.

VI.6 Results from unblinded analysis

After unblinding, we check the data-MC agreement in the signal region. Fig. 78 shows the data-MC agreement in $\phi_L \rightarrow e^+e^-$ and $\phi_L \rightarrow \mu^+\mu^-$ channels, after the cuts `signal_score>0.95` and `signal_score>0.65` respectively.

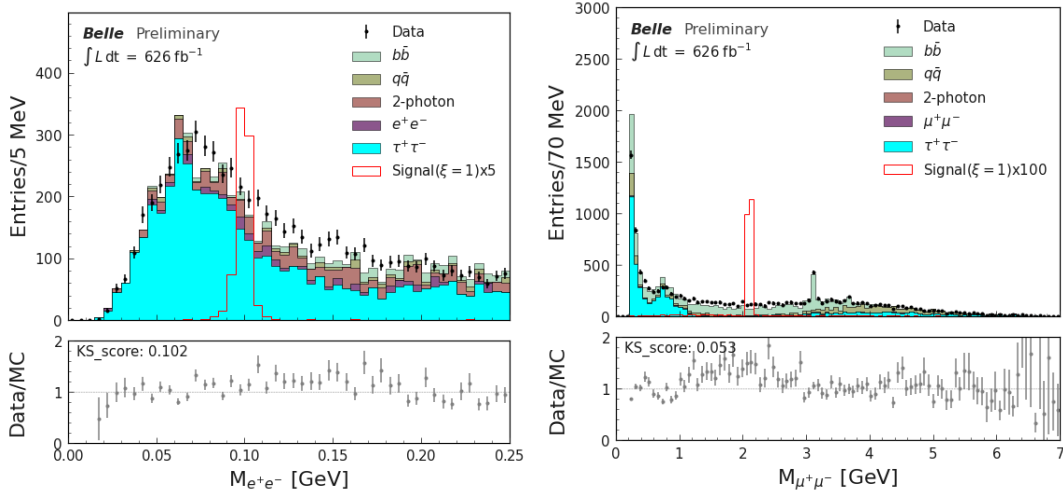


Figure 78. Distributions of e^+e^- and $\mu^+\mu^-$ invariant mass with cuts `signal_score>0.95` and `signal_score>0.65` respectively. The y-axis is in log scale.

We get fairly good data-MC agreement in both of the channels. However, in $\phi_L \rightarrow \mu^+\mu^-$ channel, we notice that the data is consistently higher than the sum of the background MC samples, between 1 GeV and 3 GeV. Since this excess doesn't match the signal shape, we suspect that this excess is because of some unsimulated 4-lepton processes, that are not present in our two-photon sample. To account for the background events from such unsimulated processes, we add a uniform distribution as another background component while fitting the signal and background distributions to data.

Systematic uncertainties

We include the following sources of systematic uncertainties while calculating the upper limit of the coupling constant ξ .

1. **Uncertainty in luminosity:** The uncertainty associated with integrated luminosity is taken to be 1.4% [36].
2. **Uncertainty in PID correction factors:** We include the effect of uncertainty in PID correction factors by propagating those errors to the calculation of event weights and producing up and down variations of the ϕ_L invariant mass distribution. We use those distributions to include this systematic uncertainty as a HistoSys in our HistFactory template.
3. **Uncertainty in tracking efficiency:** The uncertainty in charged track reconstruction is obtained from an earlier study [37], according to that a systematic uncertainty of 0.35% per track is recommended. In our analysis, we require 4 tracks in the event. So we assign an uncertainty of 1.4%.
4. **Uncertainty in track momenta:** We include the effect of uncertainty in track momenta by propagating those errors to the calculation of ϕ_L invariant mass. Then we include this uncertainty as a HistoSys in our HistFactory template. Fig. 79 shows the up and down variations for this systematic uncertainty. To get the up variation, the components of the track momenta, i.e. p_x , p_y and p_z have been replaced with $p_x + \Delta p_x$, $p_y + \Delta p_y$ and $p_z + \Delta p_z$. Then these values have been used to calculate the $\ell^+\ell^-$ invariant mass, and the histogram obtained from these modified invariant mass values is called the up variation. Similarly, the down variation has been obtained by replacing p_x , p_y and p_z with $p_x - \Delta p_x$, $p_y - \Delta p_y$ and $p_z - \Delta p_z$.
5. **Uncertainty in MC scale factors:** We include the effect of uncertainty in MC scale factors by propagating those errors to the calculation of event weights

and producing up and down variations of the ϕ_L invariant mass distribution. We use those distributions to include this systematic uncertainty as a HistoSys in our HistFactory template.

6. **Uncertainty in BDT efficiency:** We include the effect of the uncertainty in the selection efficiency of the `signal_score` cut on the signal sample. We take the difference in selection efficiencies between our train and test datasets as a measure of this uncertainty. Although this number is different for different mass points in the two channels, we find that it is, on an average, 0.7% for $\phi_L \rightarrow e^+e^-$ channel and 0.3% for $\phi_L \rightarrow \mu^+\mu^-$ channel. So we assign a conservative value of 1% for this uncertainty. Fig. 80 shows how this uncertainty is calculated for $\phi_L \rightarrow e^+e^-$ channel.

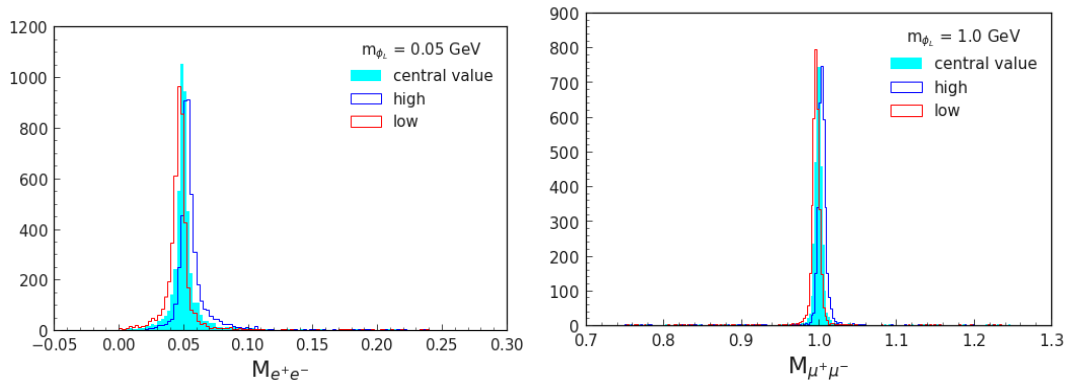


Figure 79. Example of histograms used for HistoSys uncertainties. The high and low distributions corresponds to the up and down variations of the discriminating variable for the two extremities of this systematic error.

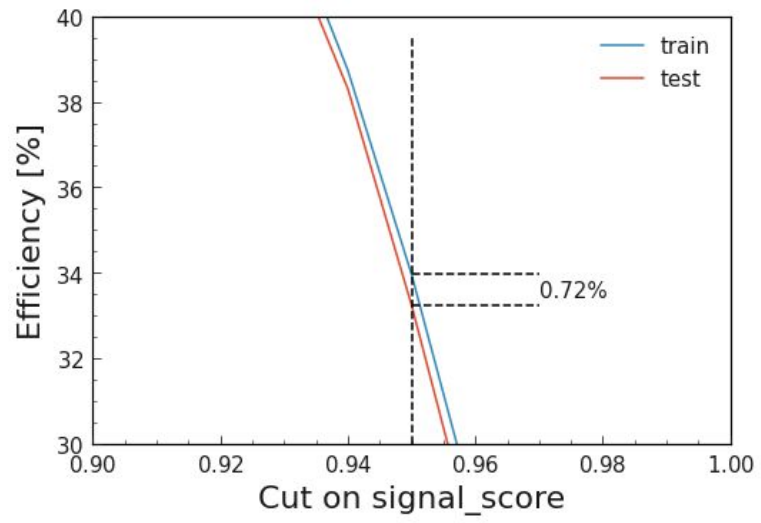


Figure 80. Estimating the systematic error associated with the BDT selection efficiency in $\phi_L \rightarrow e^+e^-$ channel.

Upper limits calculation

The statistical analysis uses a binned likelihood function $\mathcal{L}(\mu, \theta)$, constructed as a product of Poisson probability terms over all bins considered in the search. This function depends on the parameter of interest μ , and a set of nuisance parameters θ that encode the effect of systematic uncertainties in the signal and background expectations.

We perform a binned likelihood fit to the data under the signal-plus-background hypothesis, i.e. maximizing $\mathcal{L}(\mu, \theta)$ over μ and θ . The test statistic q_μ is defined as the profile likelihood ratio, $q_\mu = -2 \ln[\mathcal{L}(\mu, \hat{\theta})/\mathcal{L}(\hat{\mu}, \hat{\theta})]$, where $\hat{\mu}$ and $\hat{\theta}$ maximize \mathcal{L} , and $\hat{\theta}$ is the set of values that maximizes \mathcal{L} for a given value of μ . For the discovery, the significance (Z) is calculated by setting $\mu = 0$ in the test statistic as the null hypothesis in the profile likelihood ratio. Thus, the Z is a measure of the probability that fluctuation of the background (characterized by $\mu = 0$) can mimic the observed data. In the absence of any significant excess above the background expectation, upper limits are derived by using q_μ defined above and the CL_s method [38, 39], where the CL_s is defined as the ratio of confidence levels for the signal-plus-background hypothesis normalized by the confidence level for the background-only hypothesis. Asymptotic calculations of the likelihood ratios allow for computationally very efficient estimate of the CL_s intervals [40].

We calculate the upper limit of the coupling constant ξ with the help of `HistFactory` template.

While building our workspaces, we use the signal histograms corresponding to $\xi_{\text{gen}} = 1$ (until 4 GeV), 10 (from 4 GeV to until 5 GeV) or 100 (from 5 GeV onwards). We define our parameter of interest (POI) as the ratio of the signal cross-section and the theoretical signal cross-section for that particular value of ξ_{gen} . Since the signal cross-section is proportional ξ^2 , we can calculate the upper limit of ξ to be $\xi_{\text{gen}} \times \sqrt{\text{UL of POI}}$.

We use the `pyhf` implementation [41, 42] of the widely-used `HistFactory` p.d.f. template, as introduced in this report [43], to fit our workspace histograms and calculate the upper limit of the coupling constant ξ . We use `JAX` [44] as the computational backend for `pyhf` to speed up the numerical computation.

In the next few pages, we show the histograms used for our `HistFactory` workspaces along with the result of the POI scan, for different mass points in $\phi_L \rightarrow e^+e^-$ and $\phi_L \rightarrow \mu^+\mu^-$ channels.

Fit results for $\phi_L \rightarrow e^+e^-$ channel

Signal distributions used for fitting are obtained at the following mass points: 40 MeV, 50 MeV, 60 MeV, 70 MeV, 80 MeV, 90 MeV, 100 MeV, 120 MeV, 140 MeV, 150 MeV, 160 MeV, 180 MeV, 200 MeV. we put a cut `signal_score > 0.95` for all the mass points to suppress the background and get better upper limits on signal cross-section and the coupling constant. We choose this cut value based on our optimization study using the expected upper limit, where we found that for most of the mass points, a cut at 0.95 gives the best expected upper limit.

For each mass point, we choose the binning of our workspace histograms in the following way:

- One large bin from 0 to $(m_{\phi_L} - 10 \text{ MeV})$.
- Eight equal-width bins between $(m_{\phi_L} - 10 \text{ MeV})$ and $(m_{\phi_L} + 10 \text{ MeV})$.
- One large bin from $(m_{\phi_L} + 10 \text{ MeV})$ to 250 MeV.

The fit results of our `HistFactory` workspaces for different mass points in the $\phi_L \rightarrow e^+e^-$ channel are shown in Fig. 81, Fig. 82, Fig. 83, Fig. 84, and Fig. 85.

The result of profile log-likelihood (PLL) scan of the POI and the nuisance parameters for all mass points in this channel are listed in https://belle.kek.jp/secured/belle_note/gn1653/p11_plots_ee.pdf.

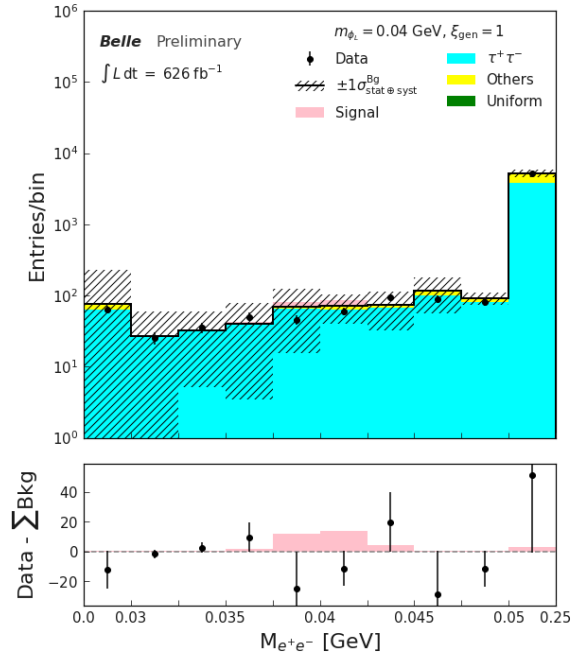


Figure 81. Fit results for the workspace histograms with $m_{\phi_L} = 0.04 \text{ GeV}$ in $\phi_L \rightarrow e^+e^-$ channel.

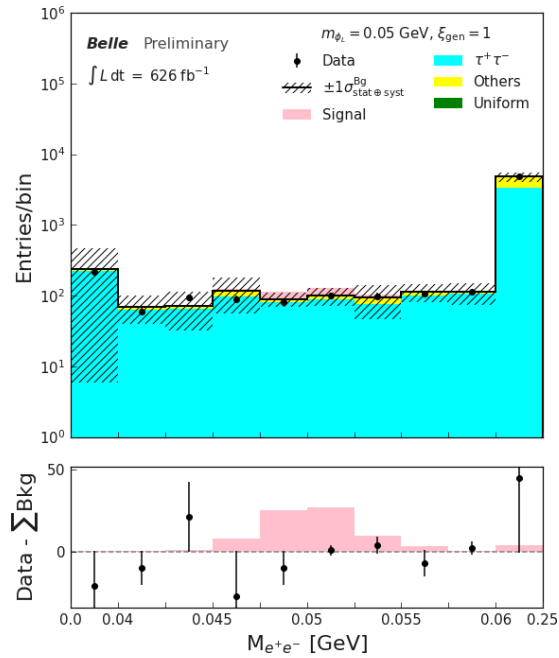


Figure 82. Fit results for the workspace histograms with $m_{\phi_L} = 0.05 \text{ GeV}$ in $\phi_L \rightarrow e^+e^-$ channel.

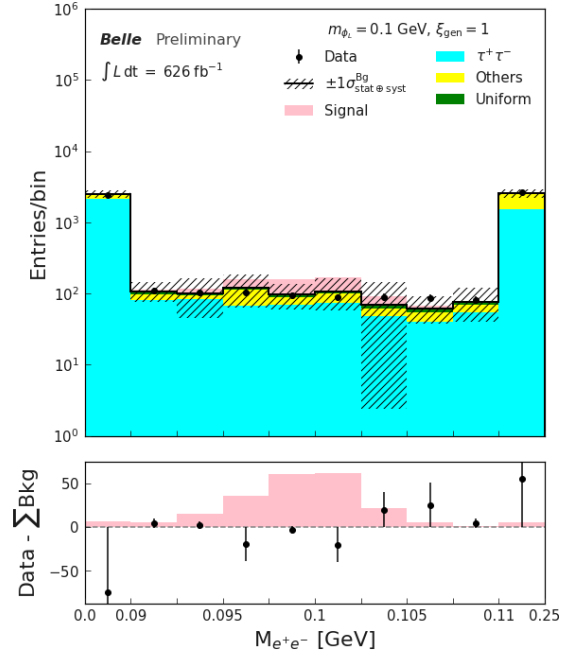


Figure 83. Fit results for the workspace histograms with $m_{\phi_L} = 0.1 \text{ GeV}$ in $\phi_L \rightarrow e^+e^-$ channel.

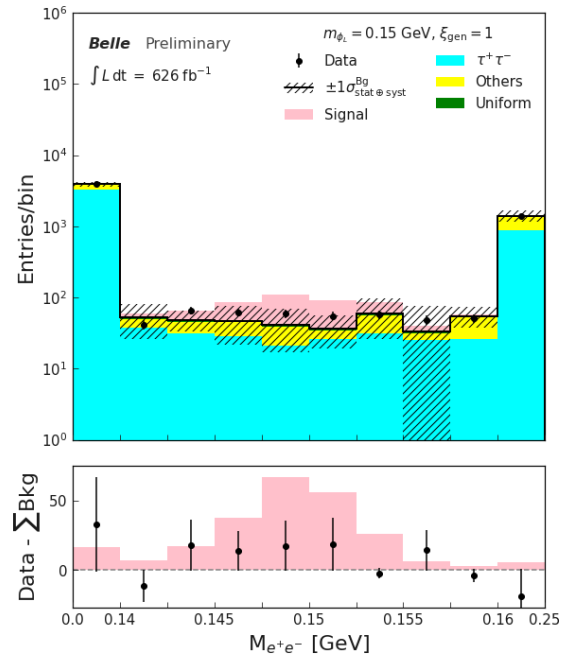


Figure 84. Fit results for the workspace histograms with $m_{\phi_L} = 0.15 \text{ GeV}$ in $\phi_L \rightarrow e^+e^-$ channel.

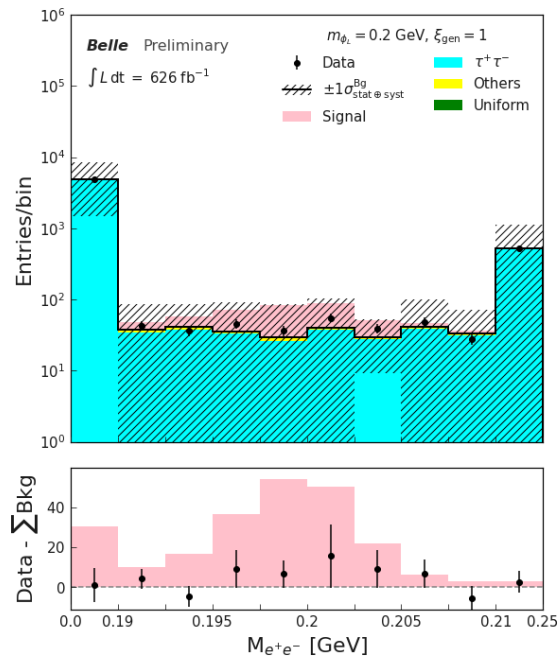


Figure 85. Fit results for the workspace histograms with $m_{\phi_L} = 0.2 \text{ GeV}$ in $\phi_L \rightarrow e^+e^-$ channel.

Fit results for $\phi_L \rightarrow \mu^+ \mu^-$ channel

Signal distributions used for fitting are obtained for the mass points at 50 MeV interval between 250 MeV and 6.5 GeV. We also include 225 MeV as the first mass point for this channel. We put a cut `signal_score > 0.65` for all the mass points in this channel, as the number of background events falls below 0.5 per bin for higher mass points if we choose a higher cut value.

For each mass point, we first calculate the width of the signal $\mu^+ \mu^-$ invariant mass distribution by doing a Gaussian fit in the range $(m_{\phi_L} - 100 \text{ MeV}, m_{\phi_L} + 100 \text{ MeV})$, where m_{ϕ_L} is the generator level mass of the ϕ_L candidate. Once we get the value of σ from the fit, we choose the binning of our workspace histograms in the described below.

For each mass point till 6.35 GeV, except the ones mentioned below, we use the following binning:

- One large bin from 0 to $(m_{\phi_L} - 2 * \sigma)$.
- 4 equal-width bins between $(m_{\phi_L} - 2 * \sigma)$ and $(m_{\phi_L} + 2 * \sigma)$.
- One large bin from $(m_{\phi_L} + 2 * \sigma)$ to 7 GeV.

For 0.225, 0.525, 0.850, 4.050, 4.450, 4.525, 5.525, 5.800, 5.825, 6.175, 6.275, 6.375 and 6.425 GeV mass points, we use the following binning:

- One large bin from 0 to $(m_{\phi_L} - 2 * \sigma)$.
- 3 equal-width bins between $(m_{\phi_L} - 2 * \sigma)$ and $(m_{\phi_L} + 2 * \sigma)$.
- One large bin from $(m_{\phi_L} + 2 * \sigma)$ to 7 GeV.

For the 5.525 GeV mass point, we use the following binning:

- One large bin from 0 to $(m_{\phi_L} - 2 * \sigma)$.
- 2 equal-width bins between $(m_{\phi_L} - 2 * \sigma)$ and $(m_{\phi_L} + 2 * \sigma)$.

- One large bin from $(m_{\phi_L} + 2 * \sigma)$ to 7 GeV.

The fit results of our `HistFactory` workspaces for different mass points in the $\phi_L \rightarrow \mu^+ \mu^-$ channel are shown in Fig. 86, Fig. 87, Fig. 88, Fig. 89, Fig. 90, Fig. 91, Fig. 92, Fig. 93, Fig. 94, Fig. 95, Fig. 96, Fig. 97, Fig. 98, and Fig. 99.

The result of profile log-likelihood (PLL) scan of the POI and the nuisance parameters for all mass points in this channel are listed in https://belle.kek.jp/secured/belle_note/gn1653/pll_plots_mumu.pdf.

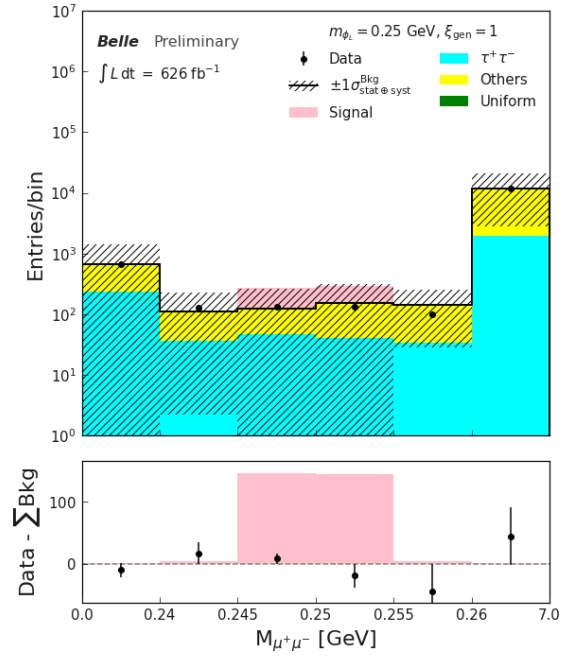


Figure 86. Fit results for the workspace histograms with $m_{\phi_L} = 0.25 \text{ GeV}$ in $\phi_L \rightarrow \mu^+ \mu^-$ channel.

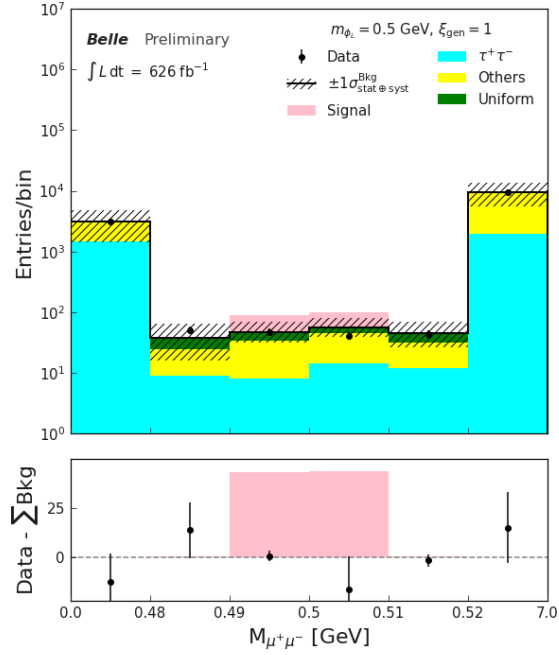


Figure 87. Fit results for the workspace histograms with $m_{\phi_L} = 0.5 \text{ GeV}$ in $\phi_L \rightarrow \mu^+ \mu^-$ channel.

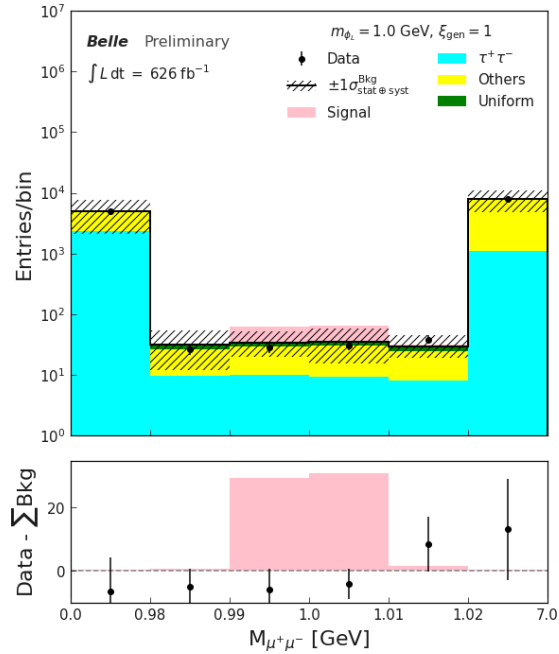


Figure 88. Fit results for the workspace histograms with $m_{\phi_L} = 1.0 \text{ GeV}$ in $\phi_L \rightarrow \mu^+ \mu^-$ channel.

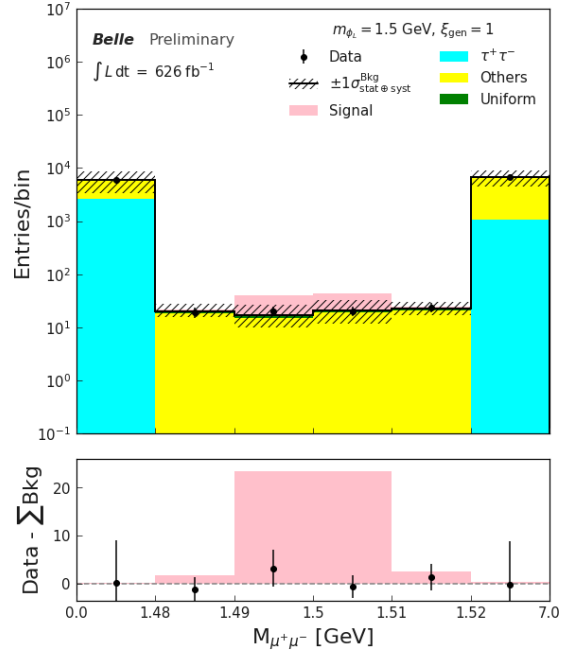


Figure 89. Fit results for the workspace histograms with $m_{\phi_L} = 1.5 \text{ GeV}$ in $\phi_L \rightarrow \mu^+\mu^-$ channel.

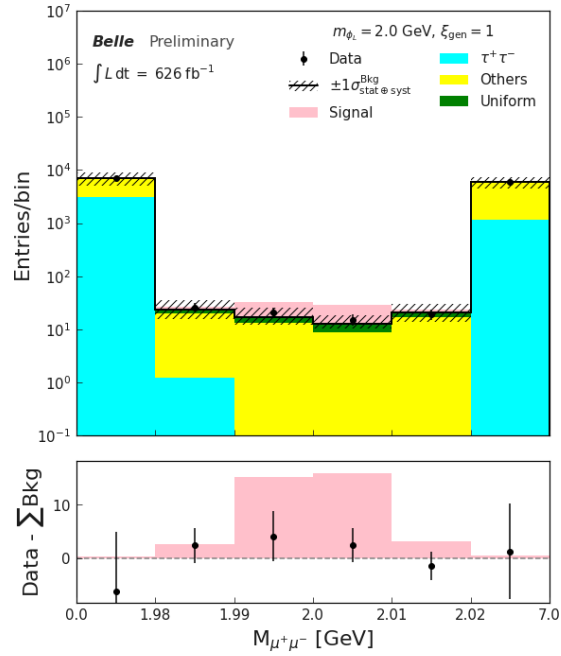


Figure 90. Fit results for the workspace histograms with $m_{\phi_L} = 2.0 \text{ GeV}$ in $\phi_L \rightarrow \mu^+\mu^-$ channel.

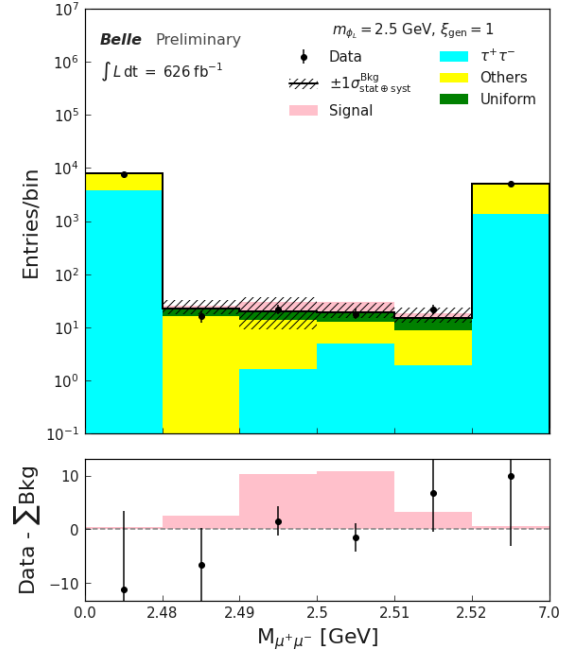


Figure 91. Fit results for the workspace histograms with $m_{\phi_L} = 2.5 \text{ GeV}$ in $\phi_L \rightarrow \mu^+\mu^-$ channel.

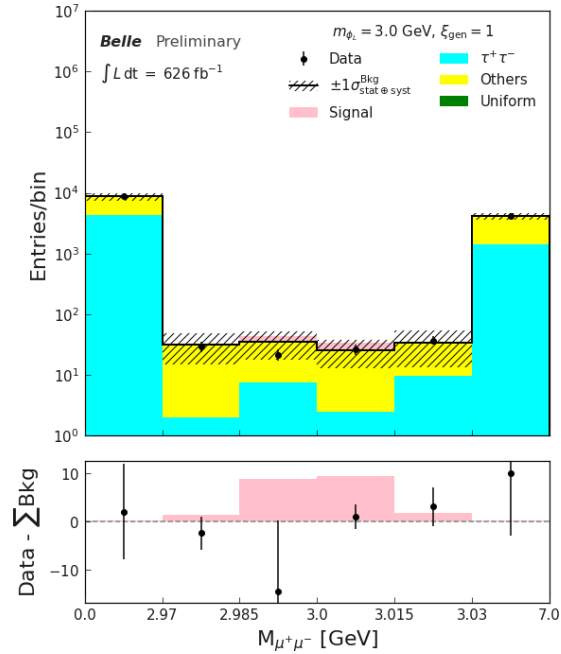


Figure 92. Fit results for the workspace histograms with $m_{\phi_L} = 3.0 \text{ GeV}$ in $\phi_L \rightarrow \mu^+\mu^-$ channel.

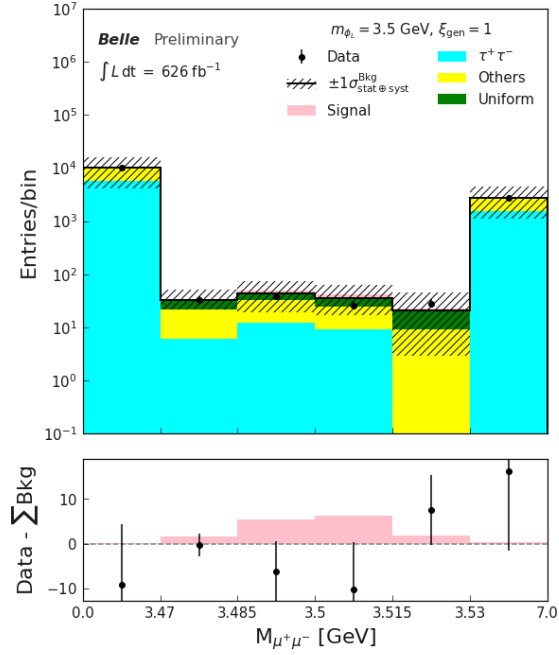


Figure 93. Fit results for the workspace histograms with $m_{\phi_L} = 3.5 \text{ GeV}$ in $\phi_L \rightarrow \mu^+ \mu^-$ channel.

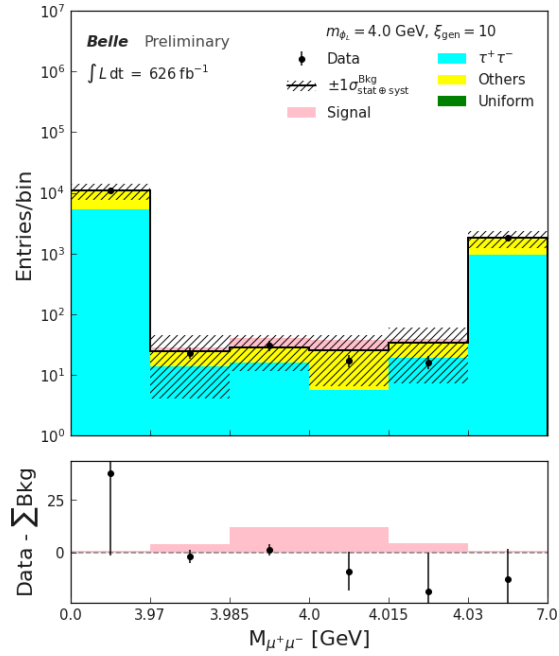


Figure 94. Fit results for the workspace histograms with $m_{\phi_L} = 4.0 \text{ GeV}$ in $\phi_L \rightarrow \mu^+ \mu^-$ channel.

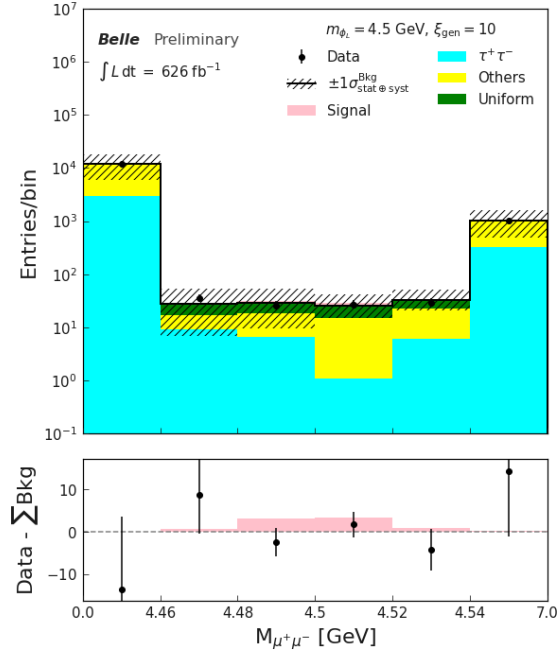


Figure 95. Fit results for the workspace histograms with $m_{\phi_L} = 4.5 \text{ GeV}$ in $\phi_L \rightarrow \mu^+\mu^-$ channel.

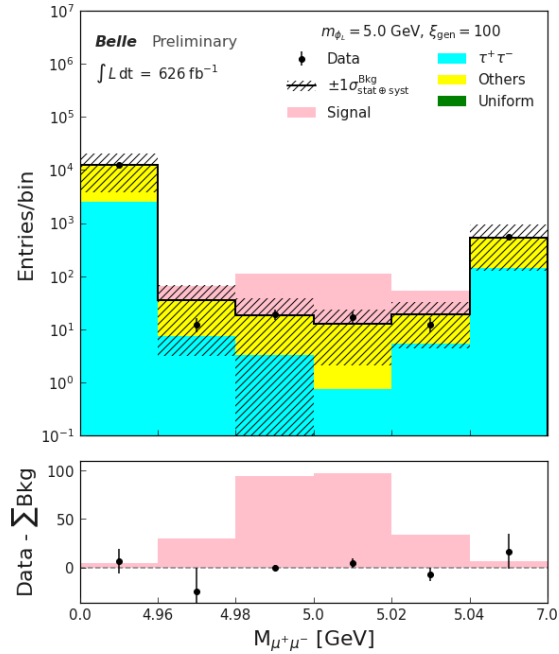


Figure 96. Fit results for the workspace histograms with $m_{\phi_L} = 5.0 \text{ GeV}$ in $\phi_L \rightarrow \mu^+\mu^-$ channel.

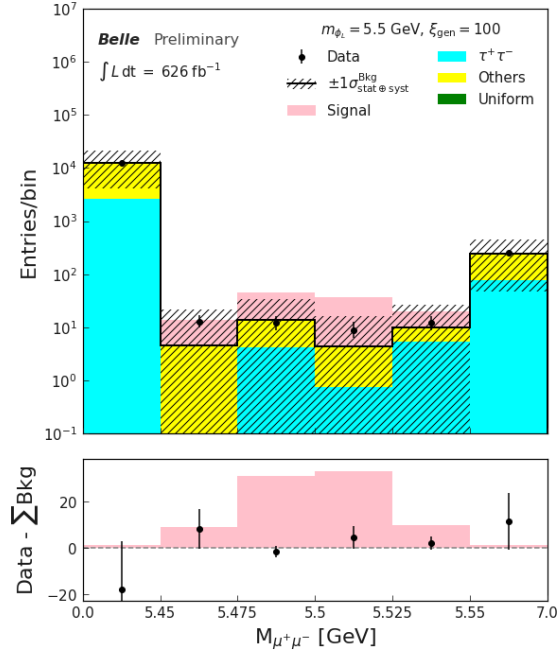


Figure 97. Fit results for the workspace histograms with $m_{\phi_L} = 5.5 \text{ GeV}$ in $\phi_L \rightarrow \mu^+ \mu^-$ channel.

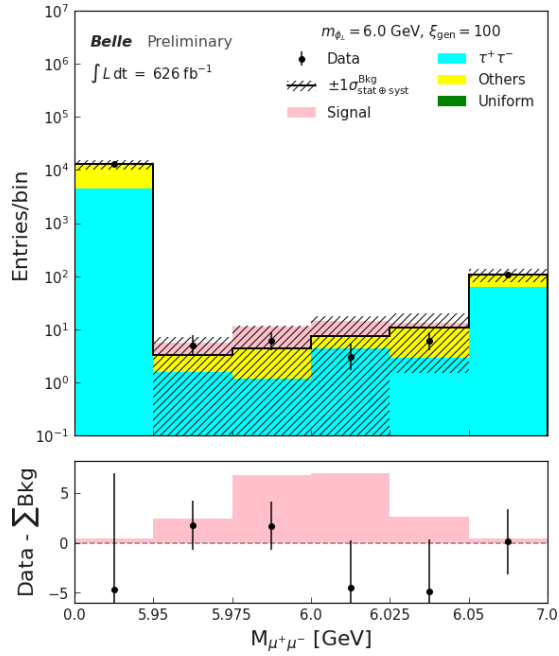


Figure 98. Fit results for the workspace histograms with $m_{\phi_L} = 6.0 \text{ GeV}$ in $\phi_L \rightarrow \mu^+ \mu^-$ channel.

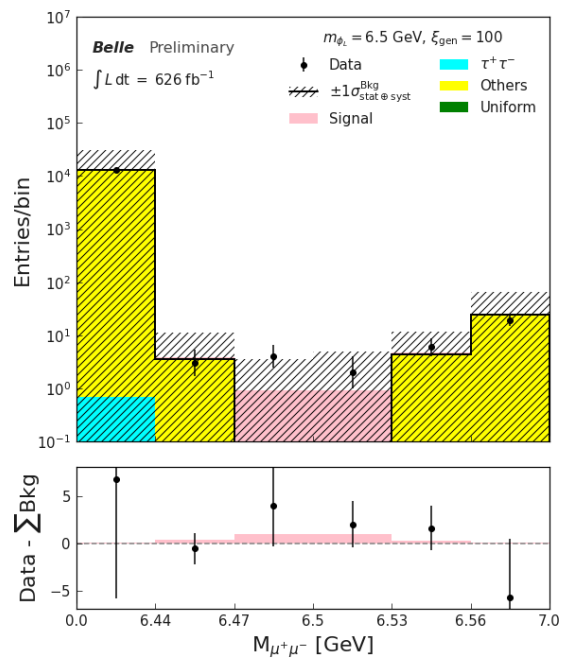


Figure 99. Fit results for the workspace histograms with $m_{\phi_L} = 6.5 \text{ GeV}$ in $\phi_L \rightarrow \mu^+ \mu^-$ channel.

Upper limits of cross-section and coupling constant

The expected and observed upper limits of the cross-section of the signal processes $e^+e^- \rightarrow \tau^+\tau^-\phi_L$, $\phi_L \rightarrow e^+e^-$ and $e^+e^- \rightarrow \tau^+\tau^-\phi_L$, $\phi_L \rightarrow \mu^+\mu^-$ are shown in Fig. 100.

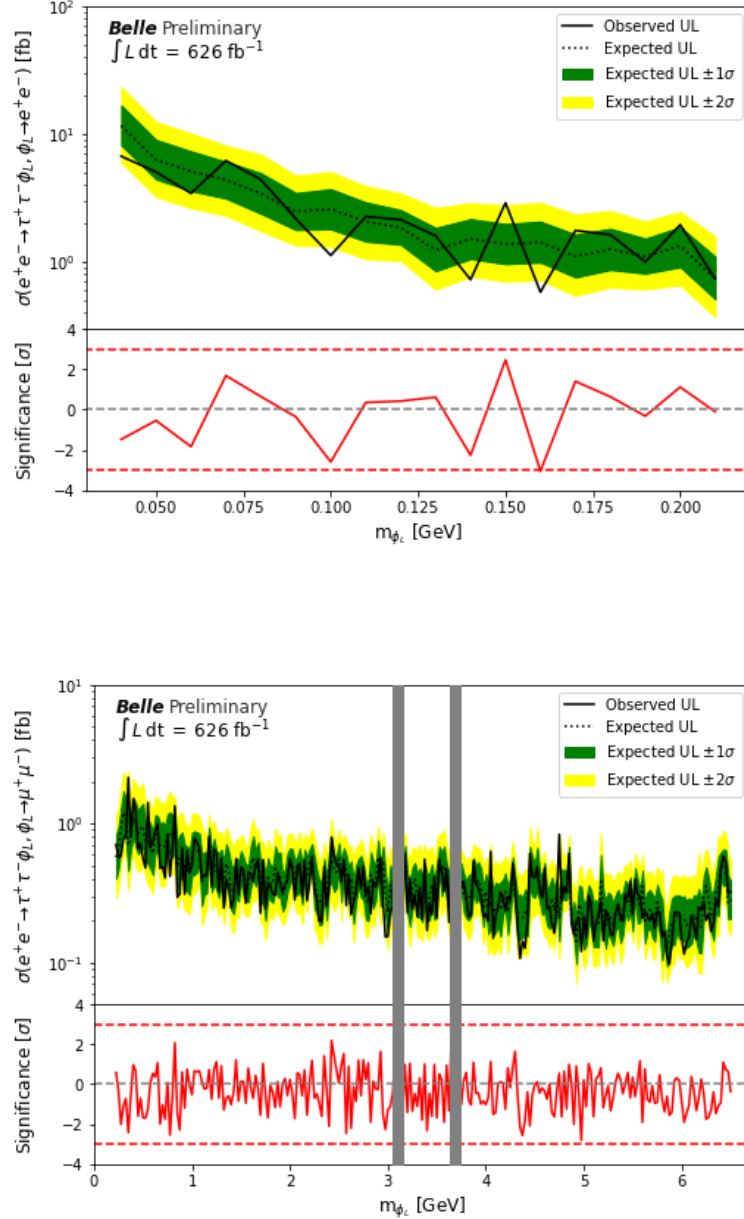


Figure 100. Observed upper limits on the cross-section (in black) at 90% CL, and observed significance (in red) for $\phi_L \rightarrow e^+e^-$ channel (top) and $\phi_L \rightarrow \mu^+\mu^-$ channel (bottom) as a function of the dark scalar mass.

The exclusion region for the coupling constant ξ obtained from this analysis is

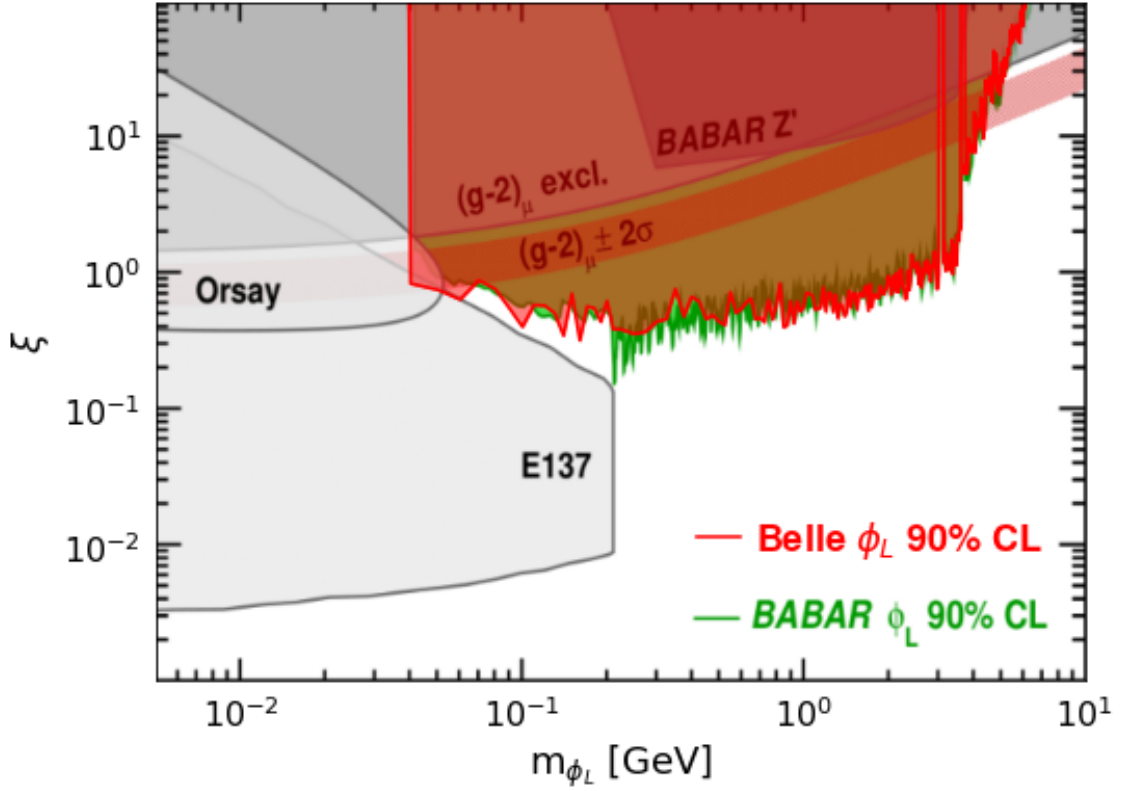


Figure 101. Observed upper limits at 90% CL on the coupling constant ξ as a function of the ϕ_L mass from our search (red), overlaid with results from *BABAR* (green) [18] and other experiments (gray) [45, 46, 47, 48, 49]. The parameter space preferred by the muon anomalous magnetic moment [16] is shown as a red band.

shown in Fig. 101. We skip the ± 50 MeV window around the nominal mass of J/ψ and $\psi(2S)$, where we expect peaking backgrounds.

CHAPTER VII

SUMMARY AND OUTLOOK

My contributions to the K-Long and Muon (KLM) and the Data Acquisition (DAQ) groups of the Belle II experiment are presented in the first part of this thesis.

As part of KLM group, I worked as the lead developer of the slow-control system and developed various control systems and monitoring tools, including the RPC gas-flow monitoring system, KLM high voltage interlock system, tools for archiving/setting important KLM status/configuration parameters, and a system for monitoring the beam-background level perceived by the KLM detector.

As part of the DAQ group, I worked on the upgrade of the DAQ database systems, the upgrade of the readout electronics to the latest PCIe40 based system, creating a user-friendly way of storing the configuration of the trigger time distribution (TTD) system along with the sub-detector frontend electronics (FEE) masking information.

As part of the Ozaki exchange program, I was stationed at KEK in Japan for two years and worked as a local troubleshooting expert for the KLM detector, as well as, the DAQ systems.

We analyzed 626fb^{-1} data collected at and around $\Upsilon(4S)$ resonance from the Belle experiment to search for the dark leptophilic scalar produced in association with $\tau^+\tau^-$ pair in e^+e^- annihilation.

We find all the mass points have significance less than 3 standard deviations (σ). Since there is no evidence of signal, we set the upper limit of the signal cross-section

at 90% confidence level. The results obtained from this analysis are comparable to the latest results published by the *BABAR* experiment.

This result excludes the parameter space with m_{ϕ_L} between [0.04, 4] GeV favored by $(g - 2)_\mu$ at 90% CL [48, 49], i.e. there is no such dark leptophilic scalar that can explain the observed excess in the anomalous magnetic moment of muon with mass less than 4 GeV.

REFERENCES

- [1] N. A. Bahcall, “Dark matter universe,” *Proceedings of the National Academy of Sciences* **112**, 12243–12245 (2015).
- [2] F. Zwicky, “Die rotverschiebung von extragalaktischen nebeln,” *Helvetica physica acta* **6**, 110–127 (1933).
- [3] Martin White, “Rotation Curves,” <https://w.astro.berkeley.edu/~mwhite/darkmatter/rotcurve.html>. Accessed: 2022-06-17.
- [4] E. Corbelli and P. Salucci, “The Extended Rotation Curve and the Dark Matter Halo of M33,” *Mon. Not. Roy. Astron. Soc.* **311**, 441–447 (2000).
- [5] K. Freese, “Review of observational evidence for dark matter in the universe and in upcoming searches for dark stars,” *EAS Publications Series* **36**, 113–126 (2009).
- [6] L. Bergström, “Dark matter candidates,” *New Journal of Physics* **11**, 105006 (2009).
- [7] SuperKEKB and Belle II, Belle II web page, accessed May-2021, https://www.belle2.org/project/super_kekb_and_belle_ii.
- [8] Y. Ohnishi *et al.*, “Accelerator design at SuperKEKB,” *Progress of Theoretical and Experimental Physics* **2013** (2013). 03A011.

- [9] M. Bona *et al.*, “SuperB: A High-Luminosity Asymmetric $e^+ e^-$ Super Flavor Factory. Conceptual Design Report,” (2007).
- [10] C. Bernardini, G. F. Corazza, G. Di Giugno, G. Ghigo, J. Haissinski, P. Marin, R. Querzoli, and B. Touschek, “Lifetime and beam size in a storage ring,” *Phys. Rev. Lett.* **10**, 407–409 (1963).
- [11] Y. Suetsugu, K. Shibata, T. Ishibashi, K. Kanazawa, M. Shirai, S. Terui, and H. Hisamatsu, “First commissioning of the superkekb vacuum system,” *Phys. Rev. Accel. Beams* **19**, 121001 (2016).
- [12] T. Abe *et al.*, “Belle II Technical Design Report,” (2010).
- [13] New electronics tested for Belle II central drift chamber. Feature Story, KEK, Japan, <http://www2.kek.jp/proffice/archives/feature/2010/BelleIICDCDesign.html>.
- [14] M. Nakao, T. Higuchi, R. Itoh, and S. Y. Suzuki, “Data acquisition system for belle II,” *Journal of Instrumentation* **5**, C12004–C12004 (2010).
- [15] J. Beacham, C. Burrage, D. Curtin, A. D. Roeck, J. Evans, J. L. Feng, C. Gatto, S. Gninenko, A. Hartin, I. Irastorza, J. Jaeckel, K. Jungmann, K. Kirch, F. Kling, S. Knapen, M. Lamont, G. Lanfranchi, C. Lazzeroni, A. Lindner, F. Martinez-Vidal, M. Moulson, N. Neri, M. Papucci, I. Pedraza, K. Petridis, M. Pospelov, A. Rozanov, G. Ruoso, P. Schuster, Y. Semertzidis, T. Spadaro, C. Vallée, and G. Wilkinson, “Physics beyond colliders at CERN: beyond the standard model working group report,” *Journal of Physics G: Nuclear and Particle Physics* **47**, 010501 (2019).
- [16] B. Abi *et al.*, “Measurement of the Positive Muon Anomalous Magnetic Moment to 0.46 ppm,” *Phys. Rev. Lett.* **126**, 141801 (2021).

- [17] B. Batell, N. Lange, D. McKeen, M. Pospelov, and A. Ritz, “Muon anomalous magnetic moment through the leptonic higgs portal,” *Phys. Rev. D* **95**, 075003 (2017).
- [18] J. P. Lees *et al.*, “Search for a Dark Leptophilic Scalar in e^+e^- Collisions,” *Phys. Rev. Lett.* **125**, 181801 (2020).
- [19] J. Alwall, R. Frederix, S. Frixione *et al.*, “The automated computation of tree-level and next-to-leading order differential cross sections, and their matching to parton shower simulations,” *JHEP* **07**, 079 (2014).
- [20] Q. Li and Q.-S. Yan, “Initial State Radiation Simulation with MadGraph,” (2018).
- [21] Q. Li and Q.-S. Yan, “Mgizr plugin for isr simulation in madgraph,” GitHub (2018).
- [22] S. Jadach, B. F. L. Ward, and Z. Was, “The Precision Monte Carlo event generator K K for two fermion final states in e^+e^- collisions,” *Comput. Phys. Commun.* **130**, 260–325 (2000).
- [23] E. Barberio and Z. Was, “PHOTOS: A Universal Monte Carlo for QED radiative corrections. Version 2.0,” *Comput. Phys. Commun.* **79**, 291–308 (1994).
- [24] S. Jadach, Z. Was, R. Decker, and J. H. Kuhn, “The tau decay library TAUOLA: Version 2.4,” *Comput. Phys. Commun.* **76**, 361–380 (1993).
- [25] R. Mertig, M. Böhm, and A. Denner, “Feyn calc - computer-algebraic calculation of feynman amplitudes,” *Computer Physics Communications* **64**, 345–359 (1991).
- [26] W. R. Inc., “Mathematica,” Champaign, IL, 2022.

- [27] S. Banerjee, D. Biswas, T. Przedzinski, and Z. Was, “Monte Carlo Event Generator updates, for τ pair events at Belle II energies,” in “16th International Workshop on Tau Lepton Physics ,” (2021).
- [28] K. Chilikin, “Belle mc generation using basf2,” B2BII meeting (2021).
- [29] K. Akai, N. Akasaka, A. Enomoto, J. Flanagan, H. Fukuma, Y. Funakoshi, K. Furukawa, T. Furuya, J. Haba, S. Hiramatsu, K. Hosoyama, T. Ieiri, N. Iida, H. Ikeda, S. Kamada, T. Kamitani, S. Kato, M. Kikuchi, E. Kikutani, H. Koiso, S. Kurokawa, M. Masuzawa, T. Matsumoto, T. Mimashi, T. Mitsuhashi, T. Nakamura, Y. Ogawa, K. Ohmi, Y. Ohnishi, S. Ohsawa, N. Ohuchi, K. Oide, E. Perevedentsev, K. Satoh, M. Suetake, Y. Suetsugu, T. Suwada, M. Tawada, M. Tejima, M. Tobiyama, S. Uno, Y. Wu, N. Yamamoto, M. Yoshida, M. Yoshioka, S. Yoshimoto, and F. Zimmermann, “Commissioning of kekb,” Nuclear Instruments and Methods in Physics Research Section A: Accelerators, Spectrometers, Detectors and Associated Equipment **499**, 191–227 (2003). KEK-B: The KEK B-factory.
- [30] A. Abashian *et al.*, “The Belle Detector,” Nucl. Instrum. Meth. A **479**, 117–232 (2002).
- [31] S. Banerjee, B. Pietrzyk, J. M. Roney, and Z. Was, “Tau and muon pair production cross-sections in electron-positron annihilations at $s^{*(1/2)} = 10.58\text{-GeV}$,” Phys. Rev. D **77**, 054012 (2008).
- [32] D. J. Lange, “The evtgen particle decay simulation package,” Nuclear Instruments and Methods in Physics Research Section A: Accelerators, Spectrometers, Detectors and Associated Equipment **462**, 152–155 (2001). BEAUTY2000, Proceedings of the 7th Int. Conf. on B-Physics at Hadron Machines.

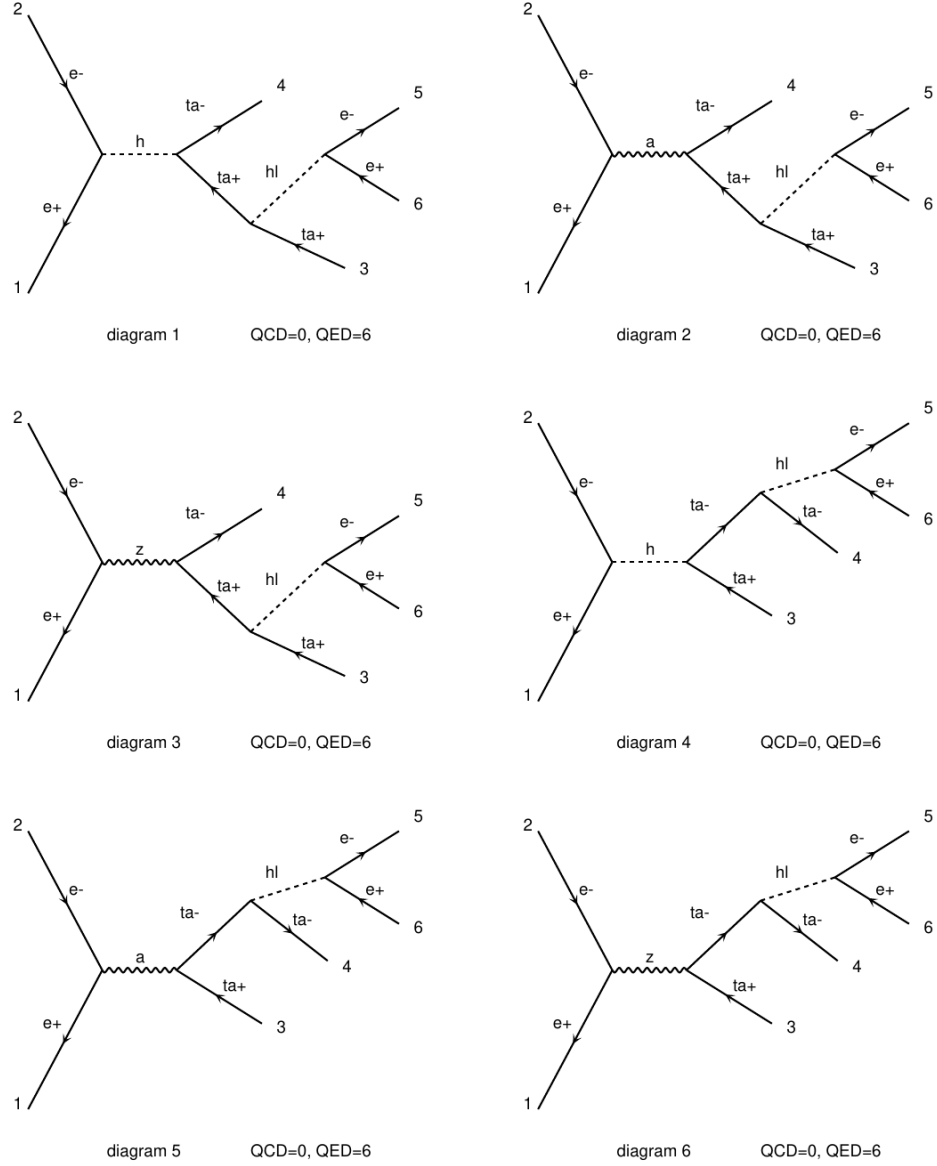
- [33] S. Jadach, E. Richter-Was, B. Ward, and Z. Was, “Monte carlo program bhlumi 2.01 for bhabha scattering at low angles with yennie-frautschi-suura exponentiation,” *Computer Physics Communications* **70**, 305–344 (1992).
- [34] F. Berends, P. Daverveldt, and R. Kleiss, “Monte carlo simulation of two-photon processes: Ii: Complete lowest order calculations for four-lepton production processes in electron-positron collisions,” *Computer Physics Communications* **40**, 285–307 (1986).
- [35] F. Pedregosa, G. Varoquaux, A. Gramfort *et al.*, “Scikit-learn: Machine learning in Python,” *Journal of Machine Learning Research* **12**, 2825–2830 (2011).
- [36] <https://belle.kek.jp/group/ecl/private/lum/lum6new.html>.
- [37] https://belle.kek.jp/secured/belle.note/gn1165/BN1165_v1.pdf.
- [38] T. Junk, “Confidence level computation for combining searches with small statistics,” *Nucl. Instrum. Meth. A* **434**, 435–443 (1999).
- [39] A. L. Read, “Presentation of search results: The CL(s) technique,” *J. Phys. G* **28**, 2693–2704 (2002).
- [40] G. Cowan, K. Cranmer, E. Gross, and O. Vitells, “Asymptotic formulae for likelihood-based tests of new physics,” *Eur. Phys. J. C* **71**, 1554 (2011). [Erratum: *Eur.Phys.J.C* 73, 2501 (2013)].
- [41] L. Heinrich, M. Feickert, and G. Stark, “pyhf: v0.6.3,” <https://github.com/scikit-hep/pyhf/releases/tag/v0.6.3>.
- [42] L. Heinrich, M. Feickert, G. Stark, and K. Cranmer, “pyhf: pure-python implementation of histfactory statistical models,” *Journal of Open Source Software* **6**, 2823 (2021).

- [43] K. Cranmer, G. Lewis, L. Moneta, A. Shibata, and W. Verkerke, “HistFactory: A tool for creating statistical models for use with RooFit and RooStats,” Tech. rep., New York U., New York (2012).
- [44] J. Bradbury, R. Frostig, P. Hawkins, M. J. Johnson, C. Leary, D. Maclaurin, G. Necula, A. Paszke, J. VanderPlas, S. Wanderman-Milne, and Q. Zhang, “JAX: composable transformations of Python+NumPy programs,” (2018).
- [45] J. P. Lees *et al.*, “Search for a muonic dark force at BABAR,” Phys. Rev. D **94**, 011102 (2016).
- [46] J. D. Bjorken, S. Ecklund, W. R. Nelson, A. Abashian, C. Church, B. Lu, L. W. Mo, T. A. Nunamaker, and P. Rassmann, “Search for Neutral Metastable Penetrating Particles Produced in the SLAC Beam Dump,” Phys. Rev. D **38**, 3375 (1988).
- [47] M. Davier and H. Nguyen Ngoc, “An Unambiguous Search for a Light Higgs Boson,” Phys. Lett. B **229**, 150–155 (1989).
- [48] Y.-S. Liu, D. McKeen, and G. A. Miller, “Electrophobic Scalar Boson and Muonic Puzzles,” Phys. Rev. Lett. **117**, 101801 (2016).
- [49] J. Liu, N. McGinnis, C. E. M. Wagner, and X.-P. Wang, “A light scalar explanation of $(g - 2)_\mu$ and the KOTO anomaly,” JHEP **04**, 197 (2020).

APPENDIX A: FEYNMAN DIAGRAMS OF THE SIGNAL PROCESS

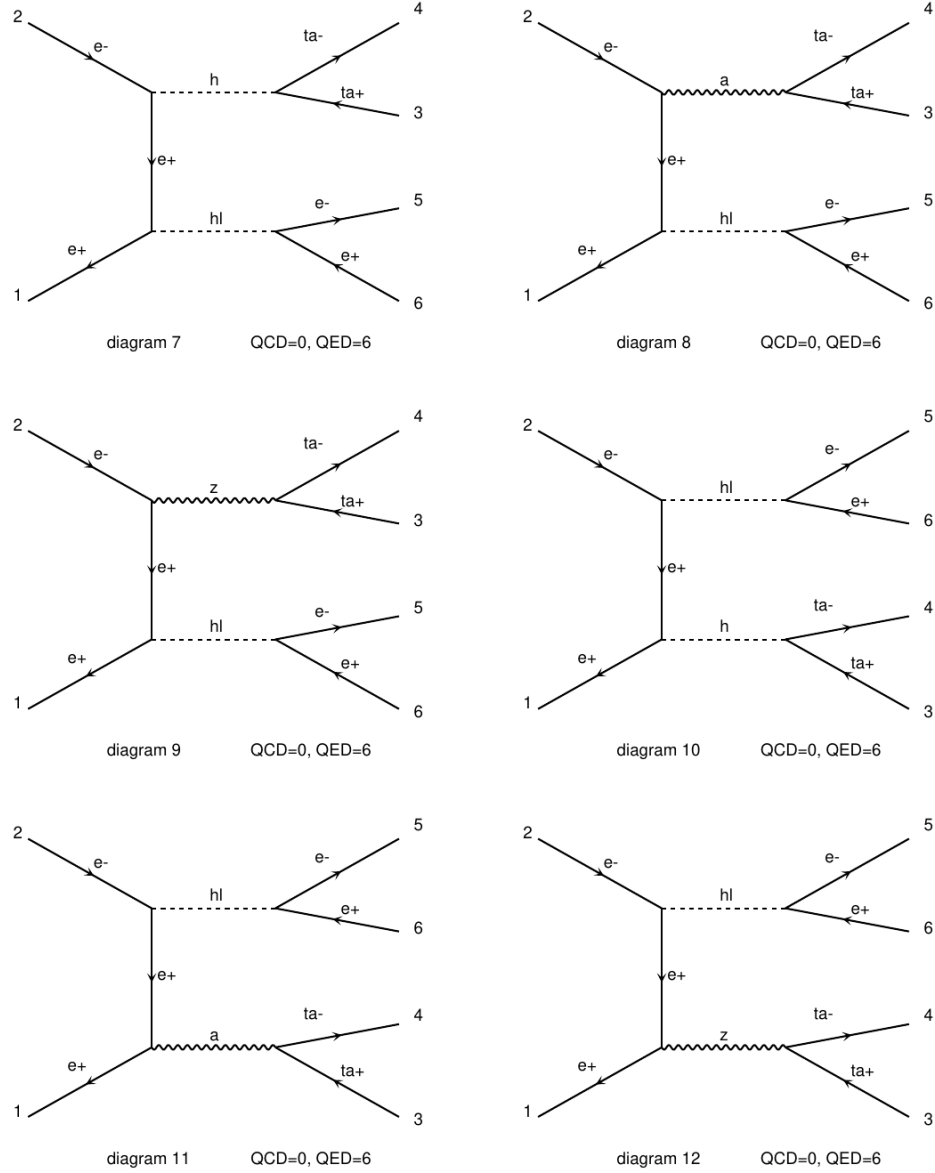
For $e^+e^- \rightarrow \tau^+\tau^-\phi_L, \phi_L \rightarrow e^+e^-$ channel

Feynman diagrams, produced by MadGraph 5 for $e^+e^- \rightarrow \tau^+\tau^-\phi_L, \phi_L \rightarrow e^+e^-$ are shown in Fig. 1 and Fig. 2.



Diagrams made by MadGraph5_aMC@NLO

Figure 1. Feynman diagrams labelled as **diagram 1** through **diagram 6** for $e^+e^- \rightarrow \tau^+\tau^-\phi_L, \phi_L \rightarrow e^+e^-$ process.

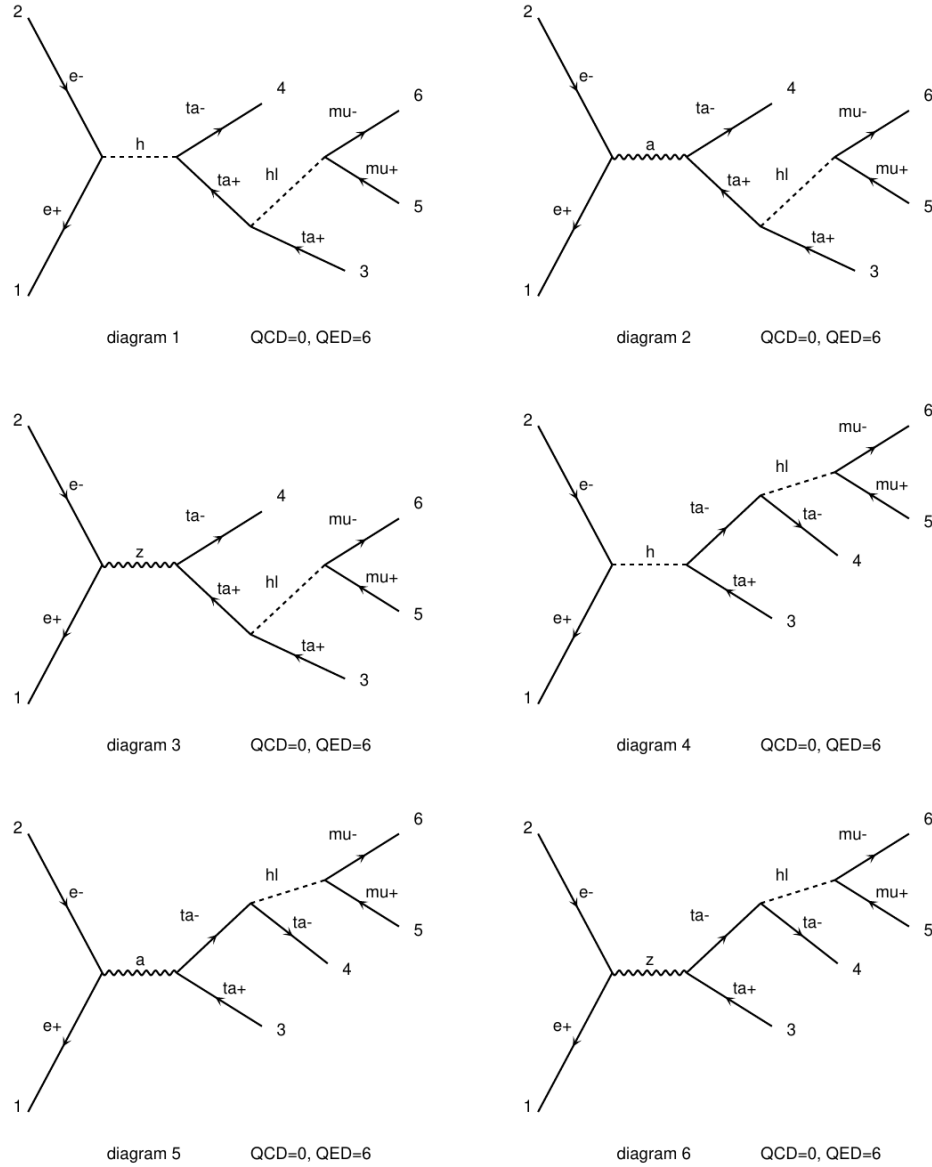


Diagrams made by MadGraph5_aMC@NLO

Figure 2. Feynman diagrams labelled as **diagram 7** through **diagram 12** for $e^+e^- \rightarrow \tau^+\tau^-\phi_L$, $\phi_L \rightarrow e^+e^-$ process.

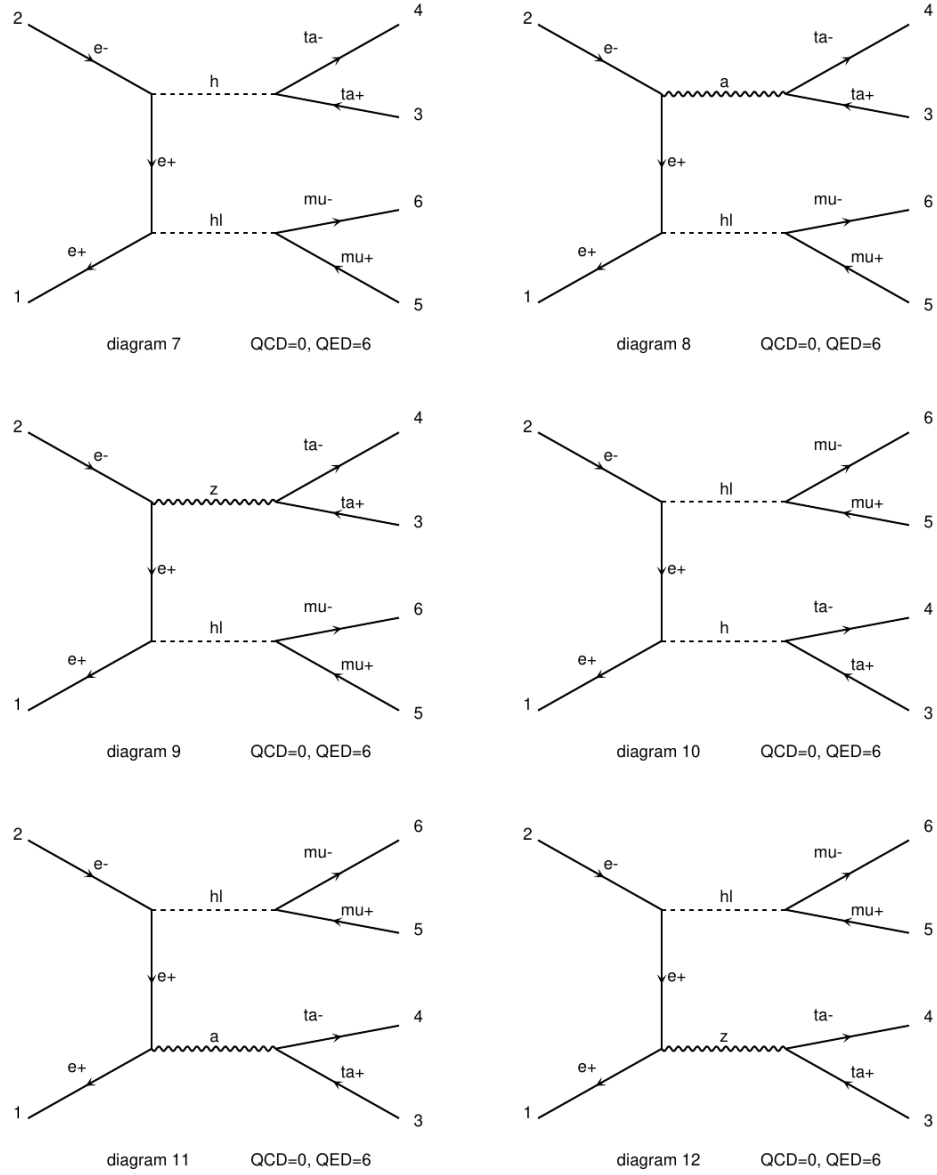
For $e^+e^- \rightarrow \tau^+\tau^-\phi_L$, $\phi_L \rightarrow \mu^+\mu^-$ channel

Feynman diagrams, produced by MadGraph 5 for $e^+e^- \rightarrow \tau^+\tau^-\phi_L$, $\phi_L \rightarrow \mu^+\mu^-$ are shown in Fig. 3 and Fig. 4.



Diagrams made by MadGraph5_aMC@NLO

Figure 3. Feynman diagrams labelled as **diagram 1** through **diagram 6** for $e^+e^- \rightarrow \tau^+\tau^-\phi_L$, $\phi_L \rightarrow \mu^+\mu^-$ process.



Diagrams made by MadGraph5_aMC@NLO

Figure 4. Feynman diagrams labelled as **diagram 7** through **diagram 12** for $e^+e^- \rightarrow \tau^+\tau^-\phi_L$, $\phi_L \rightarrow \mu^+\mu^-$ process.

APPENDIX B: COMPARISON BETWEEN TWO METHODS OF SELECTING THE ϕ_L CANDIDATE

Comparisons between the two strategies of choosing the ϕ_L candidate are shown in Fig. 5 and Fig. 6.

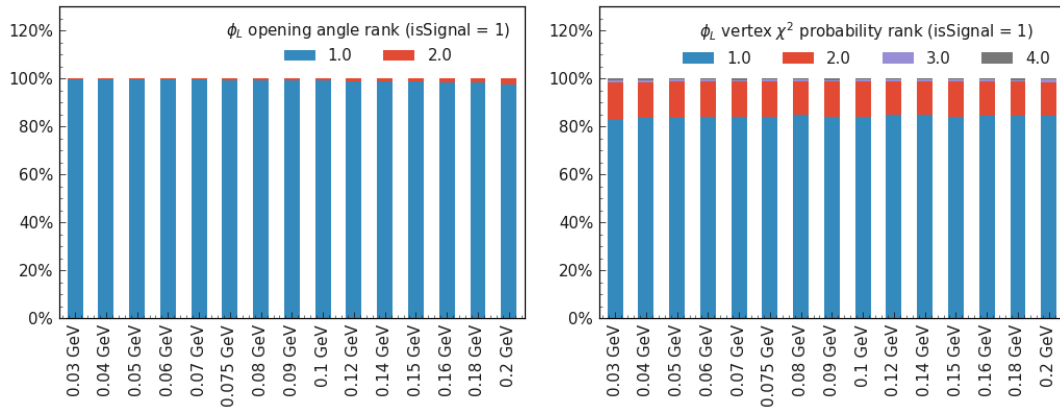


Figure 5. Comparison between two candidate selection strategies for $\phi_L \rightarrow e^+e^-$ channel.

Till 2.5 GeV, the strategy of selecting the candidate with the smallest opening angle works better. For higher ϕ_L mass points, we notice an improvement of at max 7.4% (for 5.5 GeV) if we choose the alternate strategy.

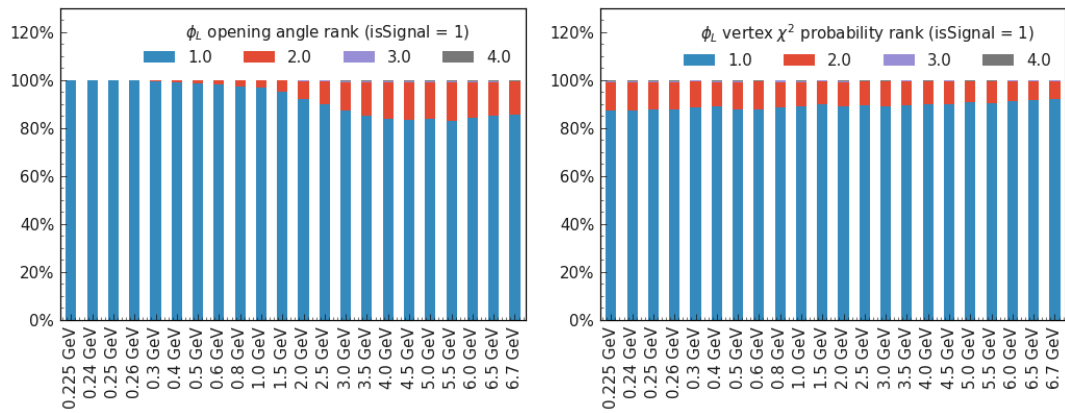


Figure 6. Comparison between two candidate selection strategies for $\phi_L \rightarrow \mu^+\mu^-$ channel.

APPENDIX C: STUDY OF THE PHOTON CONVERSION VERTICES

In the plots of Fig.7, we show the distribution for invariant mass vs transverse distance using the tracks used in our analysis, which have strict requirements that the tracks originate from close to the Interaction Point. It is thus not a surprise anymore that the features of the inner detector were not seen in the distance plot in Fig. 45.

Since the photon conversion vertices are formed inside the detector, they cannot be formed by combining two regular e^+ and e^- tracks with the standard dr and dz cuts. Instead, in BASF, these vertices are directly stored in `V_ee2` table. Since we use `basf2` for our analysis, these vertices from the `V_ee2` table are available to us as a ready-made particle list `gamma:v0mdst`.

For this study, we use the SM taupair sample and use MC truth matching to make sure at least one of the τ^+ or τ^- decays to a ρ^+ or ρ^- meson. The peaks in the distributions of Fig. 8 corresponds to the different layers of the SVD2 detector and in Fig. 9. The distributions of invariant mass vs. transverse distance for these kinds of vertices are shown in the left plot of Fig. 10.

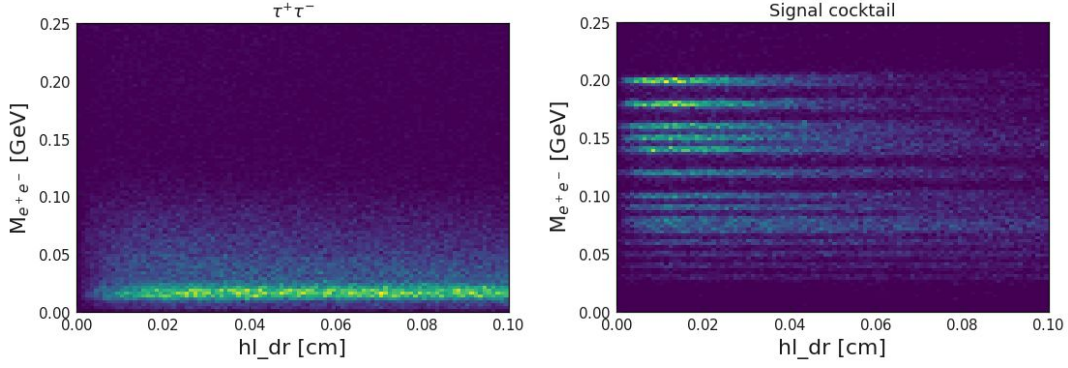


Figure 7. Distributions of e^+e^- invariant mass and transverse distance from IP for SM taupair background and signal.

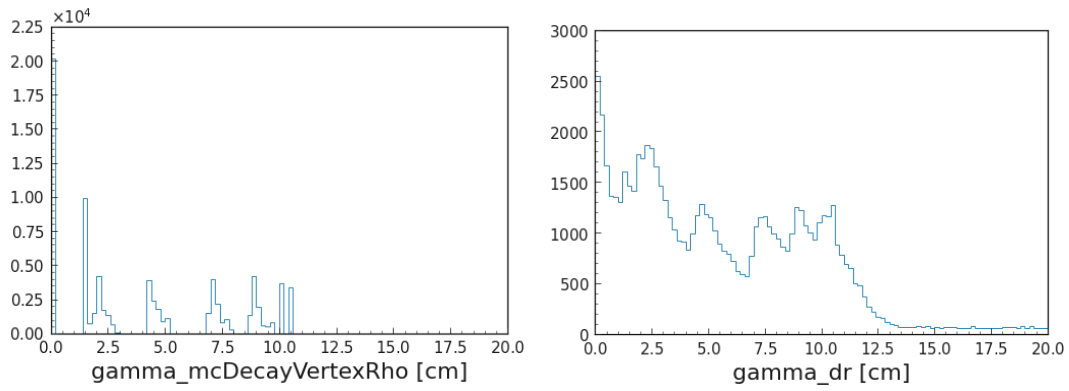


Figure 8. Generator (left) and reconstructed (right) level distributions of the transverse distance of the $\gamma \rightarrow e^+e^-$ vertex from the IP.

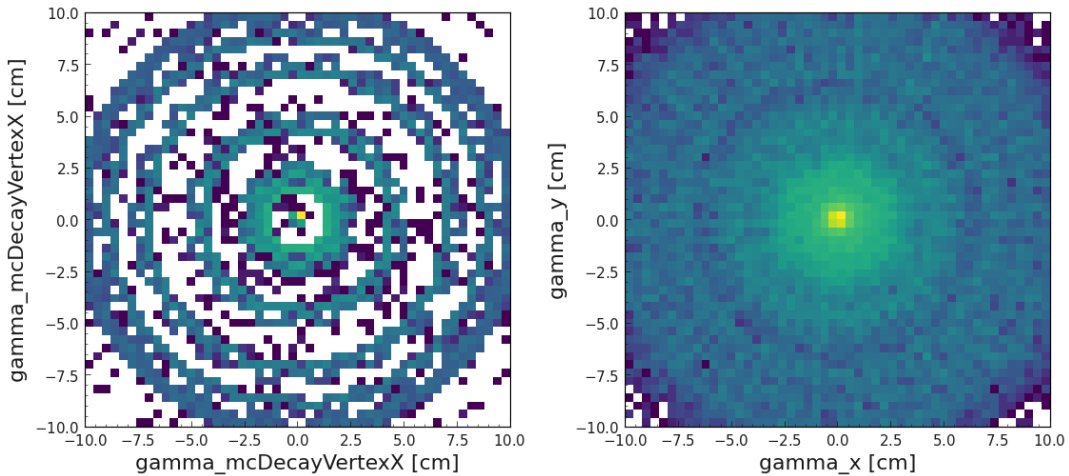


Figure 9. Generator (left) and reconstructed (right) level distributions of the position of the $\gamma \rightarrow e^+e^-$ vertex.

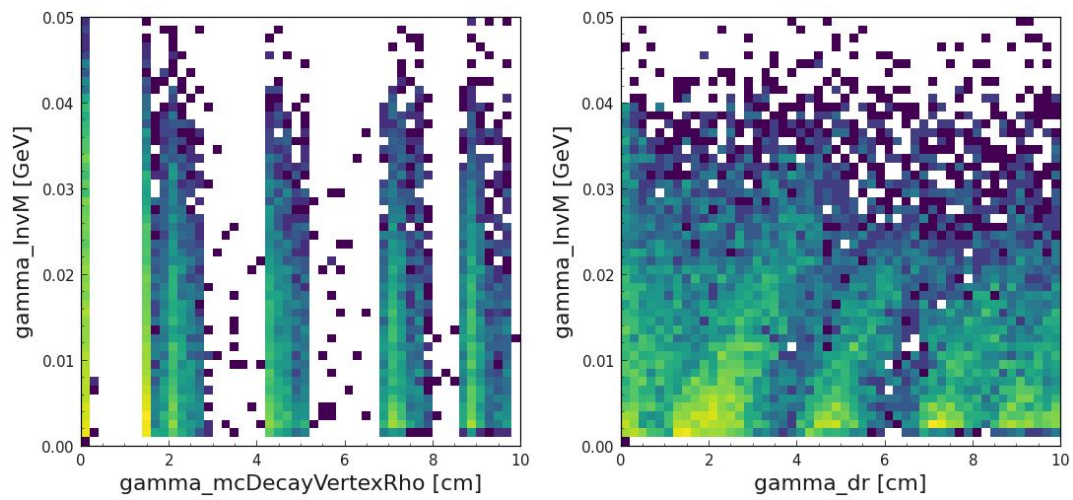


Figure 10. Generator (left) and reconstructed (right) level distributions of the position of the $\gamma \rightarrow e^+e^-$ vertex along with e^+e^- invariant mass.

APPENDIX D: DATA-MC COMPARISON PLOTS FOR BDT INPUT
VARIABLES

For $e^+e^- \rightarrow \tau^+\tau^-\phi_L$, $\phi_L \rightarrow e^+e^-$ channel

Data-MC comparison plots for the BDT input variables in $\phi_L \rightarrow e^+e^-$ channel are shown in Fig. 11- 28.

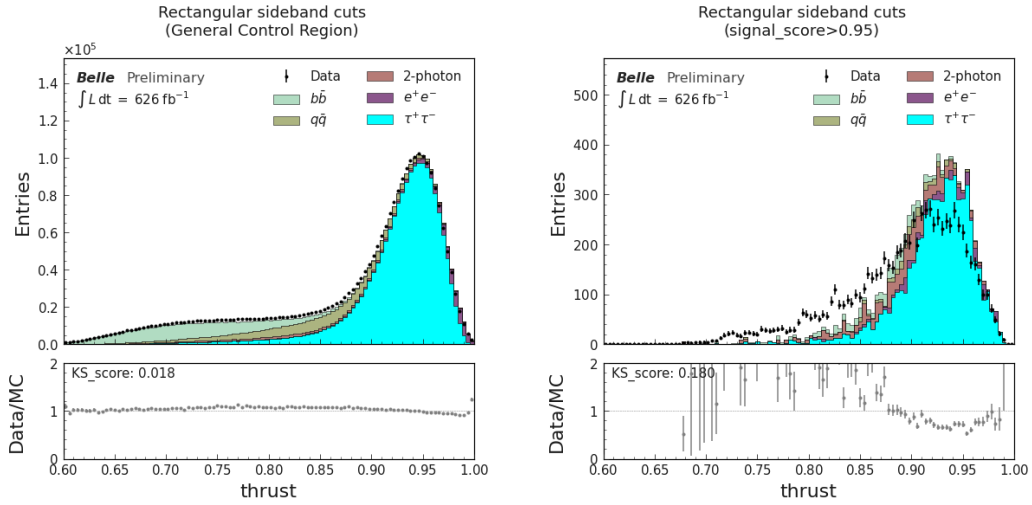


Figure 11. Distribution of a BDT input variable in general control region (left) and signal region (right).

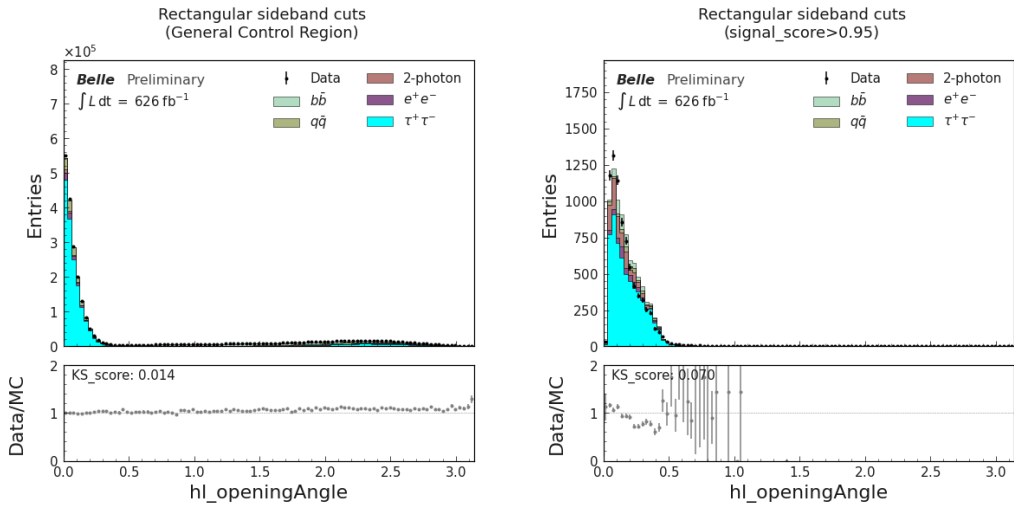


Figure 12. Distribution of a BDT input variable in general control region (left) and signal region (right).

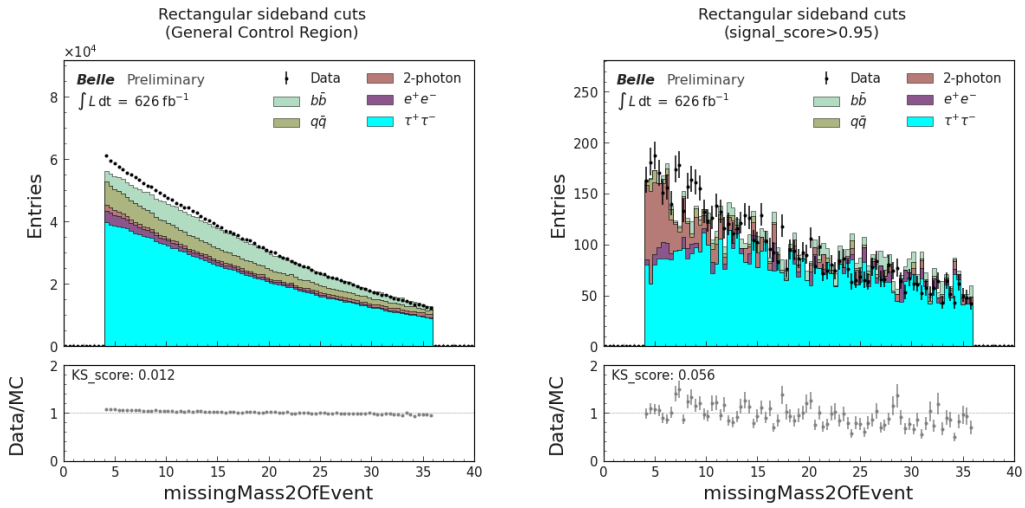


Figure 13. Distribution of a BDT input variable in general control region (left) and signal region (right).

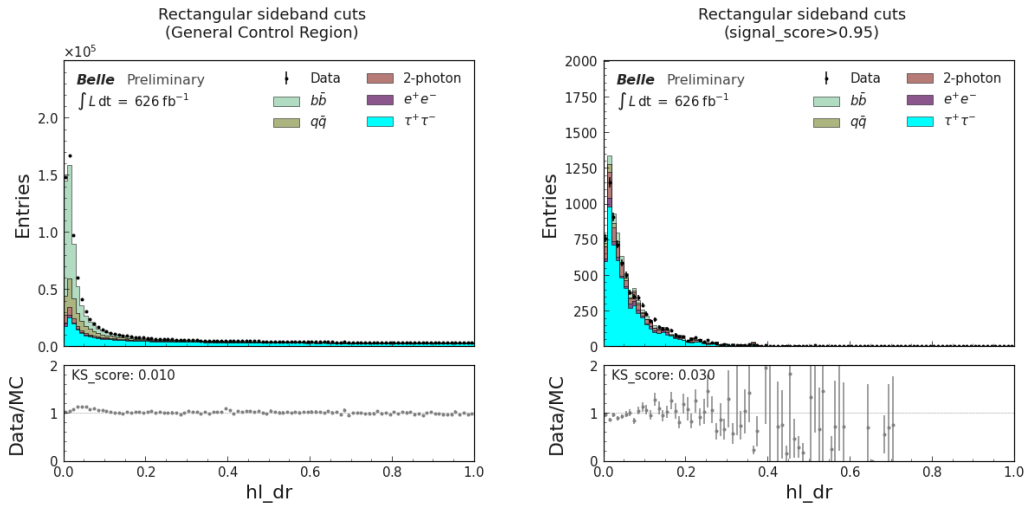


Figure 14. Distribution of a BDT input variable in general control region (left) and signal region (right).

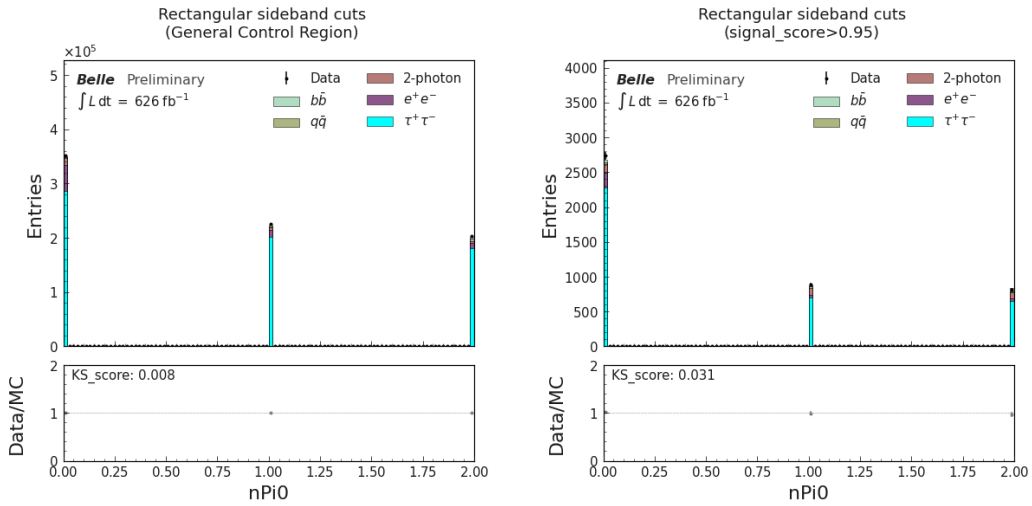


Figure 15. Distribution of a BDT input variable in general control region (left) and signal region (right).

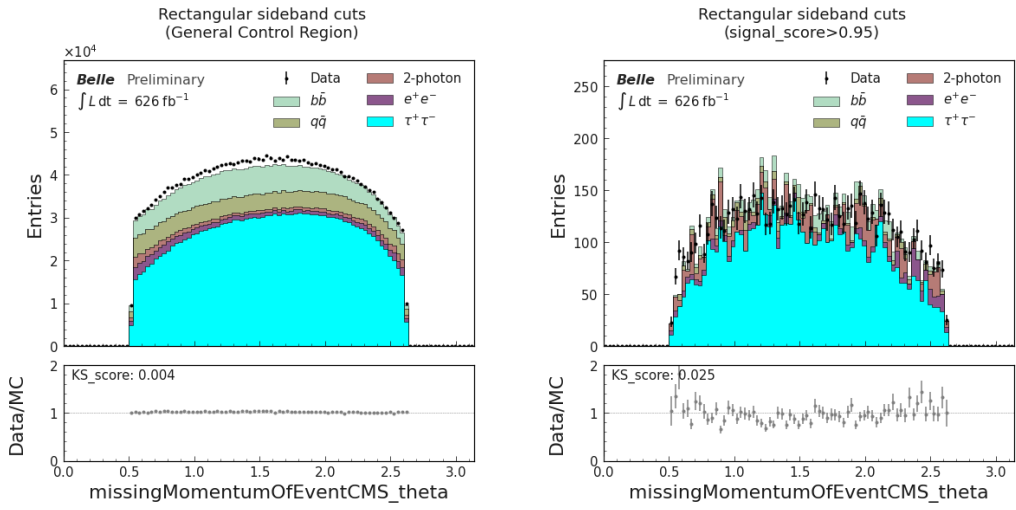


Figure 16. Distribution of a BDT input variable in general control region (left) and signal region (right).

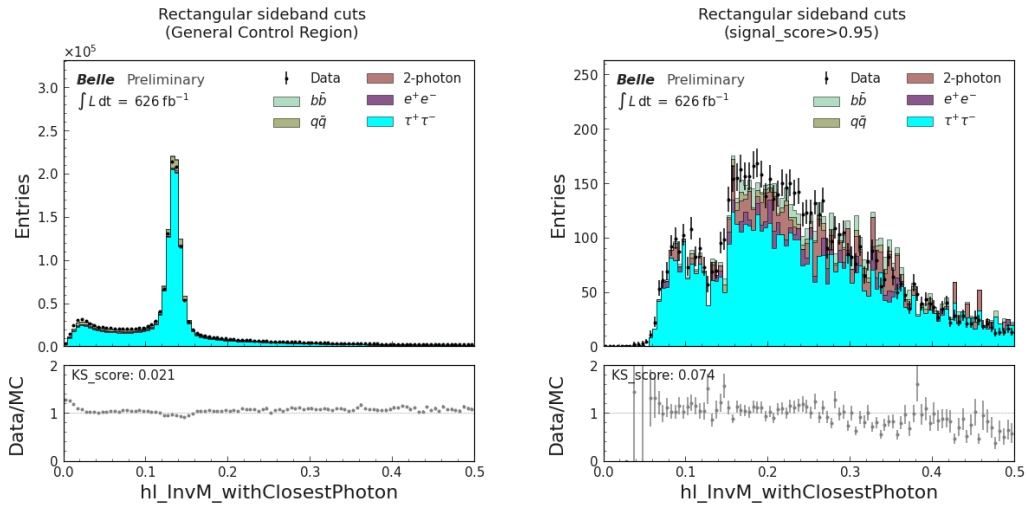


Figure 17. Distribution of a BDT input variable in general control region (left) and signal region (right).

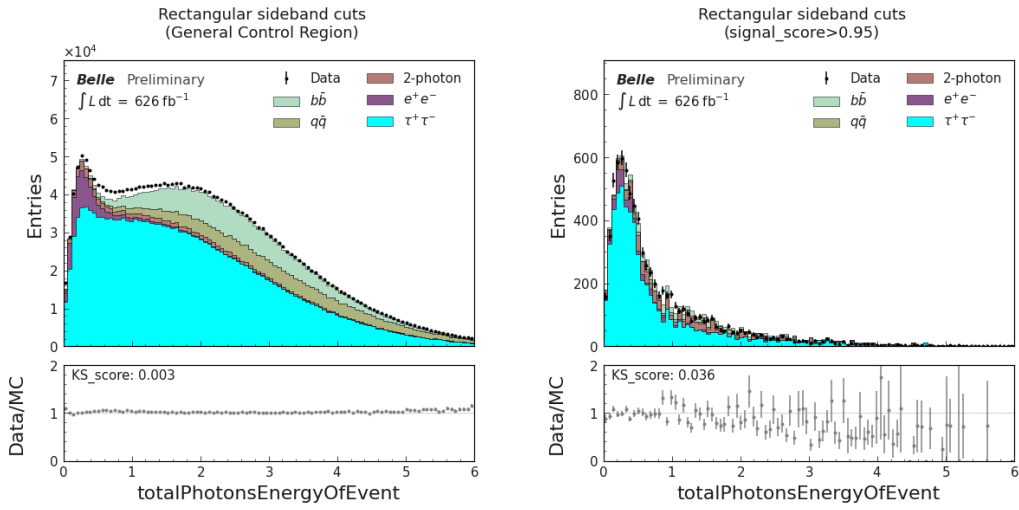


Figure 18. Distribution of a BDT input variable in general control region (left) and signal region (right).

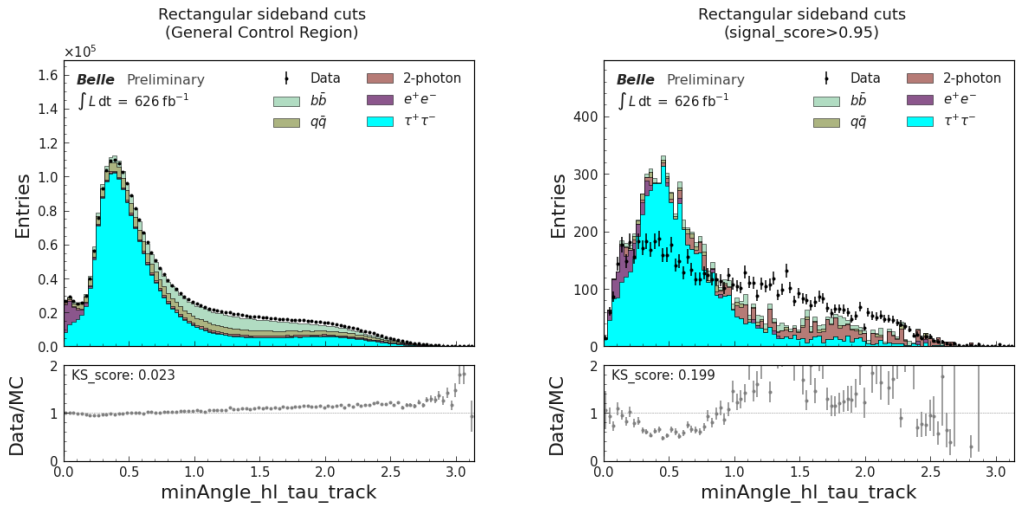


Figure 19. Distribution of a BDT input variable in general control region (left) and signal region (right).

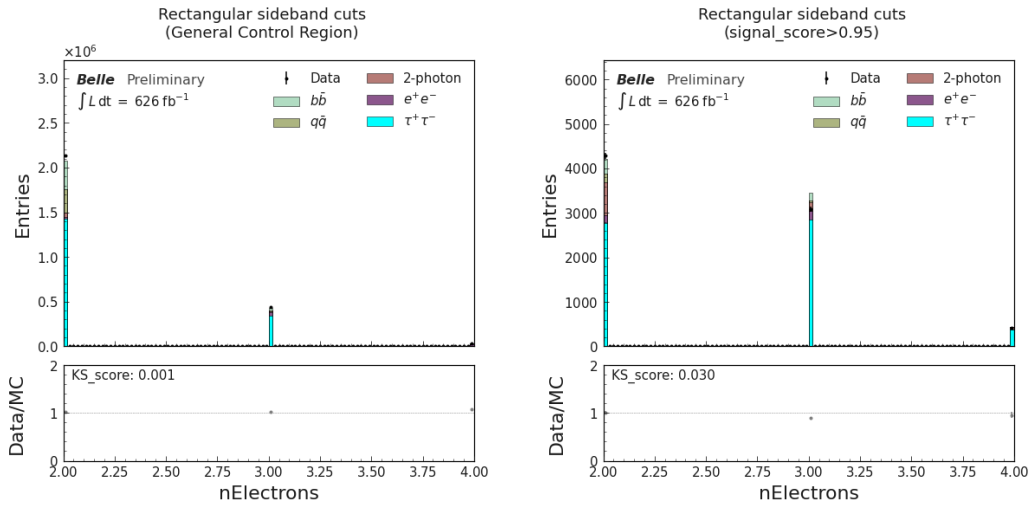


Figure 20. Distribution of a BDT input variable in general control region (left) and signal region (right).

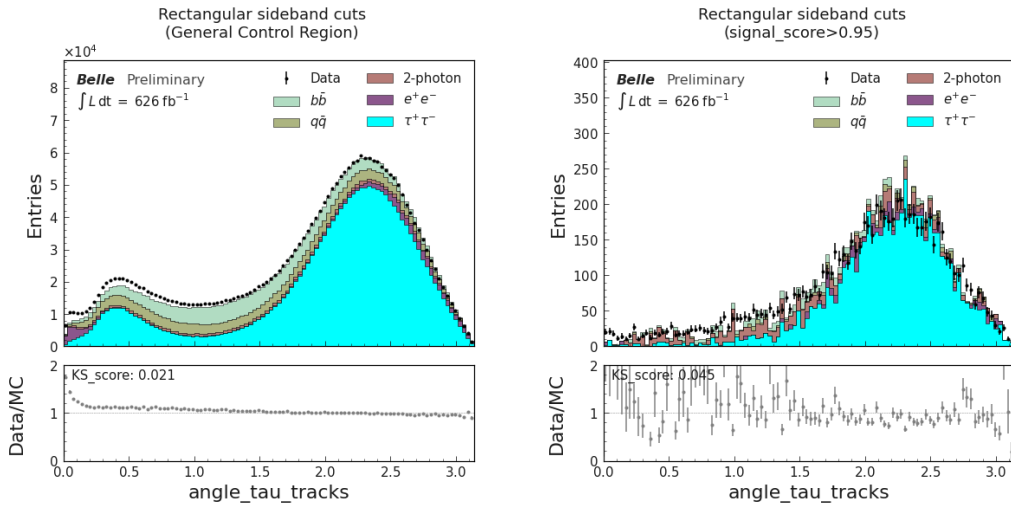


Figure 21. Distribution of a BDT input variable in general control region (left) and signal region (right).

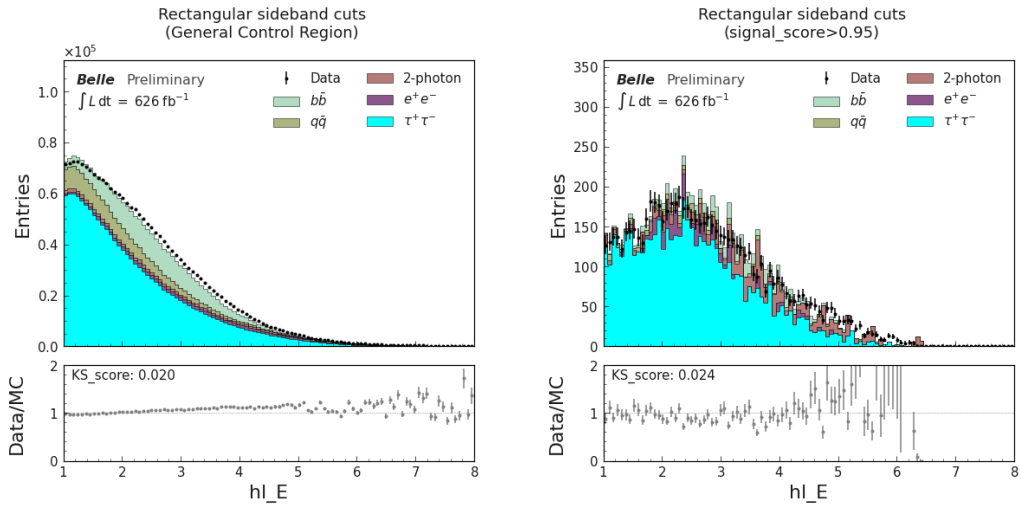


Figure 22. Distribution of a BDT input variable in general control region (left) and signal region (right).

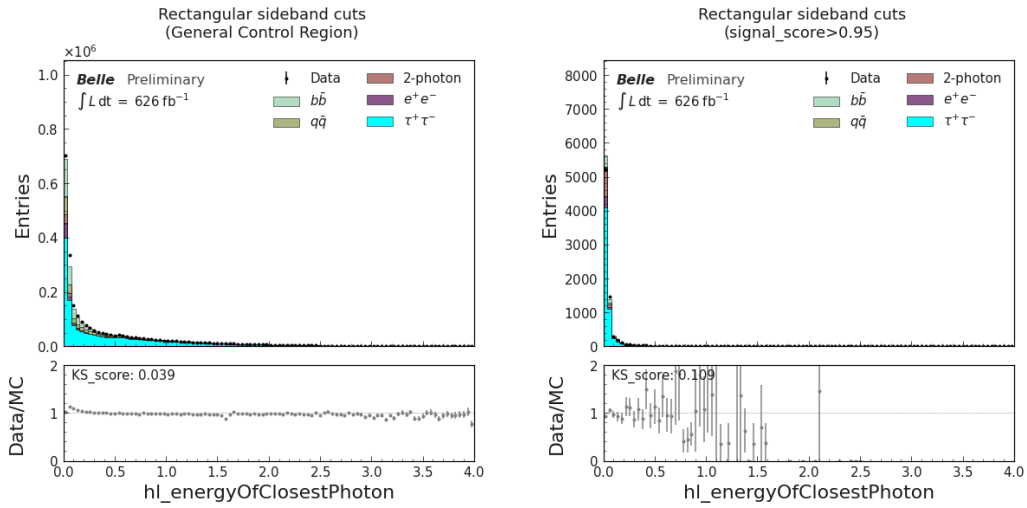


Figure 23. Distribution of a BDT input variable in general control region (left) and signal region (right).

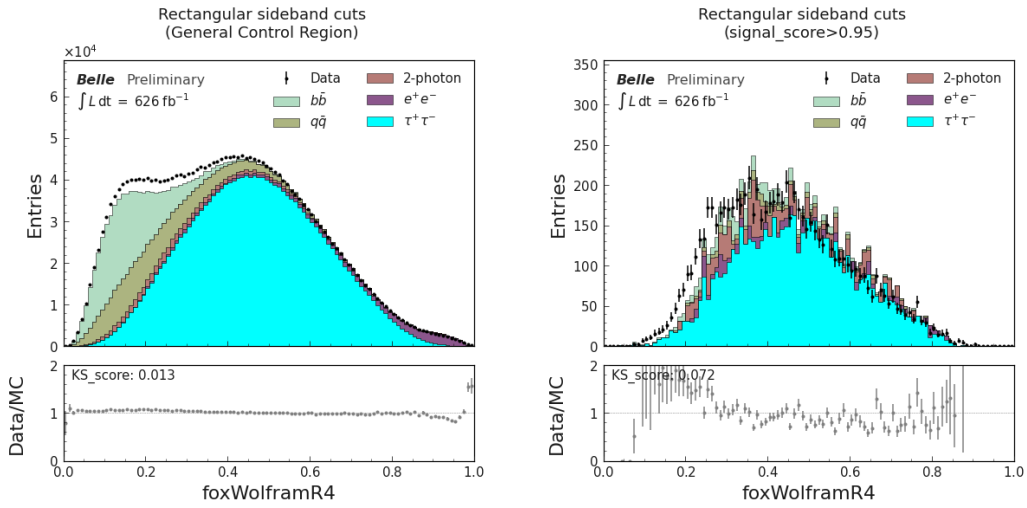


Figure 24. Distribution of a BDT input variable in general control region (left) and signal region (right).

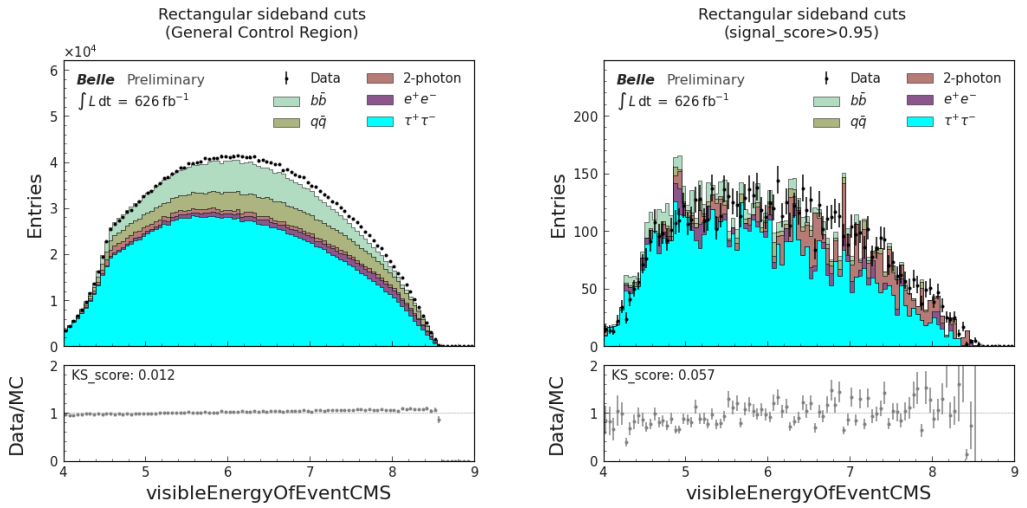


Figure 25. Distribution of a BDT input variable in general control region (left) and signal region (right).

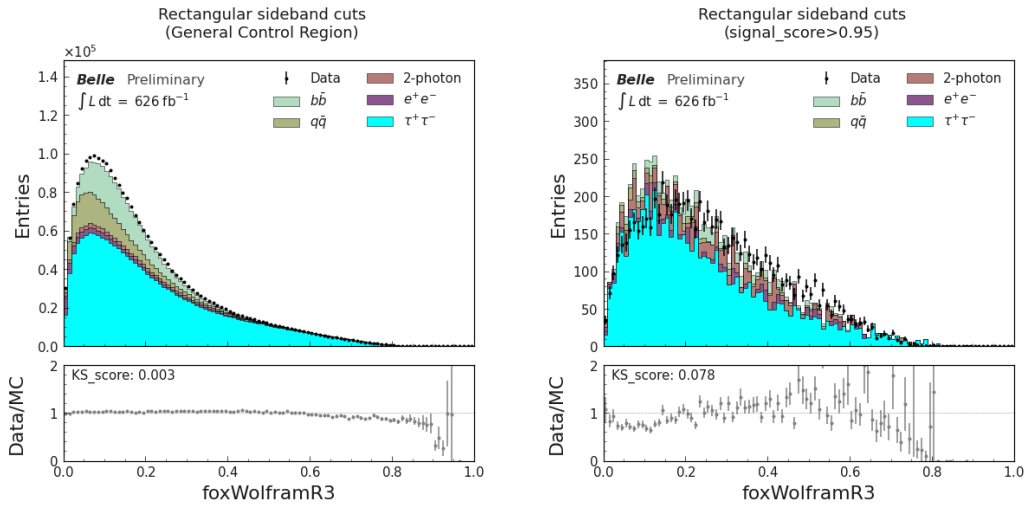


Figure 26. Distribution of a BDT input variable in general control region (left) and signal region (right).

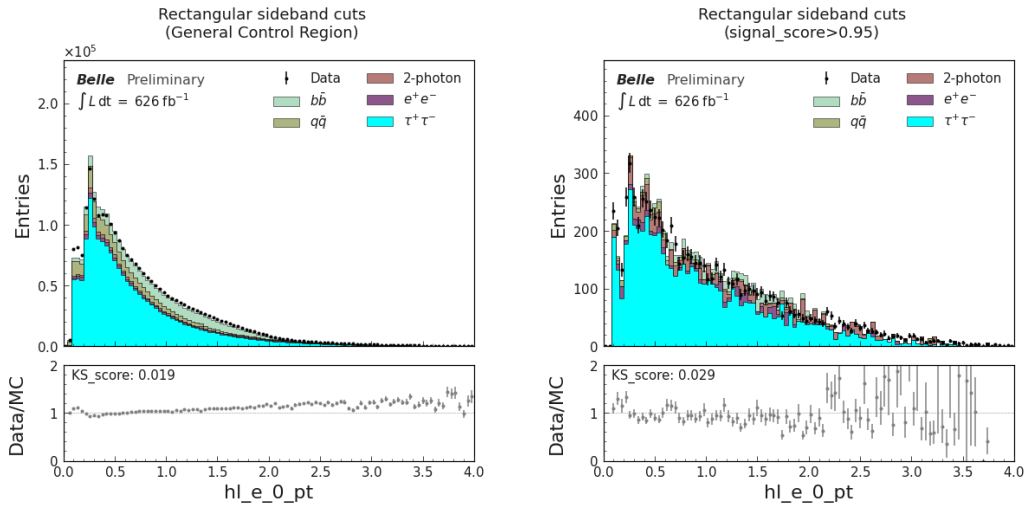


Figure 27. Distribution of a BDT input variable in general control region (left) and signal region (right).

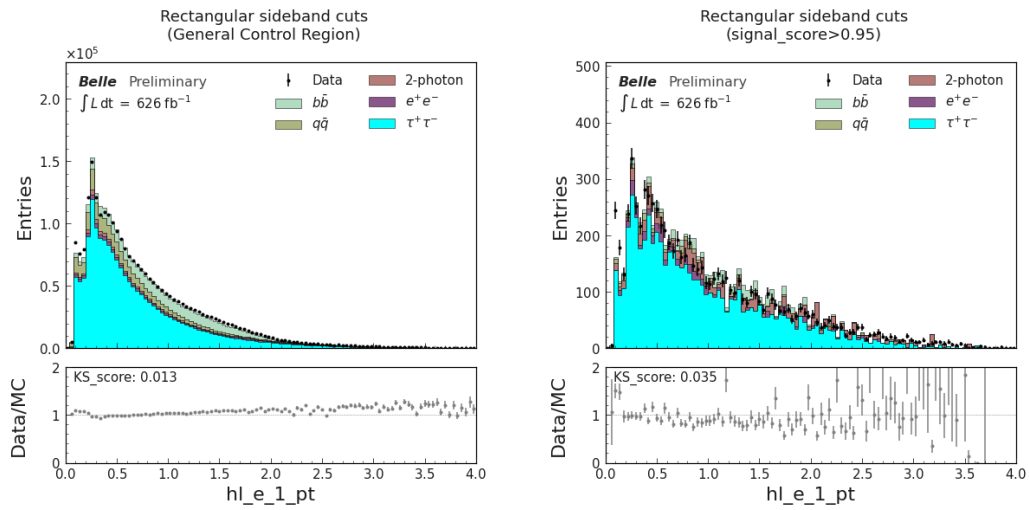


Figure 28. Distribution of a BDT input variable in general control region (left) and signal region (right).

For $e^+e^- \rightarrow \tau^+\tau^-\phi_L$, $\phi_L \rightarrow \mu^+\mu^-$ channel

Data-MC comparison plots for the BDT input variables in $\phi_L \rightarrow \mu^+\mu^-$ channel are shown in Fig. 29- 46.

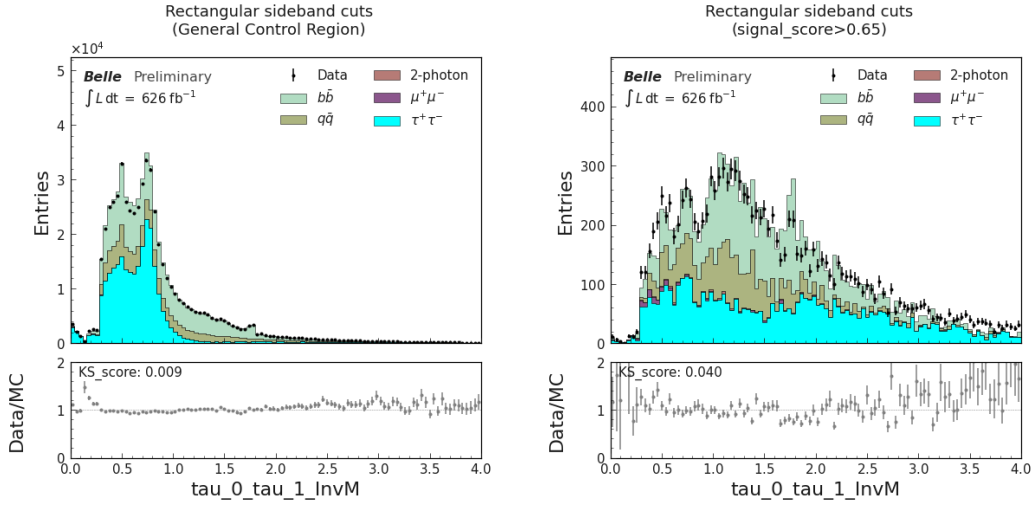


Figure 29. Distribution of a BDT input variable in general control region (left) and signal region (right).

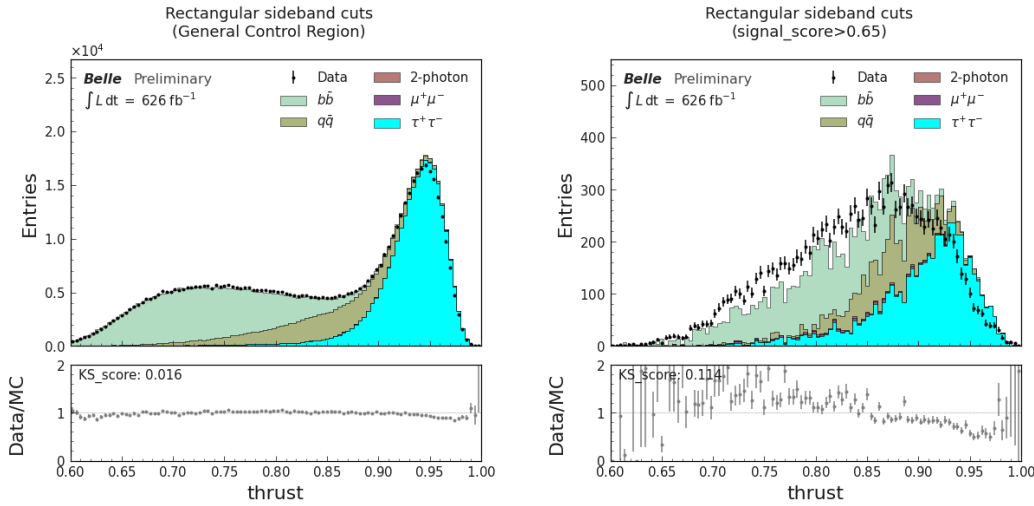


Figure 30. Distribution of a BDT input variable in general control region (left) and signal region (right).

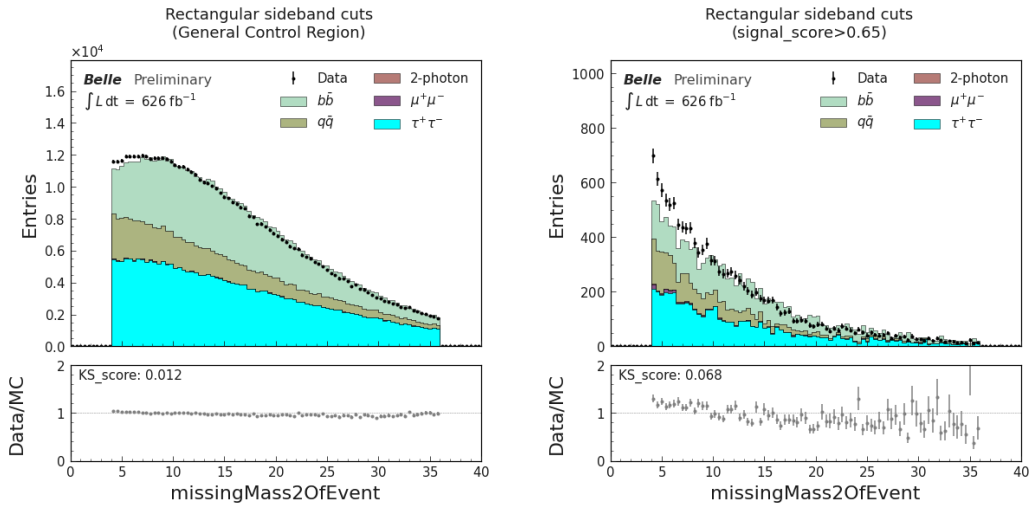


Figure 31. Distribution of a BDT input variable in general control region (left) and signal region (right).

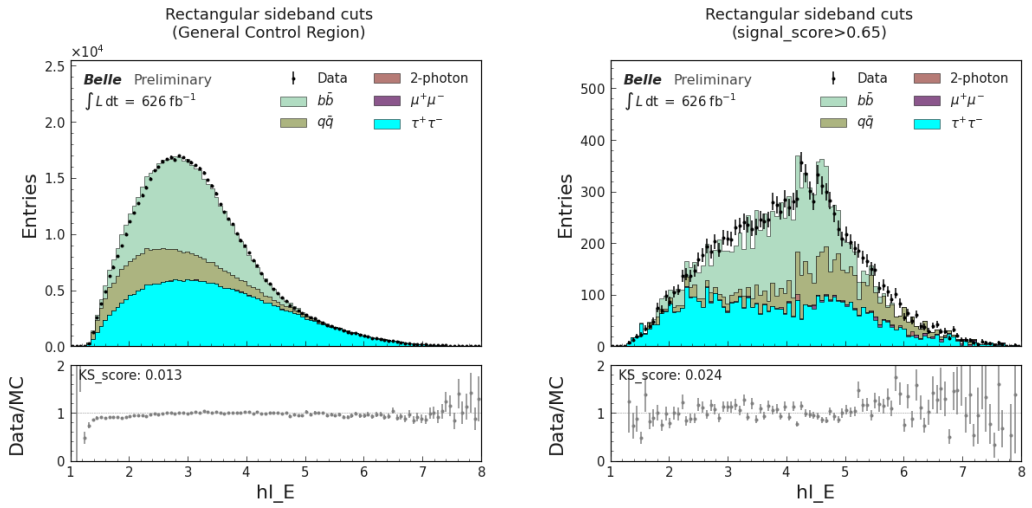


Figure 32. Distribution of a BDT input variable in general control region (left) and signal region (right).

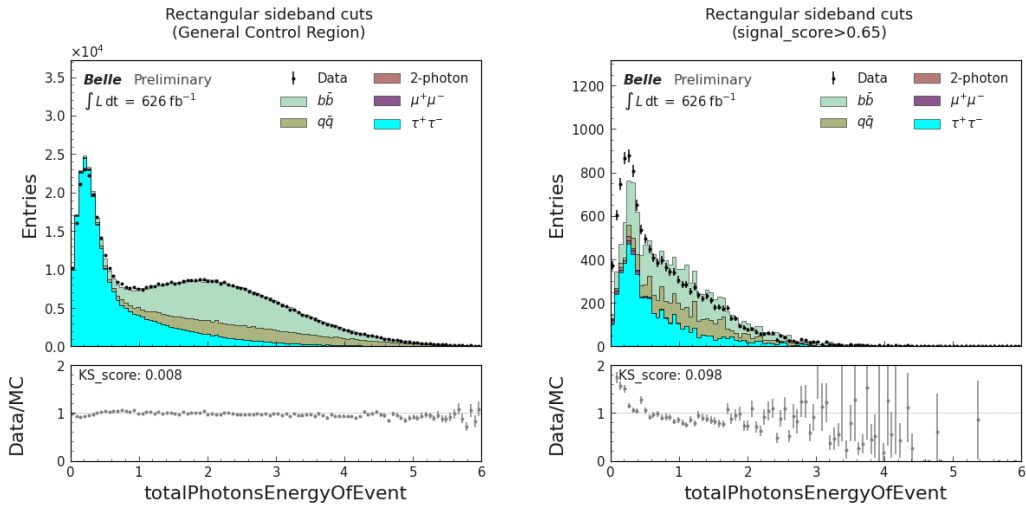


Figure 33. Distribution of a BDT input variable in general control region (left) and signal region (right).

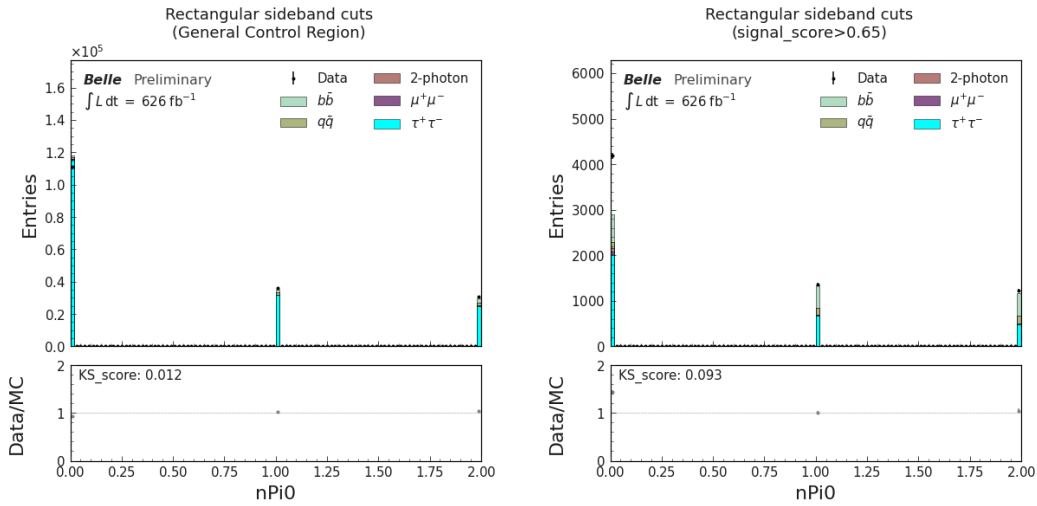


Figure 34. Distribution of a BDT input variable in general control region (left) and signal region (right).

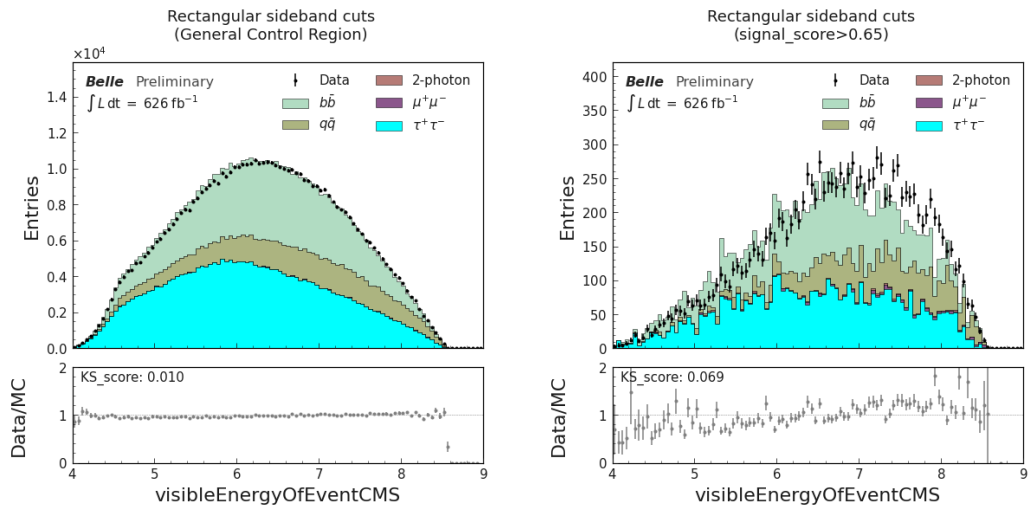


Figure 35. Distribution of a BDT input variable in general control region (left) and signal region (right).

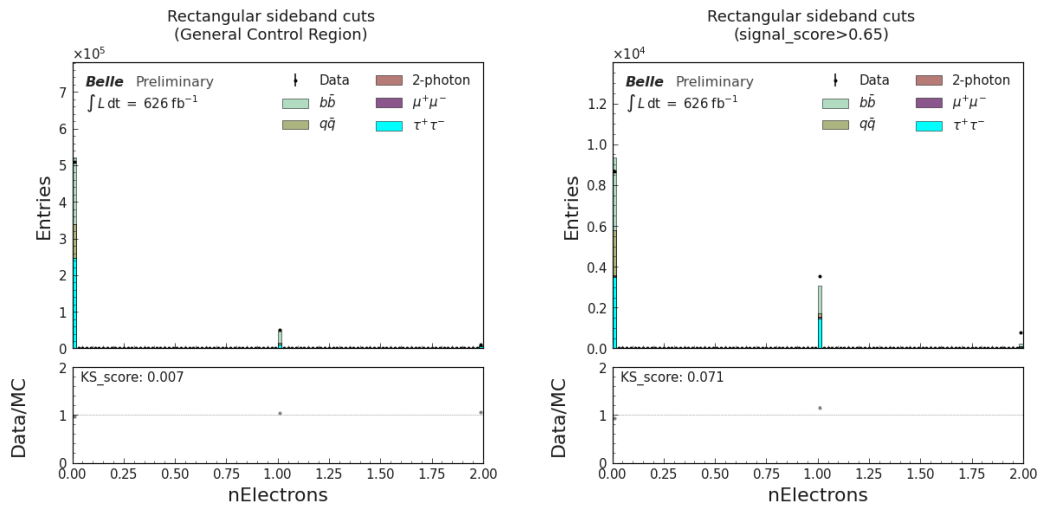


Figure 36. Distribution of a BDT input variable in general control region (left) and signal region (right).

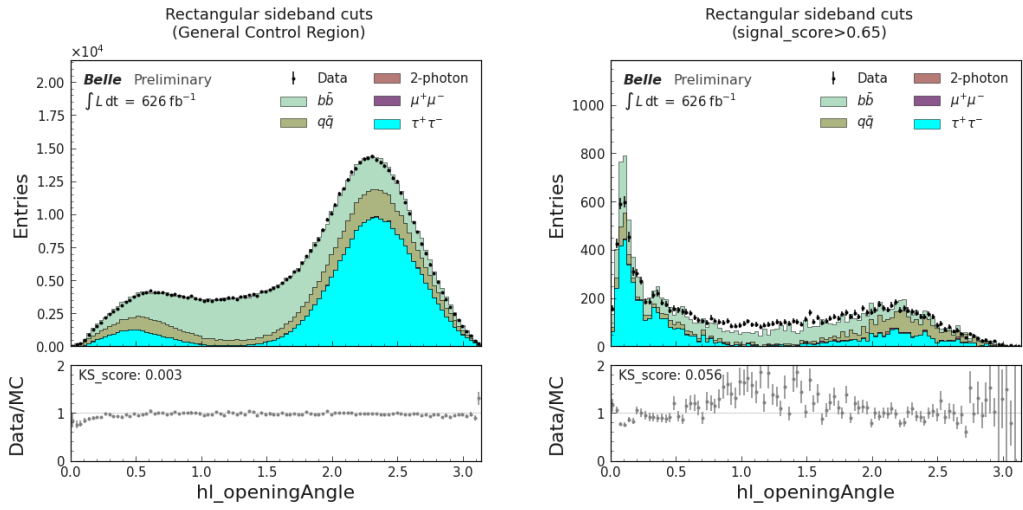


Figure 37. Distribution of a BDT input variable in general control region (left) and signal region (right).

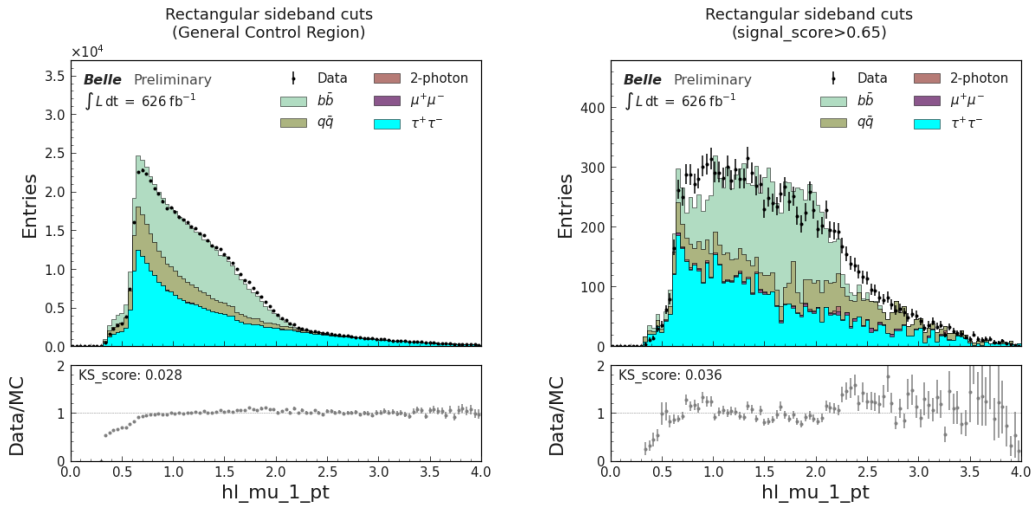


Figure 38. Distribution of a BDT input variable in general control region (left) and signal region (right).

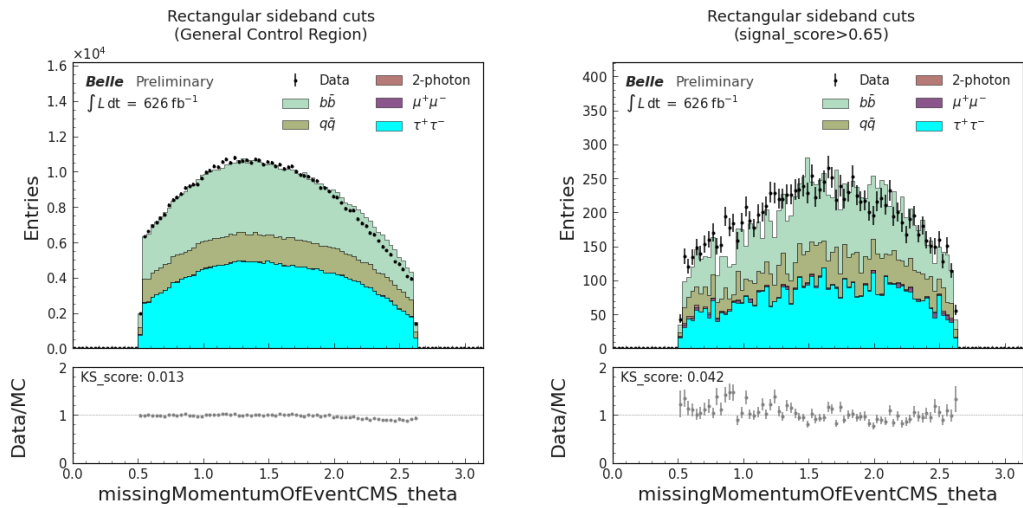


Figure 39. Distribution of a BDT input variable in general control region (left) and signal region (right).

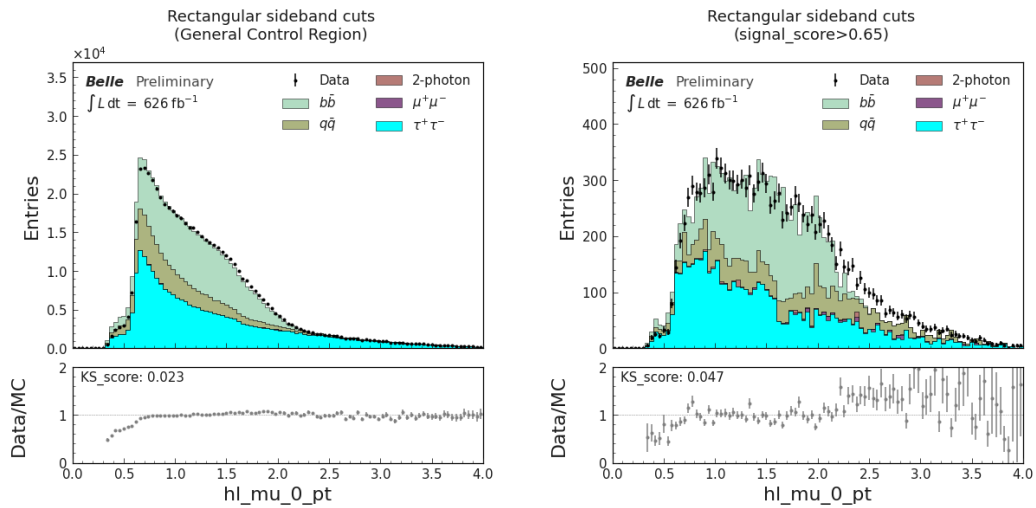


Figure 40. Distribution of a BDT input variable in general control region (left) and signal region (right).

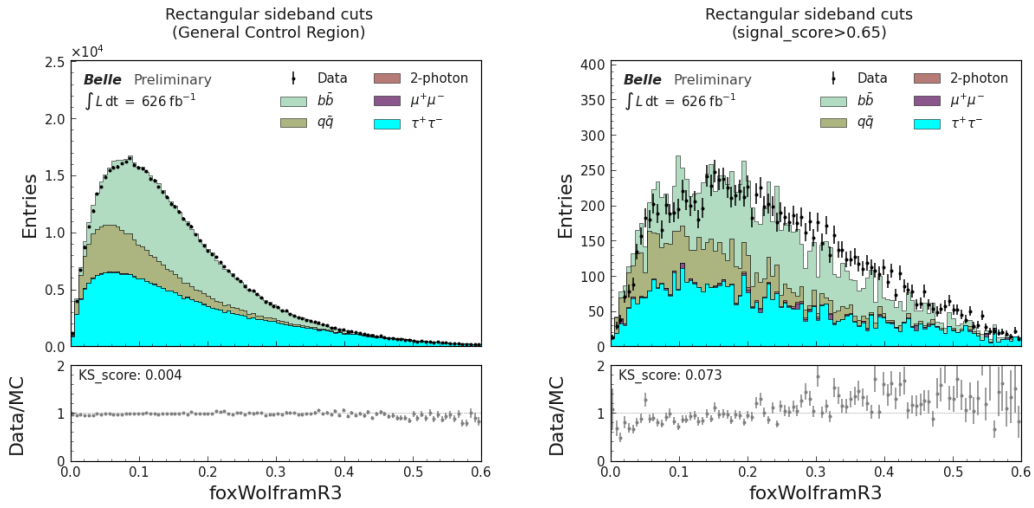


Figure 41. Distribution of a BDT input variable in general control region (left) and signal region (right).

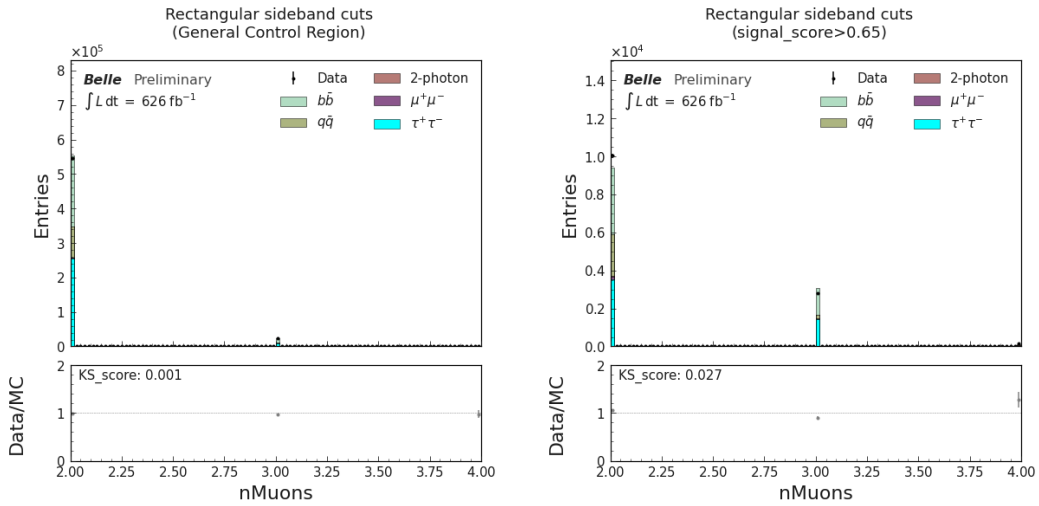


Figure 42. Distribution of a BDT input variable in general control region (left) and signal region (right).

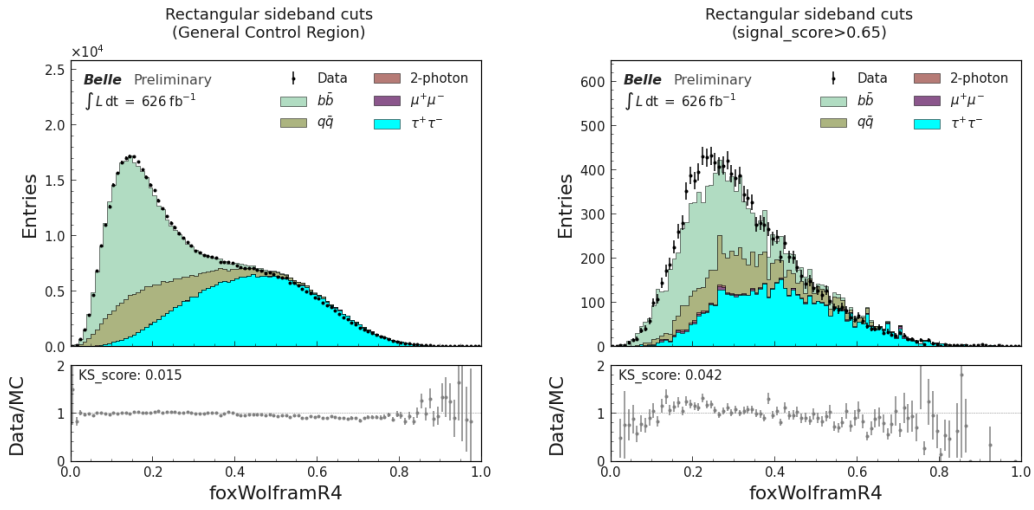


Figure 43. Distribution of a BDT input variable in general control region (left) and signal region (right).

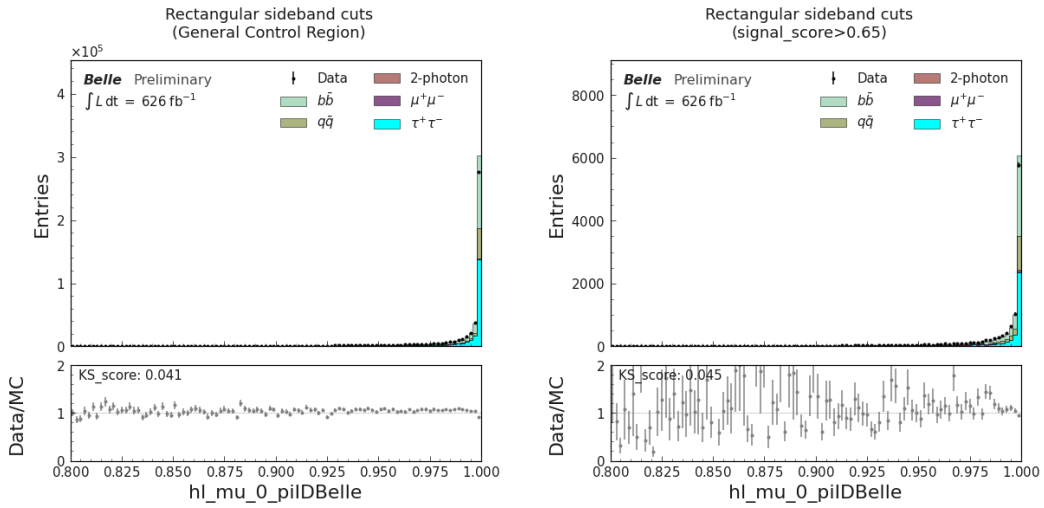


Figure 44. Distribution of a BDT input variable in general control region (left) and signal region (right).

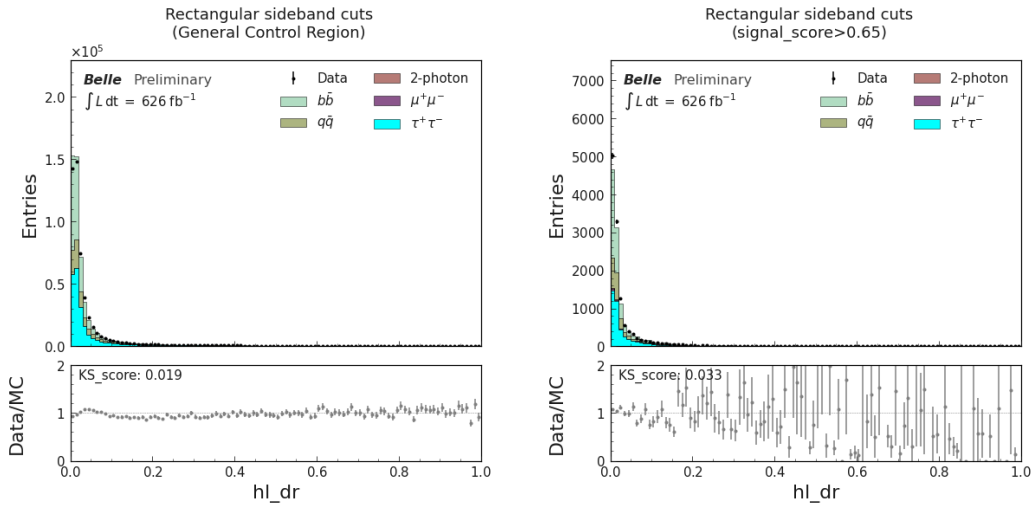


Figure 45. Distribution of a BDT input variable in general control region (left) and signal region (right).

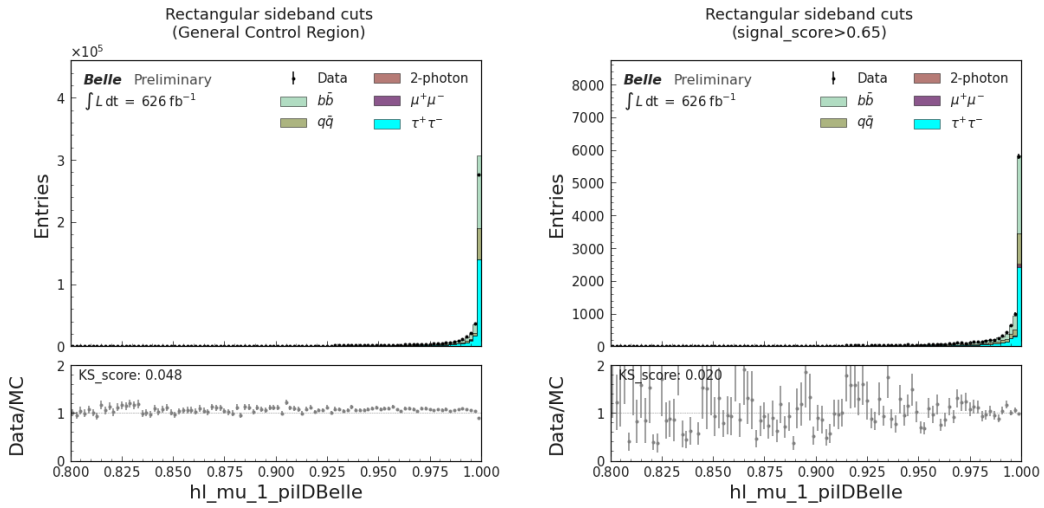


Figure 46. Distribution of a BDT input variable in general control region (left) and signal region (right).

APPENDIX E: BDT DIAGNOSTIC PLOTS

Kolmogorov-Smirnov test for overtraining detection

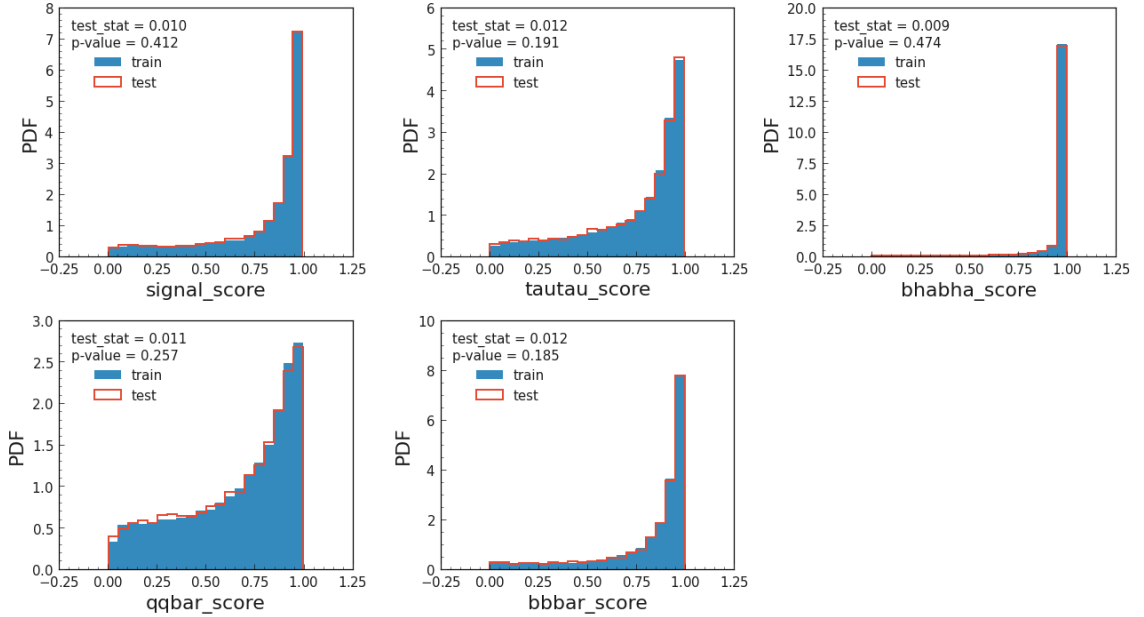


Figure 47. Distributions of each BDT score for train and test datasets, in $\phi_L \rightarrow e^+e^-$ channel. The result of the Kolmogorov-Smirnov test is shown in the plots.

Fig. 47 shows the distributions of each BDT score for train and test datasets, in $\phi_L \rightarrow e^+e^-$ channel. The result of the Kolmogorov-Smirnov test shows no evidence of overtraining.

Fig. 48 shows the distributions of each BDT score for train and test datasets, in $\phi_L \rightarrow \mu^+\mu^-$ channel. The result of the Kolmogorov-Smirnov test shows no evidence of overtraining.

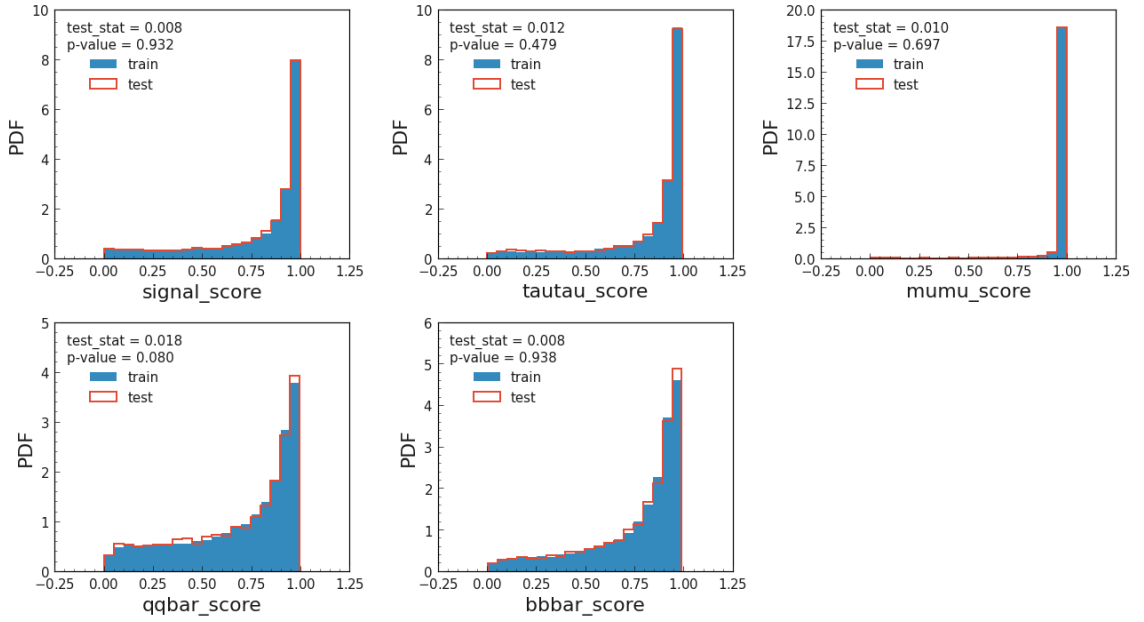


Figure 48. Distributions of each BDT score for train and test datasets, in $\phi_L \rightarrow \mu^+ \mu^-$ channel. The result of the Kolmogorov-Smirnov test is shown in the plots.

ROC curves and AUC scores

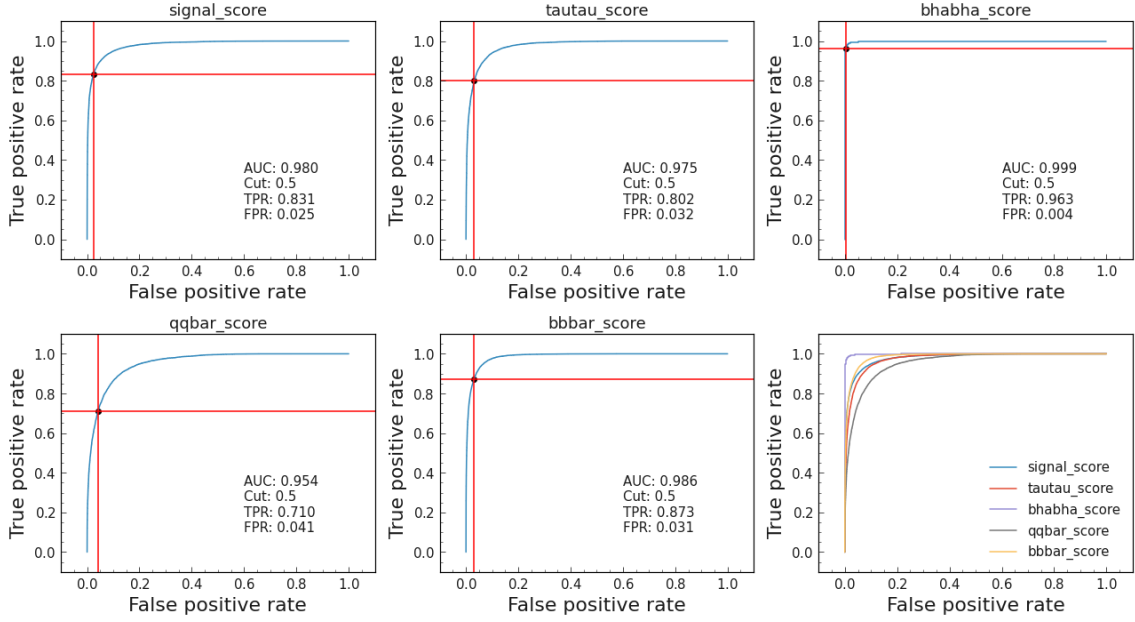


Figure 49. ROC curve for each BDT score for train and test datasets, in $\phi_L \rightarrow e^+e^-$ channel. The TPR and FPR values are shown for the cut at 0.5.

Fig. 49 shows the receiver operating characteristic (ROC) curve for each BDT score, in $\phi_L \rightarrow e^+e^-$ channel. The area under the curve (AUC) score is also shown for each BDT score. The true positive rate (TPR) and false positive rate (FPR) are shown for the cut at 0.5 for the corresponding BDT score.

Fig. 50 shows the receiver operating characteristic (ROC) curve for each BDT score, in $\phi_L \rightarrow \mu^+\mu^-$ channel. The area under the curve (AUC) score is also shown for each BDT score. The true positive rate (TPR) and false positive rate (FPR) are shown for the cut at 0.5 for the corresponding BDT score.

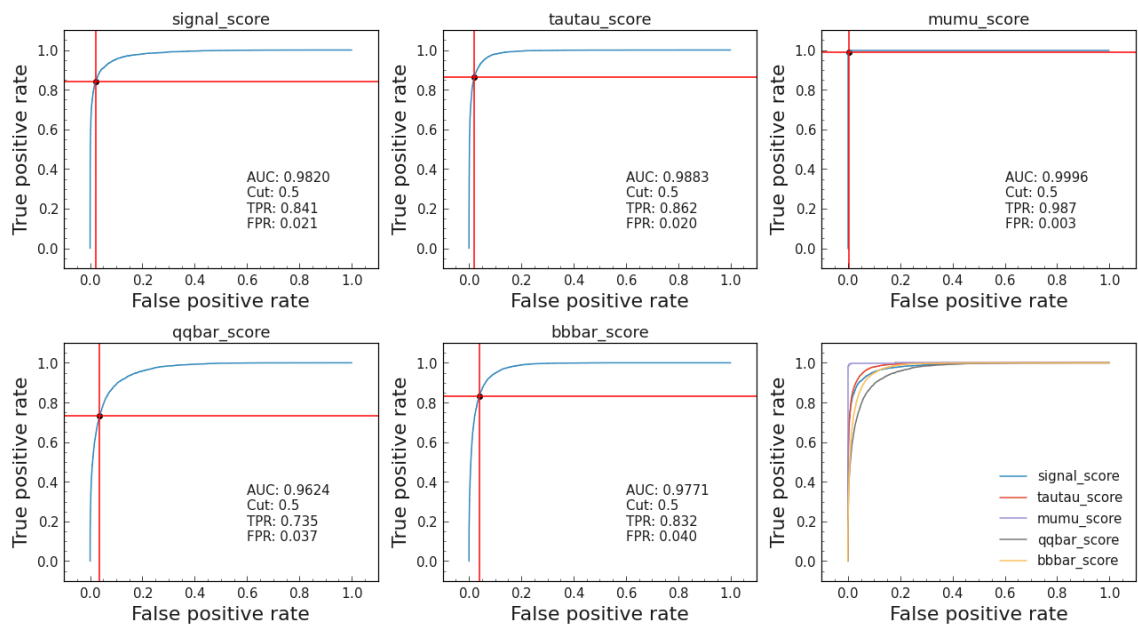


Figure 50. ROC curve for each BDT score for train and test datasets, in $\phi_L \rightarrow \mu^+ \mu^-$ channel. The TPR and FPR values are shown for the cut at 0.5.

CURRICULUM VITAE

Diptaparna Biswas

Education

M.S., University of Louisville, KY, May 2019

M.S., Indian Institute of Science, Bangalore, India, June 2017

B.S., Indian Institute of Science, Bangalore, India, June 2016

Professional Positions

Graduate Research Assistant in University of Louisville, June 2022 - July 2022

Graduate Teaching Assistant in University of Louisville, January 2022 - May 2022

Graduate Research Assistant in University of Louisville, August 2022 - December 2022

Ozaki Exchange Program Fellow, August 2019 - July 2021

Graduate Teaching Assistant in University of Louisville, August 2017 - July 2019

Honors and Awards

2022: Schwartz Award from University of Louisville, for outstanding graduate student performance.

2020: Ozaki fellowship, funded by US Department of Energy, renewed for the second year.

2019: Selected for Ozaki Exchange Program, funded by US Department of Energy.

2016: Scored full marks in physics subject test of the Graduate Record Examinations (GRE).

2016: Scored full marks in the quantitative part of general Graduate Record Examinations (GRE).

2014: Selected as fellow of Indian Academy of Science (IAS) organization.

2012: 1st year topper in National Graduate Physics Examination (NGPE).

2012: First in district and ranked in the top 20 in Higher Secondary (12th Standard) examination.

2012: All India Rank: 1434 (amongst around 500,000 students) in IIT Joint Entrance Examination.

2012: Ranked 128 (amongst 100,000 students) in West Bengal Joint Entrance Examination.

2011: Recipient of the prestigious Kishore Vaigyanik Protsahan Yojana (KVPY) fellowship, a National Program of Fellowship in Basic Sciences, funded by the Department of Science and Technology, Government of India (All India Rank - 165).

2009: National Science Olympiad medallist organized by all India Science Olympiad Foundation.

2009: National Cyber Olympiad medallist organized by all India Science Olympiad Foundation.

2008: National Talent Search Examination qualifier (8th Grade).

2007: Science Talent Search Examination, Silver medallist (7th Grade).

2006: Science Talent Search Examination qualifier (6th Grade).